Ole Vegard Solberg

3D ultrasound and navigation – Applications in laparoscopic surgery

Thesis for the degree philosophiae doctor

Trondheim, November 2010

Norwegian University of Science and Technology
Faculty of medicine
Department of circulation and medical imaging

3D ultralyd og navigasjon – Anvendelser i laparoskopisk kirurgi

Bruken av intraoperativ navigasjon har blitt et verdifullt verktøy på flere kliniske områder. Ofte er bare preoperative bilder brukt under navigasjon, og endringer som skjer under operasjonen vil dermed ikke gjenspeiles. Introduksjonen av intraoperativ 2D og 3D ultralyd kan bli et viktig verktøy innenfor feltet bildestyrt navigasjon, siden dette kan gi kirurger oppdaterte bilder å navigere ut fra i flere typer operasjoner. Denne PhD-en er et forsøk på å forbedre minimalinvasiv kirurgi, hovedsakelig gjennom å forbedre bildesyrt navigasjon, og øke kunnskapen om, og bruk av frihånds 3D ultralyd. For å oppnå dette har jeg forsket på ulike aspekter med frihånds 3D ultralyd rekonstruksjonsalgoritmer: ulike implementasjoner, beregningstid og data-kilder. I forskningsgruppen vår har vi utviklet en prototyp forsknings- og utviklings-plattform kalt CustusX, for navigasjon i minimalinvasiv kirurgi. CustusX kan importere ulike medisinske bilder og verktøy for navigasjon. Dette gir kirurger mulighet til interaktivt å styre visningen av medisinske bilder under inngrepet. Ved hjelp av CustusX har vi utforsket ulike visualiseringer av 2D og 3D bilder sammen med kirurgiske instrumenter. I mitt arbeid har jeg fokusert på bildestyring av laparo-skopisk kirurgi (kikkhullskirurgi), som er minimalinvasiv kirurgi utført gjennom små snitt. Ved å tilby ultralyd i tillegg til endoskopbilder, vil kirurgen også kunne få tilgang til sanntidsbilder under overflaten av organene. Vi har også testet en integrasjon av et mikroposisjoneringssystem med en fleksibel ultralydprobe. Denne løsningen gir korrekt posisjon på sanntids 2D ultralyd bilder, og muligheter for 3D ultralyd opptak. Vi fant ut at nøyaktigheten på de elektromagnetiske posisjons-sensorene var tilfredsstillende, og at bruken av en navigerbar fleksibel ultralydprobe er mulig i en operasjonssetting, noe som vil gi kirurgen viktig informasjon. I det oppsettet vi brukte fant vi at en rask ultralyd rekonstruksjonsalgoritme gav nesten like god kvalitet som en tregere algoritme, og at analog video gav volum med nesten like god kvalitet som digital video. Konklusjonen av dette er at 3D ultralyd rekonstruksjon kan utføres omtrent i sanntid på operasjonsstua ved hjelp av et enkelt oppsett der analog video importeres fra ultralydskanneren. Dette vil gi kirurgen verdifulle bilder for navigasjon. Bruken av navigasjon i laparoskopisk kirurgi er lovende, men teknologien må utvikles videre for å kunne bli praktisk brukbar i de fleste kliniske situasjoner.

Ole Vegard Solberg
Institutt for sirkulasjon og bildediagnostikk, NTNU
Avdeling for Medisinsk teknologi, SINTEF Teknologi og samfunn
Hovedveiledere: Toril A. Nagelhus Hernes, Hans Torp
Biveileder: Richard E. Blake
Finansieringskilder: Norges Forskningsråd (FIFOS). Helse- og sosialdepartementet (Nasjonalt kompetansesenter for 3D ultralyd). SINTEF Teknologi og samfunn, Medisinsk teknologi

Ovennevnte avhandling er funnet verdig til å forsvares offentlig for graden philosophiae doctor (PhD) i medisinsk teknologi.
Disputas finner sted i seminarrommet 2. etg., 1902 bygget, tirsdag 8. Februar 2011 kl. 1215

Abstract

The use of intraoperative navigation during surgery is becoming a valuable tool in several clinical applications. Often only preoperative images are used during navigation and changes that occur during surgery are hence not displayed. The introduction of intraoperative 2D and 3D ultrasound may provide an important addition to the field of image-guided surgery allowing more accurate guidance of various procedures due to updated images. During my thesis I have sought to improve minimally invasive therapy procedures, mainly through improving image guided navigation, and increasing the knowledge and usage of freehand 3D ultrasound volumes. In order to achieve this I have performed research on different aspects of 3D freehand ultrasound reconstruction algorithms: various implementations, computation time, quality, and input data sources. In our research group we have developed a prototype research and development platform, CustusX, for navigation in minimally invasive therapy. The system can import and display a range of medical images and tracked surgical tools, allowing surgeons to interactively control the display of medical images during surgery. By using CustusX we have explored various visualizations of different 2D and 3D images together with surgical instruments. In my work I have focused on image guidance of laparoscopic surgery, which is minimally invasive therapy performed through small incisions. By complementing endoscopy with ultrasound the surgeon will gain access to real-time information beyond the surface of the organs. The integration of micro positioning systems with tracked 2D and reconstructed 3D ultrasound with a flexible intraoperative ultrasound probe was tested. We found that the accuracy of the electromagnetic position sensors was satisfying and that the use of a navigated flexible ultrasound probe was feasible in the operating room, providing the surgeon with important information. In our setup we found that a fast ultrasound reconstruction algorithm performed almost as good as a slower algorithm, and video grabbed analog data gave volumes almost as good as the digital data. In conclusion we found that 3D ultrasound reconstruction may be performed in near real-time in the operating room using a simple setup with grabbing the analog video signal from an ultrasound scanner, providing the surgeon with valuable images for guidance. The use of navigation in laparoscopic surgery is promising, but the technology needs further development in order to be practically efficient and usable in most clinical procedures.

Preface and acknowledgements

This thesis is submitted for partial fulfillment of the requirements for the degree of PhD in Medical Technology at the Faculty of Medicine at the Norwegian University of Science and Technology (NTNU). The research work was performed at the Department of Medical Technology, SINTEF Technology and Society, in the period 2005-2010 in collaboration with the University Hospital in Trondheim (St. Olavs Hospital), the Department of Circulation and Medical Imaging, Faculty of Medicine, NTNU, and the National Centre of 3D ultrasound.

My main supervisor in the period from 2005-2007 has been Professor Hans Torp, and in the period 2007-2010 my main supervisor has been Professor II Toril A. Nagelhus Hernes, both at the Department of Circulation and Medical Imaging, Faculty of Medicine, NTNU. Toril A. Nagelhus Hernes is in addition head of the Department of Medical Technology, SINTEF Technology and Society. Professor Richard E. Blake at the Department of Computer and Information Science, Faculty of Information Technology, Mathematics and Electrical Engineering, NTNU has been co-supervisor.

During the period from 2005-2009 the work was supported by the Research Council of Norway through the FIFOS Programme Project 152831/530; The work has also been supported by the Ministry of Health and Social Affairs of Norway, through the National Centre of 3D Ultrasound in Surgery; and by SINTEF Technology and Society, where I am currently employed.

I wish to thank my supervisor Toril A. Nagelhus Hernes and my colleague Frank Lindseth for invaluable help and guidance during the work with my PhD thesis. I also like to thank all my other co-authors for contributing to the papers: Thomas Langø, Geir-Arne Tangen, Hans Torp, Richard E. Blake, Lars Eirik Bø, Sebastien Muller, Janne Beate Lervik Bakeng, Ronald Mårvik, Brynjulf Ystgaard, Anna Rethy, Torleif Sandnes, Andinet A. Enquobahrie, Luis Ibáñez, Partick Cheng, David Gobbi and Kevin Cleary. In addition I wish to thank everyone, both former and present members, at the department of Medical Technology at SINTEF Technology and Society for eagerly supplying aid when needed and for creating such a good work environment, inspiring me to start the PhD study in the first place.

Finally, I want to thank my family for all support, especially my beloved wife Inger-Lise for your love and understanding.

Trondheim, November 2010

Contents

List of papers

Paper I: Solberg OV, Lindseth F, Torp H, Blake RE, Hernes TAN. Freehand 3D Ultrasound Reconstruction Algorithms--A Review. Ultrasound Med Biol 2007; 33: 991-1009.

Paper II: Solberg OV, Lindseth F, Bø LE, Muller S, Bakeng JBL, Tangen GA, Hernes TAN. 3D ultrasound reconstruction algorithms from analog and digital data. In Press, Ultrasonics, 2010.

Paper III: Langø T, Tangen GA, Mårvik R, Ystgaard B, Yavuz Y, Kaspersen JH, Solberg OV, Hernes TAN. Navigation in laparoscopy – Prototype research platform for improved image-guided surgery. Minim Invasive Ther Allied Technol (MITAT) 2008; 17: 17-33.

Paper IV: Solberg OV, Langø T, Tangen GA, Mårvik R, Ystgaard B, Rethy A, Hernes TAN. Navigated ultrasound in laparoscopic surgery. Minim Invasive Ther Allied Technol (MITAT) 2009; 18: 36-53.

Paper V: Solberg OV, Tangen G-A, Lindseth F, Sandnes T, Enquobahrie AA, Ibáñez L, Cheng P, Gobbi D, Cleary K. Integration of a real-time video grabber component with the open source image-guided surgery toolkit IGSTK. Proceedings of Medical Imaging 2008: PACS and Imaging Informatics, San Diego, CA, USA: SPIE 2008; 6919: 69190Z-69199.

Note on contributions

Table 1: My contribution on the different phases of the papers. Divided into 3 categories: Main – I performed most of the work. Major – I performed a large part of the work, usually in collaboration with other authors (e.g. co-authorship). Minor – I gave contributions through the process, but not as much as the main author(s).

	Paper I	Paper II	Paper III	Paper IV	Paper V
Protocol and research design	Main	Main	Minor	Major	Main
Software development	Major	Major	Major	Major	Main
Data collection	Main	Main	Minor	Major	Main
Data analysis and statistics	Main	Main	Minor	Major	Main
Scientific discussions	Main	Main	Minor	Major	Main
Literature review	Main	Main	Minor	Major	Main
Writing the article	Main	Main	Minor	Major	Main

Additional publications during the PhD study

Solheim O, Selbekk T, Løvstakken L, Tangen GA, Solberg OV, Johansen TF, Cappelen J, Unsgård G. Intrasellar ultrasound in transsphenoidal surgery - a novel technique. Neurosurgery 2010; 66: 173-186.

Hernes TAN, Lindseth F, Selbekk T, Rygh OM, Tangen GA, Rasmussen I, Wollf A, Rasmussen I Solberg OV, Harg E, Augdal S, Couweleers F, Unsgaard G. Technical developments for improved 3D ultrasound guided neurosurgery - Computer-assisted 3D ultrasound-guided neurosurgery: technological contributions, including multimodal registration and advanced display, demonstrating future perspectives. International Journal of Medical Robotics and Computer Assisted Surgery 2006; 2: 1: 45-59.

Additional conference proceedings during the PhD study

Wollf A, Tangen GA, Solberg OV, Kaspersen JH, Langø T, Hernes TAN, Mårvik R. Real-time endoscope and ultrasound integration in computer assisted navigated surgery. In Proceedings of Computer Assisted Radiology and Surgery (CARS), Berlin, Germany 2005; June 22-25: 606-611.

Background

Image-guided surgery and navigation

In image-guided surgery (IGS), images are used to guide the surgical instrument to the lesion inside the patient. With the help of image guidance more patients may be treated with minimally invasive therapy. The advantages of minimally invasive therapy are shorter rehabilitation time, and reduced social costs and patient disadvantages. Optimal use of IGS requires:

- Preoperative image acquisition and image visualization for diagnostics and preoperative therapy planning.
- Registration of preoperative images and visualization in the operating room for planning just prior to surgery.
- Intraoperative image acquisition and visualization, and navigated instruments for guidance.
- Postoperative imaging and visualization for evaluation of therapy.

Computed tomography (CT) and magnetic resonance imaging (MRI) are often used as the preferred preoperative imaging modalities in IGS (Cleary and Peters 2010). Even though these modalities are possible to use during surgery, there are still some significant practical limitations, due to cost, equipment adaptation in the magnetic field, user friendliness, image quality, and radiation. Ultrasound may in many cases be a better choice for intraoperative imaging. Especially, intraoperative 3D ultrasound offers the advantages of visualizing arbitrarily oriented 2D images through the 3D volume as well as volume rendering and 3D segmentations of objects (Lindseth et al. 2003). However, compared to other modalities, ultrasound images may be more difficult to interpret, are limited to a smaller part of the body, and it may hence be difficult to use for inexperienced uses. Therefore, an optimal use of intraoperative ultrasound images may be in combination with preoperative images from other modalities. In neuro navigation IGS systems are used in daily practice (Hata et al. 1997; Gumprecht et al. 1999; Gronningsaeter et al. 2000). However, in laparoscopic surgery commercial systems are not available. Because of this we have developed the CustusX research system (fig 1) that is used for image guidance in several different clinical areas.

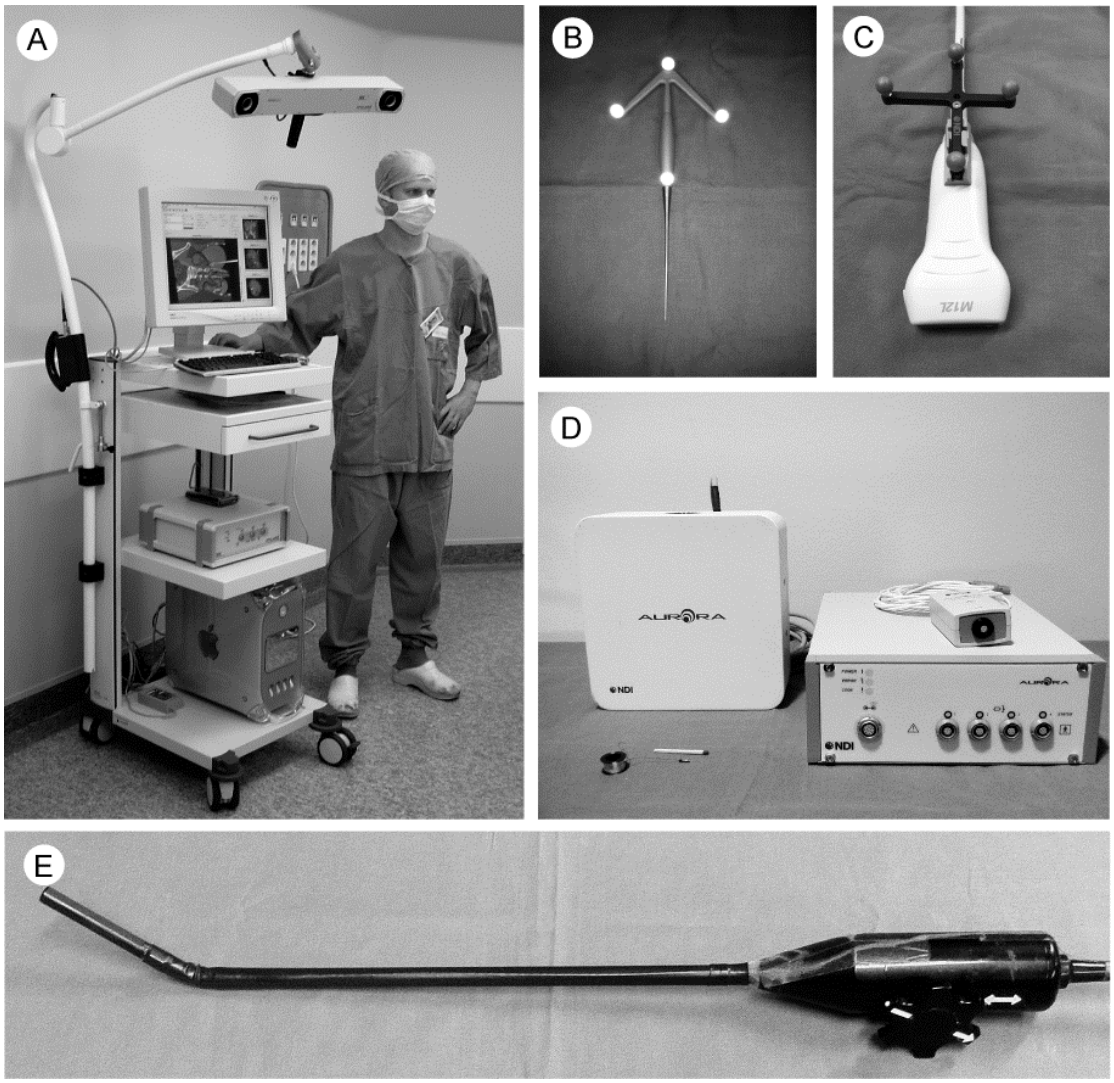

Fig. 1: a) The prototype surgical navigation system, CustusX with Polaris camera arm. b) Pointer with Polaris tracking spheres. The flash in the camera is used to illustrate the reflective spheres. c) Ultrasound probe with Polaris tracking frame. d) Aurora tracking system. A single Aurora 6D sensor (size: 0.8 x 12 mm) can be seen in the picture in front of the match. e) A laparoscopic ultrasound probe with 2 miniature 5D Aurora sensors attached to the tip.

Position tracking and instrument calibration

In IGS, tracking technologies are used for knowing the positions and orientations of the various instruments used. There are four common technologies to track medical instruments: Mechanical, acoustical, electromagnetic and optical, which are described in detail by Cinquin et al. (1995). Mechanical localizers are articulated arms that calculate the position and orientation at the tip by angle information from each joint. Acoustical position trackers consist of emitters and receivers of ultrasonic waves. Electromagnetic tracking systems generate an electromagnetic field and measure

induced electrical currents in small receiver coils. An example of this is the Aurora (NDI, Canada) system shown in fig. 1d, and embedded in the probe in fig. 1e. Optical tracking systems use multiple cameras to track passive (infrared light reflectors) or active (infrared light emitting diodes) markers placed in a rigidly defined geometry. See figs. 1a-c for an example (Polaris Spectra, NDI, Canada) of tracking cameras and tracking frames with reflectors mounted on different instruments.

To track an instrument a position sensor must be attached to the instrument or the instrument must be physically attached to the tracking system, depending on the system used. The positions from the tracking systems used in IGS are used to show the location of surgical instruments both inside and outside the body (fig. 2). A calibration procedure is needed for each instrument in order for it to be used for IGS, as the position and orientation of the tip of the instrument must be determined in relation to the attached sensor. Most instruments may be calibrated with a pointer calibration (Leotta et al. 1997), by rotating the instrument about the tip.

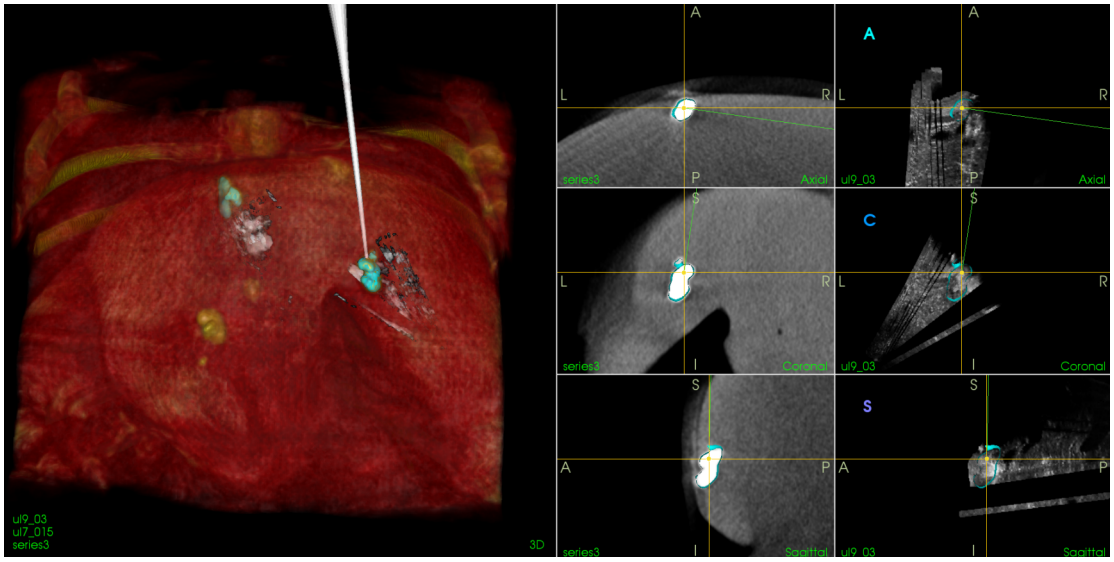

Fig. 2: 3D renderings of medical data together with a tracked pointer. To the left: Volume rendering of DynaCT in red and yellow with segmented structures from the DynaCT in cyan. In the image are also volume renderings of two different ultrasound volumes shown in gray, and a visualization of the tracked pointer. In the middle: Axial, coronal and sagittal slices through the DynaCT volume, with the segmented structures shown in cyan. To the right: Axial, coronal and sagittal images through one of the ultrasound volumes with the segmented structures from DynaCT shown in cyan. The images are taken from a pig study.

Basic ultrasound principles

The definition of ultrasound is sound waves with frequencies above the audible range (greater than 20 kHz). The ultrasound frequencies used in medicine usually range from 2-10 MHz, but higher frequencies may also be used. Higher frequencies will give higher resolution, but reduced penetration / imaging depth. In ultrasound imaging, the sound waves are usually emitted in short pulses created by piezoelectric materials. The speed of sound varies in different kind of tissue (or materials) due to differences in mass density and volume compressibility. The transitions between areas with different sound speeds generate partial reflections (or echoes). Even only the small sound variations as in body tissue will create echoes [In body tissues other than fat and bone the speed of sound only varies 0.2-0.3% (Angelsen, 2000)]. This is the basis of the pulse echo principle used for ultrasound imaging. In addition to the echoes from the tissue boundaries, also small structures within the tissue (called scatterers) create echoes, showing "structure" in otherwise homogenous tissue.

The echoes from each ultrasound pulse are sampled at certain intervals, creating data as a 1D beam. The positions of the structures are estimated using the speed of sound and the time from emission of the ultrasound pulse to the return of the echo. The possible resolution in the depth (axial) direction is dependant on the pulse length, which again depends on the ultrasound frequency and ultrasound probe and scanner hardware. Different 1D beams are placed close to each other to create a 2D image. These 1D beams are usually positioned by electronically steering and/or focusing the ultrasound beam by delaying the signals from the ultrasound probe elements in specific patterns (fig. 3). The 1D beams are usually positioned perpendicular to the ultrasound probe face for linear and curved linear ultrasound arrays (fig. 1e and figs. 4a, b). A phased array steers the beams electronically in different angles to the probe face, while annular arrays steers the beam mechanically.

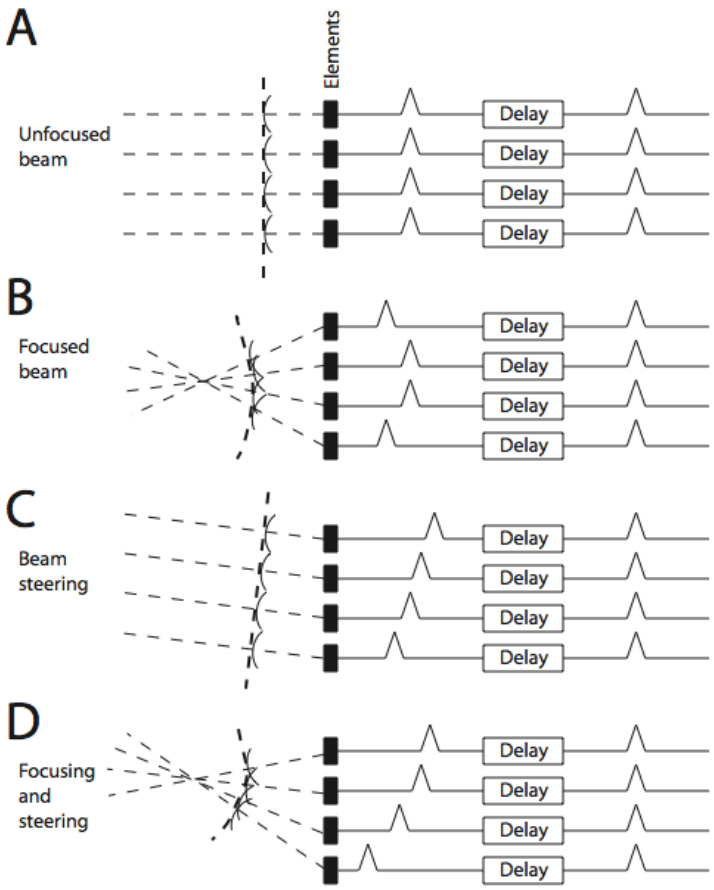

Fig. 3: Illustration of the electronic focusing and steering of an ultrasound probe. The array of an ultrasound probe consists of several elements (e.g.: 64, 128, or more). To simplify only 4 are shown in the illustrations. a) If each element emits a pulse at the same time the beam will be unfocused. b-d) The beam may be focused and/or steered by using delays to have the elements emit their pulses in certain orders.

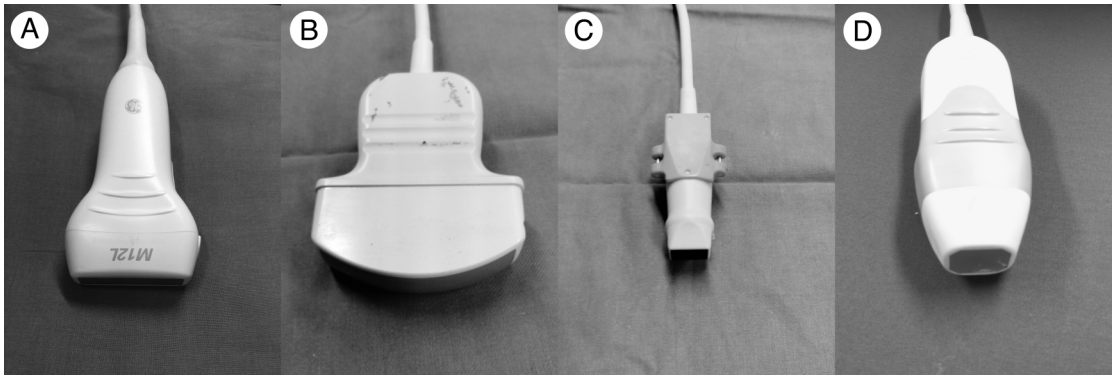

Fig. 4: Different ultrasound probe types. a) Linear array. b) Curved linear array. c) Pulsed array. d) 3D probe (2D matrix-array).

The data from the 1D beams are processed (with envelope detection and log compression) and combined into 2D images. The 1D beams of the curved linear and

phased array probes (figs. 4b, c) are in Polar coordinates and have to be translated to Cartesian, while the linear array probes (fig. 1e and fig. 4a) already have the 1D beams in Cartesian coordinates and only need to scale the images correctly. Although the 2D ultrasound images are usually presented with no thickness an ultrasound image is really a composition of signals from a "small volume" depending on the focusing of the ultrasound probe in the elevation direction. The elevation focus is often obtained by using an acoustic lens that gives a fixed elevation focus (fig. 5a). In order to get more advanced elevation focus the ultrasound probe must have more than one row of elements. These arrays of these probes are called 1.25D, 1.5D, 1.75D or 2D arrays in contrast to single-row arrays called 1D arrays (Wildes et al. 1997):

1D: Elevation aperture is fixed, and focused at a fixed range.

1.25D: Elevation aperture is variable, but focusing remains static.

1.5D: Elevation aperture, shading and focusing are dynamically variable, but symmetric about the centerline of the array.

1.75D: A 1.5D array without the symmetry constraint. Elements are large in elevation, so very little steering is possible.

2D: Elevation geometry and performance are comparable to azimuth (lateral direction), with full electronic apodization, focusing and steering.

To avoid confusion: 1D arrays create 2D images, and 2D arrays create 3D volumes. The ultrasound scanner also usually allows several configurable lateral focus points using electronic focusing (figs. 3b, d).

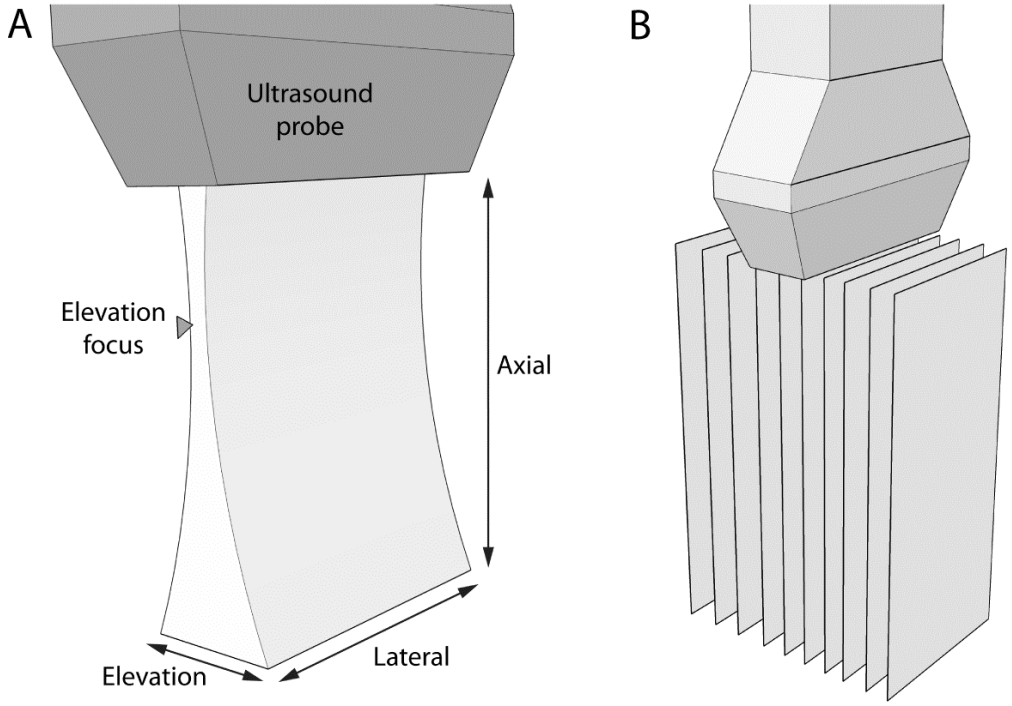

Fig. 5: Illustration of the imaging sector of an ultrasound probe and the image positions of a freehand 3D ultrasound acquisition, performed as a parallel sweep. a) Illustration of the extent of the imaging sector of an ultrasound probe. The lateral, axial and elevation direction are marked in addition to a fixed elevation focus. b) Several 2D ultrasound images may be collected together with their positions. By using a reconstruction algorithm this data may be combined to form a 3D volume. As illustrated in a) each ultrasound image has in reality some thickness, and is not as thin as shown in the illustration.

Ultrasound in image-guided surgery

Ultrasound probes may also be tracked with the help of a tracking system by attaching a position sensor to the ultrasound probe. The ultrasound images may either be shown directly in real-time with the IGS software at the correct position inside the patient's body, or used to create a 3D volume that is placed at the correct position alone or relative to already acquired images and tracked instruments (fig. 2). Due to the nature of the ultrasound images, tracking of an ultrasound probe is possible by utilizing the nature of the ultrasound speckle in the image (Laporte and Arbel 2008) or by a special probe construction such as the I-beam probe (Hossack et al. 2000). However, such tracking methods don't provide the same accuracy as position sensors.

3D ultrasound images may either be directly acquired with 3D ultrasound probes (fig. 4d) or by tracking 2D ultrasound probes (fig. 1e and figs. 4a-c). 3D ultrasound probes

consist of two types: The mechanically swept probe, basically sweeping a 1D array in a fixed pattern (Prager et al. 2010), and the 2D matrix-array transducer acquiring 3D images directly. When using tracked 2D probes a freehand scan is usually performed (fig. 5b) and the 3D image is created with a 3D reconstruction algorithm. 3D probes, especially 2D array probes, will allow both easy acquisition of near real-time 3D data and the possibilities of 3D data with time as a fourth dimension. On the other hand, the advantages of tracked 2D probes over 3D probes are:

- The data from the 3D probe are not yet easily available to third party ISG applications.
- 3D volumes can be achieved with any specialized ultrasound probe, while the selection of 3D probes is still limited.
- The volume covered by a 3D probe is much smaller than is practical in most IGS applications, however this limitation might be overcome by creating an application for combining data from the 3D probe into a larger volume.
- Currently the data stream from the ultrasound probe is limited due to physical limitations (Prager et al. 2010). This means it is possible to get a higher resolution volume from a 2D probe than a 2D array probe. (A mechanically swept 3D probe should be able to achieve resolution closer to that of a 2D probe.)
- 3D probes may interfere more with some kinds of electromagnetic tracking systems that 2D probes (Hastenteufel et al. 2006).
- The cost of 2D ultrasound probes are less than 3D probes.

A disadvantage of tracked 2D probes is that the visualized tissue must be stationary because of the time needed for the 3D acquisition. Also the need of an external tracking device makes this method more cumbersome. In addition the elevation resolution (fig. 5a) of 2D probes (figs. 4a-c) are usually much poorer than the resolution in the other directions, while a 2D array probe (3D probe) can have the same resolution in both the elevation and lateral direction.

There exist a lot of different algorithms for reconstructing 3D volumes from freehand 2D ultrasound images (Paper I). The three main algorithm groups are:

- Voxel-Based Methods. Each voxel in the 3D volume is assigned an appropriate value, based on the pixel values of the nearby 2D images.

- Pixel-Based Methods. The value of each pixel in the 2D images is added to the nearest voxel(s) in the 3D volume. When several values are added to the same voxel some sort of averaging / preference is used. After the first step of adding the pixel values an interpolation step is usually performed to fill empty voxels.
- Function-Based Methods. Functions are created based on the pixel values in the 2D images, and the 3D volume is created by evaluating these functions at regular intervals.

For a tracked ultrasound probe the position and orientation of the 2D ultrasound image must match the position of the tissue visualized, and several spatial calibration methods exist (Mercier et al. 2005; Hsu et al. 2008). In addition to the spatial calibration the ultrasound probe may also need a temporal calibration (Treece et al. 2003; Rousseau 2006) since both the signal from the positioning system and the ultrasound video may have their separate time delays.

Displaying medical images

Most medical images may be displayed either in 2D or 3D, regardless of the image source being 2D or 3D. In addition, data from several sources/modalities may be displayed together. To allow easier presentation of multimodal images a common method is to segment out interesting areas and present these as differently colored surface models. 3D display examples of multimodal images are:

- Rendering of surface models from multiple data sources.
- Volume rendering of one data source, with surface models from other data sources (fig. 6a).
- Volume rendering of multiple data sources (fig. 6b). This usually requires different coloring to distinguish the volumes from each other. Surface models may also be included (fig. 6c).

2D display examples of multimodal images:

- One data source in each 2D display. For 3D data sources, each data source may have several 2D displays showing slices in different directions (e.g. axial, coronal and sagittal: fig. 6d).
- Several data sources are shown in each 2D display, the smaller or more detailed sources obscuring others.

- Several data sources in each 2D display using blending with see-through effects (the use of colors is useful).

The physical positions of the data shown in the different 2D views may be linked, and the same position in all views may be marked with a crosshairs or similar (figs. 6b-d). 3D and 2D may also be combined in one 3D display by showing the 2D with correct placement in 3D. Several different 3D volume rendering methods width different rendering speed and quality may be used (Karadayi et al. 2009). Different transfer functions and filters may also improve the volume quality. Fast, relatively high quality volume rendering is available today with graphics processing units (GPUs).

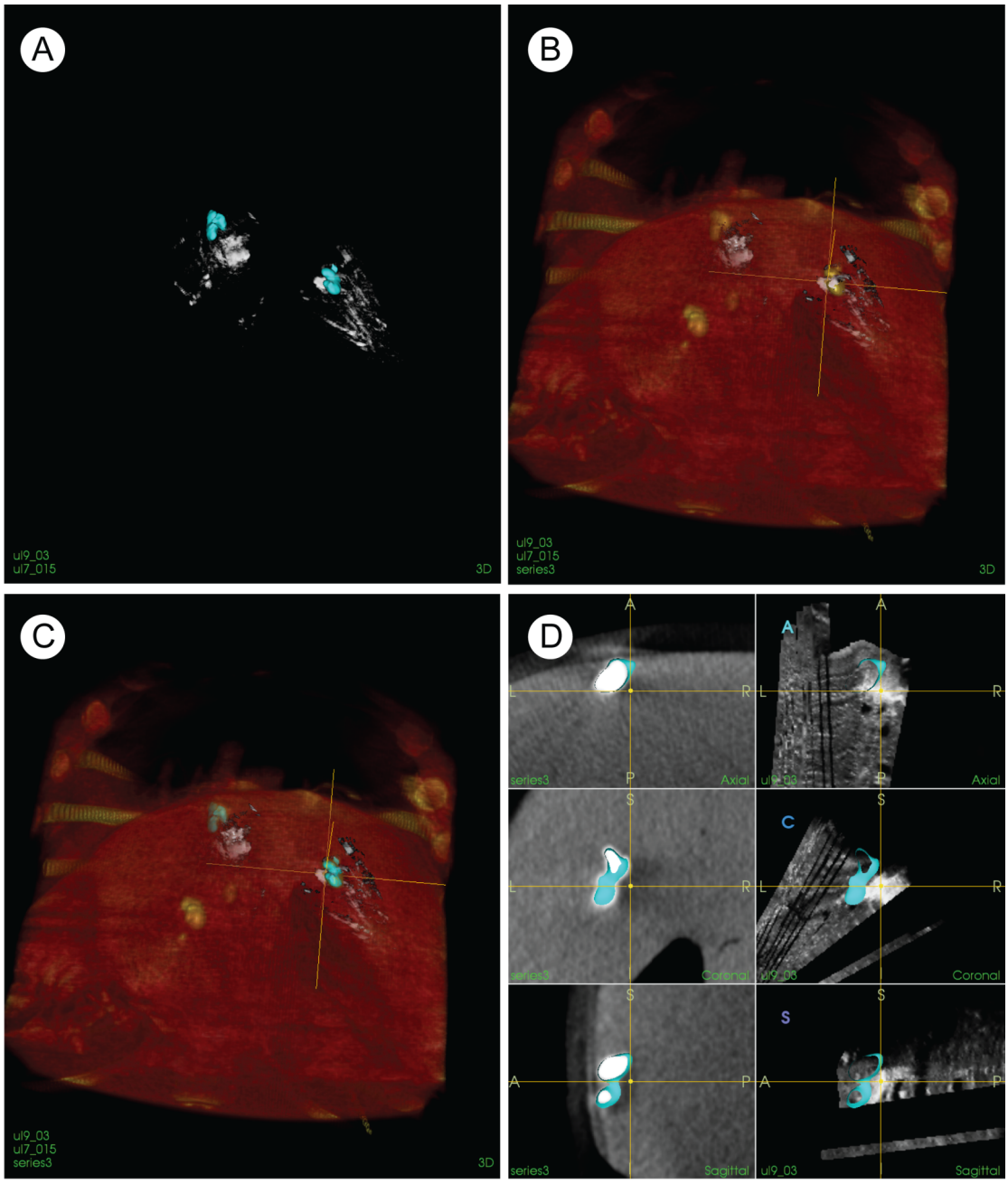

Fig. 6: Different ways of displaying medical images. The images are taken from a pig study. a) 3D rendering from one data source (ultrasound) and 3D surface models (cyan) from another (DynaCT). b) Volume rendering of two different data sources. Ultrasound is shown in gray and DynaCT in red and yellow. c) Volume renderings of ultrasound and dynaCT. In addition the surface models from the DynaCT in also shown. d) Axial, coronal and sagittal view of the two different volumes, with the corresponding position marked in each. A shift between the ultrasound and DynaCT is visible.

Aims of study

The goal of this PhD project was to develop technology that can help include more clinical cases for minimally invasive therapy. The means to achieve this goal was through research on intraoperative 3D ultrasound, both alone and in conjunction with preoperative images in a navigation system. This was accomplished through concentrating on the following topics:

- *Freehand ultrasound reconstruction algorithms*, exploring and understanding the algorithms and their quality and time consumption (Paper I and II).
- *Ultrasound reconstruction quality*, identifying and comparing the impact from different factors like: algorithms, positioning systems, distortions of electro-magnetic positioning, ultrasound data sources, and ultrasound probe calibration (Paper I, II and IV).
- *Integrating 3D ultrasound in laparoscopic surgery* by investigation the possible use and accuracy of a flexible navigated ultrasound probe (Paper III and IV).
- *Feasibility study and integration of software for a navigated surgery system*, with the aid of open source toolkits. Application for laparoscopic surgery was emphasized (Paper III, IV and V).

The usability of image-guided surgery depends partly on the usefulness of the navigation system. Correctly positioned intraoperative 2D and 3D ultrasound may enhance a navigation system and allow the surgeon to threat a wider range of clinical cases with minimally invasive therapy and more real-time information may lead to better procedures. In addition a wider use of ultrasound may lead to lower radiation doses for patients.

Summary of papers

Paper I - Freehand 3D Ultrasound Reconstruction Algorithms--A Review

3D ultrasound volumes may be created with regular 2D ultrasound probes by using both the 2D images and the position information of these images. This paper describes most freehand 3D reconstruction algorithms with illustrations and pseudo code implementations for some of the algorithms. The different algorithms were sorted into three groups: Voxel-Based Methods, Pixel-Based Methods and Function-Based Methods. An overview of algorithm time consumption was also created, based on published data.

Paper II - Comparison of methods for freehand 3D ultrasound reconstruction from analog and digital data

As described in Paper I, many 3D ultrasound reconstruction algorithms exist. Paper II compares two different reconstruction algorithms and three different data sources: Analog video, digital video and digital scan-line data. The comparisons were performed using novel comparison methods for detecting potential differences in image quality of the reconstructed volumes. The assessments were based on a number of image criteria: detectability of wire targets, spatial resolution, detectability of small barely visible structures, subjective tissue image quality, and volume geometry. In addition we also performed the more “traditional” comparison of reconstructed volumes by removing a percentage of the input data. The quality of images resulting from both reconstruction algorithms and data sources from one scanner was compared. The results showed that in our setup the choice of data source were more important than the choice of reconstruction algorithm, and that processed video performed better than the digital scan-line data, digital video performing better than analog in a few comparisons. However, the quality of the two processed video sources where difficult to separate by the comparison methods, indicating that the quality loss of using flexible video grabbing solutions over scanners with digital interface was not significant in our study. However, it must be taken into account that the conclusions are only based on comparisons performed with one probe on one specific scanner.

Paper III - Navigation in laparoscopy – Prototype research platform for improved image-guided surgery

This paper describes the use of our prototype research and development platform, CustusX, for navigation in minimally invasive therapy. CustusX can import and display a range of medical images including real-time data such as ultrasound and X-ray, during surgery. Tracked surgical tools, such as pointers, video laparoscopes, graspers, and various probes, allow surgeons to interactively control the display of medical images during the procedure. In this paper we illustrate the use of the system with examples from two pilots performed during laparoscopic therapy. Finally, we shortly describe an ongoing multicenter study using this surgical navigation system platform.

Paper IV - Navigated ultrasound in laparoscopic surgery

This paper was written as a follow up on Paper III. Laparoscopic surgery is minimally invasive therapy performed through small incisions. These small entry points limit free sight and possibility to palpate organs. Endoscopes provide an overview of organs, but ultrasound will provide real-time information beyond the surface of the organs. In this paper we have performed research in order to explore the possibility of tracked 2D and reconstructed 3D ultrasound combined with 3D CT data in the CustusX prototype navigation system. A flexible intraoperative ultrasound probe was used in the study. We presented two ways of tracking this probe: Either with optical sensors at the shaft with the flexible part locked in one position, or with electromagnetic micro-positioning sensors mounted at the tip of the probe allowing full flexibility. The integration of the micro-positioning sensors was done in our laboratory as a prototype. We evaluated the accuracy of the 3D laparoscopic solution with the electromagnetic position sensors and the use of an electromagnetic tracking in the operating room. While the root mean squared distance error of the laboratory setup was 0.3 mm the error in the operating room setup was 2.3 mm in the center of the measurement volume. However, the surgical instruments and the ultrasound probe added no further inaccuracies.

Paper V - Integration of a real-time video grabber component with the open source image-guided surgery toolkit IGSTK

The image-guided surgery toolkit (IGSTK) is an open source C++ library that provides the basic components required for developing image-guided surgery applications. This conference proceeding describes an integration of a real-time video grabber component to the IGSTK toolkit. The video grabber may be used for importing different real-time intraoperative data such as ultrasound or endoscopic cameras. The video may be displayed in either a 2D window or integrated in a 3D scene. The video grabber component design and example applications using the video grabber component were also presented.

Discussion and future work

The usefulness of Image-guided surgery (IGS) systems is dependant on high quality updated images and accurate instrument positions. In the present PhD we have focused on integrating both 2D and freehand 3D intraoperative ultrasound. The research into 3D reconstruction algorithms and the usability of flexible ultrasound probes may allow ultrasound to be used in a wider range of operations. This may lead to lower radiation doses for patients. The research may also lead to more patients being treated minimally invasive instead of open surgery resulting in shorter patient recovery time. Additionally, this work may lead to improvements in some kind of procedures, giving the surgeon more information than previously available (Solheim et al. 2010)

Some of the work I have performed during the PhD with implementing reconstruction algorithms and ultrasound data import will be included in the new version of the CustusX navigation software. Also the conclusions from the papers, especially Paper II are important for the further development of the CustusX software: Choice of data source might be more important for reconstruction quality than choice of re-construction algorithm. As video-grabbed analog video is readily available for all kinds of ultrasound scanners, it is also important to know that the quality loss by choosing video-grabbed analog video over digital video might be relatively small. However this must be evaluated for the separate scanner, or another study like Paper II could be performed including several scanners to find a general conclusion. Papers III and IV show laboratory experiments with a tracked intraoperative ultrasound probe. We will further improve the system to be suitable for use on patients to further improve the outcome in laparoscopic surgery.

Real-time 3D reconstructions and real-time 3D ultrasound

Currently, graphics processing units (GPUs) have both achieved a lot of processing power and have the ability to perform a lot of processing in parallel. Previously, there were limitations on what kind of algorithms that could be created for GPU processing, and a lot of work might be necessary to create the algorithms. Lately, GPUs have

become able to process all kinds of algorithms, and programming standards like open computing language (OpenCL) allow easier access to GPU programming.

In order to perform 3D reconstruction in real-time or near real-time the use of the parallel computing power to the GPU looks promising. This will make 3D reconstructions more convenient to use. Currently only a few papers are published on this subject (Wein et al. 2006; Karamalis et al. 2009), but more work will be performed on this subject in the future.

Even if the reconstruction is performed in real-time, this will not give a real-time 3D volume. In situations demanding real-time or fast 3D volume acquisition 2D array ultrasound probes (3D probes) are needed. Currently the 2D array probes have some limitations, as mentioned above, but some or all of these may eventually be overcome. If 3D probe resolution may match the resolution of the 2D probes for large real-time volumes the 3D probes will probably be more useful in many more applications and eventually may replace most use of 2D probes, as 3D probes may also create 2D images if necessary. Such improvements may also increase the general use of ultrasound. Another trend that may increase the use of ultrasound is ultrasound scanner miniaturization like the new Vscan ultrasound scanner from GE Healthcare. 3D probe miniaturization (Light et al. 2005) may also play an important part in the use of 3D probes becoming more widespread.

Improving the imaging of a navigation system

The usability of IGS may be improved by providing more useful information in the navigation system. This may be done by providing images from several modalities at the same time; e.g.: CT/MRI + 2D/3D ultrasound. This allows CT/MRI to be used for overview and ultrasound to be used as a source for more details or real-time information. As a surgical procedure proceeds, more and more of the original imaging may not be correct any more and real-time information is essential. In addition to provide updated images, real-time imaging modalities may be important to update positions of anatomy, which again may be used to correct information in the pre-operative images and even deform the images to match the real-time information. A way of achieving this is to register the different images to each other (Reinertsen et al.

2007). The reason for trying to reposition pre-operative images is that they may in some situations give better images or a better overview as well as give added information not available in the intraoperative imaging modality. Other important intraoperative images may be obtained from a microscope or an endoscope. In the future we may also be able to merge these images with the other imaging modalities (see example in Paper III) improving interpretation and information.

Another way of improving IGS is to provide more information from the available data, and present this information in an intuitive way for the surgeon. A method of doing this is to color certain parts of a volume instead of only presenting data in gray-scale. Such coloring may be used in a number of different ways and may improve the surgeons awareness and thus reduce the failure rate.

Dealing with inaccurate areas in a reconstructed 3D volume

3D ultrasound reconstructions from freehand scans may contain different kinds of inaccuracies (Lindseth et al. 2002). This may be due to inaccuracies in the tracking system (see Paper IV), inaccurate probe calibration, varying speed of sound, missing position data, too fast probe movement, tissue movement, or tissue deformation. Especially the electromagnetic tracking systems have poorer accuracy than the optical systems, and they are also much more vulnerable to distortions (Paper IV). While most of these inaccuracies may be difficult to detect they are usually visible in the final 3D volume. This means that they may in theory be detected or corrected by image processing techniques. Tissue deformation in the depth direction may be corrected with the method suggested by Treece and coworkers (Treece et al. 2002); using image correlation techniques for rigid and non-rigid image registration. An application not mentioned by Treece et al. (2002) is that the rigid image registration part of this method should also correct tissue movement in both 2D image directions. The corrected volume may be used directly or be compared with a volume reconstructed without this kind of correction to obtain inaccuracy information. The image correlation used in the correction process may introduce new errors so some kind of inaccuracy visualization may prove a valuable tool if the corrected volumes are to be used for navigation, allowing the user of the software to determine if the data is good enough or if new data must be collected. One way to present detected

inaccurate areas is to show them in a different color in the navigation system (see fig. 7 for an example). Even if no new data are collected the user will still be aware of the areas containing inaccurate data. Some reconstruction algorithms may easily detect missing position data or too fast probe movement from interpolation or similar techniques. Reconstructed volume data over a certain distance from known data could be tagged as inaccurate. This information have never been explicitly presented in any publication even if it may provide the surgeon with vital information, allowing him to decide if another 3D scan is necessary to get more accurate data in certain regions. The inaccurate areas could be shown as the example illustrated in fig. 7.

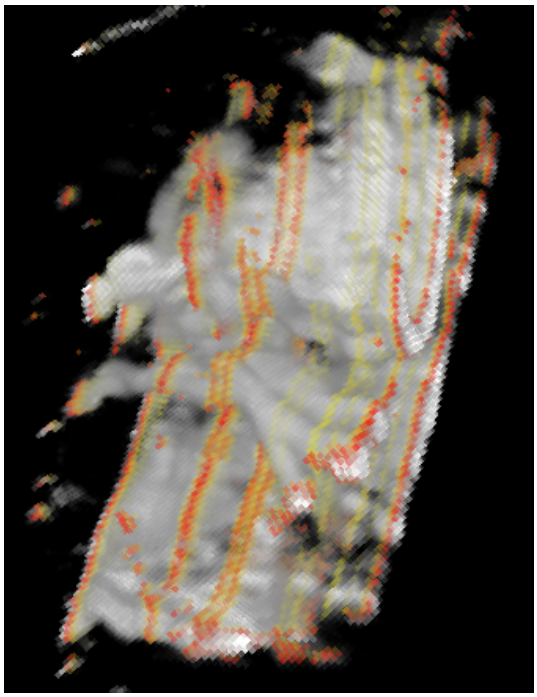

Fig. 7: Example of a 3D ultrasound volume with the inaccurate data colored. The inaccurate data in the illustration are found through interpolation in an ultrasound reconstruction algorithm, but may also be found through other techniques. The data are coded with color after how far the values are from the input data: Yellow is closer than red.

In some situations a visualization of inaccuracies may not be the best solution, as the user of the navigation software may not have the experience or the time necessary to determine the volume quality. Instead of visualizing the inaccuracies, a maximum inaccuracy may be calculated and compared to an acceptable maximum inaccuracy, and the volume may be automatically accepted or rejected. However, not all parts of a 3D volume may be equally important. To make sure only the relevant area of a

volume are considered, the user may be asked to mark a region of interest (ROI) in the 3D volume. This ROI may be used to limit the area to calculate inaccuracies and determine if the volume is to be rejected. The ROI may also be used to improve reconstruction (San José-Estépar et al. 2003) and correlation speed. In addition the ROI may improve image correlation methods by only correlating the most important areas of the images, this is especially important if the correlation are only used for rigid registrations.

Conclusion

Navigation has shown to be useful for exploring improvements in laparoscopic surgical procedures. By integrating micro positioning systems with a flexible intraoperative ultrasound probe real-time information beyond the surface of the organs can be visualized in an intuitive way for the surgeon during the intervention. We found that the accuracy of the electromagnetic position sensors was satisfying for giving valuable information for guidance. Fast ultrasound reconstruction algorithms may perform almost as good as slow algorithms, and video grabbed analog data may give volumes that are comparable to digital video data. 3D ultrasound reconstruction is obtainable in real-time or close to real-time in the operating room. In summary the use of navigation and intraoperative ultrasound in laparoscopic surgery is promising, but the technology needs further development in order to be efficient and usable in most clinical procedures.

References

Cinquin P, Bainville E, Barbe C, Bittar E, Bouchard V, Bricault L, Champleboux G, Chenin M, Chevalier L, Delnondedieu Y, Desbat L, Dessenne V, Hamadeh A, Henry D, Laieb N, Lavallee S, Lefebvre JM, Leitner F, Menguy Y, Padieu F, Peria O, Poyet A, Promayon M, Rouault S, Sautot P, Troccaz J, Vassal P. Computer assisted medical interventions. Engineering in Medicine and Biology Magazine, IEEE 1995;14:254-263.

Cleary K, Peters TM. Image-Guided Interventions: Technology Review and Clinical Applications. Annual Review of Biomedical Engineering 2010;12:119-142.

Gronningsaeter A, Kleven A, Ommedal S, Aarseth TE, Lie T, Lindseth F, Lango T, Unsgard G. SonoWand, an ultrasound-based neuronavigation system. Neurosurgery 2000;47:1373-1379; discussion 1379-1380.

Gumprecht HK, Widenka DC, Lumenta CB. BrainLab VectorVision Neuronavigation System: Technology and Clinical Experiences in 131 Cases. Neurosurgery 1999;44:97-104.

Hastenteufel M, Vetter M, Meinzer HP, Wolf I. Effect of 3d ultrasound probes on the accuracy of electromagnetic tracking systems. Ultrasound Med Biol 2006;32:1359-1368.

Hata N, Dohi T, Iseki H, Takakura K. Development of a Frameless and Armless Stereotactic Neuronavigation System with Ultrasonographic Registration. Neurosurgery 1997;41:608-614.

Hossack J, Sumanaweera TS, Napel S. Quantitative 3D ultrasound imaging using an automated image tracking technique. Proceedings of IEEE Ultrasonics Symposium, 2000;2:1593-1596.

Hsu P-W, Prager RW, Gee AH, Treece GM. Freehand 3D Ultrasound Calibration: A Review. In Advanced Imaging in Biology and Medicine. Springer Berlin Heidelberg 2008;47-84.

Karadayi K, Managuli R, Kim Y. Three-Dimensional Ultrasound: From Acquisition to Visualization and From Algorithms to Systems. Biomedical Engineering, IEEE Reviews in 2009;2:23-39.

Karamalis A, Wein W, Kutter O, Navab N. Fast hybrid freehand ultrasound volume reconstruction. Proceedings of Medical Imaging 2009: Visualization, Image-Guided Procedures, and Modeling, Lake Buena Vista, FL, USA: SPIE, 2009;7261:726114-726118.

Laporte C, Arbel T. Combinatorial and Probabilistic Fusion of Noisy Correlation Measurements for Untracked Freehand 3-D Ultrasound IEEE Trans Med Imaging 2008;27:984-994.

Leotta DF, Detmer PR, Martin RW. Performance of a miniature magnetic position sensor for three-dimensional ultrasound imaging. Ultrasound Med Biol 1997;23:597-609.

Light ED, Idriss SF, Sullivan KF, Wolf PD, Smith SW. Real-time 3D laparoscopic ultrasonography. Ultrason Imaging 2005;27:129-144.

Lindseth F, Kaspersen JH, Ommedal S, Lango T, Bang J, Hokland J, Unsgaard G, Hernes TA. Multimodal image fusion in ultrasound-based neuronavigation: improving overview and interpretation by integrating preoperative MRI with intraoperative 3D ultrasound. Comput Aided Surg 2003;8:49-69.

Lindseth F, Lango T, Bang J, Nagelhus Hernes TA. Accuracy evaluation of a 3D ultrasound-based neuronavigation system. Comput Aided Surg 2002;7:197-222.

Mercier L, Langø T, Lindseth F, Collins DL. A review of calibration techniques for freehand 3-D ultrasound systems. Ultrasound Med Biol 2005;31:449-471.

Prager RW, Ijaz UZ, Gee AH, Treece GM. Three-dimensional ultrasound imaging. Proceedings of the Institution of Mechanical Engineers, Part H: Journal of Engineering in Medicine 2010;224:193-223.

Reinertsen I, Lindseth F, Unsgaard G, Collins DL. Clinical validation of vessel-based registration for correction of brain-shift. Med Image Anal 2007;11:374-388

Rousseau F. A Novel Temporal Calibration Method for 3D Ultrasound. IEEE Trans Med Imaging 2006;25:1108.

San José-Estépar R, Martín-Fernández M, Alberola-López C, Ellsmere J, Kikinis R, Westin C-F. Freehand ultrasound reconstruction based on ROI prior modeling and normalized convolution. Proceedings of Medical Image Computing and Computer-Assisted Intervention (MICCAI), Montréal, Canada: Springer, 2003;2879:382-390.

Solheim O, Selbekk T, Løvstakken L, Tangen GA, Solberg OV, Johansen TF, Cappelen J, Unsgård G. Intrasellar Ultrasound in Transsphenoidal Surgery: A Novel Technique. Neurosurgery 2010;66:173-186.

Treece GM, Gee AH, Prager RW, Cash CJC, Berman LH. High-definition freehand 3-D ultrasound. Ultrasound Med Biol 2003;29:529-546.

Treece GM, Prager RW, Gee AH, Berman L. Correction of probe pressure artifacts in freehand 3D ultrasound. Med Image Anal 2002;6:199-214.

Wein W, Pache F, Röper B, Navab N. Backward-Warping Ultrasound Reconstruction for Improving Diagnostic Value and Registration. In Medical Image Computing and Computer-Assisted Intervention – MICCAI 2006. 2006;750-757.

Wildes DG, Chiao RY, Daft CMW, Rigby KW, Smith LS, Thomenius KE. Elevation Performance of 1.25D and 1.5D Transducer Arrays. Ultrasonics, Ferroelectrics and Frequency Control, IEEE Transactions on 1997;44:1027-1037.

Paper I

Ultrasound in Med. & Biol., Vol. 33, No. 7, pp. 991–1009, 2007
Copyright © 2007 World Federation for Ultrasound in Medicine & Biology
Printed in the USA. All rights reserved
0301-5629/07/$–see front matter

ELSEVIER

doi:10.1016/j.ultrasmedbio.2007.02.015

● *Review*

FREEHAND 3D ULTRASOUND RECONSTRUCTION ALGORITHMS—A REVIEW

OLE VEGARD SOLBERG,*†‡ FRANK LINDSETH,*† HANS TORP,‡ RICHARD E. BLAKE,§ and TORIL A. NAGELHUS HERNES*†‡

*SINTEF Health Research; Medical Technology, Trondheim, Norway; †National Center for 3D Ultrasound in Surgery, Trondheim, Norway; ‡Norwegian University of Science and Technology (NTNU), Faculty of Medicine; Department of Circulation and Medical Imaging, Trondheim, Norway; and §NTNU, Faculty of Information Technology, Mathematics and Electrical Engineering; Department of Computer and Information Science, Trondheim, Norway

(*Received* 21 *July* 2006; *revised* 31 *January* 2007; *in final form* 25 *February* 2007)

Abstract—Three-dimensional (3D) ultrasound (US) is increasingly being introduced in the clinic, both for diagnostics and image guidance. Although dedicated 3D US probes exist, 3D US can also be acquired with the still frequently used two-dimensional (2D) US probes. Obtaining 3D volumes with 2D US probes is a two-step process. First, a positioning sensor must be attached to the probe; second, a reconstruction of a 3D volume can be performed into a regular voxel grid. Various algorithms have been used for performing 3D reconstruction based on 2D images. Up till now, a complete overview of the algorithms, the way they work and their benefits and drawbacks due to various applications has been missing. The lack of an overview is made clear by confusions about algorithm and group names in the existing literature. This article is a review aimed at explaining and categorizing the various algorithms into groups, according to algorithm implementation. The algorithms are compared based on published data and our own laboratory results. Positive and practical uses of the various algorithms for different applications are discussed, with a focus on image guidance. (E-mail: ole.v.solberg@sintef.no) **© 2007 World Federation for Ultrasound in Medicine & Biology.**

Key Words: **3D ultrasound, Reconstruction methods, Positioning, Freehand acquisition, 3D imaging, Ultrasound compounding.**

INTRODUCTION

Minimally invasive surgery or image-guided surgery is an important field in therapy, becoming more and more widespread. To minimize the intervention, high demands must be made to the imaging modalities used due to image quality and accuracy. During surgery, intraoperative imaging is needed in addition to preoperative images, since changes occur during surgery. Even though the more commonly used imaging technologies such as magnetic resonance imaging (MRI) and computed tomography (CT) are possible to use during surgery, there are still some significant practical limitations, due to costs, equipment adaptation in the magnetic field, user friendliness, image quality and radiation doses. Three-dimensional (3D) ultrasound (US) is already being introduced alone or together with preoperational images for guidance of surgical applications.

Two-dimensional (2D) US is being extensively used for a variety of clinical applications and 3D US is now also more frequently demonstrated in the clinic. The main advantage of 3D US is that arbitrary 2D images through the volume may be visualized and not only images in the same plane as the US acquisition is performed, which is the only option with 2D US. 3D allows views not possible with 2D. In addition, 3D US also allows a 3D volume rendered view and 3D segmentations of objects. Two different main approaches for 3D US creation exist: using a dedicated 3D US probe or using a regular 2D US probe for acquiring the images and combining these 2D slices to a 3D volume. A 3D US probe may be a 2D array acquiring 3D volumes directly or a mechanical 3D probe consisting of a regular one-dimensional (1D) array acquiring multiple 2D images with a motor that sweeps the 1D array over the scanned area in a certain manner: linear, tilt or rotational (Fenster

Address correspondence to: Ole Vegard Solberg, SINTEF Health Research, Medical Technology, 7465 Trondheim, Norway. E-mail: ole.v.solberg@sintef.no

et al. 2001). The 3D reconstructions with motorized probes are very similar to a freehand 3D reconstruction, although the 2D image positions have a more regular pattern than that for freehand 3D US. A 2D array US probe may also be used to acquire real-time 3D volumes (also called 4D).

3D volume reconstruction from free-hand acquired 2D images usually needs position data of the 2D slices. The most common method for obtaining positioning data is to attach a position sensor to the probe: electromagnetic, optical, mechanical arm or acoustic. [See Cinquin et al. (1995) for a description of these positioning systems.] However, some systems use alternative methods such as the I-beam probe (Hossack et al. 2000), where the image positions are tracked with respect to each other with a special probe configuration and the US data. Other methods do not use any external positioning measurements at al.: the predefined operator probe movement (Downey and Fenster 1995), speckle decorrelation (Tuthill et al. 1998), frame distance estimation (Lee et al. 2001) or linear regression (Prager et al. 2003). In the literature so far, the sensorless methods have not been shown to give the same accuracy as tracking systems.

In addition to the reconstruction algorithm itself, several factors affect the 3D volume reconstruction accuracy. High quality 3D reconstructions depend on both the quality of the input 2D images and the accuracy of the position data. Tracking system inaccuracy, the ultrasound probe calibration process, sound of speed variation and tissue movement are all important error sources that are handled elsewhere (Lindseth et al. 2002; Treece et al. 2002; Mercier et al. 2005).

Earlier work has been done to explain 3D US in general (Nelson and Pretorius 1998; Fenster et al. 2001), 3D US in neurosurgery specifically (Unsgaard et al. 2006) and some of the different reconstruction algorithms and a grouping of these (Rohling et al. 1999). The article by Rohling et al. (1999) is often referred to by others for demonstrating examples of different algorithms and is sometimes also given as reference to specific algorithms as well. Some confusion exists in the literature about algorithm and group names along with some unclear algorithm origins. We believe that these problems arise from lack of a clear overview of freehand 3D US reconstruction algorithms.

The present article will, therefore, provide a thorough description and grouping of the various freehand 3D reconstruction algorithms with focus on the recently published. Although choice of positioning system and probe calibration also affects reconstruction accuracy, this will not be the focus of this article. For a comprehensive review, see the article by Mercier et al. (2005). Benefits and drawbacks of the various 3D reconstruction algorithms will be discussed with emphasize on time usage, quality, practical implementation and usefulness in image-guided surgery applications.

DESCRIPTIONS OF RECONSTRUCTION ALGORITHMS

In the following, the different reconstruction algorithms have been sorted into three groups based on implementation: Voxel-Based Methods (VBM), Pixel-Based Methods (PBM) and Function-Based Methods (FBM). VBMs traverse all voxels in a target volume and inserts corresponding pixels from the input images. PBMs traverse the input pixels and insert them into the corresponding target volume voxels. FBMs estimate functions of the input data that are used for creating the voxel grid.

Some of the algorithms in this section are explained with illustrations, shown as 2D simplification of the 3D cases. In these illustrations, the 3D voxel grid is shown as a 2D grid marking the centers of the voxels and the 2D input images are illustrated as lines where the pixel centers are marked. An overview of the different algorithms discussed in the article can be found in Table 1.

Voxel-Based Methods (VBM)

VBMs traverse each voxel in the target voxel grid and gather information from the input 2D images to be placed in the voxel. In the different algorithms, one or several pixels may contribute to the value of each voxel.

Each voxel is assigned the value of one pixel. Some methods use only one input pixel for deciding the value of a voxel. An algorithm usually implemented this way is the Voxel Nearest Neighbor (VNN) (Sherebrin et al. 1996). VNN traverses each volume voxel and assigns the value of the nearest image pixel (Fig. 1). Stradx (Prager et al. 1999) is a real-time acquisition and visualization system that uses a method that in practice works as a VNN interpolation. Stradx achieves a fast reconstruction of arbitrarily oriented 2D slices through the set of 2D images without creating a 3D volume. Stradx traverses each pixel in the target 2D slice and inserts the value of the nearest pixel in the input images. The Stradx system also supports nonplanar reslices, resampling data along a curved surface which is unrolled for display on a flat screen (Gee et al. 1999). Even though Stradx is placed in the same group as VNN, it is quite different from other reconstruction algorithms by not using a voxel grid at all.

Voxel-Based Methods With Interpolation (VBMI). VBMI use an interpolation between several input pixel values for deciding a voxel value.

1D interpolation (Berg et al. 1999) is the reconstruction implementation used in the EchoPAC-3D software (GE Vingmed Ultrasound, Horten, Norway). This

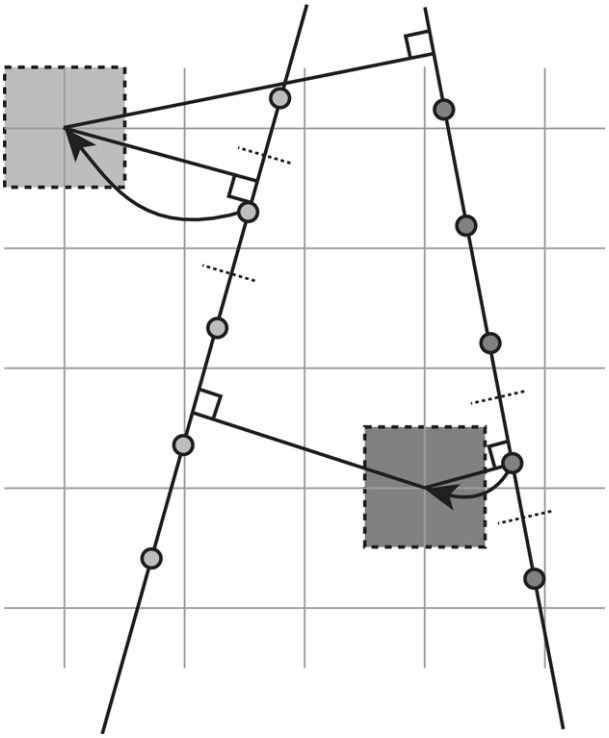

Fig. 1. VNN. A VBM that traverse each voxel and assign the value of the nearest input pixel. A normal from the voxel to the image is calculated and the nearest pixel value is inserted into the voxel. (The input images are illustrated by lines and the points in the lines illustrate the centers of the pixels. The 2D grid marks the centers of the voxels in the 3D voxel grid.)

method is based on acquiring the raw data from the US scanner, but the method can also be used with video grabbed images, since the reconstruction is done along one dimension; this may be done based on either a 2D image or a 1D scan line. Berg et al. (1999) use a tilt scan and present two interpolation methods based on the maximum angle between two enclosing scan planes. If the maximum angle is less than 20°, a linear interpolation orthogonal to a virtual scan plane in the middle of the scan planes are used (Fig. 2a). If the maximum angle is more than 20°, each 2D scan plane is defined with a certain thickness defining the region where it contributes to the interpolation (Fig. 2b). The interpolation in both cases uses a linear weight decreasing with the distance to the scan planes. The algorithm is used to create 4D volumes in a region of the human heart by also storing ECG signals. Another description of the EchoPAC-3D software (Martens and Gilja 2005) indicates that only the second method (Fig. 2b) is currently being used and that compounding may also be achieved with the same algorithm.

An interpolation from the two nearest surrounding slices is used by Trobaugh et al. (1994). This algorithm traverses the voxels and finds the two nearest 2D slices on each side of the voxel (Fig. 3). A normal is calculated to each of these slices and the four surrounding pixels are bilinearly interpolated in each plane. The final voxel value is calculated as a weighted sum with contributions from the two planes based on the distances from the voxel to the planes.

The Probe Trajectory (PT) method (Coupé et al. 2005) builds on the algorithm by Trobaugh et al. (1994). Instead of using an orthogonal projection of the closest 2D planes to a point, a probe trajectory is estimated and used for finding the corresponding pixels in the nearest 2D planes (Fig. 4). This is done by computing a "virtual" plane through the point to be calculated. First, the probe distance to this "virtual" plane is estimated by interpolating the time stamp of the two closest 2D planes. This estimate assumes a constant probe speed between these planes. Then a cubic interpolation of position parameters at the estimated time stamp is done. Four B-scans are used for this cubic interpolation. The values to be used in the interpolation can be obtained directly from the nearby planes; because the "virtual" plane will have the same in-plane 2D coordinates.

Voxel-based tri-linear interpolation (Thune et al. 1996) is based on acquiring the raw data from the US scanner. The 3D volume is then reconstructed from the 1D scan lines instead of the 2D scan converted planes. Each voxel is interpolated from the eight closest points in the scan lines.

Pixel-Based Methods (PBM)

PBMs traverse each pixel in the input images and assign the pixel value to one or several voxels. A PBM may consist of two steps: a Distribution Step (DS) and a Hole-Filling Step (HFS). In the DS, the input pixels are traversed and the pixel value applied to one or several voxels, often stored together with a weight value. In the HFS, the voxels are traversed and empty voxels are being filled. Most hole-filling methods have a limit on how far from away from known values the holes are filled, so if the input images are too far apart or the hole-filling-limits are too small there will still be holes in the constructed volume.

One pixel contributes to one voxel. In this method, each input pixel value is only applied to one voxel. Several pixels may in this way contribute to the same voxel if the algorithm supports this.

In the bin-filling stage of Pixel Nearest Neighbor (PNN), the algorithm runs through each pixel in all the 2D US images. Each pixel value is filled into the nearest voxel (Fig. 5a). Multiple contributions to the same voxel are usually averaged (Nelson and Pretorius 1997; Gobbi and Peters 2002), but different variants are possible, like

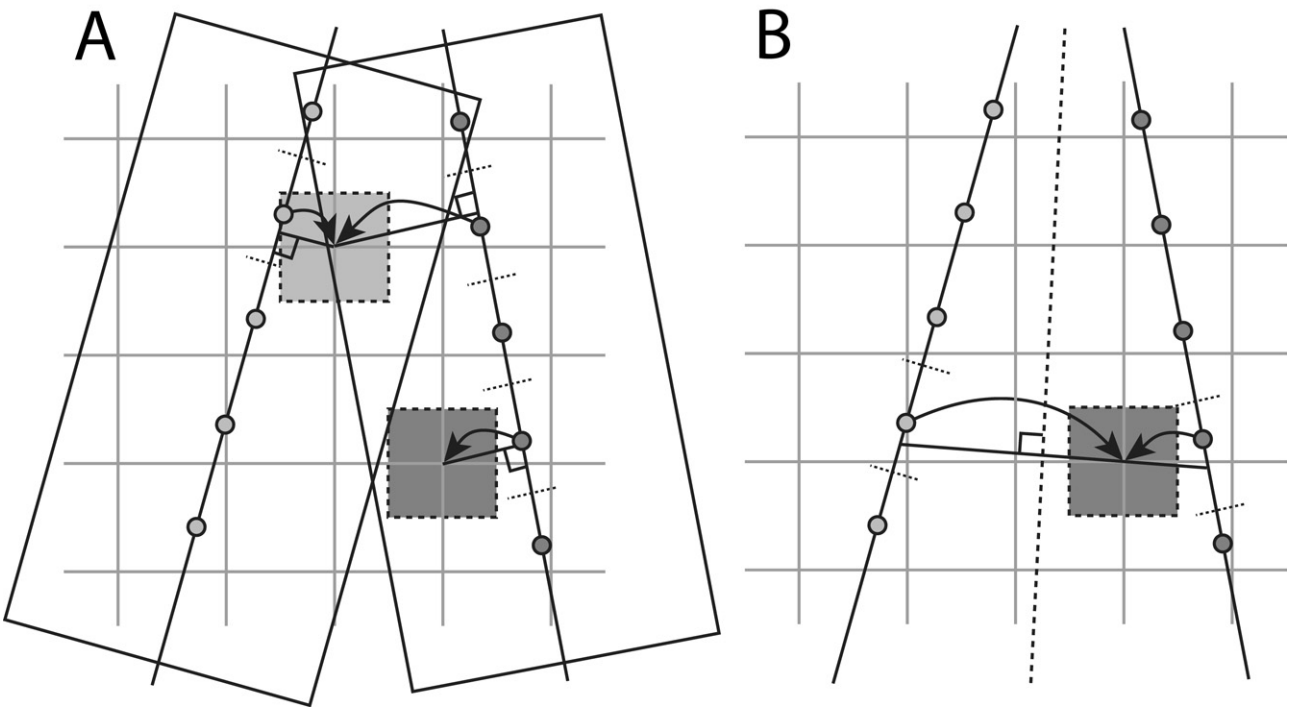

Fig. 2. 1D interpolation. (a) A VBM with 1D interpolation orthogonal to each of the nearby scan planes. Each voxel value is assigned a value orthogonal to the nearest scan planes. If more scan planes lie within a certain range an average is calculated, weighted with the inverse of the distance to the planes. (b) VBM with 1D interpolation orthogonal to a virtual middle plane. A virtual middle plane is created through the center of each voxel. The voxel value is calculated as a linear interpolation orthogonal to this plane, with use of each nearest pixel in each of the nearest enclosing planes. (In both illustrations, the input images are illustrated by lines and the points in the lines illustrate the centers of the pixels. The 2D grids mark the centers of the voxles in the 3D voxel grids.)

keeping the maximum value (Nelson and Pretorius 1997), the most recent value (Ohbuchi et al. 1992) or the first value (Trobaugh et al. 1994). Most PBMs use a PNN bin-filling as the Distribution Step (DS) and, sometimes, it may not be necessary with a Hole-Filling Step (HFS) afterwards if the input images are close enough (Gobbi and Peters 2002).

The Solus system (Carr et al. 2000) is based on the Stradx system (Prager et al. 1999). Instead of using a global VNN, the Solus system implements a localized approach to a VNN interpolation. In the DS, each 2D image is inserted into a 3D voxel grid with a predefined image thickness corresponding to the thickness of the US image (Fig. 6). The voxels intersecting the thick input image are assigned the value of the nearest pixel and the distance to the value in the voxel is stored. If the voxel already has a value only the value from the nearest pixel is used. A HFS is not used/needed because of the image thickness in the DS. The result is similar to a VNN interpolation with holes where the input 2D images are too far away from the voxels.

PNN with hole-filling from a local neighborhood. After the DS, there are usually holes in the voxel array, especially if the volume has not been scanned with a dense sampling. In the HFS, the volume from the DS is traversed and each empty voxel is attempted filled with the information of the nearby already filled voxels (Fig. 5b). Various methods have been presented for this purpose: an average of nonzero pixels from an intersecting 2D plane (McCann et al. 1988), an average or maximum (Nelson and Pretorius 1997; San José-Estépar et al. 2003a) or a median (San José-Estépar et al. 2003a) of nonzero voxels in a 3D local neighborhood, or interpolation between the two closest nonzero voxels (Hottier and Billon 1990). Nelson and Pretorius (1997) propose a method of reducing the resolution of the voxel grid in steps by a factor of two in each step (in each direction). It is unclear if they insert the 2D slices again in this reduced grid or use the already existing grid for generating the reduced version. After the reconstruction, Nelson and Pretorius (1997) propose to use a $3 \times 3 \times 3$ Gaussian or median filter to improve the volume data.

PNN with a 3D kernel around filled voxels. Instead of basing the hole-filling on the holes, it is possible to base it on the already filled voxels by applying this value with a weighting to the nearby voxels. In the HFS, these

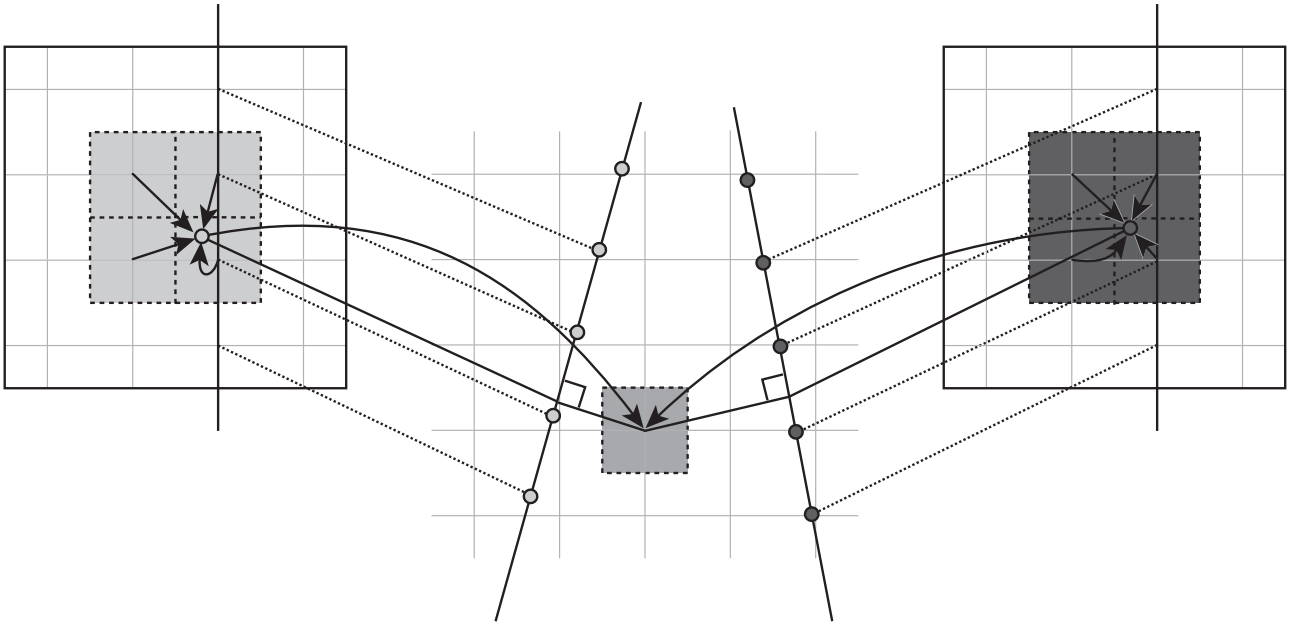

Fig. 3. VBM with interpolation from the two nearest surrounding images. A normal to each of the surrounding images is determined. A contribution from each image is determined by bilinear interpolation of the four nearest pixels. Each voxel is assigned a value based on a distance-weighted interpolation of the contributions from the two surrounding images. (The 2D grid marks the centers of the voxels in the 3D voxel grid. The input images are illustrated by lines in the voxel grid illustration, and separately by 2D grids on each side. The points in the lines illustrate the centers of the pixels.)

algorithms traverse the voxels and apply the voxel value to a local neighborhood (called kernel) around the voxels filled in the DS step.

An adaptive spherical Gaussian kernel is presented by San José-Estépar et al. (2003b). Each filled voxel is applied to the neighboring voxels with the help of a spherical Gaussian kernel (Fig. 7a). The variance of the kernel is dependent of the variance of the intensity of the nearby pixels. This pixel variance is calculated based on the PNN bin-filling step. The result is kernels of various sizes according to the density of the input data. A bank of precomputed kernels is used to speed up the interpolation process. The result is then normalized to avoid an increase in intensity values.

Normalized Convolution (Knutsson and Westin 1993) is used by San José-Estépar et al. (2003a) as a method of interpolating the data after the PNN bin-filling stage (Fig. 5a) has been performed. The Point Spread Function of the US system is used as an input to the applicability function used in the Normalized Convolution. This applicability function will determine the extent of both the kernel and the weighting that the input values are weighted with in the neighboring voxels. See Fig. 7b for illustration. The Normalized Convolution method also uses a certainty function, which is used for weighting the accuracy of the data. San José-Estépar et al. (2003a) uses this to apply a certain weight to the data locations from the bin-filling stage, while the empty voxels are weighted as empty.

3D kernel around input pixels. Instead of running a two-step algorithm like the PNN, some algorithms do both the insertion and hole-filling in the DS. These algorithms are traversing the input pixels and assigning the pixels value into the voxels in a local neighborhood (called kernel) around the pixel position. In addition to the pixel values, a weight value is associated with each voxel. The weight value is used for calculating the final voxel values when several pixels supply values to the voxel. In this process, the actual pixel positions are used, since the pixel and voxel positions are not exactly the same. This is in contrast to the PNN algorithms with a 3D kernel around the filled voxels.

Barry et al. (1997) use a spherical kernel with an inverse distance weighting. This is the most commonly used example of this kind of kernel-based algorithms. This algorithm can be seen as a simplified variant of the algorithm presented by Ohbuchi et al. (1992). The algorithm uses a spherical kernel around each pixel (Fig. 8a). This is then used to calculate a normalized distance weighted average of all pixels that lie in the neighborhood of the voxels. Barry et al. (1997) also store an ECG signal together with the input images for elimination of motion during the cardiac cycle. The user may then

Table 1. Grouping of different reconstruction algorithms

References	Implementation variant
Voxel-Based Methods (VBM): Traverse target volume and gather information	
Each voxel is assigned the value of one pixel	
Sherebrin et al. (1996)	Standard VNN (Fig. 1)
Prager et al. (1999; 2002)	VNN. Stradx (no 3D voxel volume)
Voxel-based methods with Interpolation (VBMI). Each voxel is assigned a value based on several pixels	
Berg et al. (1999), Martens and Gilja (2005)	lD interpolation (Fig. 2)
Trobaugh et al. (1994)	Two surrounding slices interpolation (Fig. 3)
Coupé et al. (2005)	Probe Trajectory (PT) (Fig. 4)
Thune et al. (1996)	Voxel-based tri-linear interpolation
Pixel-Based Methods (PBM): Traverse the 2D input images and distribute the information to the target volume; may consist of a Distribution step (DS) and an additional hole-filling step (HFS)	
DS: One pixel contributes to one voxel, no HFS	
Trobaugh et al. (1994)	DS: PNN bin-filling (Fig. 5a)
Carr et al. (2000)	VNN with image thickness. Solus (Fig. 6)
DS: PNN bin-filling, HFS: traverse empty voxels and fill these from a local neighborhood (Fig. 5)	
McCann et al. (1988)	HFS: Average from an intersecting 2D plane
Hottier and Billon (1990)	HFS: Interpolation between two closest voxels
Nelson and Pretorius (1997)	HFS: Interpolation by reduction of voxel grid
DS: PNN bin-filling, HFS: apply a 3D kernel to already filled voxels to determine impact on nearby voxels	
San José-Estépar et al. (2003b)	Adaptive Gaussian kernel (Fig. 7a)
San José-Estépar et al. (2003a)	Normalized Convolution (Fig. 7b)
DS: Apply a 3D kernel to input pixels to determine impact on nearby voxels	
Barry et al. (1997)	Spherical kernel, linear weighting (Fig. 8a)
Gobbi et al. (2001), Gobbi and Peters (2002)	Pixel trilinear interpolation (PTL)
Ohbuchi et al. (1992)	Ellipsoid Gaussian kernel, Gaussian weighting (Fig. 8b)
Meairs et al. (2000)	Ellipsoid Gaussian kernel, exponential weighting (Fig. 8b)
Function-Based Methods (FBM), see Fig. 9	
Rohling et al. (1999)	Radial basis function interpolation (RBF)
Sanches and Marques (2000; 2002)	Rayleigh reconstruction/interpolation with a Bayesian framework

The columns list references and implementation variant. Pseudo code implementations of some of the algorithms can be found in the Appendix.

specify a range within the cardiac cycle that contains the images to be used in the reconstruction.

Pixel trilinear interpolation (PTL) (Gobbi et al. 2001; Gobbi and Peters 2002) interpolation uses a $2 \times 2 \times 2$ kernel with linear weighting, when applying each pixel in the 2D images to the resulting volume. This is similar to the method presented by Barry et al. (1997)), but with a fixed cubic kernel instead of a configurable spherical kernel. Gobbi and Peters (2002) have implemented both a compounding method [similar to Ohbuchi et al. (1992), Barry et al. (1997) and Meairs et al. (2000)] and an alpha blending method for increased computation speed. The alpha blending provides interpolation without using an accumulation buffer. Only the kernel coefficient is used for determining the compounding weight of the newly inserted pixel compared with the existing voxel value. Compared with the compounding method, the alpha blending approach gives much higher weight to the last inserted pixels, than to those inserted previously.

An ellipsoid truncated Gaussian kernel with Gaussian weighting is presented by Ohbuchi et al. (1992). In this algorithm, each pixel in the input slices is convolved with a 3D ellipsoid truncated Gaussian kernel (Fig. 8b). The 3D Gaussian kernel is used as an emulation of the Point Spread Function (PSF) of the US scanner. Three values are stored for each voxel: the reconstruction value, the weight value and the age. The reconstruction value is a sum of all convolutions between the pixels and the 3D kernel that intersects the voxels. The weight value is a sum of the values of the 3D kernels that intersect the voxels. The reconstruction values are divided by the weight values to obtain a normalized value, often called a compound value. The age values of the pixels are used to calculate a decay factor that may be used for giving

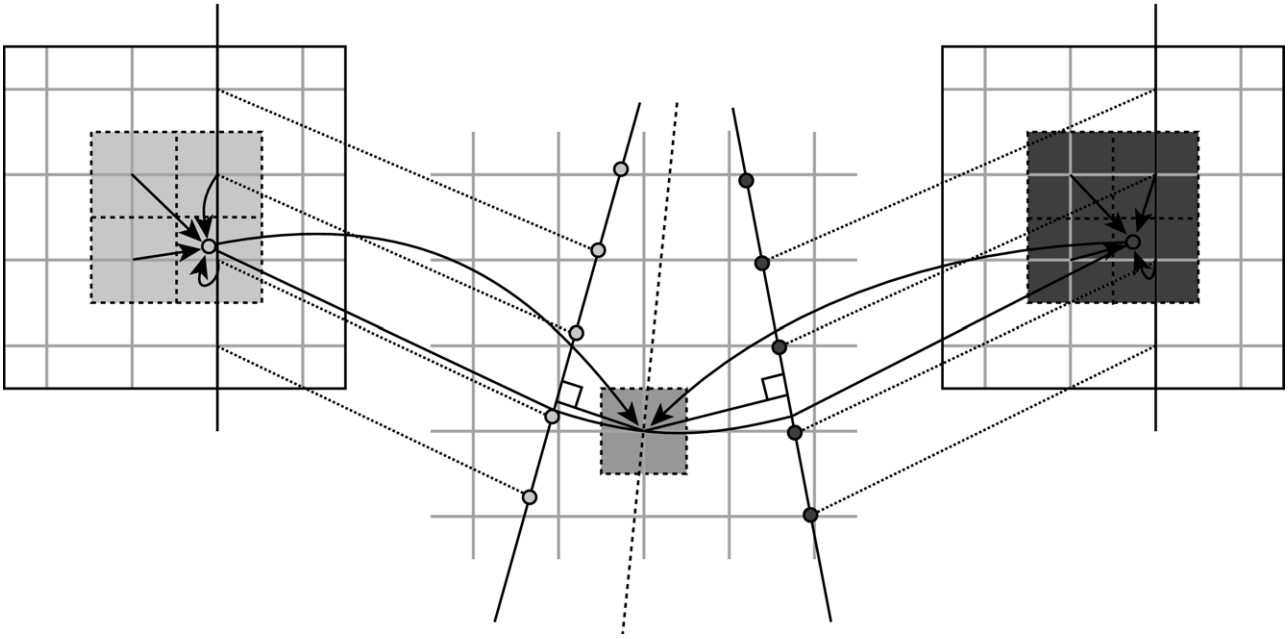

Fig. 4. VBM with interpolation from two nearest images with the PT algorithm. A virtual plane is calculated through the voxel center. The probe trajectory between the two surrounding nearest slices is estimated, assuming a constant probe speed. This probe trajectory is used to find the point on the two planes corresponding to the voxel in the virtual plane. Each of these points gets assigned a value with a bilinear interpolation of the four enclosing pixels. The voxel is assigned a value by a distance-weighted interpolation of the contributions from the two planes. (The 2D grid marks the centers of the voxels in the 3D voxel grid. The input images are illustrated by lines in the voxel grid illustration and separately by 2D grids on each side. The points in the lines illustrate the centers of the pixels.)

more weight to newer pixels than to the older ones. Ohbuchi et al. (1992) describe a method for reconstruction where the input images have both 3 degrees-of-freedom (DOF) and 6 DOF. To speed up the calculations in the 6 DOF case, the in-plane interpolation is linear instead of Gaussian.

The ellipsoid Gaussian kernel with exponential weighting by Meairs et al. (2000) is similar to the algorithm by Ohbuchi et al. (1992) with an ellipsoid kernel around the input values (Fig. 8b). An exponential weighting is used according to the distance from the estimated voxel to weight the pixel value contribution on the nearby voxels. A ECG signal allows Meairs et al. (2000) to create a 4D presentation for imaging the movement during the cardiac cycle.

Function-Based Methods (FBM)

FBMs choose a particular function (like a polynomial) and determine coefficients to make one or more functions pass through the input pixels. Afterwards, the function(s) are used to create a regular voxel array by evaluating the function(s) at regular intervals (Fig. 9).

The Radial Basis Function (RBF) interpolation (Rohling et al. 1999) is an approximation with splines that tries to use the underlying shape of the data in the volume reconstruction. A smooth function is chosen because of the smooth intensity profile of the US beam. To allow for measurement errors, the interpolation function is changed into an approximation function. An RBF is used to create the spline approximation of the volume. Instead of creating one function from all the data points, the input data are divided into small segments. This implementation is done to reduce the very large number of computations otherwise required. Overlapping windows enclose the segments to get smooth connections among the neighboring segments. Rohling et al. (1999) also propose an intelligent window-growing method that expands the window sufficiently in all directions to ensure that the RBFs for each segment closely match the RBFs of neighboring segments. All data points in the window are used to calculate the RBF for that segment. The result of the computations is a localized trivariate spline.

The Rayleigh reconstruction/interpolation with a Bayesian framework (Sanches and Marques 2000) estimates a function for the tissue by statistical methods. This is done by Bayesian estimation methods, where a Rayleigh distribution is used to describe the US data. The computational speed of the algorithm is improved by

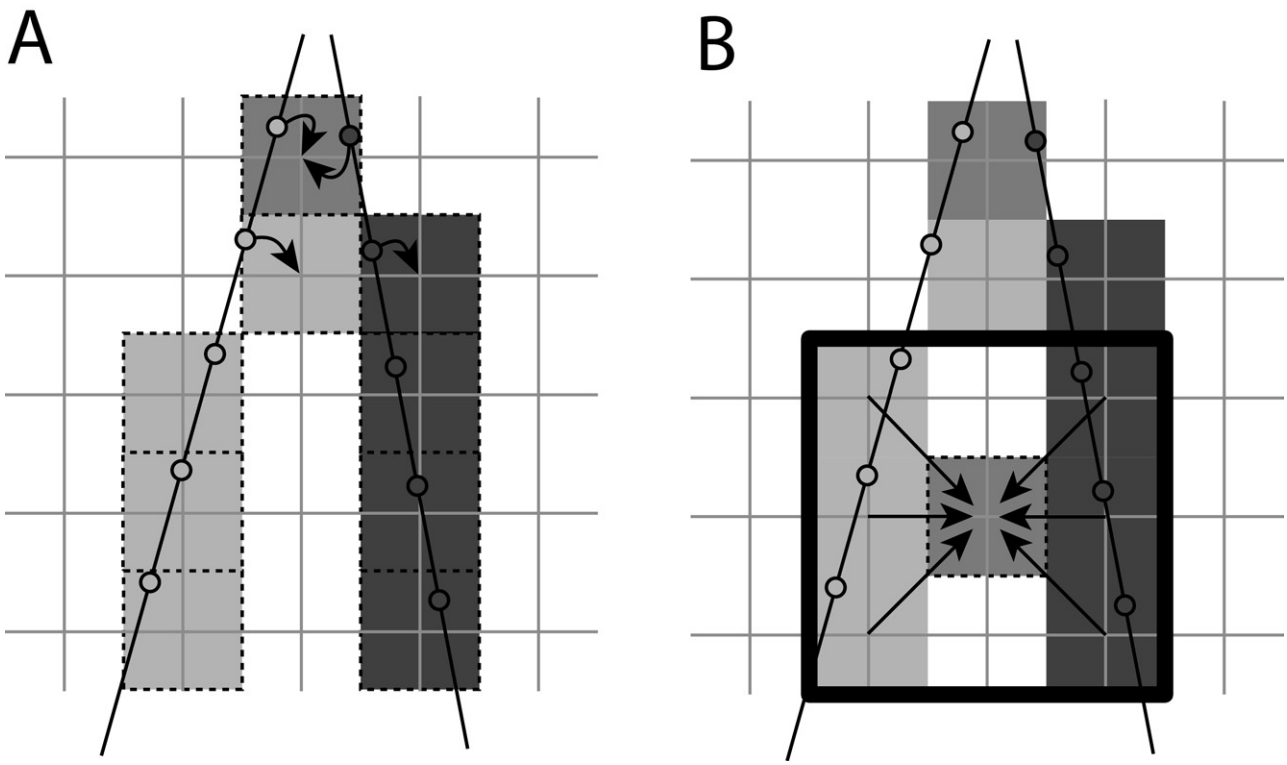

Fig. 5. (a) PBM DS: PNN bin-filling stage, each voxel is assigned the value of the intersecting pixel(s). This is done by traversing each pixel and assigning the pixel value to the voxel occupying the pixel position. Multiple contributions to the same voxel are handled either by using an average of all values or by storing the maximum or the latest value. (b) PBM HFS: PNN hole-filling from a neighborhood around the hole, each empty voxel is assigned a value based on the nearest already filled voxels. This value may either be an average or median, or an interpolation between the two closest nonzero voxels. (In both illustrations, the input images are illustrated by lines and the points in the lines illustrate the centers of the pixels. The 2D grids mark the centers of the voxles in the 3D voxel grids.)

running the first iterations on low resolution versions of the voxel volume (Sanches and Marques 2002).

COMPARISON AND DISCUSSION

In this article, the algorithms are grouped based on how they are implemented. This is an alternative to the grouping used in the literature (Rohling et al. 1999) where algorithms are sorted into groups according to how they work: Voxel Nearest Neighbor (VNN) interpolation, Pixel Nearest Neighbor (PNN) interpolation and Distance Weighted (DW) interpolation. The group name Distance Weighted (DW) interpolation (Rohling et al. 1999) is sometimes confused with the method inverse Distance Weighted interpolation (Barry et al. 1997), which is also often referred to as DW. Some articles are not clear on which algorithms they refer to, or if they refer to a group or an algorithm. To avoid misunderstandings in the literature, the actual algorithm names with references should be used instead of group names, since the different algorithms inside a group may have different properties.

When choosing and implementing the algorithms for clinical use, it is important to take certain aspects into account, especially due to the practical application in which the algorithm is to be used. In the following, the various algorithms are compared and discussed according to: Analog versus digital US image import, VBM versus PBM, deciding Region-of-Interest (ROI), algorithm computation time, reconstruction quality, real-time versus high-quality implementations, postprocessing supporting algorithms and practical considerations. Some essential data (computation time, size of input data and hardware used) disclosed from published material are described in Table 2. Table 3 contains data obtained from our own laboratory experiments where we have tested some reconstruction algorithms due to performance with current computers. The most important parameters, as speed and quality are discussed related to the usage in applications for image-guided surgery.

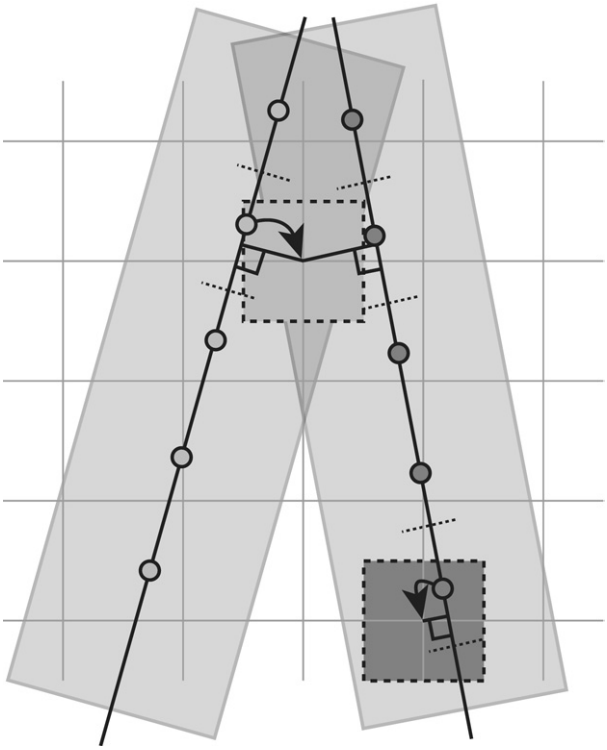

Fig. 6. A PBM implementation of VNN with image thickness. Each 2D image is inserted into a 3D voxel grid with certain thickness determining how large a part of the volume should be updated when inserting the 2D images. The gray area is updated with the pixel values of the nearest image while the white area is left empty. If several image areas intersect a voxel, the pixel value from the nearest image is used. (The input images are illustrated by lines, and the points in the lines illustrate the centers of the pixels. The 2D grid marks the centers of the voxles in the 3D voxel grid.)

Analog versus Digital US Image Import

Most reconstruction algorithms are based on analog video grabbed data. The frame rate of the video stream and video grabber is usually fixed while the frame rate of the US scanner depends on various parameters like application, probe, frequency, visualization depth and number of focus points. This difference in frame rate results in additional inaccuracies between positions and images, and frames are lost if the frame rate of the US scanner is higher than that of the video stream and video grabber. If the frame rate on the scanner is lower than that of the video stream, then the input video stream will contain duplicates of certain frames. In addition, the resolutions of the video grabbed data are usually higher than necessary, resulting in more input data to process and thus more processing time. Meairs et al. (2000) have used coded information in their analog video images for identifying duplicates that may be removed. An even more accurate approach is the one used by Thune et al. (1996) and Berg et al. (1999), where the original data from the US scanner is used. The advantage of this approach is obvious: it allows any frame rate to be used on the US scanner and use of the correct image resolution. Digital data in the form of reconstructed 2D images or 1D scan lines might lead to higher image quality. 1D scan lines will in addition lead to reduction of input data, possibly resulting in reduced processing time. Use of 1D scan lines is interesting for use in image-guided surgery, since both image quality and fast processing time are important parameters. However, most ultrasound scanners use several layers of image processing on the finished 2D images. Some of these processing methods are unpublished algorithms and will, therefore, be lost when working directly with 1D scan lines instead of working on processed digital or analog 2D images. Another disadvantage is that, in contrast to other algorithms based on video grabbed input data, these solutions require access to the digital data on the US scanner. This is the strategy of the SonoWand system (Gronningsaeter et al. 2000).

Voxel-Based Methods (VBM) Versus Pixel-Based Methods (PBM)

As seen in Table 1, most algorithms are either voxel-based or pixel-based. A PBM could be constructed as an iterative method, building the volume along with the images being collected and, thus, be made into a real-time reconstruction (given a fast enough implementation). One possible drawback is that this method will have more problems determining holes in the volume and expanding the neighborhood to fill these. The voxel-based approach can easily determine if there are holes to be filled since these methods traverse through all the voxels. The disadvantage of doing this is that the algorithm must wait for all the data to be collected before the reconstruction may start, thus, making a real-time reconstruction harder. This could be partly overcome by limiting the user to perform the sweep in a specified manner, then after a specified time of delay start the reconstruction of the area recently scanned. If the user sweeps over the reconstructed area again, some calculations could be redone. Still, there will be more delay than with a PBM. A disadvantage of filling all the voxels, like VBMs often do, is that very sparsely sampled areas are shown to contain data, while the nearest real data values might lie relatively far away.

Deciding Region-of-Interest (ROI)

Most reconstruction algorithms create the volume in a regular voxel grid. The properties of this grid must somehow be defined, like: orientation, size of the grid and size of the voxels. Sometimes the user has to define a key US frame that will help position the regular grid (Barry et al. 1997; Rohling et al. 1999). This key frame is typically centrally located and should contain a complete cross-section of the object to be visualized. The

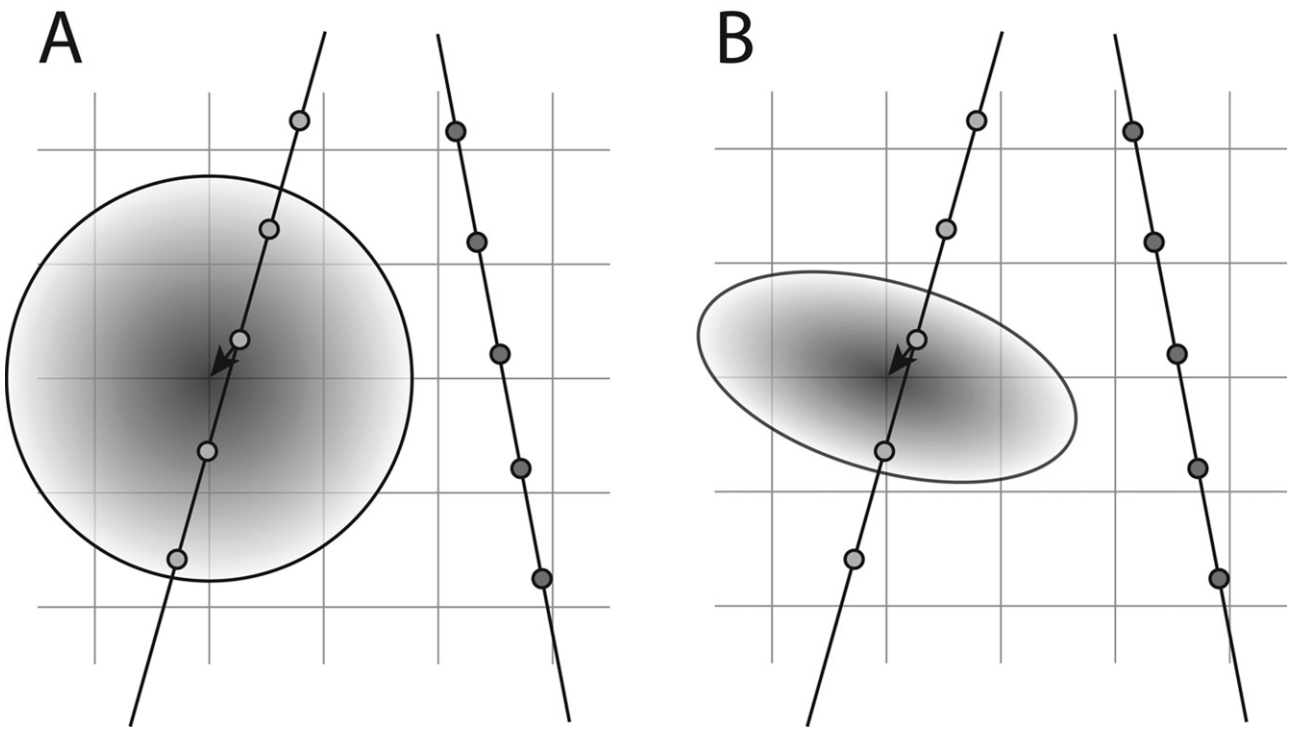

Fig. 7. (a) PBM HFS: PNN hole-filling with a spherical kernel around a voxel. First the pixel values are inserted into the nearest voxel. Then the voxel values are added to the neighboring voxels with a spherical kernel function with a Gaussian weighting. The weighting determines how much the voxels should affect nearby voxels. The variance of the kernel is dependent on the voxel-variance calculated in the bin-filling step, meaning the extent of the kernel should vary according to the uncertainty of the data. (b) PBM HFS: PNN hole-filling with an ellipsoid kernel around a voxel. First the pixel values are inserted into the nearest voxels. Then a normalized convolution with an ellipsoid kernel is performed on each voxel. The PSF of the US system have been used to define the kernel shape and weighting. (In both illustrations, the input images are illustrated by lines and the points in the lines illustrate the centers of the pixels. The 2D grids mark the centers of the voxles in the 3D voxel grids.)

axes of the grid are set equal to the axes of the key frame and the grid origin is typically set to the key frame center. Voxel size may be determined by the theoretical US resolution in focus. Another approach is to use an already defined voxel grid, like the grid of an already acquired MRI volume (Gobbi et al. 2001). Instead of creating a voxel grid large enough to contain all data from all imported images, the grid could be restricted to only contain a small ROI. San José-Estépar et al. (2003b) have proposed a method for greatly reducing the ROI, giving the reconstruction algorithm a much smaller voxel grid to reconstruct. This approach allows a computational increase since it may reduce the amount of input data considerably. A disadvantage is that the ROI estimation has to wait for the data collection to be completed. Also the reconstruction has to wait until the ROI estimation step is complete. This makes this particular technique inappropriate for real-time reconstruction, unless the ROI estimation has been run in an initialization procedure in advance. However, for computationally demanding algorithms, the waiting time is short compared with the potentially large saving in processing time. For real-time reconstructions some problems may arise determining the properties of the voxel grid. Gobbi et al. (2001) uses a pre set voxel grid decided by an already acquired MRI volume. If no previous voxel grid exists, it might be possible to have an algorithm guess the extent, by knowledge of the starting position, movement direction and type of probe movement (translation, tilt, rotation). The direction and the type of movement could be decided in advance. A dynamic expansion of the voxel grid may also be possible, but may also be too slow for a real-time implementation.

Algorithm computation time

Computation time is critical in practice when a result is wanted in or close to real-time, as is in the operation theatre. Several articles contain data about speed and quality of reconstruction algorithms. Data for comparisons of some of these can be found in Table 2.

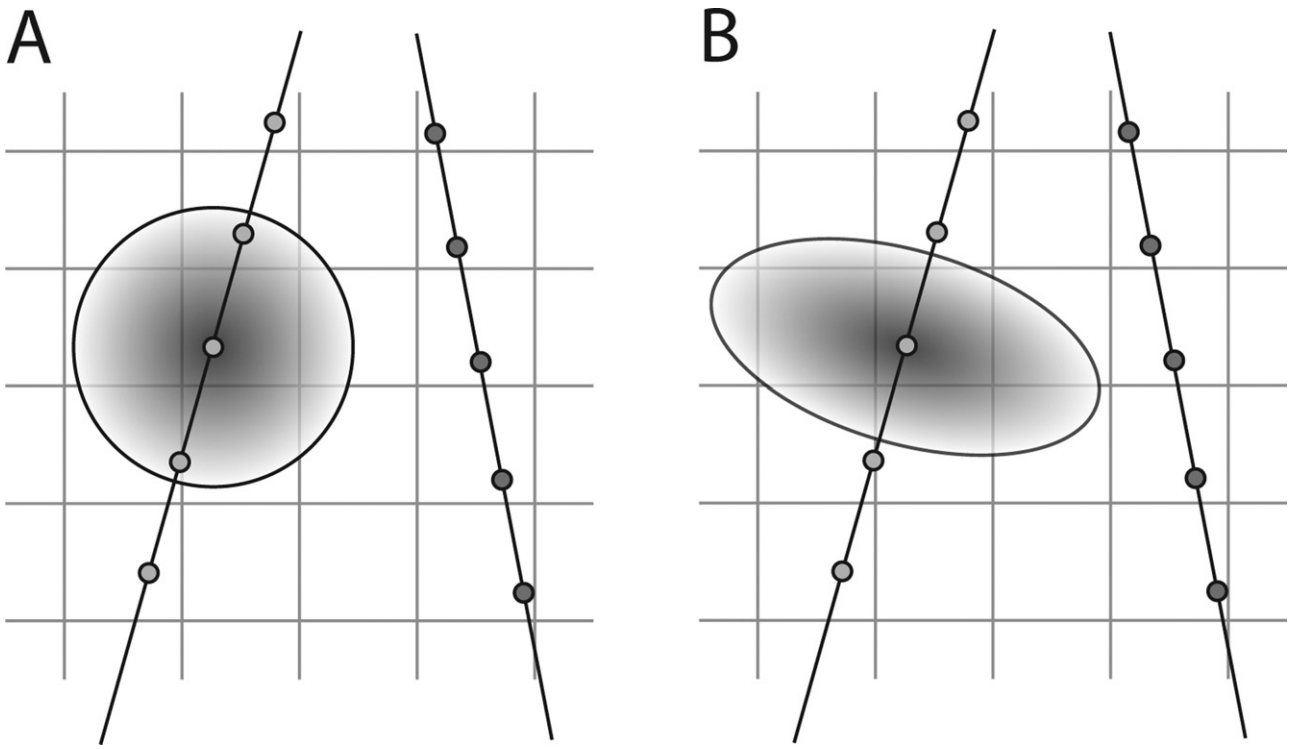

Fig. 8. (a) PBM DS with a 3D spherical kernel around each pixel. A contribution from each pixel is added to a set of nearby voxels, determined by a spherical kernel around the pixel. The contribution is weighted with the inverse of the distance. (b) PBM DS with a 3D ellipsoid Gaussian kernel around a pixel. Each pixel is added to a set of nearby voxels, with extent and weighting determined by an ellipsoid Gaussian kernel. (In both illustrations: The input images are illustrated by lines, and the points in the lines illustrate the centers of the pixels. The 2D grids mark the centers of the voxles in the 3D voxel grids.)

Only algorithms with accessible values have been included and some of the table values are estimated based on the available material and descriptions in the referred articles. The year of the article and the hardware used for the algorithm implementation has been included and must be taken into account. Some of the algorithms might be optimized for speed, while others may not. These factors are based on both programming performance and choice of programming language, so the comparisons in the table are not absolutes. Some algorithms may have a performance that allow real-time or close to real-time implementation variants (Gobbi et al. 2001; Gobbi and Peters 2002), while others may use hours on the reconstructions. To indicate computation times relevant to current computers, results from own laboratory implementations of algorithms similar to some of these reconstruction algorithms are included in Table 3. Simple algorithms like VNN and PNN are relatively fast, while the algorithms using input from a neighborhood (like a 3D kernel) around each voxel use more time. One way of decreasing the computation time is to reduce the size of this kernel. Berg et al. (1999) have taken this a step further by interpolating only along 1D in the out-of-plane direction. This may be a reasonable simplification, since the data in the in-plane directions is already reconstructed in the 2D US images. The advantage is a large decrease in computation time, at the cost of a more inaccurate reconstruction compared with using 3D interpolation. Gobbi and Peters (2002) achieves a real-time implementation by using a small kernel ($2 \times 2 \times 2$) and also manage to reduce computation time further by using alpha blending instead of compounding, with the side effect of a much higher weight on the last pixel contributing to each voxel. If the algorithm or input data are inaccurate, a suitable method of reducing computation time is to simply increase the voxel size in the output volume. This will also reduce the need of hole filling (compare Fig. 10 f to i with Fig. 10 r to u).

Reconstruction Quality

Ultrasound quality is usually defined by probe resolution, an aspect that also should be used when comparing 3D US. The most commonly used 3D reconstruction quality or accuracy estimator is to remove various amounts of input data and test the algorithms ability to recreate the removed data. A form of Mean Square Error

Table 2. Algorithm speed comparison, based on published data

Algorithm	Reconstruction computation time	Specified input image size	Hardware used	References
Voxel-Based Methods (VBM)				
Stradx	0.1 sec per any-plane slice		Regular PC (in 2002)	Prager et al. (1999; 2002)
Two surrounding slices interpolation	54 sec per image*	256 × 256	SUN SPARC-station 1	(Trobaugh et al. 1994)
Probe Trajectory (PT)	0.8–2.6 sec per image*	510 × 441	3.2 GHz Pentium 4	Coupé et al. (2005)
Pixel-Based Methods (PBM)				
Real-time PNN	0.033 sec per image	Cropped from 320 × 240	2 CPU 933 MHZ Pentium workstation	Gobbi and Peters (2002)
1D interpolation	0.06 sec per image†	Up to 512 samples with up to 128 beams	300 MHz Pentium PC	Berg et al. (1999)
Real-time PTL (Kernel: 2 × 2 × 2)	0.05 sec per image (alpha blending) 0.08 sec per image (compounding)	Cropped from 320 × 240	2 CPU 933 MHZ Pentium workstation	Gobbi and Peters (2002)
Spherical kernel, linear weighting (Kernel varying between 3 × 3 × 3 and 4 × 4 × 4)	0.6 sec per image*	Half the size of S-VHS PAL (S-VHS PAL = max 400 analog lines)	100 MHz silicon graphics Indy R4600	Barry et al. (1997)
Ellipsoid kernel, off-plane: Gaussian interpolation, in-plane: linear interpolation	2.6 sec per image*	512 × 480 (Reconstructed into a 128 × 128 × 128 volume)	HP9000/700 workstation	Ohbuchi et al. (1992)
Ellipsoid kernel, Gaussian weighting	1.5 sec per image*	128 × 128 (Reconstructed into a 128 × 128 × 128 volume)	IBM RS6000 model 560 workstation	Ohbuchi et al. (1992)
Function-Based Methods (FBM)				
RBF	Several hours for 219 images	328 × 409 and 480 × 413 masked	Silicon Graphics Indy workstation	Rohling et al. (1999)

* Estimate based on article

† Estimated value, based on article. Real rate is probably lower due to image combinations prior to the reconstruction. The resolution with this frame rate is a bit unclear.

(MSE) is used for describing the accuracy (Rohling et al. 1999; Sanches and Marques 2000; San José-Estépar et al. 2003a, 2003b; Coupé et al. 2005). Barry et al. (1997) compare number of pixels identified by a segmentation process. Sanches and Marques (2000) calculate signal to noise ratio (only on synthetic data) and log-likelihood in addition to MSE.

The basic VNN algorithms take only the nearest pixel into account regardless of distance. This may display volume areas as sharp, even if they contain no real values (Rohling et al. 1999). The Stradx system (Prager et al. 1999) tries to increase the accuracy of the VNN algorithm by skipping one step of interpolation by reconstructing 2D slices through the volume directly, without using a voxel grid. The disadvantage is that only 2D slices may be visualized since no 3D volume exists. The Solus system (Carr et al. 2000) avoids the generation of values in areas far away from the real data by allowing pixels to update voxels at only a certain distance away. This leaves holes in the volume as an indication of a too sparsely sampled volume. VNN algorithms are shown as the most inaccurate method in most comparisons (Rohling et al. 1999; San José-Estépar et al. 2003a, 2003b; Coupé et al. 2005). PNN algorithms are often more accurate by assigning the pixel values to the nearest voxels. The holes may be filled by combining values from a local neighborhood (as demonstrated by laboratory experiments: compare Fig. 10 f to i with Fig. 10 j

Table 3. Own laboratory results of algorithm computation times of some Pixel-Based Methods (PBM)

Algorithm implementation	Reconstruction computation time	Related algorithms
PNN with only bin-filling	0.04 sec per image	Trobaugh et al. (1994), Gobbi and Peters (2002)
PNN with bin-filling and 3 × 3 × 3 hole-filling (averaging)	0.067 sec per image	McCann et al. (1988), Hottier and Billon (1990), Nelson and Pretorius (1997)
3D kernel around voxels. Spherical kernel, Gaussian weighting	0.15 sec per image with 3 × 3 × 3 kernel	San Jos-Estépar et al. (2003b)
3D kernel around voxels. Ellipsoid kernel, Gaussian weighting	0.66 sec per image with 3 × 5 × 9 kernel	San José-Estépar et al. (2003a), San José-Estépar et al. (2003b)
3D kernel around pixels. Spherical kernel, Gaussian weighting	1 sec per image with 3 × 3 × 3 kernel	Ohbuchi et al. (1992), Barry et al. (1997), Meairs et al. (2000), Gobbi and Peters (2002)
3D kernel around pixels. Ellipsoid kernel, Gaussian weighting	2.5 sec per image with 3 × 5 × 9 kernel	Ohbuchi et al. (1992), Meairs et al. (2000)

All reconstructions are implemented in C++ and run on an AMD Athlon 64 Processor 3000+, 1.81 GHz. Input consist of 413 video grabbed US images with a resolution of 720x537, stored on the computer hard drive. Only a masked sector is used of each image; the sector size is 46% of the total image size. The volumes are reconstructed into a 288x247x253 voxel grid with a voxel size of 1.0 mm. Related algorithms that can be expected to have a similar computation time are listed.

to m) or by applying 3D kernels to the already filled voxels. This allows several pixels to contribute to the values of each voxel, which is an improvement over the VNN algorithms. The disadvantage of the PNN algorithms is that actual pixel positions are not used directly, but first resampled by inserting the pixels into the nearest voxels in a regular voxel grid. This error can be made small by using voxels that are smaller than the resolution of the US probe resolution, but this will result in an increased computation time and more holes that need to be filled. VBMI and PBMs with a 3D kernel around pixels (for an example see Fig. 10 n to q) use the pixel positions directly for determining the impact each pixel will have on the nearby voxels. This may improve the accuracy, but may also result in slower computation time (Table 3). The input pixels impacts on the voxels are calculated with different weighting functions based in one way or another on the pixels distance from the voxel. Functional algorithms (Rohling et al. 1999; Sanches and Marques 2000, 2002) may provide even more accurate volumes, but at the cost of highly increased computation time.

Future 3D US quality comparisons should also include a comparison analogous to the probe resolution, a measure of the quality of regular 2D US probe. A resolution-phantom could be scanned and reconstructed with 3D reconstruction algorithms. The algorithms ability to create volumes that distinguish between close point-spread sources is a good measure of resolution. The difference in the algorithms will probably be highly visible when the point-spread sources are lying between image planes. Algorithms that create compounded volumes (like VBMI, PBM with kernels and FBM) will probably show increased resolution, especially if the volumes consist of 2D images from different directions. However this compounding may reduce in-plane resolution in the final volume. Huang et al. (2005) propose a method that will preserve the resolution in all directions. They divide the US into different volumes for different directions and merge the volumes in the Fourier domain

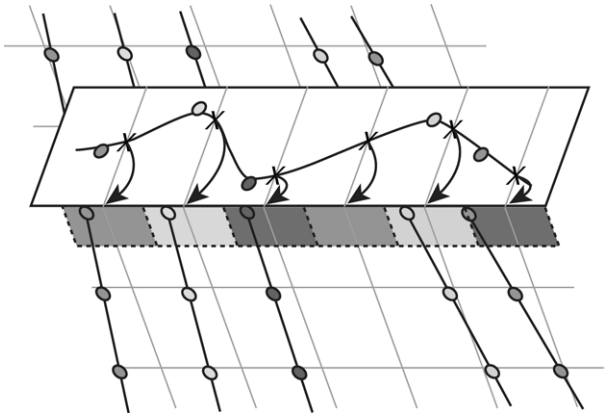

Fig. 9. Functional interpolation, visualized along one dimension. A function through the input points (pixel values) is estimated. To obtain the final voxel values the function is evaluated at regular intervals. (The input images are illustrated by lines, and the points in the lines illustrate the centers of the pixels. The 2D grid marks the centers of the voxles in the 3D voxel grid. The vertical lines represent the regular grid, in which the result is to be placed. The curve illustrates the function made on basis of the input data. The Xs on the curve show the resulting data values gained by evaluating the constructed function at regular intervals corresponding to the target grid.)

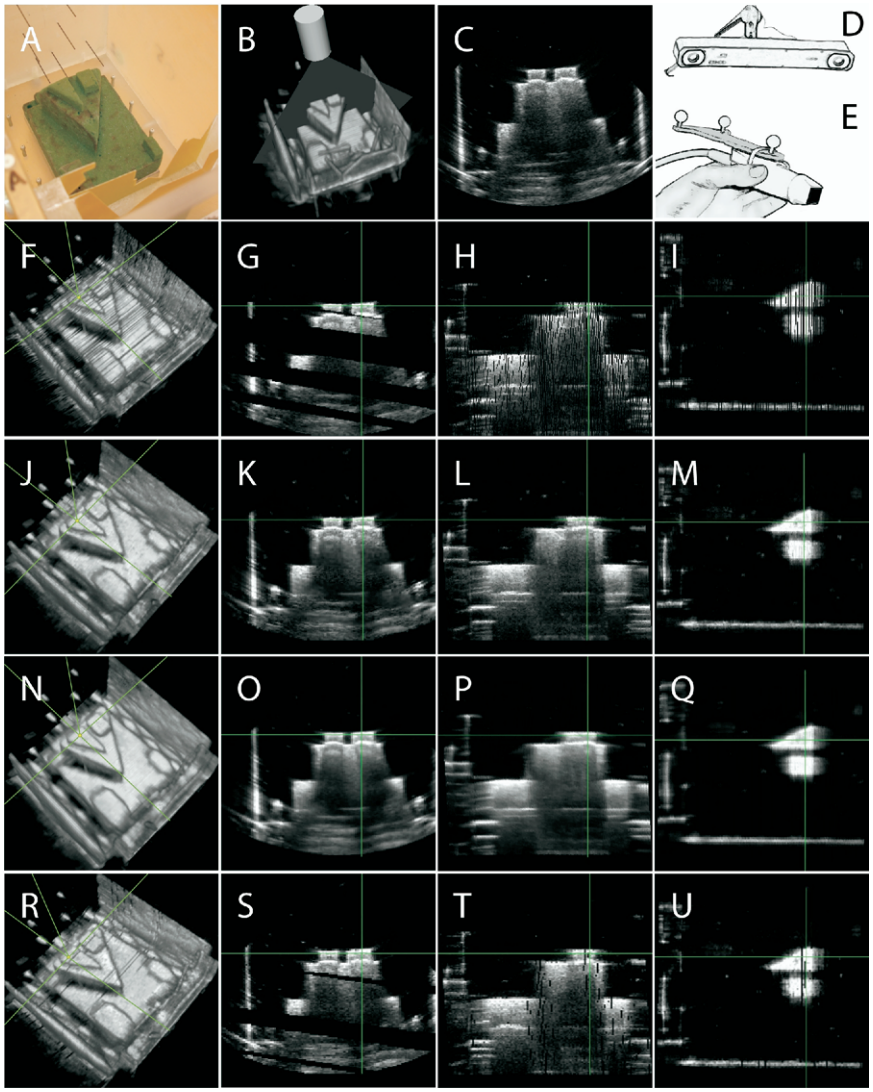

Fig. 10. Laboratory results showing the quality of 3D reconstructed volumes using various reconstruction algorithms and by scanning a US laboratory-phantom. The phantom is made of oasis and was submerged in water and scanned with a freehand translation with a 2D US probe over the area of interest. The scanner used was SystemFiVe GE (Vingmed Ultrasound, Horten, Norway) with a 5 MHz Phased Array (FPA) US probe. Frequency was set to 5.7 MHz, focus positions: 4.9, 6.7 and 11.0 (cm), frames per s: 10.6. The data were imported with a video grabber with a rate of 25 images per s running on a computer. The reconstructed US volumes and slices through the volumes were visualized with own visualization software (SINTEF, Trondheim, Norway). **(a)** Photograph of laboratory-phantom used in the tests. **(b)** Illustration of the US probe position and US 2D scan plane position in relation to the phantom. **(c)** A input 2D image scan (source data from US scanner). **(d)** Illustration of the Polaris optical position tracking used (NDI, Waterloo, Ontario, Canada) **(e)** Illustration of the US probe with an attached frame with reflecting spheres. **(f)** Volume reconstructed with only a Distribution Step (DS) using the PNN bin-filling and a voxel size of 0.6 mm, resulting in several holes in the volume. The 0.6 mm voxel size corresponds to the theoretical azimuth US resolution in the closest focus point. Cross hairs show orthogonal slicing through the volume displayed in (g) to (i). **(g)** to **(i)** Three orthogonal image slices through the volume in (f). The holes in the volume are clearly visible. **(j)** Volume reconstructed as in (f) (PNN bin-filling in the DS), but with an additional Hole Filling Step using an average over a $3 \times 3 \times 3$ neighborhood to fill the empty voxels. Voxel size is 0.6 mm as in (f). An increase in time consumption can be seen compared with a reconstruction without hole-filling (f) to (i) (see Table 3). **(k)-(m)** Orthogonal image slices through the volume in (j). The holes in (f) are now filled. By comparing (k) with (g) it is possible to see that the voxels filled in the HFS are more blurred than the voxels from the DS [also observed by Rohling et al. (1999)]. **(n)** Volume reconstructed with an ellipsoid kernel ($3 \times 3 \times 7$) around each pixel with Gaussian weighting and voxel size 0.6 mm. **(o)** to **(q)** Orthogonal image slices through the volume in (n). Comparing (n) to (q) with the other images it is possible to see that both the volume and the slices are smoother than the others, because the algorithm allows the input samples to influence nearby samples. **(r)** Volume reconstructed with only a DS using the PNN bin-filling, as in (f), but with a larger voxel size of 1.0 mm,

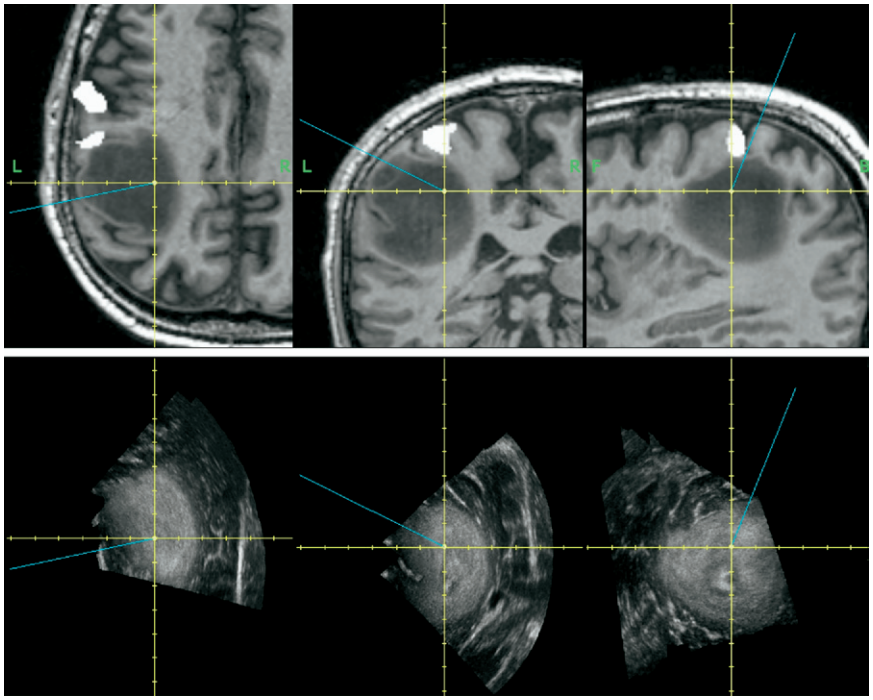

Fig. 11. 3D Ultrasound acquired with the commercial system SonoWand (MISON AS, Trondheim, Norway) (Gronningsaeter et al. 2000). (Top) Orthogonal 2D slices through a MR volume of a patient with brain tumor. The slices are selected due to the position of the surgical instrument. (Bottom) Orthogonal slices through an ultrasound volume corresponding to the MR slices. None of the slices correspond exactly to the US scan plane. The US volume is recorded in about 20 to 30 s and another 30 s were used for reconstruction. The image quality of ultrasound may in many cases be comparable to that of MRI.

by weighting the frequency components according to the signal noise ratio.

Other highly important factors for reconstruction quality (especially for compounded volumes) are position sensor accuracy, probe calibration (Mercier et al. 2005) and tissue movement (Treece et al. 2002). Probe calibration defines the transformation between the 2D ultrasound images and the position sensor attached to the probe and inaccuracies in this probe calibration may have a significant impact on overall accuracy (Lindseth et al. 2002).

For positioning systems, spatial accuracy in the reconstructed volume, could be used as a measure of quality in addition to sensor accuracy measurements. Measurements could be done by performing distance or volume measurements (Barry et al. 1997) of objects with known distances or volumes, and the spatial accuracy would illustrate inaccuracies and drift. This could also define accuracy of sensorless reconstruction like predefined operator probe movement (Downey and Fenster 1995) and speckle decorrelation (Tuthill et al. 1998), which probably would give much lower spatial accuracy than using positioning systems. Drift and noise on magnetic positioning systems would most likely result in poorer spatial accuracy than for optical positioning systems.

Even if compounded volumes may be more accurate and visually pleasing, tissue movement and position inaccuracy may reduce the volume quality greatly, resulting in blurred volumes. In these cases, a simpler algorithm will give better results, so in many cases the more advanced algorithms may not result in better overall volume quality. To achieve highest possible quality in the volumes, the algorithm type must be selected based on position accuracy and the data acquisition situation.

opposed to the images (f) to (q), using 0.6 mm voxel size. The larger voxel size allows this faster algorithm to fill most of the volume leaving only a few holes. This reconstruction algorithm may be implemented in real-time [see Table 3 and Gobbi and Peters (2002)]. **(s)** to **(u)** Orthogonal image slices through the volume in (r) clearly demonstrate that most of the holes are filled with the larger voxel size.

Real-time versus high-quality implementations

Although some of the advanced algorithms may not yet be implemented in real-time with current hardware, some less computationally intensive algorithms have already been implemented and others may be possible to implement. One possibility is to provide the advantages of both real-time and high-quality implementations by using several algorithms. Applications may provide a real-time view straight away and at the same time calculate a higher quality volume in the background, to be shown when ready. Gobbi et al. (2001) uses this method to some degree by first presenting a real-time reconstruction consisting of every third input image and presenting the final result afterwards. This method can be taken further by combining more methods and using even more computationally demanding algorithms. A possible combination for image-guided surgery could consist of three algorithms: a real-time presentation of a PNN volume without hole-filling during data acquisition. After the data acquisition is finished a PNN volume with hole-filling is presented. After a few minutes, a more accurate volume with a 3D kernel around input pixels is presented If the high quality volumes are not needed right away, this may be a possible solution. The lower quality volumes will probably be sufficient for determining the quality of the final volume in advance. Such applications could also be able to select or tune algorithms based on the available hardware.

In the case of sparsely located input 2D frames, PBMs might be a fast alternative but will leave a lot of holes in the volume. The hole-filling part could consume some time if the whole volume is to be filled. In this case the VBMs might be a better choice providing a fast reconstruction. VNN implementations will provide a fast reconstruction, but the more accurate VBMI may also be reasonably fast for image-guided surgery. VBMI range from fast 1D interpolation to an interpolation from the nearest frames (Trobaugh et al. 1994; Coupé et al. 2005) or scan line points (Thune et al. 1996). The algorithm by Coupé et al. (2005) may offer an improvement by calculating the probe trajectory. In ultrasound, different image depths are acquired at different times, dependent on number of focus points. If these acquisition parameters are known this could be used to improve the algorithm further by taking data acquisition times into account in addition to probe trajectory. This could result in an even better accuracy, also for more densely sampled data.

Algorithms supporting postprocessing

Some algorithms support certain postprocessing steps better than others. The construction of a regular voxel grid allows the use of multiple volume processing algorithms after the reconstruction. Segmentation is often performed based on 3D volumes. It is much easier to segment from volumes that are smoothened and have an increased signal to noise ratio as for example function based methods, VBMIs or PBMs with 3D kernels. Most algorithms taking several pixels into account for each voxel have the effect of smoothing the volume: the higher number of pixels used, the smoother the resulting volume. The functional algorithms create very smooth volumes by taking large volume areas into account for the local functions. The effect of using several pixels for deciding a voxel value is that this produces compounded volumes, which are more pleasing to the eye, have reduced speckle, improved spatial coherence and improved signal to noise ratio. The disadvantage is that small structures may be lost. Barry et al. (1997) have shown that segmentations from heavily compounded volumes (using a spherical kernel) give much better results than segmentations from 2D US slices. Another approach is to smooth the volume after creation, for example like the filtering approach presented by Nelson and Pretorius (1997). This approach and the methods that use 3D kernels around voxels (instead of pixels) may produce the same kind of smooth volumes, but with a lower accuracy since pixel positions are not equal to voxel positions.

Practical Considerations and Future Work

To be used in the clinic, freehand US 3D reconstruction algorithms must be integrated with existing clinical equipment or otherwise made easily accessible. The most important parameters for practical implementation are speed and quality. Currently, the Solus system (Carr et al. 2000) offers a clinical interface to the Stradx system (Prager et al. 1999, 2002). The Stadx system (latest version called Stradwin) is currently being used for targeting of radiotherapy for breast cancer treatment through the radiotherapy planning system Orpheus from Qados, Berkshire, England. The Norwegian company, MISON, has the commercially available SonoWand system (Gronningsaeter et al. 2000) for use of freehand 3D US in neuronavigation. The reconstruction method in this system uses raw data from the US scanner and reconstructs the volume from the 1D scan lines (with an unpublished method) within 30 s (Unsgaard et al. 2002). Examples of 3D US volumes acquired with the SonoWand system (MISON) are shown in Fig. 11. Both due to reconstruction time and image quality promising results for use in image-guided surgery are presented. Corresponding planes of preoperative MRI shows that the image quality of ultrasound may improve toward that of MR. This may improve future diagnostics and may also result in improvements when the US volume is to be

used for guidance and control of surgical procedures (Kaspersen et al. 2003). Such image fusion between intraoperative 3D US and preoperative modalities may improve the quality of the surgical procedure (Lindseth et al. 2003).

CONCLUSION

With basis in the literature of 3D reconstruction algorithms, this article has described various algorithms and sorted them into three groups based on implementation method: Voxel-Based Methods (VBM), Pixel-Based Methods (PBM) and Function-Based Methods (FBM). Different practical applications will require different solutions, leading to the conclusion that future 3D ultrasound applications should probably consist of several reconstruction algorithms. These reconstruction algorithms should be either real-time or other kinds of fast reconstruction algorithms in collaboration with slower high-quality algorithms to ensure high quality image data. Even though high quality volumes are presented in image-guided surgery, speed is almost equally important. Therefore, algorithms capable of providing results in real-time or close to real-time, such as implementations of VNN, PNN, a small kernel around input pixels or VBMI with interpolation over a limited area for each voxel will be the most useful ones. Slower algorithms might be added as support to the fast ones. Faster computers as well as algorithms optimized for speed will result in faster versions of the higher quality algorithms optimizing the usage of 3D ultrasound reconstruction in image-guided surgery.

Acknowledgments—This work was supported by the Research Council of Norway, through the FIFOS Programme Project 152831/530; the Ministry of Health and Social Affairs of Norway, through the National Centre of 3D Ultrasound in Surgery; and by SINTEF Health Research. We also want to thank Geir Arne Tangen, Thomas Langø, Steinar Ommedal, Jon Bang, scientists at SINTEF and Veerle de Smedt (NTNU) for valuable contributions to the laboratory set-up, Atle Kleven (MISON) for information about the SonoWand system, and Nancy Eik-Nes for the text review of the initial version of the article.

REFERENCES

Barry CD, Allott CP, John NW, et al. Three-dimensional freehand ultrasound: Image reconstruction and volume analysis. Ultrasound Med Biol 1997;23:1209–1224.

Berg S, Torp H, Martens D, et al. Dynamic three-dimensional freehand echocardiography using raw digital ultrasound data. Ultrasound Med Biol 1999;25:745–753.

Carr JC, Stallkamp JL, Fynes MM, et al. Design of a clinical free-hand 3D ultrasound system. Proceedings of Medical Imaging 2000: Ultrasonic Imaging and Signal Processing, San Diego, CA, USA: SPIE 2000;3982:14–25.

Cinquin P, Bainville E, Barbe C, et al. Computer assisted medical interventions. IEEE Engineering in Medicine and Biology Magazine 1995;14:254–263.

Coupé P, Hellier P, Azzabou N, Barillot C. 3D freehand ultrasound reconstruction based on probe trajectory. Proceedings of Medical Image Computing and Computer-Assisted Intervention (MICCAI), Palm Springs, CA, USA: Springer, 2005;3749:597–604.

Downey DB, Fenster A. Vascular imaging with a three-dimensional power Doppler system. Am J Roentgenol 1995;165:665–668.

Fenster A, Downey DB, Cardinal HN. Three-dimensional ultrasound imaging. Phys Med Biol 2001;46:R67–R99.

Gee A, Prager R, Berman L. Non-planar reslicing for freehand 3D ultrasound. Proceedings of Medical Image Computing and Computer-Assisted Intervention (MICCAI), Cambridge, UK: Springer-Verlag, 1999, 1679:716–725.

Gobbi DG, Lee BKH, Peters TM. Correlation of preoperative MRI and intraoperative 3D ultrasound to measure brain tissue shift. Proceedings of Medical Imaging 2001: Visualization, Display, and Image-Guided Procedures, San Diego, CA, USA: SPIE, 2001;4319:264–271.

Gobbi DG, Peters TM. Interactive intra-operative 3D ultrasound reconstruction and visualization. Proceedings of Medical Image Computing and Computer-Assisted Intervention (MICCAI), Tokyo, Japan: Springer, 2002;2489:156–163.

Gronningsaeter A, Kleven A, Ommedal S, et al. SonoWand, an ultrasound-based neuronavigation system. Neurosurgery 2000;47:1373–1379,discussion 1379–1380.

Hossack J, Sumanaweera TS, Napel S. Quantitative 3D ultrasound imaging using an automated image tracking technique. Proc IEEE Ultrason Symp 2000;2:1593–1596.

Hottier F, Billon AC. 3D echography: Status and perspective. In: Hohne KH, Fuchs H, Pizer SM, eds. 3D imaging in medicine. Berlin Heidelberg: Springer-Verlag 1990;F 60:21–41.

Huang W, Zheng Y, Molloy JA. 3D Ultrasound Image Reconstruction from Non-Uniform Resolution Freehand Slices. Proceedings of IEEE International Conference on Acoustics, Speech, and Signal Processing (ICASSP'05), Philadelphia, PA, USA: IEEE, 2005;2:125–128.

Kaspersen JH, Sjølie E, Wesche J, et al. Three-dimensional ultrasound-based navigation combined with preoperative CT during abdominal interventions: A feasibility study. Cardiovasc Intervent Radiol 2003;26:347–356.

Knutsson H, Westin CF. Normalized and differential convolution: Methods for interpolation and filtering of incomplete and uncertain data. Proceedings of IEEE Computer Society Conference on Computer Vision and Pattern Recognition, New York, NY, USA: IEEE, 1993;CVPR 93:515–523.

Lee JH, Kim SH, Kim NC. Reconstruction of 3D ultrasound image from freehand scanned frames using frame-by-frame isotropic correlation function. Proceedings of Three-Dimensional Image Capture and Applications IV, San Jose, CA, USA: SPIE, 2001;4298:195–202.

Lindseth F, Kaspersen JH, Ommedal S, et al. Multimodal image fusion in ultrasound-based neuronavigation: Improving overview and interpretation by integrating preoperative MRI with intraoperative 3D ultrasound. Comput Aided Surg 2003;8:49–69.

Lindseth F, Langø T, Bang J, Nagelhus Hernes TA. Accuracy evaluation of a 3D ultrasound-based neuronavigation system. Comput Aided Surg 2002;7:197–222.

Martens D, Gilja OH. The EchoPAC-3D software for image analysis. In: Ødegård S, Gilja OH, Gregersen H, eds. Basic and new aspects of gastrointestinal ultrasonography. Advanced series in biomechanics. Singapore: World Scientific Publishing, 2005:305–329.

McCann HA, Sharp JC, Kinter TM, et al. Multidimensional ultrasonic imaging for cardiology. Proceedings of IEEE 1988;76:1063–1073.

Meairs S, Beyer J, Hennerici M. Reconstruction and visualization of irregularly sampled three- and four-dimensional ultrasound data for cerebrovascular applications. Ultrasound Med Biol 2000;26:263–272.

Mercier L, Langø; T, Lindseth F, Collins LD. A review of calibration techniques for freehand 3-D ultrasound systems. Ultrasound Med Biol 2005;31:449–471.

Nelson TR, Pretorius DH. Interactive acquisition, analysis and visualization of sonographic volume data. Int J Imag Systems Technol 1997;8:26–37.

Nelson TR, Pretorius DH. Three-dimensional ultrasound imaging. Ultrasound Med Biol 1998;24:1243–1270.

Ohbuchi R, Chen D, Fuchs H. Incremental volume reconstruction and rendering for 3-D ultrasound imaging. Proceedings of Visualization

in Biomedical Computing '92, Chapel Hill, NC, USA: SPIE, 1992;1808:312–323.
Prager RW, Gee A, Berman L. Stradx: Real-time acquisition and visualization of freehand three-dimensional ultrasound. Med Image Anal 1999;3:129–140.
Prager RW, Gee A, Treece G, Berman L. Freehand 3D ultrasound without voxels: volume measurement and visualisation using the Stradx system. Ultrasonics 2002;40:109–115.
Prager RW, Gee AH, Treece GM, Cash CJC, Berman LH. Sensorless freehand 3-D ultrasound using regression of the echo intensity. Ultrasound Med Biol 2003;29:437–446.
Rohling R, Gee A, Berman L. A comparison of freehand three-dimensional ultrasound reconstruction techniques. Med Image Anal 1999; 3:339–359.
San José-Estépar R, Martín-Fernández M, Alberola-López C, et al. Freehand ultrasound reconstruction based on ROI prior modeling and normalized convolution. Proceedings of Medical Image Computing and Computer-Assisted Intervention (MICCAI), Montréal, Canada: Springer, 2003a;2879:382–390.
San José-Estépar R, Martín-Fernández M, Caballero-Martínez PP, Alberola-López C, Ruiz-Alzola J. A theoretical framework to three-dimensional ultrasound reconstruction from irregularly sampled data. Ultrasound Med Biol 2003b;29:255–269.
Sanches JM, Marques JS. A Rayleigh reconstruction/interpolation algorithm for 3D ultrasound. Pattern Recog Lett 2000;21:917–926.
Sanches JM, Marques JS. A multiscale algorithm for three-dimensional free-hand ultrasound. Ultrasound Med Biol 2002;28:1029–1040.
Sherebrin S, Fenster A, Rankin RN, Spence D. Freehand three-dimensional ultrasound: Implementation and applications. Proceedings of Medical Imaging 1996: Physics of Medical Imaging, Newport Beach, CA, USA: SPIE, 1996;2708:296–303.
Thune N, Gilja OH, Hausken T, Matre K. A practical method for estimating enclosed volumes using 3D ultrasound. Eur J Ultrasound 1996;3:83–92.
Treece GM, Prager RW, Gee AH, Berman L. Correction of probe pressure artifacts in freehand 3D ultrasound. Med Image Anal 2002;6:199–214.
Trobaugh JW, Trobaugh DJ, Richard WD. Three-dimensional imaging with stereotactic ultrasonography. Comput Med Imaging Graph 1994;18:315–323.
Tuthill TA, Krucker JF, Fowlkes JB, Carson PL. Automated three-dimensional US frame positioning computed from elevational speckle decorrelation. Radiology 1998;209:575–582.
Unsgaard G, Ommedal S, Muller T, Gronningsaeter A, Nagelhus Hernes TA. Neuronavigation by intraoperative three-dimensional ultrasound: Initial experience during brain tumor resection. Neurosurgery 2002;50:804–812,discussion 812.
Unsgaard G, Rygh OM, Selbekk T, et al. Intra-operative 3D ultrasound in neurosurgery. Acta Neurochir (Wien) 2006;148:235–253.

APPENDIX: ALGORITHM IMPLEMENTATIONS

The Appendix contains pseudo code implementations to some of the algorithms presented in the paper. Most papers do not supply detailed information about the algorithms, so the algorithms in this appendix are reconstructed based in the published information and may not be exactly similar to the actual algorithms used. Furthermore, the pseudo code implementations only show a possible implementation, and not all possible improvements. Especially when it comes to algorithm computation time, a lot of different improvements are possible.

VBM: VNN

Algorithm described by McCann et al. (1988), Sherebrin et al. (1996) and Rohling et al. (1999). See Fig. 1 for illustration.

VNN simple implementation

- For each voxel
  - Find nearest pixel:
    - Calculate a normal to each input image
    - The shortest normal gives the closest image
    - The pixel closest to the normal is the pixel nearest the voxel
  - Insert value of nearest pixel into the voxel

VNN faster implementation

Assumes that the ultrasound scan is a translation (or tilt) scan performed in only one direction and not back and forth.

- For each voxel
  - Find nearest pixel:
    - Calculate a normal only to the input image before and after the voxel
    - The shortest normal gives the closest image
    - The pixel closest to the normal is the pixel nearest the voxel
  - Insert value of nearest pixel into the voxel

VBM: VBMI

Two surrounding slices interpolation

Algorithm described by Trobaugh et al. (1994). See Fig. 3 for illustration.

- For each voxel
  - Find two nearest surrounding 2D slices
    - Calculate normal to each slice
    - Interpolate between the four pixels at the contact point of the normal
  - Interpolate between the results from the two slices based on the distances

Two surrounding slices with probe trajectory estimation

Algorithm described by Coupé et al.(2005). See Fig. 4 for illustration.

- For each voxel
  - Find two nearest surrounding 2D slices
  - Compute a "virtual" plane through the voxel by estimating a probe trajectory
  - For each of the two (or four) surrounding slices
    - Interpolate between the four pixels at the contact point of the trajectory
  - Interpolate between the results from the two (four) slices based on the distances

Voxel-based tri-linear interpolation

Algorithm described by Thune et al. (1996).

- For each voxel
  - Interpolate between the eight surrounding points in the input scan lines

PBM: PNN

PNN bin-filling stage with averaging

Algorithm described by Hottier and Billon (1990), Nelson and Pretorius (1997) and Rohling et al. (1999). See Fig. 5a for illustration.

- For each pixel
  - Find the voxel the pixel belongs to
  - If voxel have no value
    - voxelValue = pixelValue
    - pixelCounter = 1
  - Else if voxel have a value
    - Assign an average of all pixels:

$$\text{voxelValue} = \frac{\text{voxelValue} * \text{pixelCounter} + \text{pixelValue}}{\text{pixelCounter} + 1} \quad (1)$$

Paper II

3D ultrasound reconstruction algorithms from analog and digital data

Ole Vegard Solberg[1, 2, 3], Frank Lindseth[1, 2, 4], Lars Eirik Bø[1, 2], Sebastien Muller[1, 2], Janne Beate Lervik Bakeng[1, 2] , Geir Arne Tangen[1, 2], Toril A. Nagelhus Hernes[1, 2, 3]

[1] SINTEF Technology and Society; Department of Medical Technology; Trondheim; Norway

[2] National Centre for 3D Ultrasound in Surgery; Trondheim; Norway

[3] Norwegian University of Science and Technology (NTNU); Faculty of Medicine; Department of Circulation and Medical Imaging; Trondheim; Norway

[4] Norwegian University of Science and Technology (NTNU); Faculty of Information Technology, Mathematics and Electrical Engineering; Department of Computer and Information Science; Trondheim; Norway

Abstract

Freehand 3D ultrasound is increasingly being introduced in the clinic for diagnostics and image-assisted interventions. Various algorithms exist for combining 2D images of regular ultrasound probes to 3D volumes, being either voxel-, pixel- or function-based. Previously, the most commonly used input to 3D ultrasound reconstruction has been digitized analog video. However, recent scanners that offer access to digital image frames exist, either as processed or unprocessed data. To our knowledge, no comparison has been performed to determine which data source gives the best reconstruction quality. In the present study we compared both reconstruction algorithms and data sources using novel comparison methods for detecting potential differences in image quality of the reconstructed volumes. The ultrasound scanner used in this study was the Sonix RP from Ultrasonix Medical Corp (Richmond, Canada), a scanner that allow third party access to unprocessed and processed digital data. The ultrasound probe used was the L14-5/38 linear probe. The assessment is based on a number of image criteria: detectability of wire targets, spatial resolution, detectability of small barely visible structures, subjective tissue image quality, and volume geometry. In addition we have also performed the more “traditional” comparison of reconstructed volumes by removing a percentage of the input data. By using these evaluation methods and data from the specific scanner, the results showed that the processed video performed better than the digital scan-line data, digital video being better than analog

video. Furthermore, the results showed that the choice of video source was more important than the choice of tested reconstruction algorithms.

Key words: 3D ultrasound, reconstruction methods, ultrasound sources, digital ultrasound, ultrasound comparison, freehand acquisition, 3D imaging, ultrasound compounding

1. Introduction

The use of 2D ultrasound for a variety of clinical applications is becoming more common. Compared to other imaging modalities like magnetic resonance imaging (MRI) and computed tomography (CT), ultrasound has the advantages of being cheaper, smaller and more flexible, it has no radiation and it is easier to introduce during surgery. 3D freehand ultrasound offers even more flexibility, and combined with position tracking it is found useful in minimally invasive image-guided surgery (IGS) [1].

1.1. Image sources and reconstruction algorithms

The most commonly used input to freehand 3D reconstructions is digitized analog video, either first stored on a video tape and digitalized with an analog video frame grabber [2-4] or obtained instantly by connecting the video frame grabber directly to the video output of the ultrasound scanner [4-18]. Some researchers state that they use digital data from the scanner. In most cases, such data is unavailable to third party users, but exceptions exist like the Sonix RP scanner (Ultrasonix Medical Corp., Richmond, Canada). Some groups also gain access to the digital data by collaborating with the ultrasound scanner manufacturers [19-23].

Different algorithms for reconstructing 3D volumes from freehand ultrasound exist. In summary these are [24]:

- Voxel-Based Methods (VBM). Include the Voxel Nearest Neighbor (VNN) where each voxel is assigned the nearest pixel [8] and algorithms where each voxel is assigned a value based on several of the nearest pixels [19, 21, 25-27]. In this group are also algorithms that skip the creation of a voxel volume and reconstruct a 2D slice or surface directly [28, 29].
- Pixel-Based Methods (PBM). Range from algorithms like the one-step Pixel Nearest Neighbor (PNN) where 2D input images are inserted directly into a

target volume [25] to two-step PNN where a second step fills empty voxels afterwards [2, 3, 30-32] to algorithms where input pixels are added with a 3D kernel [6, 17, 33, 34].

- Function-Based Methods (FBM). Algorithms where functions are made based on the input pixels and the target volume is created by evaluating these functions at regular intervals [35, 36].

For 3D probes [37, 38], the process is digital from acquisition to reconstruction. The DICOM 2008 standard (DICOM 2008, Suppl. 43) also has defined structures for 3D ultrasound volumes. 3D probes still have the disadvantage of poorer resolution compared to 2D probes. 3D probes on the other hand have the advantage of allowing real-time 3D volumes, while 2D probes may only provide real-time 2D images. In IGS, the positions of the data are also necessary in order to navigate in the 3D volume, so a position sensor must be attached to the ultrasound probe and the relation between the sensors and image data must be defined (probe calibration). In the present study we have evaluated the differences between image volumes originating from different ultrasound data sources and various 3D reconstruction algorithms using a broad range of both quantitative and qualitative comparisons methods.

2. Materials and methods

2.1. Ultrasound data import

The ultrasound scanner used (Fig. 1, Sonix RP, Ultrasonix Medical Corp., Richmond, Canada) has a research interface allowing real-time access to digital data from the scanner. A 7.5 MHz linear probe (Fig. 1, L14-5/38, Prosonic, Gyeongbuk, South Korea) [39] operating at 10 MHz scanning frequency was used to acquire all images analyzed in this study.

Three different video streams were imported simultaneously:

- Analog video, converted from PAL S-Video with a video-to-FireWire converter (DFG/1394-1e, The Imaging Source, Germany).
- Digital scan converted video, processed by the ultrasound scanner for viewing on a screen.
- Unprocessed digital data delivered as 1D scan lines, only envelope detected and log-compressed.

The digital image sources were imported directly from the ultrasound scanner over a crossed LAN (Local Area Network) cable. The three video streams were imported simultaneously in different threads on a PC with four CPU kernels (Fig. 1, Intel® Core™2 Quad Processor Q6700 2.66 GHz). Each time an image was received on the computer, a time stamp was created and assigned to the image. A depth setting of 4 cm was used on the scanner for all image acquisitions. This resulted in a pixel size (width x depth) of 0.147x0.147 mm for the analog video, 0.097x0.097 mm for the digital video, and 0.150x0.077 mm for the unprocessed "video". The images from the analog and digital video were cropped to only contain the ultrasound data. The difference in pixel sizes between the unprocessed video and digital video is due to the ultrasound scanners internal processing of the video. The pixel size difference between the digital and analog video comes from lesser resolution in the video grabbing hardware. All data sources supplied 8 bit pixels.

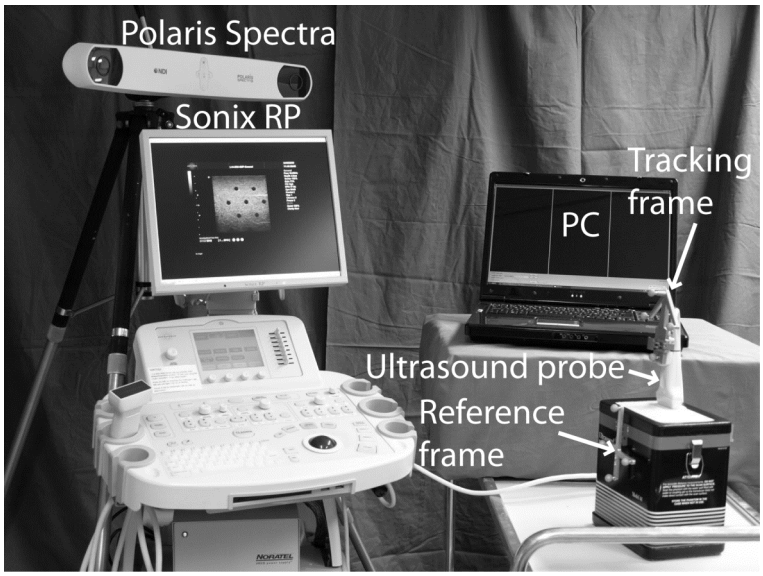

Fig. 1. System setup. Polaris Spectra optical positioning system, Sonix RP ultrasound scanner, ultrasound probe with tracking frame, ultrasound phantom with tracking reference frame, and PC for data import.

2.2. Position tracking and probe calibration

For freehand 3D ultrasound reconstruction, positions and orientations of the 2D images are needed. Several methods for obtaining these positions exist [24, 40]. In our study we used an optical positioning system (Fig. 1, Polaris Spectra, Northern Digital Inc., Canada), consisting of a tracking frame attached to the ultrasound probe and a camera unit that were used for calculating the position and orientation of this frame. The positions were

obtained using the Image-Guided Surgery Toolkit (IGSTK) [41-43]. As with the video streams, time stamps for the positions were created and assigned by the software at the time the positions were received. The positions were imported with the same application importing the three video streams, but run as a separate thread.

For the 2D ultrasound image to be correctly aligned with the output from the positioning system, a calibration is necessary. We used the spatial calibration method and phantom developed by Chen et al. [18], with threads stretched between the sidewalls in two parallel, 'N'-shaped configurations. A tracking frame was mounted on the phantom and the positions of the threads relative to this frame were measured. The corresponding structures were identified in the ultrasound images using an automatic segmentation algorithm. The relationship between the image plane and the positioning system was then found using a least-squares minimization method. We also implemented a temporal calibration based on the work by Treece et al. [44] except that we detected a point instead of a line. This temporal calibration was used to synchronize the imported positions with the images. The temporal calibration method matched the vertical movement of one of the segmented points in the 2D images to the vertical movement of the ultrasound probe as reported by the positioning system. Using the temporal calibration, 23.86 ms was subtracted from the analog video time-tags to match the time-tags of the positions, 2.56 ms was added to the digital video time-tags and 0.32 ms to the time-tags of the unprocessed images. The total mean error from the spatial calibration was 1.05 mm, with a RMS value of 1.13 mm and a standard deviation of 0.42 mm. These results were used in the reconstructions and display of data in the following tests.

2.3. Reconstruction algorithms

Two pixel-based 3D reconstruction algorithms were compared in this study. The first is called Pixel Nearest Neighbor [2, 3, 24, 30] and is a relatively fast two-step method. The first step inserts each image pixel in the input 2D images into the target 3D volume based on the position and orientation of the images. The chosen implementation overwrites any existing data in the 3D volume with the most current 2D image. The second step is an interpolation step that traverses the voxels of the target volume and attempt to fill empty voxels with the average value of the nearby voxels. The interpolation first tries to interpolate a voxel with the voxel values from the 3x3x3 grid around it. If all these voxels are empty a 5x5x5 grid is used and after that a 7x7x7 grid, and if there is still no voxel values within this

range the voxel is left empty. The second reconstruction algorithm uses a 3D kernel around the input pixels. Several variations of the input kernel are described [6, 17, 24, 33, 34, 45], and we used an ellipsoid truncated Gaussian weighted kernel around the input pixels [17, 24]. The size of the kernel is usually set to fill holes in the volume, but we used a novel method of approximately matching the theoretical ultrasound resolution in all three dimensions. For the comparisons we used two slightly different sizes of this kernel, resulting in three different reconstructed volumes:

- Pixel Nearest Neighbor.
- Small 3D ellipsoid kernel around input pixels.
- Large 3D ellipsoid kernel around input pixels.

The reconstruction algorithms were set to create volumes that used the full range of 8 bits to produce volumes that were similar in intensity. The voxel size of all reconstructed volumes were set to 0.2 mm as a compromise between resolution and processing time, the voxels sizes being larger than the input pixel sizes.

2.3.1. Determining kernels for the 3D kernel based reconstruction algorithm

As an approximation of the two-way pulse-echo response of the ultrasound imaging system we have decided to use a 3D Gaussian function. This function is best known as the probability density function for a normal distribution, and in 1D it is given by the formula

$$f(x \mid \mu,\sigma) = \frac{1}{\sigma\sqrt{2\pi}} e^{-\frac{(x-\mu)^2}{2\sigma^2}}, \tag{1}$$

where μ is the mean and σ is the standard deviation. In 3D this becomes

$$f(\mathbf{x} \mid \boldsymbol{\mu},\boldsymbol{\Sigma}) = \frac{1}{(\sqrt{2\pi})^3\sqrt{|\boldsymbol{\Sigma}|}} e^{\frac{-(\mathbf{x}-\boldsymbol{\mu})^T\boldsymbol{\Sigma}^{-1}(\mathbf{x}-\boldsymbol{\mu})}{2}}, \tag{2}$$

where $\boldsymbol{\mu} = (\mu_x, \mu_y, \mu_z)$ is the mean vector, and $\boldsymbol{\Sigma}$ is the covariance matrix.

The actual pulse-echo response may be approximated as a product of two sinc functions. The formula for a rectangular aperture in the lateral and elevation direction (Fig. 2) may be derived from Angelsen [46, p5.54]:

$$H(x,\lambda) = \operatorname{sinc}\left(\frac{x}{\lambda_t f_{\#t}}\right)\operatorname{sinc}\left(\frac{x}{\lambda_r f_{\#r}}\right), \tag{3}$$

where H is the two-way pulse-echo response, x is distance in either the lateral or elevation direction (Fig. 2). $\lambda = c/f$ is the wavelength, $f_{\#} = F/D$ is the f-number, c is the speed of sound, f is the ultrasound center frequency, F is the focal position (depth for the calculation) and D

is the effective aperture size. The transmit (t) and receive (r) directions may have different λ and $f_{\#}$. Acoustic absorption reduces the pulse center frequency, resulting in a lower center frequency for the received pulse compared to the transmitted pulse. For a Gaussian pulse envelope the frequency is reduced by the following formula [47]:

$$f_r(z) = f_t - \frac{\alpha B^2 z}{4\ln 2}, \tag{4}$$

where z is the propagation distance, $\alpha = (a\ln 10)/20$ is the average constant of the absorption coefficient. A commonly used value for a is 0.5 dB/cmMHz. B is the -6 dB bandwidth of the imaging pulse. In the axial direction (see Fig. 2) the pulse-echo response is dependant of the form of the transmitted pulse, but is often approximated as a Gaussian function.

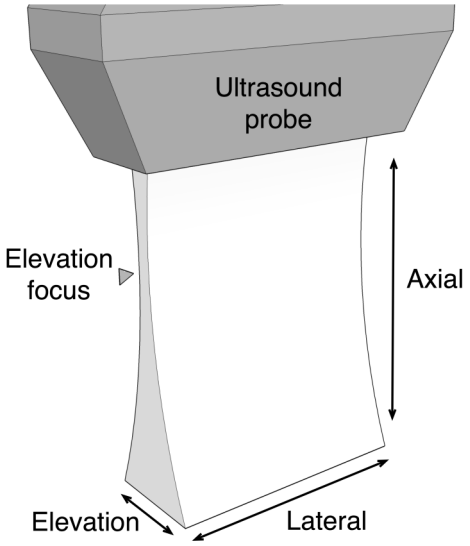

Fig. 2. Illustration of the imaging sector of an ultrasound probe. The lateral, axial and elevation direction are marked in addition to the fixed elevation focus.

To calculate the theoretical size of the focus of an ultrasound probe in the lateral or elevation direction the function (3) can be evaluated at -6 dB. However, for the Gaussian function we use the width of the main lobe, equal the first zero in the narrower of the two sinc functions in (3). The resulting value was used as the limit for a 99.7% confidence level for a 1D Gaussian distribution (total pulse width obtained from (4) corresponds to 6 standard deviations, so the standard deviation (σ) is estimated simply by dividing the width of the main lobe by 6). The ultrasound scanner uses a Gaussian-like apodization on the elements to dampen the side lobes of the transmitted pulse. This apodization will also create a wider

main lobe than indicated by the formula (3), which are for a situation without apodization [46, p5.56 - p5.58].

The ultrasound probe had a fixed elevation focus of 16 mm (Ultrasonix Medical Corp., Richmond, Canada) and the ultrasound scanner allows the operator to set several variable focus points in the axial direction. Three focus points were used and at least one was set near the fixed elevation focus. The probe size in the lateral direction is 38 mm, but the effective aperture size varies according to depth (dynamic aperture). The aperture sizes for both transmit and receive were calculated with parameters read from the scanner and code obtained from Ultrasonix. According to information obtained from Ultrasonix the fractional Bandwidth of the probe is minimum 70% of the center frequency at -6 dB, the center frequency being 7.2 MHz, resulting in a bandwidth of 5.04 MHz. The theoretical lateral and elevation resolutions in focus for the used ultrasound probe are illustrated in Fig. 3A by evaluating formula (3) at -6 dB, while the calculations of the total width of the main lobe are shown in Fig. 3B. The imaging frequency used is 10 MHz, and the speed of sound in tissue is set to 1540 m/s.

The size in the elevation direction (element height) is 4 mm (Ultrasonix Medical Corp., Richmond, Canada). The theoretical resolution in the axial direction equals half the pulse length [46, p1.22], i.e.

$$\Delta a = \frac{cT_p}{2} = \frac{c}{2B}, \tag{5}$$

where T_p is the pulse length in time. With a bandwidth of 5.04 MHz the best theoretical axial resolution is 0.153 mm (5). However, as we wanted to find a value to use for the limit of the 99.7% confidence level of a 1D Gaussian function, the full pulse length should be used: 0.306 mm.

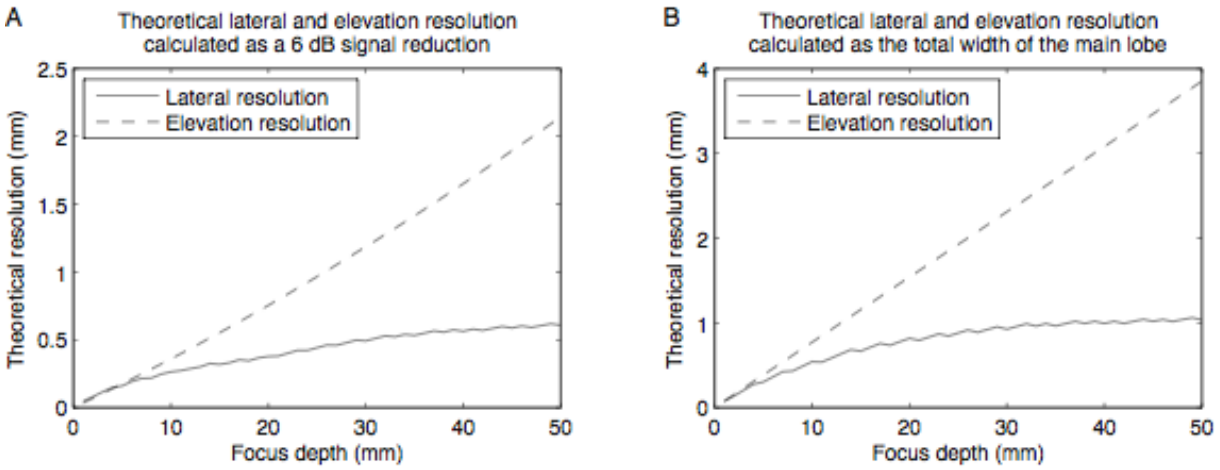

Fig. 3. Plot of the theoretical lateral and elevation resolution in focus for a few selected depths for the L14-5/38 probe operating at 10 MHz. (A) The resolutions shown as a 6 dB signal reduction, calculated from (3) and (4). The corresponding axial resolution is 0.154 mm for all depths, calculated from (5). (B) The resolutions illustrated as the total width of the main lobe from (3).

The resolution values in all three dimensions were used to create the covariance matrix $\mathbf{\Sigma}$ for the 3D Gaussian function (2) and thus define the extent of the truncated kernel. For the small kernel we used an imaging depth of 19 mm to calculate the lateral resolution (= 0.78 mm), and for the large kernel we used a depth of 32 mm (= 0.99 mm). To speed up reconstruction computation time we reduced the total kernel size by calculating the elevation resolutions at somewhat shallower depths. The elevation resolutions were calculated for the depth of 18 mm (= 1.39 mm) for the small kernel and for the depth of 24 mm (= 1.85 mm) for the large kernel. In the 3D reconstruction, the 3D Gaussian function was oriented according to the 2D ultrasound images, and discrete values of the function were used to match the target 3D voxel grid. For the axial resolution we used a resolution of 0.171 mm instead of 0.306 mm, due to initially calculating the axial resolution for 9 MHz instead of 5 MHz. We truncated the 3D Gaussian kernel at 95% confidence level and then increased the kernel size to include the same number of voxels on both sides of the input pixel. Since the axial resolution was so high this resulted in a kernel size of only one voxel in the axial direction. However, the current implementation of the reconstruction requires a larger kernel in this direction, so we increased the kernel size in the axial direction to three voxels.

2.4. Data collection

All acquisitions were performed as freehand translation sweeps with the 3 different data streams imported simultaneously. To minimize errors from the position-to-image

synchronization, and to make sure that the reconstructions got enough data to fill holes, all sweeps were performed with a slow, smooth motion. One scan thus resulted in input data from three different data sources, all showing images from the same structures. The digital video after scan conversion was the same images as presented on the screen of the ultrasound scanner. These images were processed by the scanner for viewing and all user-controlled functions, such as the gain function on the scanner's control panel were applied by the scanner. The analog data is a video signal output from the ultrasound scanner. The signal was converted from digital to analog by the scanner, and again to a digital signal by the video grabber. Throughout this paper the images used for the 3D reconstructions are called "input images" while images used directly in the comparisons are called "original images". In the comparisons the same images were never used as both input and original images even if the images may be similar and acquired in approximately the same positions. Both input images and original images came from all three data sources, and while input images were acquired as a stack of several images original images were only acquired as single images.

2.5. Tests for comparing reconstruction algorithms and data sources

2.5.1. Compare the reconstruction algorithms' ability to correctly recreate removed data (test 1)

To compare the quality difference of different reconstructions based on the same input data the method of removing a percentage of input data [31, 32, 35, 48, 49] was used. We scanned a section of the underside of the forearm on two healthy volunteers with two translation scans along the arm of one volunteer and two translation scans across the arm of the other volunteer. The scans along the forearm gave images that only changed slightly from one image to the next, while the images from the scans across the forearm changed more rapidly. Before reconstruction, 0%, 25%, 50%, 75%, 100%, 300%, 500% and 700% of the data of one of the input 2D ultrasound images was randomly removed. Random pixels were removed from one slice for the percentages below 100%, and whole slices were removed for the percentages 100% - 700%, e.g.: for 300% three slices were removed. After reconstruction, all pixel values of this input image were compared with the voxel values from the corresponding positions in the reconstructed volumes and the RMS value of the differences was calculated. The orientation of the reconstructed volume was based on the orientation of the input image from which the data was removed. This procedure was

performed on four different positions without holes in each volume, and statistical analyses were used to compare the performance of the reconstruction algorithms.

2.5.2. Compare the reconstructed volumes' ability to display existing structures (test 2)

Measurements of the reconstructed volumes' ability to retain the resolution in the 2D images and of the resolution they manage to obtain in the elevation direction were performed. A comparison was performed by human observers on how well tissue was visualized. The human observers were technical researchers with knowledge of ultrasound imaging ranging from medium to expert. The reconstructed volumes from one scan resulted in a set of volumes with various combinations of the three data sources and three reconstruction algorithms. Original 2D ultrasound images from the ultrasound scanner were acquired simultaneously as a selection of 2D anyplane slices from the reconstructed volumes in the same position and orientation (Fig. 4C and Fig. 4D). Statistical comparisons were performed between reconstruction algorithms/original 2D ultrasound images and video sources. All volunteers were presented with the same set of images on the same computer with brightness and contrast levels unchanged.

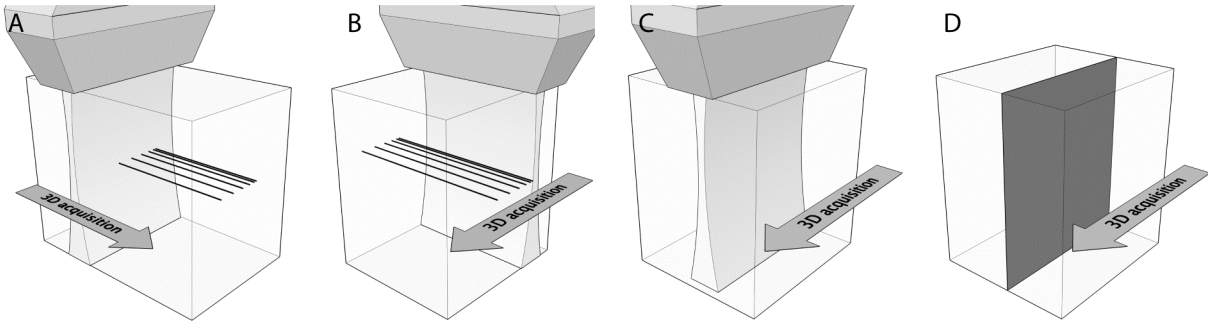

Fig. 4. Illustrations of ultrasound sectors. The 3D acquisition scan direction is indicated, and the reconstruction volume is shown as a transparent box. (A) A 3D scan along the threads of a resolution phantom. The threads are seen as points in the ultrasound sector. (B) A 3D scan across the threads of a resolution phantom. The threads are seen as lines in the ultrasound sector. (C) Illustration of a single original ultrasound image acquired orthogonal to the input images in the 3D reconstruction. (D) Illustration of a 2D anyplane through the 3D volume in the same position as the original image in (C).

2.5.2.1. Visual comparisons of structures placed increasingly closer (test 2a)

Measuring the volume resolutions was accomplished by scanning an ultrasound resolution phantom, with six small structures (threads) that are placed with distances of 1, 2, 3, 4 and 5 mm (Model 040, CIRS Inc., VA, USA). The threads of the CIRS 040 phantom are

0.1 mm in diameter and made of Nylon Monofilament. The threads were scanned with three translation sweeps both along (Fig. 4A) and across (Fig. 4B) the threads to measure resolutions both in the lateral and elevation direction (Fig. 2) of the ultrasound input planes. 2D images were obtained by collecting original ultrasound images with position and orientation (Fig. 4C). This position and orientation were used to create 2D anyplanes through the reconstructed 3D volumes (Fig. 4D). These images were presented in random order and evaluated by eight volunteers that were given two questions to answer for each image: "Count how many separate bright structures you can see and rate how easy it is to identify those you can see (1-5, where 1 is easy and 5 hard)".

2.5.2.2. Comparisons based on image measurements of spatial resolution (test 2b)

The images in test 2a of the CIRS 040 phantom also contained a separate thread, which was used for measurements of resolution: Both the original and a resampled (downsampled) version of the original image were used, and resolution were measured in positions corresponding with the anyplanes through the 3D volumes. Axial and lateral spatial resolutions were measured directly from the 2D ultrasound images by plotting gray level profiles through the center of the scanned wires [50]. The maximum pixel value was used as the center value for each thread. Parabolic curves were matched to these plots and evaluated at -6 dB and -20 dB. Only the values above -6 dB were used for matching the parabolic curves both in the original 2D images and in 2D anyplanes obtained from the 3D volumes. Measurements in the elevation direction were possible to perform on anyplanes through the 3D volumes scanned across the threads (Fig. 4B). Each measurement was performed on the same wire at a depth of approximately 27 mm in three different scans.

2.5.2.3. Visual comparisons of small, barely visible structures (test 2c)

The CIRS 044 (Model 044, CIRS Inc., VA, USA), an ultrasound phantom with small cylinders of varying size, was used to compare the visibility of small structures after a reconstruction. Three ultrasound translation sweeps were performed on the smallest cylinders on the CIRS 044 phantom, both lengthwise and crosswise. These small cylinders have measurements of 1.5 mm (diameter) and 2.4 mm (length) specified in the fabrication sheet. Original single 2D images were acquired showing as many cylinders as possible, all cylinders appearing as circles in the ultrasound image. Anyplane images (Fig. 4D) through

the 3D volumes were created from the same position and orientation as the collected original images (Fig. 4C). Eight people were presented 2D images, in random order, showing small objects and presented with two questions for each image: “Count how many separate dark structures you can see, and rate how easy it is to identify those you can see (1-5, where 1 is easy and 5 hard).” When presented with several images of varying quality, the test person may “learn” where the structures should be, and this may enable them to identify more structures in a poor image that they would do otherwise. To allow for this the test subjects were also asked to rate (1-5) how easy it was to identify the structures they could identify, and they were also shown an illustration of the corresponding section of phantom beforehand. The 2D images were either an original 2D ultrasound image showing the structures or a 2D anyplane obtained from a 3D volume. The anyplanes from the 3D volumes were either approximately orthogonal or parallel to the 2D images from which the 3D volume was created.

2.5.2.4. Visual comparisons of tissue data orthogonal to the scanning direction (test 2d)

A section of the underside of the forearm of two healthy volunteers was scanned with freehand translation sweeps. One person was scanned with two sweeps along the arm while the other was scanned with two sweeps across the arm. Original single 2D images were acquired approximately orthogonal to the 3D acquisition sweeps for comparison (Fig. 4C) and corresponding anyplane images through the 3D volumes were collected (Fig. 4D). A group of eight people were presented with different 2D images in random order, showing tissue data from the same location. They were presented with sets of 3 or 4 images and asked the following question: “Sort the images according to quality and give each image a quality score (1-5), where 1 is best and 5 is worst.” The images were original 2D ultrasound images of the tissue or anyplanes obtained from reconstructed 3D volumes approximately orthogonal to the input 2D images. The sets of 3 images showed the 3 different input sources, being all original 2D images or all anyplane images from a specific reconstruction algorithm. The sets of 4 images showed an original 2D ultrasound image and anyplane images from different reconstruction algorithms, all images being from the same input source.

2.5.3. Compare the correctness of the reconstructed volume's geometry (test 3)

A geometry comparison is a measurement on how well a reconstruction manages to recreate a known phantom geometry. Statistical comparisons based on both data sources and reconstruction algorithms were performed.

The CIRS 044 have a set of cylinders with specified measurements of 3mm (diameter) * 6 mm (length). Three ultrasound translation sweeps were performed on these structures in both the lengthwise and crosswise direction. Original single 2D ultrasound images with 3D positions and orientations were acquired for each data set both along and across the cylinder. Both height and width of the structure in the image was measured, resulting in measurements of cylinder length in the lateral direction and diameter height in the axial direction for the images along the cylinder, and measurements of diameter width in the lateral direction and diameter height in the axial direction. Three measurements were performed in the original image and three in an image processed with a levels function of an image processing application. The levels function was used to spread out the pixel intensities so that they fill the whole 8-bit range. The reason for this was to try to emulate the processing in the image reconstructions where a similar function was used for the whole volume.

2D anyplane images were created through the reconstructed 3D volumes at positions and orientations matching that of the original 2D images. The same structure measurements were done on these anyplane images and the differences were compared and tested for variations in reconstruction algorithm and data source quality. The anyplane images covered measurements in the elevation direction in addition to measurements in the lateral and axial direction. The elevation measurements were received from cylinder length in the scans along the cylinder and from the cylinder width measurements in the scans across. The same person performed all analyses, repeating each measurement three times. The cylinder measurements performed on the original ultrasound images were used as the gold standard for the comparisons.

2.6. Statistical comparisons

All data were compared using statistical methods using the SPSS Statistics software (SPSS 16 for Mac, SPSS Inc., IL, USA). All statistical tests were performed with a 5% confidence level (α = 5%). To check if all groups came from the same distribution, an overall test was applied. In case of rejection, each group was tested against the others.

Each group was tested for normal distribution using the Shapiro-Wilk (SW) test to check for the possibility to use parametric statistics. For unrelated samples, if normality was accepted for all groups the Analysis of Variance (ANOVA) test was used for the overall statistics and the Bonferroni multiple-comparisons procedure was used for the pairwise comparisons. If normality was rejected the non-parametric Kruskal-Walis (KW) test was used for the overall statistics and the Mann-Whitney-Wilcoxon (MWW) test was used for the pairwise comparisons. For test 1 with related samples the Friedman test was used for the overall statistic and the Wilcoxon Signed Rank (WSR) test was used for the pairwise comparisons. All statements in the text regarding differences (e.g.: performed better/poorer than, better/worse result, harder to identify, more accurate detection) are based on statistically significant results, even if this not mentioned explicitly every time.

3. Results

3.1. Compare the reconstruction algorithms' abilities to correctly recreate removed data (test 1)

The differences between the slice with the removed data and the data values from the anyplanes in the same positions in the reconstructed volumes were plotted as curves with RMS results for each removed percentage. See Fig. 5 as one example showing the RMS values from the different reconstructed volumes using the digital video as input in the scans across the forearm. All RMS values for the different removed percentages were combined for the statistical comparisons (Table 1). Table 1 shows results from the scans taken either across or along the forearm. Statistically significant differences were found between the following reconstruction algorithms: In the scans across the forearm, representing data with high degree of variation, the large kernel performed poorer than the other two reconstruction algorithms for the digital data, and for the unprocessed video the small kernel performed better than the large. Also when combining the data from all three video sources the small kernel performed better than the large. In the scans along the forearm, representing data with little variation, the PNN reconstruction gave a better result than the others for the analog and digital video while it gave a worse result for the unprocessed data. For the unprocessed data in the scan along the forearm the large kernel reconstruction performed better than the small kernel that performed better than the PNN reconstruction. The differences between the scan across and along the forearm were visible as higher mean values in the scans across the arm

(Table 1). When comparing values in Table 1 it was only possible to compare values from the same data source because of the different characteristics of the data sources.

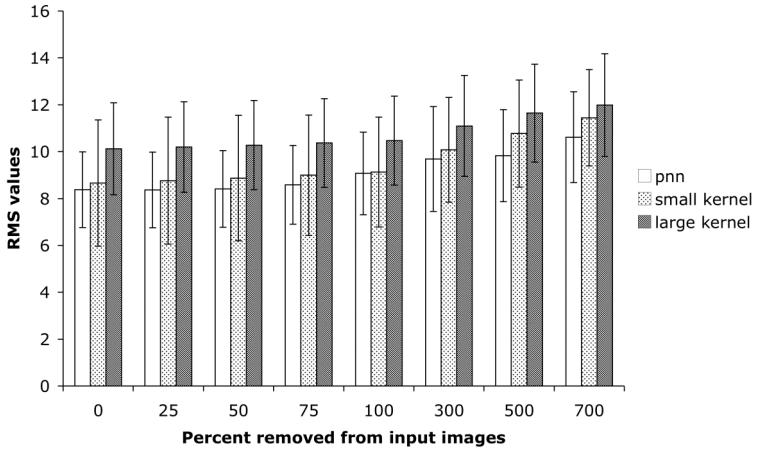

Fig. 5. RMS values for the three different reconstruction algorithms for the digital video acquired across the forearm. Mean and standard deviation values are presented for each removed percentage. All RMS measurements for the large kernel are larger than the other two, and the difference is statistically significant.

Table 1. RMS values obtained by removing a percentage of data (0-700% removed) from selected input images. The scans across the forearm represent data with large variations while the scans along the forearm represent data with little variation from one image to the next. The values in the table between data sources are not comparable.

	Scan across arm (large variation between images)		
	Analog	Digital	Unprocessed
PNN	8.38±2.42	9.12±2.45	16.93±3.43
Small kernel	7.57±1.46	9.59±1.98	16.10±2.96
Large kernel	7.50±1.37	10.77±2.01	17.12±3.19

	Scan along arm (small variation between images)		
	Analog	Digital	Unprocessed
PNN	5.04±1.01	6.83±1.31	14.07±0.99
Small kernel	5.68±0.96	7.41±1.52	13.21±1.40
Large kernel	5.83±1.04	7.49±1.52	12.86±1.17

3.2. Visual comparisons of structures placed increasingly closer (test 2a)

The data from the comparisons can be illustrated as graphs showing the number of threads and the difficulty to identify the threads (Fig. 6, Table 2). The compared images came from scans both along (Fig. 4A) and across (Fig. 4B) the threads (See also Fig. 7A and

Fig. 7B for examples of the images), the scans along the threads representing a comparison in the lateral direction of the ultrasound images and the scans across the threads representing a comparison in the elevation direction as related to the ultrasound image (Fig. 2).

The results showed no statistically significant differences between the reconstruction algorithms, each with a median of 5 identified structures (Table 2). The identification of only 5 structures means that the structures with the distance of 1 mm could not be separated. Comparing the results from the anyplanes through the reconstructed volumes with the original 2D ultrasound images, the original images gave statistically significantly better results with a median of 6 identified structures (Table 2), meaning that the structures with the smallest distance of 1 mm could be separated in the majority of the observations. The comparison of the data sources showed that for all tests except the structure count from the scan along the threads, the unprocessed data produced volumes where fewer structures could be identified and they were harder to identify.

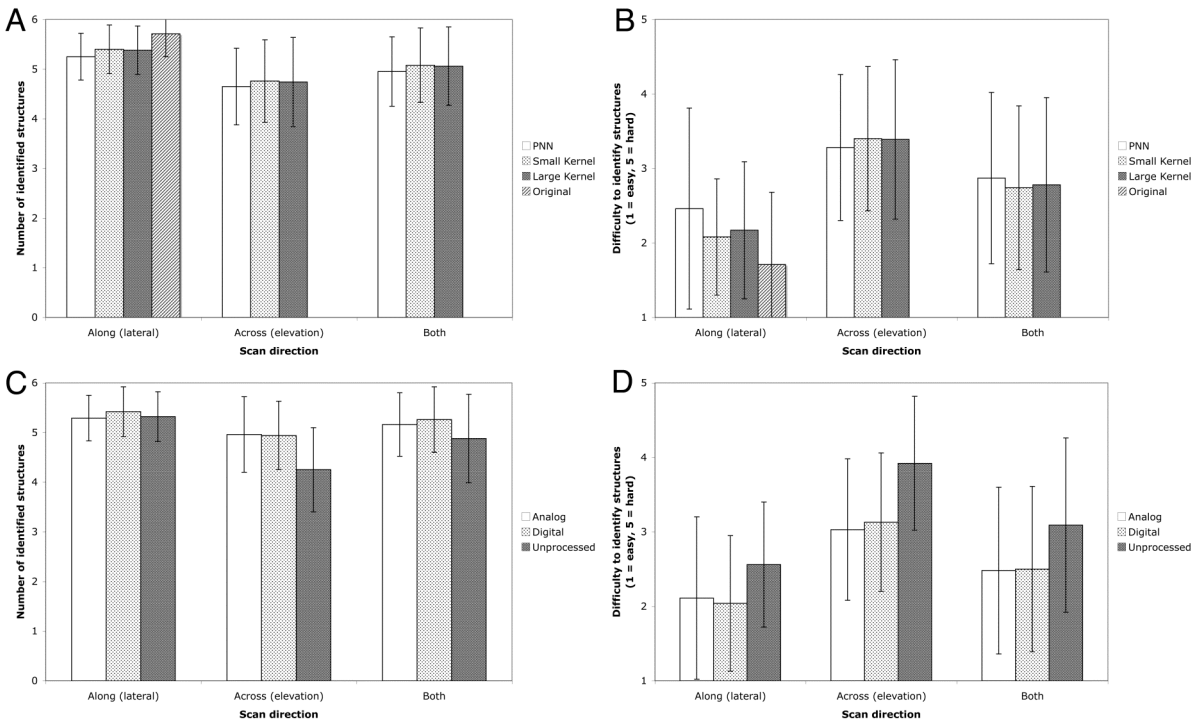

Fig. 6. Identification of 6 structures placed increasingly closer. Results from the scans along, across and both combined. Mean and standard deviation values are shown in the graphs. The six threads were identified by eight volunteers. (A) Number of identified threads for the reconstruction algorithms and original images. (B) The difficulty to identify the threads for the reconstruction algorithms and original images. (C) Number of identified threads for the different data sources. (D) The difficulty to identify the threads for the different data sources.

Table 2. Number of identified small structures. Mean and standard deviation values for the different combinations of reconstruction algorithm and data source.

	Scan along structures (lateral direction)				Scan across structures (elevation direction)			Both scan directions combined		
	PNN	Small kernel	Large kernel	Original	PNN	Small kernel	Large kernel	PNN	Small kernel	Large kernel
Analog	5.17±0.38	5.33±0.48	5.38±0.49	5.50±0.52	4.83±0.82	5.00±0.72	5.04±0.76	5.00±0.65	5.17±0.63	5.21±0.65
Digital	5.42±0.50	5.46±0.51	5.38±0.49	5.94±0.25	4.88±0.74	4.92±0.65	5.04±0.69	5.15±0.68	5.19±0.64	5.21±0.62
Unprocessed	5.17±0.48	5.42±0.50	5.37±0.49	5.69±0.48	4.25±0.61	4.38±0.97	4.12±0.95	4.71±0.71	4.90±0.93	4.75±0.98

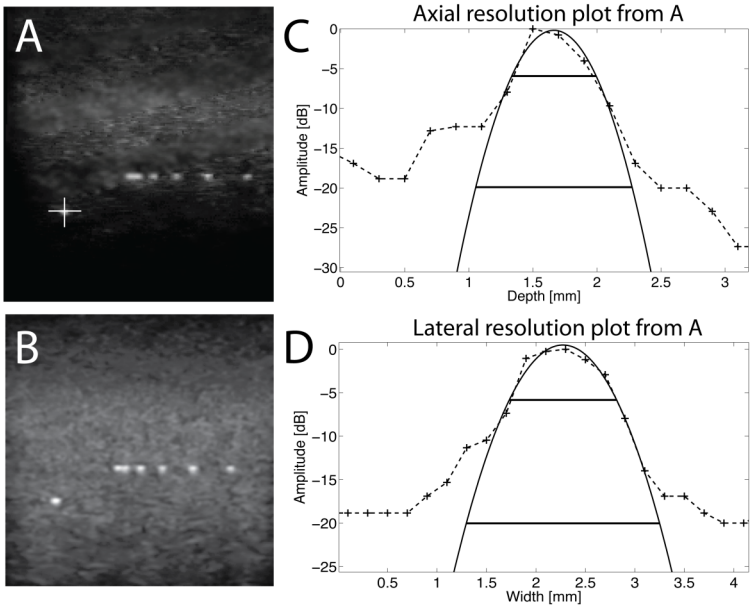

Fig. 7. Example of thread size as a measurement of spatial resolution in the axial and lateral direction. The images are based on an anyplane image from a PNN reconstructed volume with analog video as input. (A) The anyplane slice through the ultrasound volume with an illustration of where (crosshairs) the intensity plots in the axial and lateral direction were collected. The horizontal measurement give the elevation resolution when the anyplanes come from the volumes scanned across the threads. The other structures in this image were used in test 2a. (B) The original ultrasound image from the analog video. Pixel values have been modified with the levels function of an image processing application to provide an image with more contrast in the paper. (C) A dB plot of the intensity values in the axial direction from (A) with a fitted parabolic curve. (D) A dB plot of the intensity values in the lateral direction from (A) with a fitted parabolic curve.

3.3. Comparisons based on image measurements of spatial resolution (test 2b)

Parabolic curves were matched to plots through the centers of the scanned wires (Fig. 7) and these curves were evaluated at 6 dB and 20 dB levels below the maximum value. The 6 dB values are presented in Table 3.

There were no statistically significant differences between the thread measurements from the different reconstruction algorithms, but they performed better than the original

images in some of the tests: In the lateral direction all reconstruction algorithms gave better results than both the original images and the resampled version of these images for both 6 dB and 20 dB. For 6 dB, the measurements in the lateral direction based on the anyplanes through the reconstructed volumes had a mean thread width of 1.17 mm while the original images had a mean width of 1.32 mm. In the axial direction for the 6 dB evaluations, only the small kernel was better than the original images with a mean thread height of 0.67 mm compared to the mean height of the original images of 0.80 mm. Both the small and the large kernel performed better than the resampled original images. When fewer groups were compared compared without regard to the other groups more differences were detected also for the axial resolution: For 6 dB the PNN algorithm performed better than both the resampled and original images, and also the large kernel performed better than the original images. For 20 dB both the PNN and small kernel reconstruction performed better than the original images. For the 20 dB evaluations in the axial direction, all reconstruction algorithms gave better results than the resampled original images while none showed statistically significant difference from the original images. The results from the data sources showed that the unprocessed ultrasound performed poorer than both analog and digital video in both axial and lateral direction for 6 dB and 20 dB with a measured mean axial thread height for 6 dB of 0.79 mm and a measured mean lateral thread width of 1.49 mm compared to a measured axial thread height of 0.69 mm and measured lateral width of 1.21 mm for the processed video sources. The only difference in the elevation direction was that analog video performed better than unprocessed video for 20 dB.

Table 3. Image measurements of spatial resolutions. The results are presented as mean and standard deviation values in mm, and the measurements are from a fitted parabolic curve evaluated as 6 dB (see Fig. 7 for example).

	Analog			Digital			Unprocessed		
	Axial	Lateral	Elevation	Axial	Lateral	Elevation	Axial	Lateral	Elevation
PNN	0.65±0.09	1.15±0.04	1.86±0.38	0.66±0.15	1.08±0.15	1.58±0.50	0.76±0.20	1.22±0.19	1.90±0.43
Small k.	0.69±0.05	1.18±0.05	2.10±0.31	0.62±0.07	1.11±0.06	2.31±0.62	0.71±0.05	1.23±0.08	2.37±0.51
Large k.	0.69±0.06	1.16±0.07	2.10±0.32	0.65±0.08	1.16±0.08	2.24±0.50	0.74±0.07	1.28±0.06	2.34±0.47
Original	0.74±0.01	1.28±0.01	-	0.69±0.03	1.28±0.03	-	0.98±0.03	1.80±0.03	-
Resamp.	0.76±0.01	1.27±0.02	-	0.73±0.02	1.25±0.01	-	0.78±0.02	1.45±0.02	-

3.4. Visual comparisons of small, barely visible structures (test 2c)

Examples of the images presented to the eight volunteers are shown in Fig. 8. The original images allowed more accurate structure detection than the anyplanes through the reconstructed volumes both for the number of structures identified (Fig. 9, Table 4) and the difficulty to identify the structures, by deviating from the true number of structures (eleven) by a median of 0. The deviation for the large kernel had a median of 2.5 structures, which was statistically significantly better than the PNN reconstruction with a median deviation of 4 structures from the true number. The small kernel could not be separated from the other reconstructions with a median deviation of 3 structures. For the scans along the cylinders the anyplanes from the PNN reconstruction did not allow the volunteers to identify the same number of structures as the other reconstructions with a median deviation of 3 structures compared to the others with medians of 1 structure deviation. The structures in anyplanes from the PNN reconstructions were more difficult to identify than the small kernel. In the scans across the cylinders there were no statistically significant differences between the reconstruction algorithms with a combined median deviation of 6 structures. The results from comparing only two groups with each other also showed that the structures in the volumes from the PNN reconstruction were statically more difficult to identify than both the other reconstruction algorithms for the scan direction along the cylinders and for both directions combined. The image sources could not be statistically significantly separated for the scan along the cylinders with a combined median deviation from the true number of 1 structure. In the scan across the cylinders, the unprocessed data performed poorer than the other image sources with a median deviation of 7 structures compared to a median of 6 for the digital video and 5 for the analog video. The digital and analog video could, however, not be separated through statistical significance. When combining both scan directions, the analog video with a median deviation of 3 performed statistically significantly better than the unprocessed data with a median deviation of 4. The digital video with a median deviation of 3 could not be separated from the other algorithms.

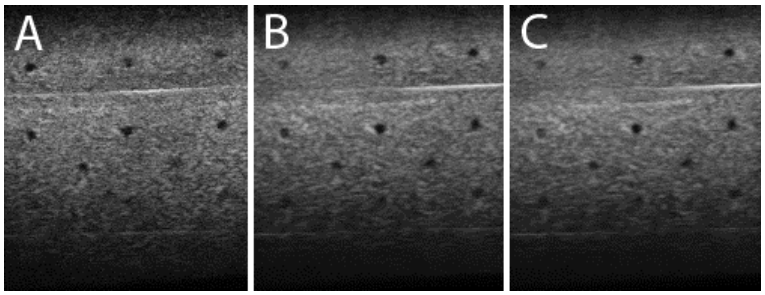

Fig. 8. Example of anyplane images of small structures (cylinders). The anyplanes are from reconstructions based on digital video as input. The scan direction of the input images are along the cylinders. (A) PNN reconstruction. (B) Small kernel reconstruction. (C) Large kernel reconstruction.

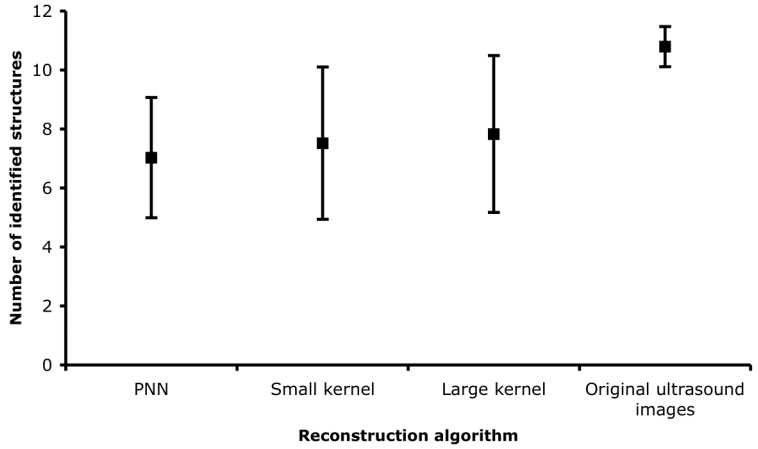

Fig. 9. Number of identified structures. The results are shown as the deviation from the true number of structures (=11) presented as mean and standard deviation values. Results from the three different reconstruction algorithms compared with original ultrasound images. The results from both the scans across and along the structures are combined.

Table 4. Comparisons based on the number of identified structures. The values shown are the deviation from the true number of structures (=11) presented as mean and standard deviation values.

	Both scan directions combined				Scan across cylinders (elevation direction)			Scan along cylinders (lateral direction)		
	PNN	Small kernel	Large kernel	Original	PNN	Small kernel	Large kernel	PNN	Small kernel	Large kernel
Analog	3.63±1.47	3.17±2.30	2.83±2.30	0.25±0.77	4.54±1.28	5.12±1.36	4.88±1.39	2.71±1.00	1.21±0.98	0.79±0.41
Digital	3.75±2.02	3.23±2.55	2.90±2.78	0.19±0.54	5.04±1.73	5.46±1.56	5.29±1.83	2.46±1.35	1.00±0.66	0.50±0.72
Unprocessed	4.52±2.46	4.04±2.82	3.77±2.81	0.19±0.75	6.62±0.97	6.58±0.93	6.42±0.93	2.42±1.47	1.50±1.38	1.12±0.80

3.5. Visual comparisons of tissue data (test 2d)

Fig. 10 contain examples of the images used in the comparisons showing both original ultrasound images and anyplanes through reconstructed volumes, all originating

from the same position. The differences between the reconstruction algorithms were not statistically significant, but all performed worse than the original images both with respect to ordering and quality. The data sources could not be separated in the scans along the forearm, and the quality score could also not be separated in the scans across the forearm. The results from the ordering in the scans across the forearm showed that the digital video was preferred, followed by the unprocessed data, and the analog video was evaluated as the worst quality. When combining the answers from both scan directions the ordering gives the same result as for scans across the forearm, but now also the quality score shows the analog video to perform poorer than the other sources.

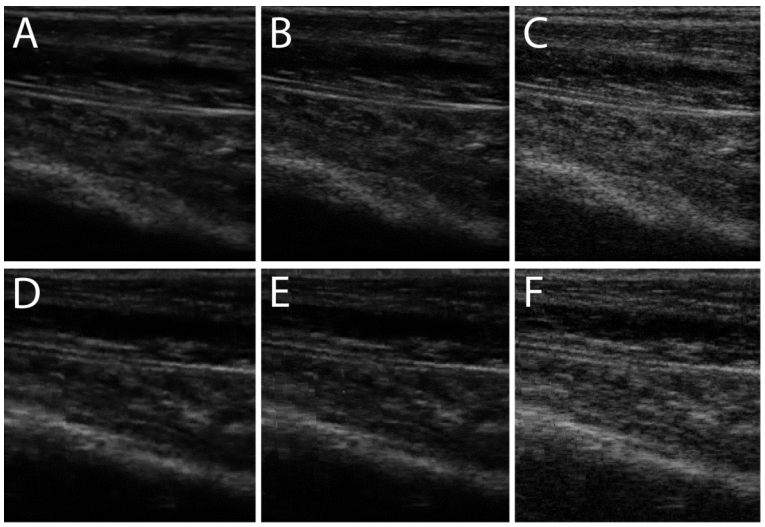

Fig. 10. Original ultrasound images and anyplanes of the underside of the forearm. All images are originating from the same position. All anyplane images are reconstructed with a small kernel, and the anyplanes are obtained orthogonal to the reconstruction input images (See Fig. 4C and Fig. 4D). (A) Original analog image. (B) Original digital image. (C) Original unprocessed image. (D) Anyplane with analog ultrasound video as reconstruction input. (E) Anyplane with digital ultrasound video as reconstruction input. (F) Anyplane with unprocessed ultrasound data as reconstruction input.

3.6. Compare the correctness of the reconstructed volume's geometry (test 3)

None of the reconstruction algorithms could be separated from the original ultrasound images (used as gold standard) while also being different from the other reconstruction algorithms (Table 5). For the scans across the cylinder the analog and digital video differs from the original images in the length measurements, by a difference in measured mean value of 0.33 mm for the analog video and 0.16 mm for the digital video (Table 6). The unprocessed data differs from the original images in the width measurements, by a difference in measured mean width of 0.28 mm (Table 6).

Table 5. Comparisons of reconstruction algorithms based on distance measurements. The measurements were performed on the length (= 6.66 mm), width (= 3.06 mm) and height (= 3.07 mm) of a small cylinder. The differences in mm are shown for the results that are statistically significantly different from the original images ("gold standard"). The term NS means not statistically significant.

Scan direction		Length	Width	Height
Both		NS	NS	NS
Along cylinder	PNN	0.27	NS	NS
	Small k.	0.36		
	Large k.	0.42		
Across Cylinder	PNN	0.13	NS	NS
	Small k.	0.22		
	Large k.	0.25		

Table 6. Comparisons of input ultrasound sources based on distance measurements. The measurements were performed on the length (=6.66 mm), width (= 3.06 mm) and height (= 3.07 mm) of a small cylinder. The differences in mm are shown for the results that are statistically significantly different from the original images ("gold standard"). The term NS means not statistically significant.

Scan direction		Length	Width	Height
Both		NS	NS	NS
Along cylinder	Analog	0.29	NS	NS
	Digital	0.32		
	Unprocessed	0.44		
Across cylinder	Analog	0.33	NS	NS
	Digital	0.16	NS	
	Unprocessed	NS	0.28	

4. Discussion

In image-guided surgery it is important to have reliable images available from all directions, and the quality of the reconstructed 3D ultrasound data to be used for guidance and therapy is important. In this paper we have studied if the choice of 3D reconstruction algorithm and input data source may affect image quality and resolution in a 3D volume as evaluated by various methods. A quick summary of the results is presented in Table 7.

Table 7. Short summary of the most important results from the different comparison tests.

Comparison result	Test 1a. Remove data	Test 2a. Identification of close structures	Test 2b. Image resolution measurements	Test 2c. Identification of small structures	Test 2d. Tissue data comparisons	Test 3. Geometry measurements
Reconstruction algorithms	Large k. worst (for varying images)	Equal performance	Equal performance	PNN worst	Equal performance	PNN barely best Large k. middle Small k. barely worst
Data sources	-	Unprocessed worst	Unprocessed worst	Unprocessed worst	Digital best, Unprocessed middle, Analog worst	Indecisive (Digital slightly better)

4.1. Comparing the performance of the reconstruction algorithms

Our study showed that the performance of the 3D ultrasound reconstruction algorithms varied from test to test. The small kernel reconstruction algorithm performed slightly better overall than the two other tested algorithm implementations, but a conclusion depends on how the tests are being weighted due to importance. If all tests are to be equally weighted, the choice of reconstruction algorithm doesn't matter, and a good choice may be the fastest algorithm, PNN. All quality measures may, however, not be equally important, and the preferred algorithm may be selected based on intended application.

The method of removing input data and measuring the reconstruction algorithms success at recreating removed data is the "classical" comparison test of reconstruction algorithms [35]. For the scan along the forearm, the PNN algorithm surprisingly has the best performance for the analog and digital video. However, this scan direction creates images that change only slightly from one image to the next. For the unprocessed data, however, the PNN reconstruction has the worst performance, probably because of the increased level of information in these images. The scans across the forearm were more interesting, since they gave more variation from one image to the next, and the ability to perform well under such situations is more important in a practical situation, so these results were given more weight in Table 7 and our conclusions. For the scans across the forearm the reconstruction with the largest ellipsoid kernel around input pixels performed worse than the smallest kernel for the digital video and the unprocessed data. The reconstruction with the largest kernel performed also worse than the PNN reconstruction for the digital video. The reason for the poorer performance of the large kernel may be that we used a lateral resolution for the

reconstruction based on a depth of 32 mm when the image depth was 40 mm, and thus blurring the data too much in a large part of the reconstructed volume.

In addition to test 1, only test 2c and test 3 showed any statistical differences in reconstruction algorithms. All the comparisons of counted small structures in test 2c showed that the PNN reconstruction performed poorer than the small kernel in two cases and also poorer than the large kernel in two cases (Table 4). When only comparing two groups at a time in test 3, the PNN algorithm performed better than the small kernel in one comparison and better than the large kernel in three. However, the differences in measured mean values were very small: less than the size of the volume cells (< 0.2 mm), so even if the differences were statistically significant they may not result in much practical difference.

In image-guided surgery it is most important to identify very small structures in the correct location, so the small or large kernel may be a better choice than the current implementation of the PNN algorithm. However, it should be noted that the small structures in test 2c were so small that a minor position change made the structures disappear. In the test we used the position of a single ultrasound image showing all the structures. The nature of the PNN reconstruction algorithm implementation just replacing existing data in the 3D volume with the latest data might have changed the position of the small structures just enough that they could not be identified. This does not mean that they could not have been identified in a neighboring position, just that the PNN reconstruction algorithm introduced a small position bias. It is possible to remove this bias by changing the bin-filling [24] of the PNN implementation to an averaging [30, 34] or by keeping the maximum value [30] instead of using only the most recent value.

4.2. Comparing reconstructions with directly acquired original ultrasound images

All tests, except test 1, may be used to test for differences between original, directly acquired 2D ultrasound images and anyplanes through the reconstructed volumes. Most tests showed the original ultrasound images to perform better than the anyplanes, but test 2b showed the opposite.

An interesting result from test 2b was that the means acquired for resolution measurements on anyplanes from the reconstructions showed better resolutions than those measured on the original images (Table 3). The downsampling of the original ultrasound images seemed to lead to slightly better results, but this difference was not enough to explain why the anyplanes in the lateral direction from the reconstructions performed better

than original ultrasound images for this test. Also, in the axial direction for the 6 dB reduction, the small kernel obtained better results than both sets of original data, and when fewer groups were compared also the other algorithms performed better than both sets of original data. However, the explanation to the differences may be that the reconstruction algorithms processed the input data to make full use of the 8-bit range, while the original images were unprocessed. This processing increased the distance between the pixel values and the 6 dB and 20 dB measurements were not at the same level for the anyplanes and the original images. Another interesting observation was obtained when comparing results for 6 dB reductions in Table 3 with the theoretical results shown in Fig. 3. The differences between measured and theoretical resolutions were quite large: The measured axial resolution was about 4.7 times larger than the theoretical, the measured lateral resolution about 2.7 times larger and the measured elevation resolution about 2.1 times larger. For the axial direction, the assumption about a very short transmitted pulse for the theoretical calculation was clearly too optimistic, and the transmitted pulse was probably several wavelengths long. The thickness of the thread may also lead to a slightly increased measurement, even if the thread diameter was only 0.1 mm. When imaging the thread we made sure that a focus point was at the approximate depth of the thread so that the lateral resolution should be comparable to the theoretical values. However, the formula for the lateral resolution (3) did not take into account apodization, and this may explain some of the difference. The available data of the ultrasound probe may also provide additional information: The probe center frequency is 7.2 MHz, and even if the imaging frequency was set to 10 MHz, the real center frequency of the submitted pulse may be closer to 7.2 MHz. In addition the absorption in the imaged area of the ultrasound phantom was 0.7 dB/cmMHz. Using f_t = 7.2 MHz in (3) and a = 0.7 dB/cmMHz in (4) resulted in the measured lateral resolution being only 1.8 times larger than the theoretical resolution, and measured elevation resolution being only 1.4 times larger than the theoretical. The elevation focus is fixed at depth 16 mm, and compared to the wire depth of 27 mm the difference for the elevation direction was quite understandable. To explore the differences between the theory and practical results further it may be necessary to perform hydrophone measurements of the transmitted pulse, especially to determine the differences in axial resolution.

Test 2c showed that directly acquired ultrasound images performed better than the reconstruction algorithms for the purpose of identifying small structures in phantoms. Test 2d showed that the human observers prefered directly acquired ultrasound images to anyplanes through reconstructions, also for tissue data. Test 3 measuring all axes of a

cylinder showed that in most cases the distances measured on anyplanes was not different from directly acquired ultrasound images. Still, Table 5 and 6 showed that images related to the lateral and elevation reconstruction directions gave significant differences from the original ultrasound data for larger distances (lengths measurements) but not for smaller measurements (width measurements), except for the unprocessed data. Another interesting result was that all the length measurements in anyplanes in the lateral direction (scans across cylinder) were larger than the measurements in the original images while the length measurements in the elevation direction (scans along cylinder) were smaller. The reason for this difference may be inaccuracies in the probe calibration, as this comparison test is dependant of accurate orientation. The original images for the length measurements were obtained orthogonal to the input images in the scan along the cylinder, and a small difference in orientation may have resulted in a relatively large difference in length measurement.

4.3. Difference between data sources

Both processed video sources performed generally better than the unprocessed data. The digital video was the data source with the best results throughout all the tests. However, it could not be separated from the analog video in tests 2a, 2b, 2c and 3. On the other hand, it performed better than the analog video in the tissue comparison test 2d. The analog video showed good results in several tests and was often better than the unprocessed data, but not statistically significantly better than the digital video in any of the comparisons. However, in the volunteers' evaluation of the tissue data, the analog video performed poorer than both the digital and unprocessed video.

When observing the input video sources, it was obvious that the unprocessed data had more information with the higher resolution, while the processed video sources represented a resampling of the sampled data, which could lead to a loss of information. So far not much work is published comparing the quality of the unprocessed with processed data. Use of the unprocessed data could probably lead to better results in comparisons; however, our results indicate the opposite conclusion. The reason for this may be that the reconstruction algorithms do not process the data as thoroughly as the ultrasound scanner does. This result may be seen as a proof that the image processing done in the ultrasound scanner does improve the image quality as seen from the user perspective even if the resolution may be somewhat reduced. Another important aspect of this is that if unprocessed

data are used directly there may be a reduction of quality and the images may be harder to interpret even if the data contain more information. To prevent this, a processing similar to that of the ultrasound scanner could be performed. It should however be noted that all comparisons are based on data from a single scanner using one ultrasound probe, and the quality of the unprocessed and processed data may wary between different probes and scanners, and the results of our study can hence not be generalized.

4.4. Comparing input sources and reconstruction algorithms

Several studies try to compare the performance and quality of the reconstruction algorithms [24, 31, 32, 35, 36, 48, 49]. The most commonly used comparison method is the method of removing a percentage of the input data and then determining the algorithms ability to recreate this data. A Root Mean Squared (RMS) error value or an equivalent value is usually used to disclose the quality difference. A specific slice is selected, usually in the middle of the ultrasound volume, and a set of different percentages are selected for removal of data [35]. Coupé et al. [48] uses a variation over this and removes input slices (1, 2, 3, 4, 5 and 6) over the whole input data set and calculates a mean and standard deviation for the MSE (Mean Squared Error) values of the different slices. The advantage of this method is that it is an objective method that may be done automatically and is usable with most kinds of ultrasound data.

Drawbacks of this method are that it only compares one aspect of reconstruction quality and the results are dependant of the imaged tissue. In addition, this comparison method is not suitable to compare different ultrasound data sources as we have done in this paper. We have still used this existing method, but in addition we have devised several additional tests for the purpose of comparing both reconstruction algorithms and data sources for the reconstructions.

It is important to note that in our use of the test we performed the statistical comparisons over the full range of removed data (0, 25, 50, 75, 100, 300, 500 and 700 percent) without regard to the data having more samples in the range from 0% to 100%, leading to a higher weight given to this range. Also, a situation may arise where the RMS values of one reconstruction algorithm are better for one range of percentages but worse for another range when compared to another reconstruction algorithm. In this situation, the statistical tests of the whole range may be indecisive, while a test of a smaller range might give a result. The described situation happened for the combination of all data sources in the

scan along the forearm, and as may be seen in Table 1 this test could not differentiate between the data sources. We decided not to perform any additional tests of specific smaller ranges as we wanted to focus on the overall score.

Several of the tests we have used in this paper deal with the practical resolution of the ultrasound images and volumes, especially tests 2a, 2b, 2c and 3. However, test 2c was also highly dependent on accurate positions of the small structures or the ultrasound probe positions related to the structures. Some of the differences between the reconstruction algorithms and original 2D ultrasound images may be due to small errors in the probe calibration having a total mean error of 1.05 mm. The structures being only 1.5 mm in diameter and 2.4 mm long may easily be missed with this calibration accuracy since the comparisons were based on a position and orientation with the structures visible in the original images. A small error in either position or orientation may lead to several missing structures. One of the important features of ultrasound is how good the image quality appear to a human and how easy it is to interpret the image. Test 2d try to test these aspects, but the test is very unspecific. To detect more important differences a set of specific tests could be created asking volunteers (preferably clinical ultrasound users) to evaluate sets of images from different clinical cases.

We have tried to create tests that may represent different uses of the ultrasound volumes, but the range of tests is not exhaustive. Our comparison tests also have a varying degree of manual interaction and may not be practical in all situations. Several other tests could be devised in addition to the tests we have performed in this paper. One idea is to perform an automatic segmentation of a known structure and compare volume sizes [33]. However, our initial experiments showed that the segmentation algorithms that we had access to created quite different segmented volumes from the same reconstructed ultrasound volume with only small changes in parameters, and it was difficult to get comparable segmentations from volumes originating from different input sources. Another possible test is the comparison of measurements of relatively large distances. An automated method like the one described in Lindseth et al. [51] might be possible, and this test may detect more and larger differences than the test we have performed in this paper, which only compares measurements of small distances.

The general problem with comparison tests for reconstructed ultrasound volumes is that there are several error sources that may affect the results, and these error sources may be larger than the factors we want to compare. Our method of comparing several aspects of the reconstructed volumes is a way to limit the error sources when looking at all tests combined.

Still the error sources should be minimized before the comparisons. We have also applied statistical comparisons of all the data collected in the tests since this gives a better way of knowing if one value really is better than another or if it only is natural variation.

4.5. Relevance and further work

3D probes may be used for acquisition of 3D data instead of 2D probes. 3D probes will allow both easy acquisition of near real-time 3D data and the possibilities of 3D data with time as a fourth dimension. However, in IGS, tracked 2D probes have a few advantages over 3D probes: The data stream from the ultrasound probe is limited, so still it is possible to get a higher resolution volume from a 2D probe. In IGS, positioned intraoperative data is easier to correlate to preoperative data, so a tracking sensor is usually needed. 3D probes are shown to interfere more with electromagnetic tracking systems that 2D probes [52]. The volume covered by a 3D probe is much smaller than is practical in most IGS applications, and to overcome this limitation, an application must be created that combines data from the 3D probe. The data from the 3D probe are not easily available to third party ISG applications, needed to integrate the data with preoperative data, or for combining the data into larger volumes.

Most new ultrasound scanners support the DICOM standard so that it should be possible to get access to digital data for 3D reconstructions. Even if only a stack of 2D images is stored, a 3D reconstruction is still possible with this data if the 2D images are tagged with accurate global time-tags. The positions may then be recorded at the same time with their own time-tags, and a time calibration [44, 53] may be performed to match the positions with the images. Most applications for 3D ultrasound reconstructions require a near real-time implementation, and currently the video grabber approach is the fastest solution in most cases for freehand 3D reconstructions, as DICOM don’t support real-time images yet. However, DICOM working group 24 focuses on developing DICOM standards and services for Image Guided Surgery [54]. This work may result in real-time protocols that open up for easily accessible real-time digital ultrasound images suitable for 3D reconstructions. Another option is the method we have used in this paper by using an ultrasound scanner that allows real-time access to digital data.

All comparisons of data in this paper are performed with data from a single scanner using one ultrasound probe. To get more general results it would be interesting to collect data from more scanners and probes. Only a few ultrasound scanners supply unprocessed

data (e.g. RF) to third parties without special collaboration agreements. However, a study using data from various scanners and probes could make it easier to arrive to general conclusions regarding choice of input data. Examples of scanner producers with scanners that may supply unprocessed data are: Winprobe (North Palm Beach, FL, US), VeraSonics (Redmond, WA, US), and Terason (Burlington, MA, US), in addition to the Sonix RP scanner from Ultrasonix used in our study.

5. Conclusion

The present study shows that the choice of data source may be more important than the choice of reconstruction algorithm in order to achieve high quality image volumes from tracked freehand 2D ultrasound data. Furthermore, scan converted digital and analog data gave better results than unprocessed ultrasound data in our comparison tests performed with one scanner. Overall, digital video performs slightly better than analog video, but in most cases the two video sources were difficult to separate by the comparison methods, indicating that the quality loss of using flexible video-grabbing solutions over scanners with a digital interface may not be significant. It must be taken into account that the conclusions on data source quality were based on comparisons performed on data from a single scanner using one ultrasound probe, and that quality and processing may differ between probes and scanners. More work including comparison tests on several scanners and probes should therefore be performed in order to obtain more general conclusions. By giving all the comparisons the same weight, no reconstruction algorithm of those tested performs significantly better than the others in terms of image quality indicating that the fastest reconstruction method should be chosen, e.g. PNN. However, in general, the reconstruction algorithm must be selected according to the application and the intended usage of the 3D volume.

Acknowledgements

This work was supported by the Research Council of Norway, through the FIFOS Programme Project 152831/530 and Medical Imaging Laboratory (MI Lab); the Ministry of Health and Social Affairs of Norway, through the National Centre of 3D Ultrasound in Surgery; and by SINTEF Technology and Society. We want to thank Thomas Kuiran Chen and Purang Abolmaesumi at Queen's University, Kingston, Canada for supplying us with both a phantom and C++ code for ultrasound probe calibration. We also want to thank

Reidar Brekken (SINTEF, NTNU), Rune Hansen (SINTEF, NTNU) and Hans Torp (NTNU) for discussions regarding ultrasound theory, Sjur Gjerald (NTNU) for aid with laboratory work, Thor Andreas Tangen (NTNU) and Jochen Deibele (NTNU) for help with the Ultrasonix scanner, and we like to thank the rest of the people at SINTEF Technology and Society, Medical Technology for volunteering for some of the comparison tests. The authors are thankful to the reviewers, who provided comprehensive and constructive suggestions and indicated that in addition to Ultrasonix there are two other systems on the market that allow access to the RF data: Winprobe (and possibly Verasonics).

References

[1] G. Unsgaard, O. M. Rygh, T. Selbekk, T. B. Muller, F. Kolstad, F. Lindseth and T. A. Hernes, Intra-operative 3D ultrasound in neurosurgery, Acta Neurochir. (Wien). 148 (2006) 235-253.

[2] H. A. McCann, J. C. Sharp, T. M. Kinter, C. N. McEwan, C. Barillot and J. F. Greenleaf, Multidimensional ultrasonic imaging for cardiology, in: the IEEE, IEEE, 1988, pp. 1063-1073.

[3] F. Hottier and A. C. Billon, 3D echography: status and perspective, in: K. H. Hohne, H. Fuchs and S. M. Pizer (Eds.) 3D Imaging in Medicine, Springer-Verlag Berlin Heidelberg, 1990, pp. 21-41.

[4] S. K. Nadkarni, D. Boughner and A. Fenster, Image-based cardiac gating for three-dimensional intravascular ultrasound imaging, Ultrasound Med. Biol., 31 (2005) 53-63.

[5] R. W. Prager, A. Gee, G. Treece and L. Berman, Freehand 3D ultrasound without voxels: volume measurement and visualisation using the Stradx system, Ultrasonics, 40 (2002) 109-115.

[6] S. Meairs, J. Beyer and M. Hennerici, Reconstruction and visualization of irregularly sampled three- and four-dimensional ultrasound data for cerebrovascular applications, Ultrasound Med. Biol., 26 (2000) 263-272.

[7] J. N. Welch, J. A. Johnson, M. R. Bax, R. Badr and R. Shahidi, A real-time freehand 3D ultrasound system for image-guided surgery, in: Ultrasonics Symposium, IEEE, San Juan, Puerto Rico, 2000.

[8] S. Sherebrin, A. Fenster, R. N. Rankin and D. Spence, Freehand three-dimensional ultrasound: implementation and applications, in: Medical Imaging 1996: Physics of Medical Imaging, SPIE, Newport Beach, CA, USA, 1996, pp. 296-303.

[9] S. Ogawa, K. Itoh, K. Omoto, X. Cheng, A. Ohya and I. Akiyama, Three dimensional ultrasonic imaging for diagnosis of breast tumor, in: Ultrasonics Symposium, IEEE, Sendai, Japan, 1998, pp. 1677-1680.

[10] V. R. Amin, B. Wang, M. Sonka and R. M. Lauer, Three-dimensional ultrasound imaging of vessel wall for evaluating atherosclerosis risk and disease, in: Medical Imaging 2002: Ultrasonic Imaging and Signal Processing, SPIE, San Diego, CA, USA, 2002, pp. 255-263.

[11] R. N. Rohling, A. H. Gee and L. Berman, Automatic registration of 3-D ultrasound images, Ultrasound Med. Biol., 24 (1998) 841-854.

[12] O. H. Gilja, T. Hausken, S. Olafsson, K. Matre and S. Odegaard, In vitro evaluation of three-dimensional ultrasonography based on magnetic scanhead tracking, Ultrasound Med. Biol., 24 (1998) 1161-1167.

[13] P. R. Detmer, G. Bashein, T. Hodges, K. W. Beach, E. P. Filer, D. H. Burns and D. E. Strandness, Jr., 3D ultrasonic image feature localization based on magnetic scanhead tracking: in vitro calibration and validation, Ultrasound Med. Biol., 20 (1994) 923-936.

[14] A. Moskalik, P. L. Carson, C. R. Meyer, J. B. Fowlkes, J. M. Rubin and M. A. Roubidoux, Registration of three-dimensional compound ultrasound scans of the breast for refraction and motion correction, Ultrasound Med. Biol., 21 (1995) 769-778.

[15] C. Laporte and T. Arbel, Combinatorial and Probabilistic Fusion of Noisy Correlation Measurements for Untracked Freehand 3-D Ultrasound IEEE Trans. Med. Imaging, 27 (2008) 984-994.

[16] O. V. Solberg, G.-A. Tangen, F. Lindseth, T. Sandnes, A. A. Enquobahrie, L. Ibanez, P. Cheng, D. Gobbi and K. Cleary, Integration of a real-time video grabber component with the open source image-guided surgery toolkit IGSTK, in: Medical Imaging 2008: PACS and Imaging Informatics, SPIE, San Diego, CA, USA, 2008, pp. 69190Z-69199.

[17] R. Ohbuchi, D. Chen and H. Fuchs, Incremental volume reconstruction and rendering for 3-D ultrasound imaging, in: Visualization in Biomedical Computing '92, SPIE, Chapel Hill, NC, USA, 1992, pp. 312-323.

[18] T. K. Chen, A. D. Thurston, R. E. Ellis and P. Abolmaesumi, A real-time freehand ultrasound calibration system with automatic accuracy feedback and control, Ultrasound Med. Biol., 35 (2009) 79-93.

[19] S. Berg, H. Torp, D. Martens, E. Steen, S. Samstad, I. Hoivik and B. Olstad, Dynamic three-dimensional freehand echocardiography using raw digital ultrasound data, Ultrasound Med. Biol., 25 (1999) 745-753.

[20] D. Martens and O. H. Gilja, The EchoPAC-3D software for image analysis, in: S. Ødegård, O. H. Gilja and H. Gregersen (Eds.) Basic and New Aspects of Gastrointensial Ultrasonography. Advanced series in Biomechanics, World Scientific Publishing, 2005, pp. 305-329.

[21] N. Thune, O. H. Gilja, T. Hausken and K. Matre, A practical method for estimating enclosed volumes using 3D ultrasound, Eur. J. Ultrasound, 3 (1996) 83-92.

[22] A. Gronningsaeter, A. Kleven, S. Ommedal, T. E. Aarseth, T. Lie, F. Lindseth, T. Lango and G. Unsgard, SonoWand, an ultrasound-based neuronavigation system, Neurosurgery, 47 (2000) 1373-1379; discussion 1379-1380.

[23] F. Lindseth, J. Bang and L. Thomas, A robust and automatic method for evaluating accuracy in 3-D ultrasound-based navigation, Ultrasound Med. Biol., 29 (2003) 1439-1452.

[24] O. V. Solberg, F. Lindseth, H. Torp, R. E. Blake and T. A. Nagelhus Hernes, Freehand 3D Ultrasound Reconstruction Algorithms--A Review, Ultrasound Med. Biol., 33 (2007) 991-1009.

[25] J. W. Trobaugh, D. J. Trobaugh and W. D. Richard, Three-dimensional imaging with stereotactic ultrasonography, Comput. Med. Imaging Graph., 18 (1994) 315-323.

[26] W. Wein, F. Pache, B. Röper and N. Navab, Backward-Warping Ultrasound Reconstruction for Improving Diagnostic Value and Registration, in: Medical Image Computing and Computer-Assisted Intervention – MICCAI 2006, 2006, pp. 750-757.

[27] A. Karamalis, W. Wein, O. Kutter and N. Navab, Fast hybrid freehand ultrasound volume reconstruction, in: Medical Imaging 2009: Visualization, Image-Guided Procedures, and Modeling, SPIE, Lake Buena Vista, FL, USA, 2009, pp. 726114-726118.

[28] G. M. Treece, R. W. Prager, A. H. Gee and L. Berman, Correction of probe pressure artifacts in freehand 3D ultrasound, Med. Image Anal., 6 (2002) 199-214.

[29] Y. Zhang, R. Rohling and D. K. Pai, Direct surface extraction from 3D freehand ultrasound images, IEEE Computer Society, Boston, Massachusetts, 2002.

[30] T. R. Nelson and D. H. Pretorius, Interactive acquisition, analysis, and visualization of sonographic volume data, Int. J. Imag. Systems Technol., 8 (1997) 26-37.

[31] R. San José-Estépar, M. Martín-Fernández, P. P. Caballero-Martínez, C. Alberola-López and J. Ruiz-Alzola, A theoretical framework to three-dimensional ultrasound reconstruction from irregularly sampled data, Ultrasound Med. Biol., 29 (2003) 255-269.

[32] R. San José-Estépar, M. Martín-Fernández, C. Alberola-López, J. Ellsmere, R. Kikinis and C.-F. Westin, Freehand ultrasound reconstruction based on ROI prior modeling and normalized convolution, in: Medical Image Computing and Computer-Assisted Intervention (MICCAI), Springer, Montréal, Canada, 2003, pp. 382-390.

[33] C. D. Barry, C. P. Allott, N. W. John, P. M. Mellor, P. A. Arundel, D. S. Thomson and J. C. Waterton, Three-dimensional freehand ultrasound: image reconstruction and volume analysis, Ultrasound Med. Biol., 23 (1997) 1209-1224.

[34] D. G. Gobbi and T. M. Peters, Interactive intra-operative 3D ultrasound reconstruction and visualization, in: Medical Image Computing and Computer-Assisted Intervention (MICCAI), Springer, Tokyo, Japan, 2002, pp. 156-163.

[35] R. Rohling, A. Gee and L. Berman, A comparison of freehand three-dimensional ultrasound reconstruction techniques, Med. Image Anal., 3 (1999) 339-359.

[36] J. M. Sanches and J. S. Marques, A multiscale algorithm for three-dimensional free-hand ultrasound, Ultrasound Med. Biol., 28 (2002) 1029-1040.

[37] S. I. Nikolov, J. P. G. Gonzaléz and J. A. Jensen, Real time 3D visualization of ultrasonic data using a standard PC, Ultrasonics, 41 (2003) 421-426.

[38] S. Eulenstein, T. Lange, M. Hünerbein, P. M. Schlag and H. Lamecker, Ultrasound-based navigation system incorporating preoperative planning for liver surgery, International Congress Series, 1268 (2004) 758-763.

[39] S.-W. Huang, K. Kim, Kim, R. S. Witte, R. Olafsson and M. O'Donnell, Inducing and Imaging Thermal Strain Using a Single Ultrasound Linear Array, IEEE Transactions on Ultrasonics, Ferroelectrics and Frequency Control, 54 (2007) 1718-1720.

[40] P. Cinquin, E. Bainville, C. Barbe, E. Bittar, V. Bouchard, L. Bricault, G. Champleboux, M. Chenin, L. Chevalier, Y. Delnondedieu, L. Desbat, V. Dessenne, A. Hamadeh, D. Henry, N. Laieb, S. Lavallee, J. M. Lefebvre, F. Leitner, Y. Menguy, F. Padieu, O. Peria, A. Poyet, M. Promayon, S. Rouault, P. Sautot, J. Troccaz and P. Vassal, Computer assisted medical interventions, Engineering in Medicine and Biology Magazine, IEEE, 14 (1995) 254-263.

[41] K. Cleary, L. Ibáñez, D. Gobbi, P. Cheng, K. Gary, S. Aylward, J. Jomier, A. Enquobahrie, H. Zhang, H.-s. Kim and M. B. Blake, IGSTK: The Book, 2.0 ed., Signature Book Printing, Gaithersburg, Maryland, USA, 2007.

[42] A. Enquobahrie, P. Cheng, K. Gary, L. Ibáñez, D. Gobbi, F. Lindseth, Z. Yavi, S. Aylward, J. Jomier and K. Cleary, The Image-Guided Surgery Toolkit IGSTK: An Open Source C++ Software Toolkit, J. Digit. Imaging, 20 (2007) 21-33.

[43] K. Gary, L. Ibáñez, S. Aylward, D. Gobbi, M. B. Blake and K. Cleary, IGSTK: An open source software platform for image-guided surgery, IEEE Computer, 39 (2006) 46-53.

[44] G. M. Treece, A. H. Gee, R. W. Prager, C. J. C. Cash and L. H. Berman, High-definition freehand 3-D ultrasound, Ultrasound Med. Biol., 29 (2003) 529-546.

[45] D. G. Gobbi, B. K. H. Lee and T. M. Peters, Correlation of preoperative MRI and intraoperative 3D ultrasound to measure brain tissue shift, in: Medical Imaging 2001: Visualization, Display, and Image-Guided Procedures, SPIE, San Diego, CA, USA, 2001, pp. 264-271.

[46] B. A. J. Angelsen, Ultrasound Imaging, Emantec AS, Trondheim, Norway, 2000.

[47] K. A. Wear, The effects of frequency-dependent attenuation and dispersion onsound speed measurements: applications in human trabecular bone, IEEE Transactions on Ultrasonics, Ferroelectrics and Frequency Control, 47 (2000) 265-273.

[48] P. Coupé, P. Hellier, N. Azzabou and C. Barillot, 3D freehand ultrasound reconstruction based on probe trajectory, in: Medical Image Computing and Computer-Assisted Intervention (MICCAI), Springer, Palm Springs, CA, USA, 2005, pp. 597-604.

[49] J. M. Sanches and J. S. Marques, A Rayleigh reconstruction/interpolation algorithm for 3D ultrasound, Pattern Recognition Letters, 21 (2000) 917-926.

[50] J. M. Thijssen, G. Weijers and C. L. de Korte, Objective Performance Testing and Quality Assurance of Medical Ultrasound Equipment, Ultrasound Med. Biol., 33 (2007) 460-471.

[51] F. Lindseth, T. Lango, J. Bang and T. A. Nagelhus Hernes, Accuracy evaluation of a 3D ultrasound-based neuronavigation system, Comput. Aided Surg., 7 (2002) 197-222.

[52] M. Hastenteufel, M. Vetter, H. P. Meinzer and I. Wolf, Effect of 3d ultrasound probes on the accuracy of electromagnetic tracking systems, Ultrasound Med Biol, 32 (2006) 1359-1368.

[53] F. Rousseau, A Novel Temporal Calibration Method for 3D Ultrasound, IEEE Trans. Med. Imaging, 25 (2006) 1108.

[54] H. U. Lemke, Summary of the white paper of DICOM WG24 'DICOM in Surgery', in: Medical Imaging 2007: PACS and Imaging Informatics, SPIE, San Diego, CA, USA, 2007, pp. 651603-651613.

Paper III

Minimally Invasive Therapy. 2008; 17:1; 17–33

informa
healthcare

ORIGINAL ARTICLE

Navigation in laparoscopy – prototype research platform for improved image-guided surgery

T. LANGØ[1,2], G. A. TANGEN[1,2], R. MÅRVIK[2,3,4,5], B. YSTGAARD[2,6], Y. YAVUZ[4], J. H. KASPERSEN[1,2], O. V. SOLBERG[1,2,5] & T. A. N. HERNES[1,2,5]

[1]*SINTEF Health Research, Dept. Medical Technology, Trondheim, Norway,* [2]*National Center for 3D Ultrasound in Surgery, Trondheim, Norway,* [3]*The Operating Room of the Future, Trondheim, Norway,* [4]*National Center for Advanced Laparoscopic Surgery, St. Olavs Hospital, Trondheim, Norway,* [5]*Norwegian University of Science and Technology (NTNU), Trondheim, Norway, and* [6]*Department of Surgery, St. Olavs Hospital, Trondheim Norway*

Abstract

The manipulation of the surgical field in laparoscopic surgery, through small incisions with rigid instruments, reduces free sight, dexterity, and tactile feedback. To help overcome some of these drawbacks, we present a prototype research and development platform, *CustusX*, for navigation in minimally invasive therapy. The system can also be used for planning and follow-up studies. With this platform we can import and display a range of medical images, also real-time data such as ultrasound and X-ray, during surgery. Tracked surgical tools, such as pointers, video laparoscopes, graspers, and various probes, allow surgeons to interactively control the display of medical images during the procedure. This paper introduces navigation technologies and methods for laparoscopic therapy, and presents our software and hardware research platform. Furthermore, we illustrate the use of the system with examples from two pilots performed during laparoscopic therapy. We also present new developments that are currently being integrated into the system for future use in the operating room. Our initial results from pilot studies using this technology with preoperative images and guidance in the retroperitoneum during laparoscopy are promising. Finally, we shortly describe an ongoing multicenter study using this surgical navigation system platform.

Key words: *Surgical navigation, image-guided surgery, laparoscopy, minimally invasive surgery, ultrasound*

Introduction

Laparoscopic surgery is generally performed through small incisions using long, thin, and rigid instruments. The manipulation of the surgical field with this technique reduces free sight, dexterity, and tactile feedback, compared to open surgery. Images from modalities such as computed tomography (CT), magnetic resonance imaging (MRI), and ultrasound can, in combination with navigation technology, be used to plan a procedure, to guide laparoscopic instruments down to lesions, e.g. liver tumors, in a safe manner through narrow channels, and to help the surgeons monitor the surgical resection as well as to control the result, i.e. quality assessment.

Image-guided surgery

Image-guided surgery (IGS) involves several important steps, of which some are more critical than others for obtaining optimal and safe therapy:

- Preoperative image acquisition, data processing, and preoperative image visualization for optimal diagnostics as well as satisfying preoperative therapy decision-making and planning.

Correspondence: T. Langø, SINTEF Health Research, Dept. of Medical Technology, 7465 Trondheim, Norway. Fax: +47 93070800. E-mail: thomas.lango@sintef.no

ISSN 1364-5706 print/ISSN 1365-2931 online © 2008 Taylor & Francis
DOI: 10.1080/13645700701797879

- Accurate registration of preoperative image data and visualization in the operating room (OR) for accurate and optimal planning just prior to surgery.
- Intraoperative imaging for updating images for guidance as well as intraoperative visualization and navigation for safe, efficient and accurate IGS in the OR.
- Postoperative imaging and visualization for adequate evaluation of patient treatment.

The last step is sometimes performed in the OR for quality assessment.

The majority of available systems for IGS have thus far been designed for neurosurgery (1–3), but systems and prototype solutions for other clinical applications and therapies are emerging, such as for ear, nose, and throat (ENT) procedures (4–6), breast (7–9), prostate (10–12), orthopedics (13–15), bronchoscopy (16), hepatic and liver surgery (17–19), and endovascular therapy (20). In the most advanced systems commercially available today, the surgeon is provided with two-dimensional (2D) and three-dimensional (3D) visual "road maps" of a patient's anatomy with representations of the tracked surgical instrument overlaid on the images. Some groups limit their systems to the planning phase of abdominal surgery. Systems have been designed for planning hepatic surgery (21–23), since the operability of liver tumors depends on their relation to intrahepatic vascular structures. Soler and coworkers (23) confirmed their findings with radiologists, and concluded that their solution will improve planning of hepatic surgery by more precisely delineating liver pathology and its relation to normal structures. Lamade and coworkers showed how a 3D presentation of individual patient liver anatomy facilitated perception of pathology and how their system allowed calculation of complete resection protocols, which could be quantified and modified interactively (21).

Tracking technologies for image-guided surgery

There are four common technologies to track medical instruments: Mechanical, acoustical, electromagnetic, and optical. The role of a tracking system in this context is to determine the position and orientation of a sensor attached to the instrument. A calibration procedure determines the position and orientation of the tip of the instrument in relation to the sensor attached to the instrument. Mechanical localizers are articulated arms whose tip position can be determined by the angles formed by each joint. Acoustical position trackers are composed of speakers/emitters, which produce ultrasonic waves that are detected by microphones/receivers. The idea behind the electromagnetic system is to attach receiver coils to the instrument to be tracked. The system measures the induced electrical currents in the receiver coils when they are moved within a magnetic field generated by either an alternating current (AC) or direct current (DC) transmitter (24). The position can then be calculated based on the strength of the current induced in the coils. The AC and DC devices are both sensitive to some types of metallic objects located in the vicinity of the transmitter or receiver and to magnetic fields generated by power sources and devices such as cathode-ray tube monitors. Therefore, both types of electromagnetic systems are challenging to use in an environment like an OR, where various metallic objects are moved around in the field (25). The general idea with optical tracking is to use multiple cameras to track markers distributed on a rigid structure, whose geometry is specified beforehand. At least three markers in an asymmetric spatial configuration are necessary to determine the position and orientation of the rigid body in space. Adding additional markers allows a better camera visibility of the tracked object and improves the measurement accuracy. In addition, both the visibility of the tracked object and the accuracy of its 3D position and orientation are dependent on the position of the markers (26). The markers can be infrared light emitting diodes (active markers), or infrared light reflectors (passive markers) in the shape of spheres or discs. Both passive (27) and active (28) markers have been used for tracking of medical instruments in IGS. To track multiple objects simultaneously the markers attached to each object must have a unique spatial configuration. For more details on any of the tracking technologies, we refer to Meyer and Biocca (29) or Cinquin (30).

Registration of preoperative patient data

Image-to-patient registration is a required step in any intraoperative navigation system based on preoperative images. Most registration methods can be characterized as point-based, surface-based or voxel/volume-based (31). Point-based methods optimize the alignment of corresponding points in two images or in one image and in physical space, and are the underlying methods for patient registration based on skin fiducials or anatomical landmarks. Surface-based methods try to match corresponding surfaces. Herline and coworkers (32) developed a surface registration method based on CT images for use in liver surgery and tested it on a liver phantom with embedded phantom tumors. They achieved an accuracy of 2.9 mm RMS (root

mean square) value for the entire surface of the phantom liver. This indicates the possibilities of registration in laparoscopic IGS, even to individual internal organs during surgery. For image-to-image registration the two surfaces are extracted from the image data, and for image-to-patient registration the physical space surface is either generated by sweeping over the skin with a tracked pointer or using a 3D laser camera (33). Voxel-based methods are used for image-to-image registration and for matching two volumes by optimizing their similarity. Correlation or mutual information (34) is often used to calculate the similarity. It should be mentioned that if an intraoperative imaging modality is available, the preoperative images could be registered to the patient or physical space by using a volume-based image-to-image registration technique between the pre- and intraoperative data.

Intraoperative imaging and navigation in laparoscopy

In conventional laparoscopic surgery, the visible surface area is limited to the range of the image captured by the laparoscope. This surface-view technology is limited because the surgeon must mentally correlate the patient's anatomical structures through medical images with the operative field to determine the location of vital anatomical structures that lie beyond the view of the monocular laparoscope.

The major challenges to achieve satisfying IGS for mobile organs in the abdomen, in particular liver procedures, are accurate registration of preoperative images to the patient and how to update these images due to changes that occur during surgery. There can be no presumption of even piece-wise rigidity, except for procedures in the retroperitoneum as we have previously shown (35). In liver surgery, intraoperative ultrasound, without navigation, has become the standard for solving this (36–39). The problem with traditional laparoscopic ultrasound has been the orientation or lack of spatial cues to ease the interpretation and understanding of the ultrasound images. Ellsmere and coworkers have developed a system to provide spatial cues to the surgeons, improving their ability to interpret the laparoscopic ultrasound images (37). Their key method is to show the ultrasound image relative to a 3D model of the aorta or with an orientation display with laparoscopic video images. This improves the physician's ability to correctly identify key structures in the ultrasound images. Sjølie and coworkers demonstrated ultrasound guidance of a radiofrequency ablation probe into model liver tumors to show the benefits of 3D ultrasound compared to two 2D techniques (40). Several groups have also demonstrated the usefulness of ultrasound image-guidance during local treatment of liver tumors (41–44). In addition, Harms and coworkers describe a setup for 3D ultrasound-based navigation in laparoscopy (38). They compared 3D laparoscopic ultrasound with 3D transcutaneous ultrasound and 3D CT scan, using CT as the gold standard. They reported that laparoscopic ultrasound in combination with navigation and tracking technology has, in addition to being technically feasible, the potential to become a valuable tool for planning and improving interventions guided by laparoscopic ultrasound. Another group used laparoscopic ultrasound to match targets on a phantom liver to the corresponding targets in a CT scan of the phantom for IGS purposes (45). In an attempt to track liver motions during insufflation, one group of researchers developed an interactive IGS system for liver surgery with tracking of a laparoscope and an ultrasound probe (17). They found that the instruments could be accurately tracked to within 1.4 to 2.1 mm error and that liver motion was approximately 10 mm in patients. They concluded that interactive IGS was feasible for both open and laparoscopic hepatic procedures and could improve operative localization in future developments (43).

In this paper we present a prototype research and development platform for navigation in laparoscopic surgery that overcomes many of the limitations of conventional laparoscopy by providing the surgeon with a view beyond the surface of organs. The system is presented in detail and we illustrate its use with examples from two clinical pilots and laboratory tests. Surgeons and radiologists can use the system during planning and follow-up of surgical procedures. The system is capable of importing and displaying various medical images, also real-time data such as ultrasound during surgery. Tracked surgical tools, such as pointers, video laparoscopes, graspers, and various probes, allow the surgeons to interactively control the display of medical images during the procedure.

Material and methods: Laparoscopic navigation system

Equipment

The prototype research and development navigation platform for laparoscopic surgery *CustusX* (Figure 1A, SINTEF, Trondheim, Norway), comprises optical position tracker cameras (Figure 1A, Polaris®, NDI, Waterloo, Ontario, Canada), an electromagnetic position tracking transmitter (Figure 1B–C, Aurora®, NDI, Waterloo, Ontario,

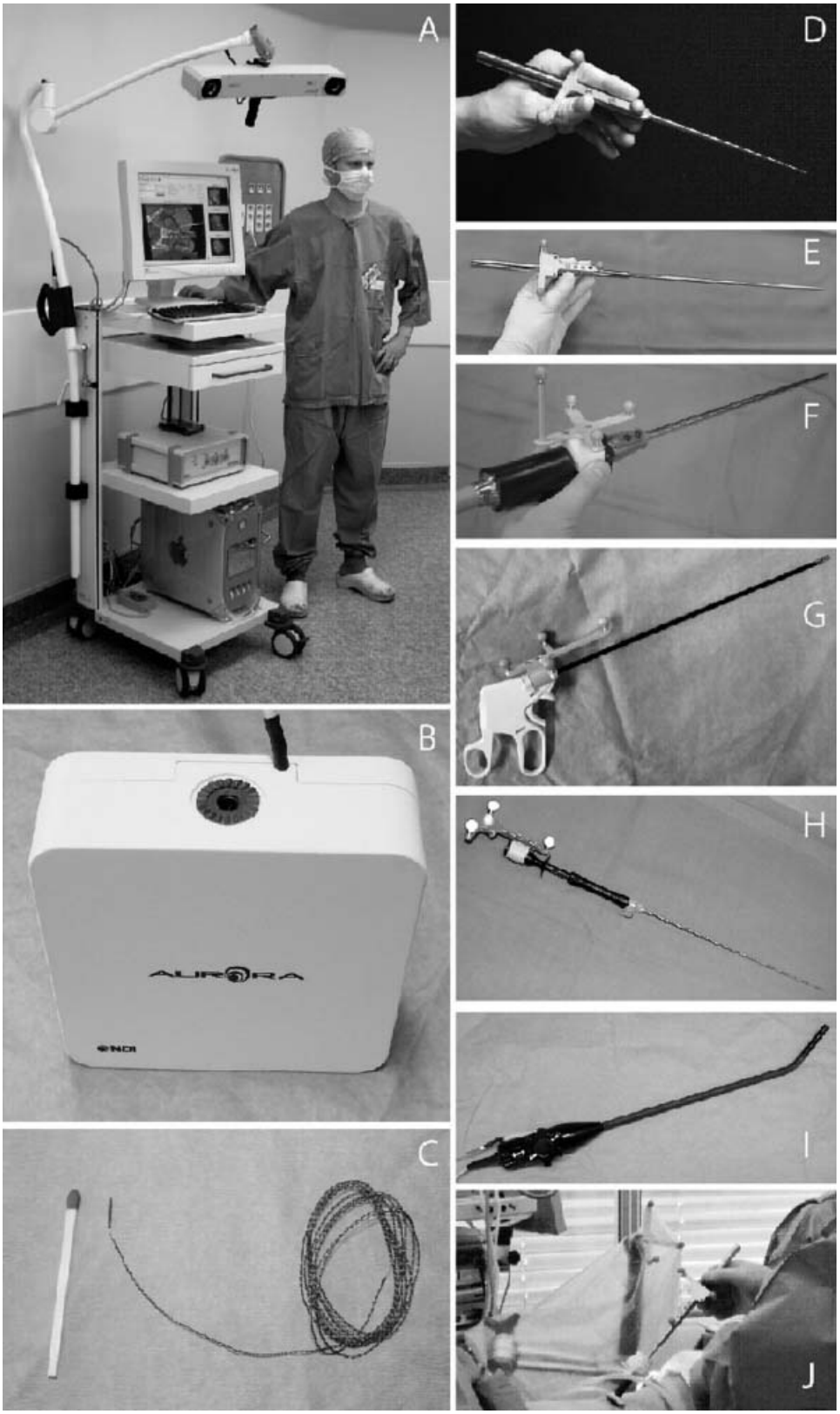

Figure 1. Our own prototype surgical navigation system can be used with optical (A, shown with Polaris, NDI, Canada) or electromagnetic (B, shown with Aurora, NDI, Canada) tracking (5 DOF sensor shown in C). Various surgical tools can be tracked with these position and orientation tracking systems; a preoperative planning pointer (D, also used for patient registration), a dedicated intraoperative laparoscopic pointer (E), video laparoscope (F), graspers for navigation during resection (G), radio frequency ablation probes (H), flexible ultrasound probe with electromagnetic tracking sensors on the tip (I). The patient reference frame can be seen in image J together with the laparoscopic pointer in use.

Canada), a desktop computer (Macintosh PowerPC, Apple, Cupertino, CA, USA), navigation pointers (Figure 1D–E), snap-on tracking devices for various laparoscopic instruments (Figure 1F–H), laparoscopic ultrasound probe with integrated tracking (Figure 1I), a patient reference tracking frame (Figure 1J), and our own developed software for processing of medical data, visualization, and navigation.

Tracking of rigid and flexible instruments

We have made snap-on tracking devices for such tools such as video laparoscopes (Figure 1F), graspers (Figure 1G), and radio frequency ablation probes (Figure 1H). The optical position tracking devices attached to the surgical tools comprise three to four reflecting spheres. For the devices with four spheres, one can be elevated from the plane of the other three for optimal tracking conditions at oblique angles between the tracking cameras and the tracking frame. When using ultrasound in a surgical navigation system, a position sensor must be attached to the ultrasound probe and a calibration procedure must be performed. Probe calibration is the procedure of determining the mathematical transformation matrix, describing the position and orientation of the real-time 2D ultrasound image relative to the position sensor attached to the probe. We refer to Mercier et al. (46) for an in-depth discussion of the various methods to perform probe calibration. We have incorporated an electromagnetic sensor (Figure 1C) into the laparoscopic ultrasound probe shown in Figure 1I (6 MHz prototype Tetrad laparoscopic ultrasound probe, System FiVe scanner, GE Vingmed Ultrasound, Norway). To obtain tracking of all six degrees of freedom (DOF), we used two five-DOF sensors at approximately 90° angle to each other at each side of the tip of the probe. Having the electromagnetic sensors attached to the tip of the ultrasound probe makes it possible to obtain image positions even when the probe is flexed at the tip. Our probe is able to flex stepwise as much as 90° in two directions.

Software modules and integration

The software system modules integrated into the navigation system are shown in figure 2. Our system

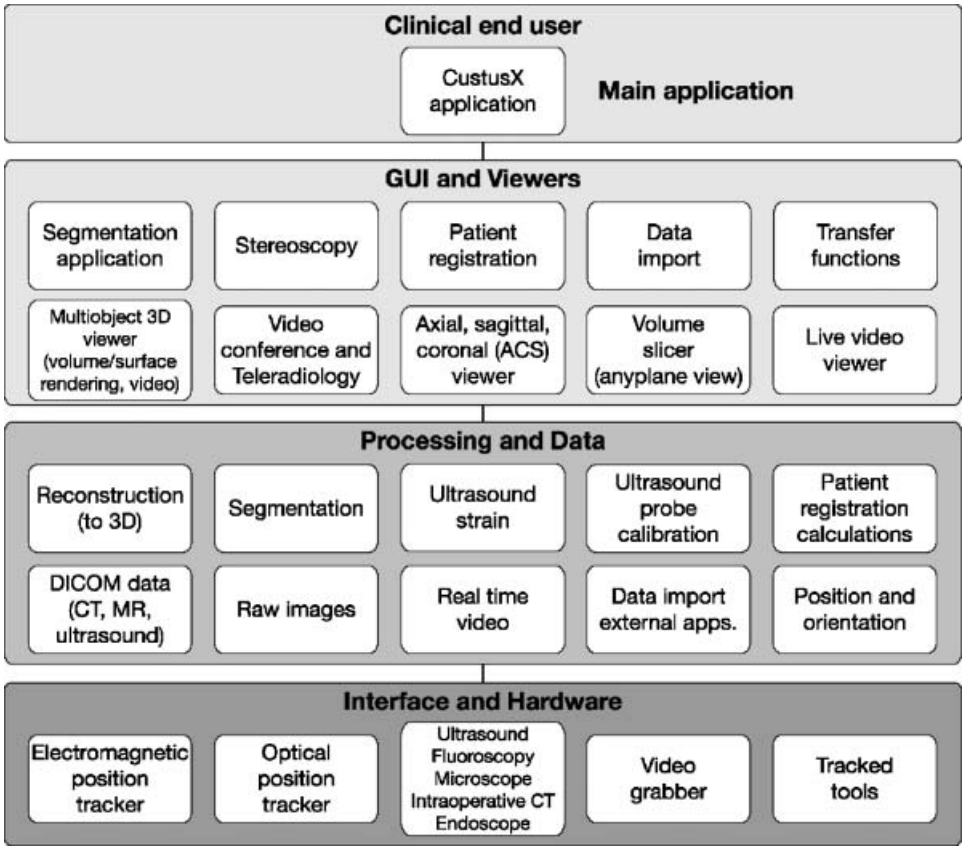

Figure 2. Surgical navigation platform software modules. Hardware interfaces ensure the access to various images and other data, processing algorithms prepare the data, while the graphical user interface presents the data to the end user of the system, the laparoscopic surgeon in this case.

is based on the open source libraries VTK (Visualization ToolKit) (47) and ITK (Insight Segmentation and Registration Toolkit) (48). Medical data are captured through the hardware interface modules or read in by Digital Imaging and Communication in Medicine (DICOM) or raw data import modules. The system can capture data through video grabbing or by dedicated connections through digital interface protocols, e.g. digital ultrasound images or radio frequency echo signals directly from internal scanner protocols. DICOM images are imported and reconstructed either directly in our own software or the system can use other software to perform tasks on the images that are not built into our navigation system software. We have developed a plug-in for OsiriX (49) for export of DICOM images to our system after processing in OsiriX. OsiriX is a multidimensional DICOM viewer designed for display and interpretation of large sets of multidimensional and multimodal images such as PET-CT and MRI/CT. Position and orientation measurements from tracking devices attached to tools are also read directly through a generic tracking interface to most tracking technologies. The imported images are reconstructed into 3D volumes or passed to the 2D video viewer directly. 3D data can be filtered or segmented prior to visualization. Segmentations are performed using our semi-automatic segmentation method based on a starting point within the structure/organ. The surface of the structure is determined with a fast-marching level-set algorithm (48). For an effective and proper extraction of a surface of an organ, input parameters of the algorithm must be adjusted due to variations in the characteristics of the imaging modalities, such as CT and MR with and without contrast. The organ to be segmented also influences the settings for these parameters. In certain cases we use third party software such as InsightSNAP (50), e.g. for manual segmentations of smaller structures that might be hard to extract automatically.

Visualization of medical data

The research navigation system platform is capable of displaying images in many different manners as shown in Figure 3:

- Conventional 2D orthogonal slicing (Figure 3A)
- 2D anyplane/oblique slicing (Figure 3B–C), the 2D plane is shown inside a 3D volume-rendered scene
- Stereoscopic visualization (Figure 3D)
- Surface visualization of segmented structures (Figure 3E–F)
- Volume rendering with dynamic transfer functions (Figure 3G)
- Combinations of several views (Figure 3B–C)

We can display several volumes simultaneously in the navigation display and interactively set dynamic transfer functions to volume-rendered objects. Using different transfer functions, and colors, for the different volumes allows us to easily distinguish them in the display window. Our volumes are rendered using a common technique where the 3D volume is saved in the graphics memory as a series of 2D slices. These textures are mapped on 2D proxy geometry which in turn is rendered normally in order from the furthest to the nearest relative to the camera. The source data for the volumes is sampled from any of several modalities for medical image acquisition. We have successfully worked with CT, MRI, fMRI (functional MRI in neurosurgery), MR angiography, CT angiography, MR diffusion tensor imaging, and 3D tissue- and power Doppler ultrasound data sets. The individual voxels' intensities are transformed into color and opacity values by the transfer functions after the proxy geometry/textures are rendered. The dynamic transfer functions are applied to the source volume on the graphics processor to allow real-time adjustment of the transfer functions in order to reduce processing time in the operating room.

While the surface model view (Figure 3E–F) or volume view (Figure 3G) provide overview, the orthogonal slices or the anyplane slice (Figure 3A–C) provide important details from the original preoperative images. The conventional orthogonal slicing technique: Axial, Coronal, and Sagittal (ACS), is important to the surgeon as the original images are displayed without any image processing applied.

The graphical user interface of our system is shown in Figure 4A–B. During a surgical procedure, the operator can start patient registration, change visualization settings etc., directly from this interface. Figure 3G shows an example when using a linear transfer function setting with low intensity values removed. For all the methods, crosshairs or a small sphere can be drawn to show the tip position of the tracked instrument. Position tracking of the instruments can be turned off to allow manual inspection, using the mouse and/or keyboard to rotate and zoom in on the volume obtaining positions not physically accessible by means of positioning of the navigation instruments. The operator can also detach the multimodal view or ACS windows from the user interface and move one or both of them to a second monitor (as will be shown later). The buttons for changing set-up and

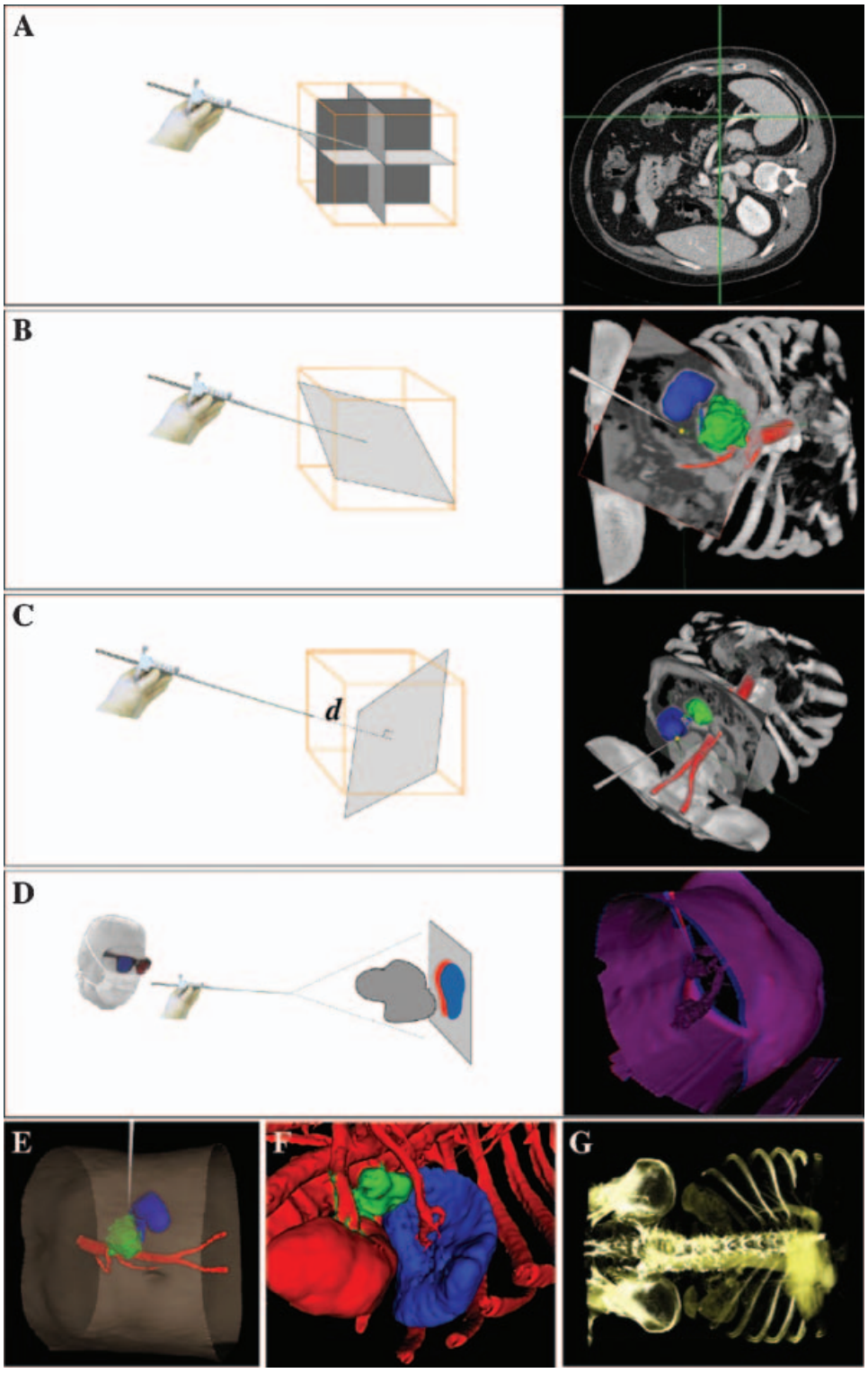

Figure 3. Visualization of medical images in the navigation system. (A) Orthogonal slicing (only axial slice shown) from 3D reconstructed CT data with overlaid cross hairs (green) showing the position of the laparoscopic tool. (B) Anyplane slicing with the surgical tool in plane. (C) Anyplane slicing with the tool perpendicular to the slice. An offset (*d*) can be set in front of the tracked instrument as illustrated. The tool in-plane functionality is most useful while using the navigation pointer (Figure 1E), grasper (Figure 1G) or RFA probe (Figure 1H), while the perpendicular-to-plane modality can be useful when using navigation with the video laparoscope (Figure 1F). (D) Stereoscopic visualization using red/blue glasses. (E) Surface segmentations of aorta (red), kidney (blue), tumor (adrenal gland, green), and transparent skin (brown). (F) A zoom of another clinical case, this time the spleen is seen in blue and the tumor (adrenal gland) is located very close to the renal arteries and the kidney (red). (G) Volume-rendering with low intensity values removed. In B–C combined visualizations can be seen: Surface segmentations, volume with low intensity values removed, anyplane slice and surgical tool.

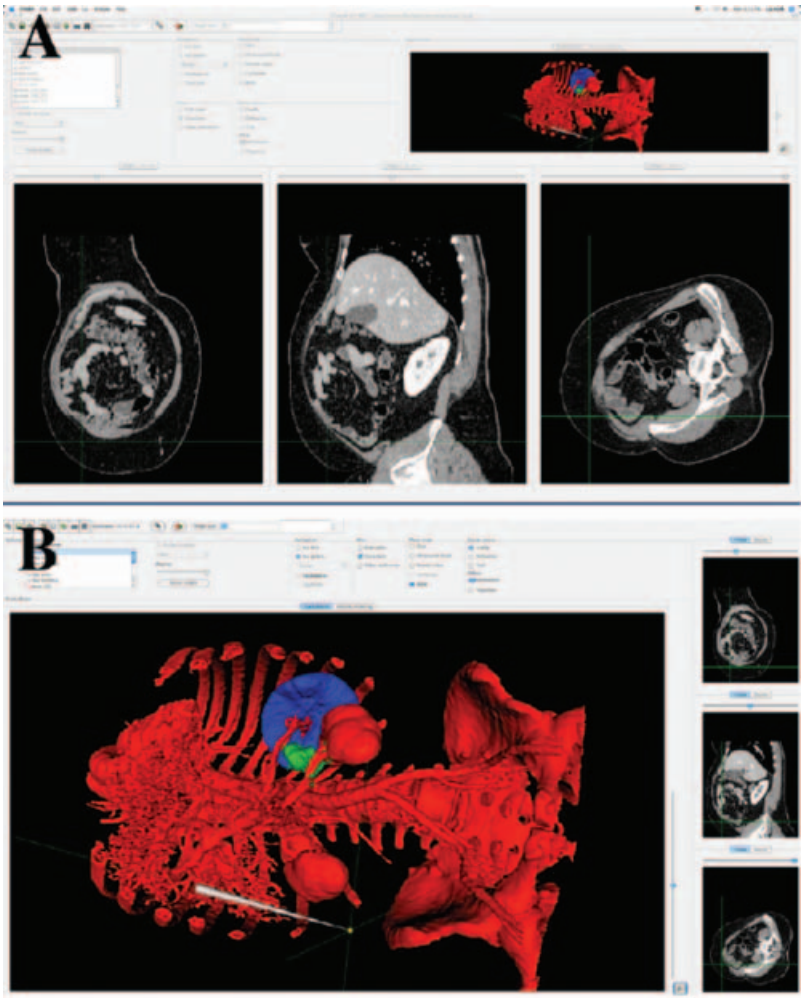

Figure 4. Graphical user interface for the main navigation system application *CustusX*. The views show intraoperative tracking of a surgical instrument inside the abdomen in the surface-rendering window. A) Start-up screen with preoperative CT data in ACS view at the bottom and surface rendering of segmented objects in the top right corner. The surface rendering shows skeleton, blood vessels and kidneys in red, spleen in blue and adrenal gland (tumor) in green. B) The surface rendering window is prioritized and made the largest compared to the ACS view. The windows can be detached from the user interface and can be moved onto a second monitor. The user can also zoom in on this view and rotate it as shown in figure 3F.

parameters are still available on the operator monitor, while the surgeons only see the medical images with the tracked tools superimposed.

Pilot tests of navigation in laparoscopy

We have used the navigation platform in several clinical cases for development and pilot testing of functionality described above. The system has been used for planning and for overview and guidance/navigation during laparoscopy. The majority of the cases were adrenalectomies (removal of benign, functioning adrenal tumors such as aldosteronomas and pheochromocytomas), while we also tested the system during resection of a primary tumor in the retroperitoneum, one retroperitoneal Scwannoma tumor, and one laparoscopic release of celiac artery compression syndrome. The common factor for these pilot cases was surgery in the retroperitoneum, since for these procedures the anatomic shift is smaller than for e.g. the liver. This is an important aspect as we are using preoperative images. Nevertheless, we make sure to acquire the CT or MR images with the patient in the same position as he/she will have on the operating table (explained below).

In this paper, we concentrate on key technological experiences and describe the use of the navigation system using sample images from two pilot cases, both adrenalectomies. We acquired consent from the patients and conducted the pilots in the *Operating Room of the Future* for laparoscopic surgery at St. Olavs Hospital/NTNU (Trondheim, Norway). We are conducting a multicenter study based on

these pilot tests and a research protocol approved by the scientific board of the hospital and the Regional Committee for Medical Research Ethics (REK, Norway). The results from this study will be published later. The measurements are based on parameters such as definition of resection border, trocar placement, time spent on various tasks, subjective score measures as feeling secure/safe, locating and avoiding injury to blood vessels or urethras, complications, endoscopic video, and surveillance video recordings.

The typical flow of data and the logistics of using the navigation system in a laparoscopic procedure are illustrated and summarized in Figure 5.

Prior to surgery

Prior to surgery, usually the day before, MR or CT images, i.e. DICOM data, were acquired and imported into the navigation system software for reconstruction into a 3D volume. The MR/CT images were obtained with the patient in the same position as what was planned to be the case in the OR to minimize errors/shift due to gravity on the OR table. Skin fiducials, donut-shaped markers (15 mm diameter, 3 mm thick, 4 mm hole) filled with MR/CT contrast fluid, were glued to the patient prior to scanning. These disposable markers were used for the patient registration procedure in the OR and, hence, the patient must keep these on until surgery, usually the following day. Next, the surfaces of essential organs and structures were extracted from the image data using methods described above. Usually, we segmented the tumor, aorta, smaller vessels in the vicinity of the tumor, organs close to the tumor, and other important anatomic structures close to the resection border. For the adrenalectomy cases used as examples in this article, we segmented the adrenal gland, aorta with side branches, kidney closest to the adrenal gland, and in one case the

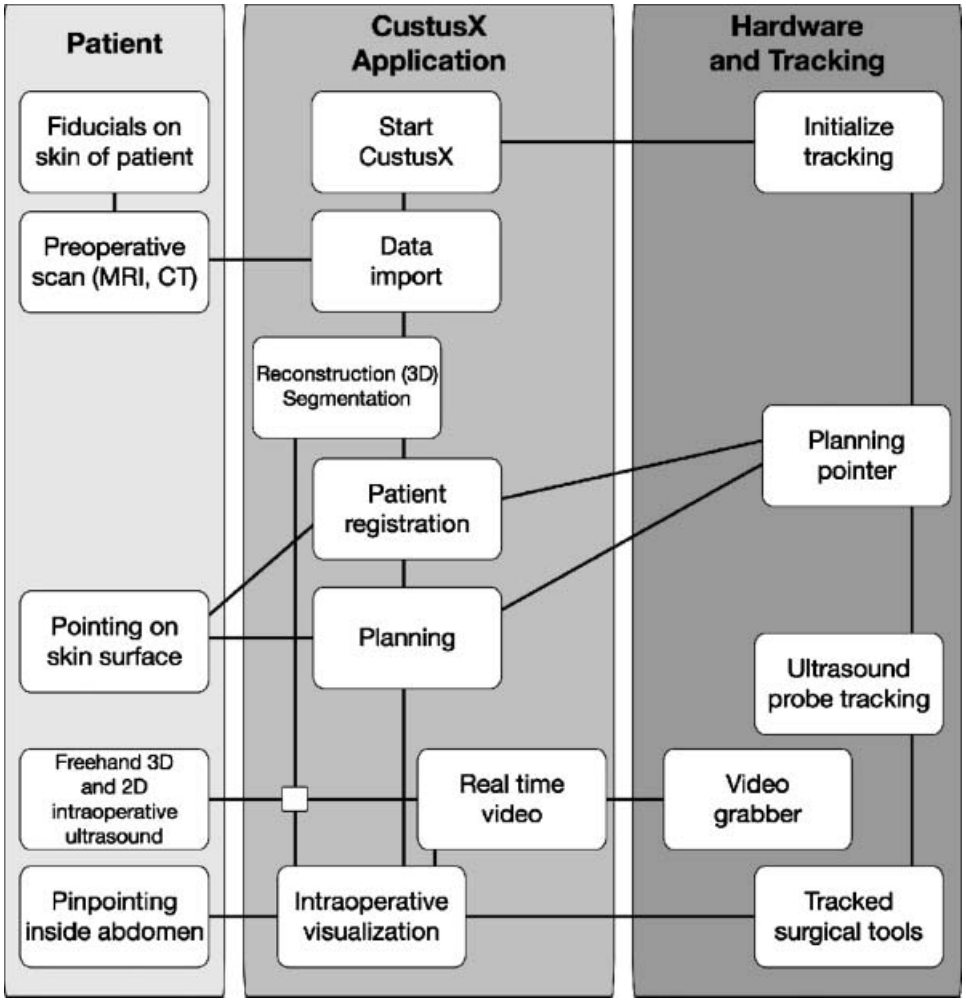

Figure 5. The diagram shows the logistics for navigation in laparoscopy. The ultrasound feature is not always used in laparoscopy and has not been clinically tested for the miniature tracking sensor and flexible ultrasound probe combination presented later in this paper.

spleen. Next, the registration points, i.e. the skin fiducials/markers, in the images were marked and saved for quick registration of images to the patient inside the OR.

Navigation in the OR

In the OR, preoperative images were registered to the patient using a non-sterile pointer before sterile preparation of the patient. The surgeon placed the pointer tip in one skin fiducial at a time and the navigation system sampled each of their positions in space. These physical locations were then matched to the image points found earlier based on a least-square fit approach. The accuracy of the registration was calculated in the matching algorithm and verified by physically pointing on the patient and visually inspecting the match on the navigation system display. Next, fiducials were removed and the patient was prepared for surgery. After insufflation, the procedure was planned in more detail, including the placement of the trocars, by using the navigation system and a sterile pointer.

Initial experiences from pilot studies

The tracking of the video laparoscope and grasper enabled the surgeons to use the navigation system anytime throughout the laparoscopic procedure, without having to switch to a dedicated navigation instrument like the laparoscopic navigation pointer. The surgeons could use the video laparoscope to see both directly with the video feed while at the same time attaining a 3D view of anatomy located beyond the surface of the organs with the navigation system as shown in Figure 6A–B.

A particularly useful display technique was the combined view with the 3D surface-models and the 2D anyplane image (Figure 3B), most likely because this view enabled the operator to turn off the 3D display of surface-modeled objects or make them semi-transparent so that detailed information from the anyplane image could be clearly seen simultaneously.Thus, detailed information from 2D images could be enhanced, while at the same time maintaining the overview that the surface model or volume view provided. The stereoscopic visualization technique seemed to be most useful during the planning phase of the procedure as it implied putting on special glasses, which was inconvenient during surgery. This method enabled the surgeons to obtain depth perception, and thus improve the understanding of anatomic relationships, especially for complex vessel structures in close vicinity of the tumor. Volume rendering of

Figure 6. The photos show the navigation system in use during laparoscopic surgery. (A) Surgeon's and assistant's view using navigation in laparoscopy. The surgeons can see both the video laparoscope live image and the navigation display. We can track several instruments and one instrument can control the view direction. This makes it possible to have a view in the navigation display that corresponds to the view direction of the laparoscopic camera. (B) The optical tracking cameras must be placed so that there is a free line of sight to the tracked tools and the reference frame, which can be seen in the lower right part of the photo. In this case, the surgeon is setting the navigation view by tracking the video laparoscope and the tracked laparoscopic navigation pointer is shown in the same 3D scene, as can be seen in the navigation display in (A).

data, however, added a certain degree of depth perception to a visualization of 3D image data without the use of glasses, and this seemed to be particularly useful during surgery.

As previously published (35), the total duration of the registration and the planning procedure, which was approximately five minutes, did not add significantly to the total operation time, as this was performed while other preparations were completed

in the OR. Furthermore, the placement of the trocars seemed to be easier because the surgeon was able to interactively "see through" the patient from various directions. In all cases, adequate access to the tumor and other structures later in the procedure was obtained, possibly caused by satisfactory placement of the trocars. After insufflation and trocar positioning, the navigation system was only used intraoperatively in the retroperitoneum since navigation was based only on preoperative images (MRI, CT) in the pilot tests. As surgery progressed, the system was still useful, because the most interesting parts of the patient anatomy were still located beyond the visible surface in the video laparoscope view. The surgeons felt that the safety was increased in a majority of the cases due to the use of the navigation system. This was based on the added information available to the surgeon, allowing him to proceed with more confidence during dissection of the tumors, and also the fact that important blood vessels could be revealed and visualized on the navigation system prior to and during dissection. The navigation display was a useful tool for obtaining an overview and understanding of the anatomy during the procedure. It provided the surgeon with new and enhanced information on important structures not visible from the endoscope image. The skin surface of the patient did not match the position of the sterile pointer in the images due to insufflation, but the match of preoperative information in the navigation display and organ position located at the retroperitoneum was still good enough for practical intraoperative guidance. This has also earlier been verified intraoperatively (20,35).

Discussion and further developments

New technological advancements open up new possibilities in treatment with the laparoscopic technique. In this paper, we have demonstrated the use of a research and development platform for navigation in laparoscopy. We have described the system and pointed out some advantages compared to conventional laparoscopic surgery using only endoscopic video.

However, one of the main challenges in using navigation technology in laparoscopic surgery is to maintain high accuracy throughout the procedure. The overall clinical accuracy in IGS, in general, is the difference between the locations of a surgical tool indicated in the images and the physical location inside the patient. This accuracy determines the delicacy of the work that can be done based on the images. In neurosurgery, it has been demonstrated that for navigation based on preoperative images, the main contributors to navigation inaccuracy are the registration process and the fact that preoperatively acquired images do not reflect the intraoperative changes that occur during surgery (51). A mismatch between image information displayed on the computer screen, and what is physically taking place inside the patient, can only be evaluated using well-defined physical reference points in the patient. In laparoscopy, this can be achieved by pinpointing such a structure through the trocars, using a pre-calibrated laparoscopic pointer (35), with the visual aid of the laparoscopic camera. An observed mismatch between the pointer tip in the images and its position in physical space could be the direct result of inaccuracy in the registration procedure or, if the mismatch exceeds some threshold, we can conclude that an anatomic shift has occurred after registration of the images to the patient.

Most conventional IGS systems operate under the assumption that the tissue being operated on can be treated as a rigid body, which does not change its form between the time the preoperative images are acquired and the time the surgery is performed. This is not the case and tissue movements are much more important to deal with in laparoscopic IGS than concerns about image resolution, patient registration errors, and tracking accuracy. Several approaches exist to counteract the problem of shifting anatomy due to surgical manipulations in the body, which in turn causes the preoperative images to become outdated. The two most important approaches are direct navigated surgery based on intraoperative ultrasound imaging, which is becoming routine in neurosurgery (1,52,53), and shifting or even morphing the preoperative images based on intraoperative data such as ultrasound (54). The changes can also be reduced by acquiring the preoperative images while the patient is in the same position as he or she will be on the operating table during surgery (35). However, the last approach only counteracts shifts due to gravity. Nevertheless, this effect is important in abdominal IGS because the operator in laparoscopy is usually most interested in the non-resected tissue. In addition, as long as the procedure is located in the retroperitoneum, most changes in anatomy are probably small and may be compensated for by using 3D ultrasound to acquire updated images.

Navigation based on intraoperative 3D ultrasound is associated with a similar but independent error chain, as navigation based on preoperative images. Ultrasound probe calibration and varying speed of sound are the main contributors to this error, as well as changes in anatomy after 3D ultrasound acquisition. If, however, navigation is based on

intraoperative 3D ultrasound scans, the accuracy will be close to what can be found in laboratory evaluations. This navigation accuracy will be maintained throughout the operation as long as the 3D map is continuously updated and the ultrasound data is reconstructed with a sound velocity matching that of the imaged objects.

In the following, we describe solutions we believe will improve accuracy and user friendliness of future intraoperative navigation in laparoscopic therapy, as well as in other minimally invasive therapy.

Markerless registration of the patient

Preoperative images will continue to be useful for planning, overview, and guidance in laparoscopic surgery, as shown in Figures 3, 4, and 6. However, the current method of registering preoperative images to the patient in the operating room using fiducials, as described earlier, is an inconvenient and time-consuming approach. A new markerless registration method for matching preoperative images to the patient on the operating table is currently being investigated and tested in our laboratory. One method is based on matching a surface model, extracted from preoperative MRI or CT data of the patient's abdomen, to a corresponding surface generated from the patient in the operating room, using a structured light-measuring technique (55). The surface model of the preoperative images is extracted and generated using a fast marching level set algorithm (56) followed by the marching cubes algorithm. The structured light-measuring technique is based on illuminating an area of the patient's body with a sequence of light patterns while capturing the view with a camera. From the

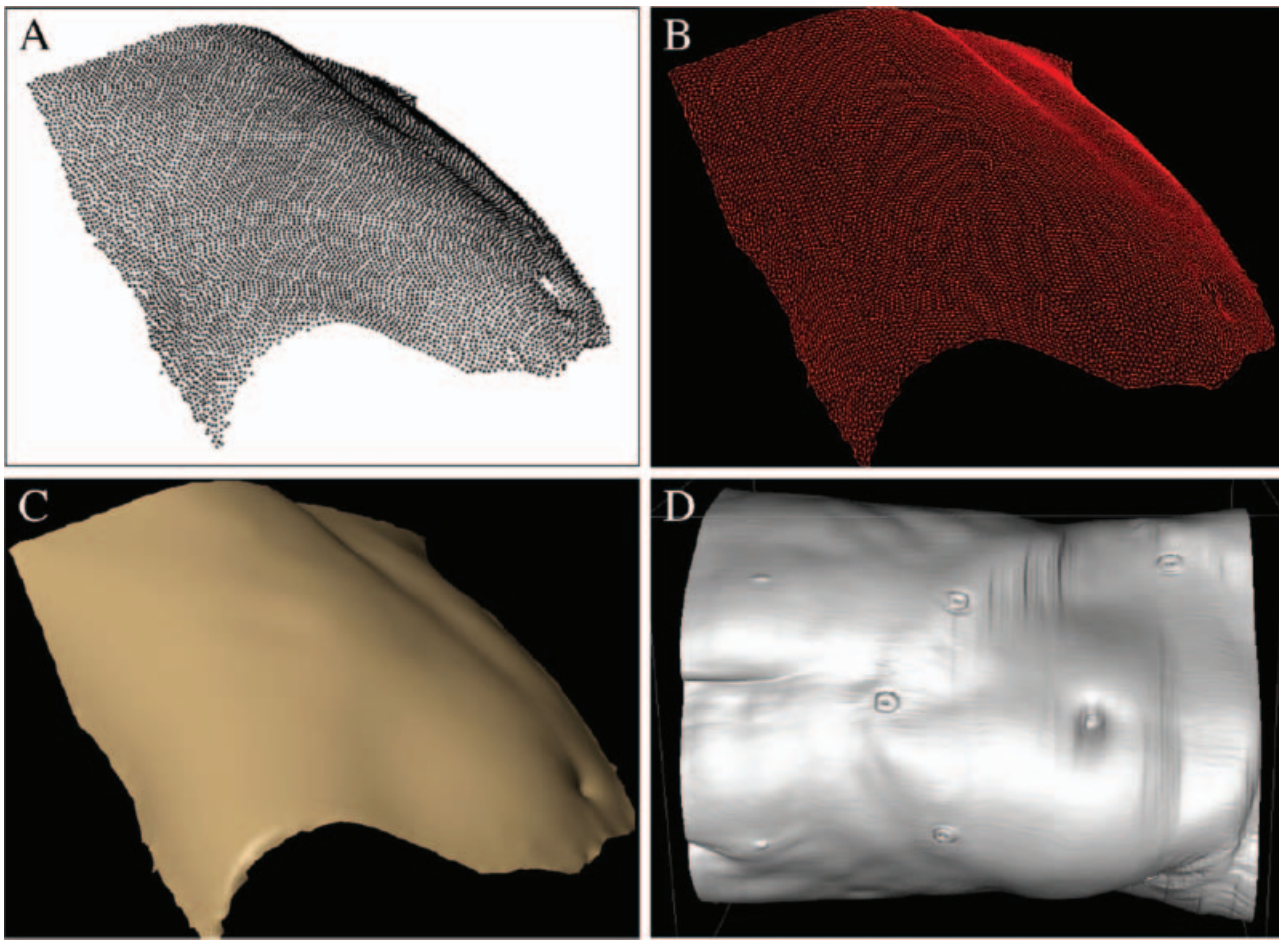

Figure 7. A method for markerless image-to-patient registration based on the structured light surface measurement technique. (A) Point cloud from structured light measurement of the abdominal surface of a healthy volunteer. (B) Triangle mesh made from the cloud points. (C) Surface interpolated over the mesh. (D) Example of a surface generated from a 3D CT scan of a patient. The algorithm starts from an initial transform between the segmented surface from preoperative MRI or CT and the structured light-generated surface in the operating room. The basic principle of the algorithm is to first find the closest point on the surface generated from MRI or CT for each of the points in the structured light-generated surface. The second step is to calculate a new and better transform based on all the corresponding point pairs and apply the transform. Finally, this procedure is repeated until a stop criterion is met.

observed scenes, coordinates of many points, distributed across the surface of the object, can be obtained. The collection of points, point cloud, is then modeled using a multilevel B-spline approximation to give a surface description of the object that can be registered to the corresponding segmented surface of the preoperative images (Figure 7).

Intraoperative ultrasound and multivolume visualization

Unlike the skull, the vertebrae, or the long bones, in abdominal procedures like liver and prostate surgery there can be no presumption of even piece-wise rigidity. This means that intraoperative image acquisition becomes even more important than in other clinical IGS disciplines. Combining intraoperative ultrasound and navigation technology, it is possible to show the 2D real-time ultrasound images in their correct orientation relative to the patient MR/CT data and surgeon's view (52,57). This solves the orientation problem during scanning using ultrasound, which can be particularly problematic when using laparoscopic ultrasound, as the video laparoscope provides an image from a different angle than the ultrasound probe, none of them necessarily originating from the same angle as the operator view.

We are implementing and evaluating a 3D laparoscopic ultrasound solution based on electromagnetic miniature position and orientation sensors at the tip of a flexible laparoscopic ultrasound probe as shown in Figure 8A. To illustrate the possibilities of this solution, we have performed 3D ultrasound scans of an abdominal phantom (Figure 8B, CIRS Inc., Virginia, USA). The probe calibration, which determines the position and orientation of the 2D ultrasound image scan plane relative to the sensors, was performed using our in-house developed 2D based alignment method and phantom (27). This solution will enable us to track the real-time 2D image inside the abdomen of the patient, and to perform 3D freehand ultrasound acquisitions. We can also show the 2D real-time ultrasound image correctly oriented inside a volume-rendering of the preoperative data. Such a view makes it easier to interpret the real-time 2D ultrasound image and will provide the surgeon with an indication of any anatomic shift that has occurred since the preoperative data acquisition and registration, as well as an improved understanding and interpretation of the ultrasound image.

Illustration of multimodal and multivolume view with 3D ultrasound and 3D CT is shown in Figure 9A–E. The images are acquired from the set-up in Figure 8. A non-linear transfer function was applied to the CT volume to enhance the visualization of the liver of the phantom and to better show the ultrasound volume. We believe that this feature will be important when visualizing intraoperative ultrasound data together with preoperative CT data from a patient during intraoperative navigation. The ultrasound will show updated information that the surgeon relies on during surgery, at the same time keeping the advantages from CT, such as better overview and understanding of the anatomy and pathology.

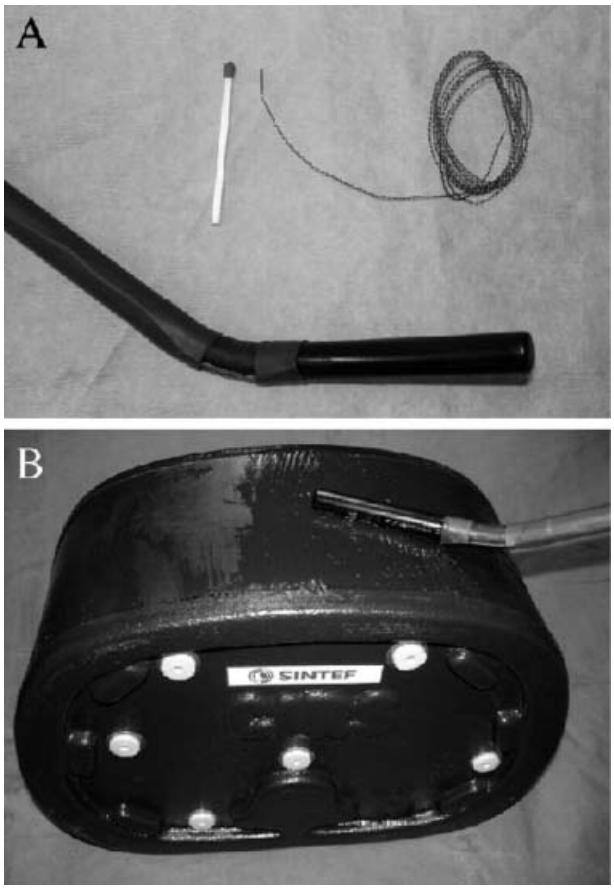

Figure 8. (A) The photo shows one raw 5 DOF electromagnetic tracking sensor (Aurora, NDI, Canada) and the tip of the flexible ultrasound probe with two such sensors integrated. The two sensors are placed at approximately 90° angle relative to each other on each side of the probe array. (B) Abdominal multimodal phantom (model 057, CIRS Inc., Virginia, USA) showing the laparoscopic ultrasound probe during a freehand 3D scan. A water-based gel is used to achieve proper acoustic coupling between the probe array and the phantom.

Multimodality visualization and image fusion

Image fusion techniques might be beneficial when several information sources are available, such as CT, MRI, ultrasound, and laparoscopic video. This is because it is most likely easier to perceive an integration of two or more volumes in the same

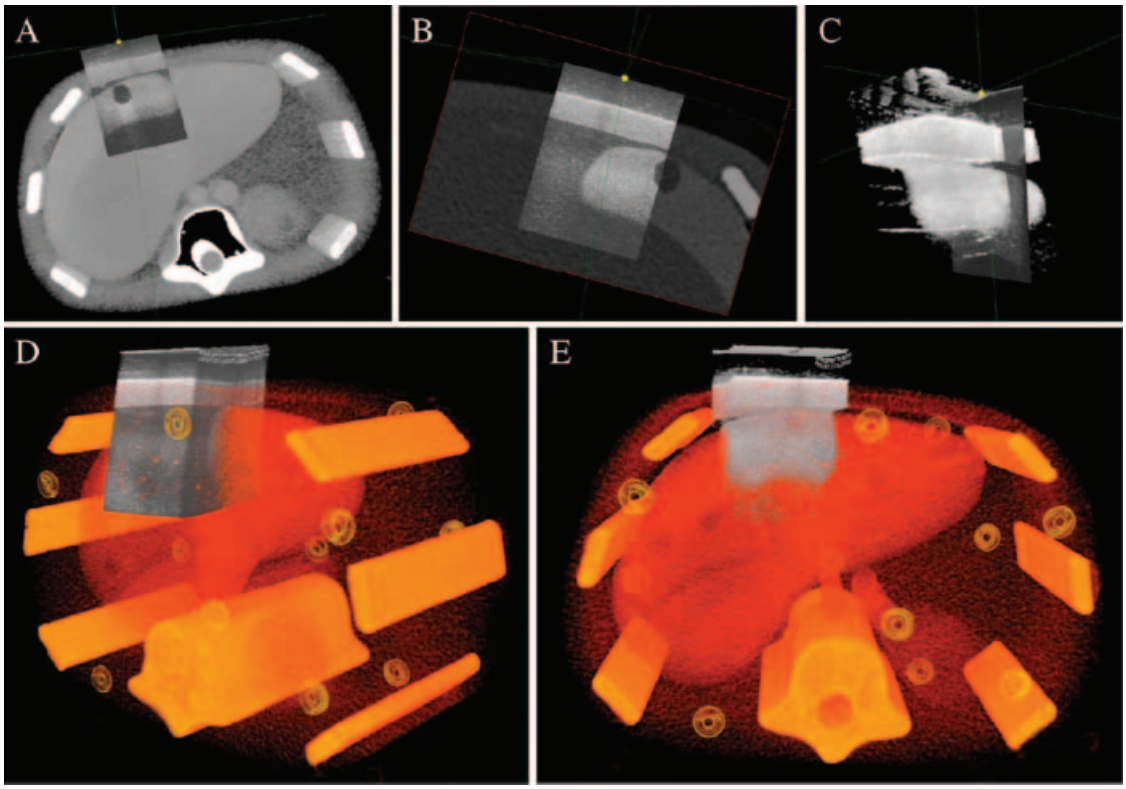

Figure 9. A) The figure shows a 2D real-time ultrasound image, acquired from a tracked ultrasound probe, inside a 3D volume rendering of a CT volume from an abdominal phantom (Figure 8B). B) The multimodal display shows a 2D real-time ultrasound image superimposed on a corresponding anyplane, i.e. reformatted, from the CT volume. The anyplane/oblique CT slice is controlled by the ultrasound probe position and orientation as explained previously in figure 3B–C. The extent of the CT slice can be interactively changed as well as the brightness/contrast levels by clicking and dragging the mouse on the borders of the image or in the image, respectively. C) The 3D rendering shows a real-time 2D ultrasound and a 3D ultrasound volume. D) The 3D volume rendering illustrates multivolume display with 3D ultrasound in grey scale and 3D CT in color. E) The 3D volume rendering shows the same scene as in D from a slightly different angle with a low level threshold applied to the 3D ultrasound volume. In D and E, the solid bars holding the phantom together are seen along with the fiducials.

scene than mentally fusing the same volumes presented in their own display windows. It also provides the opportunity to pick relevant and needed information from the most appropriate of the available datasets. Ideally, relevant information should not only include anatomical structures for reference and pathological structures to be targeted (CT/MRI and US tissue), but also important structures to be avoided, like blood vessels (CT/MR contrast, ultrasound Doppler). A technique that is becoming popular is ''virtual endoscopy'' (58) or image-enhanced endoscopy. This approach uses computer graphics to simulate the view seen by an endoscope placed in a body cavity, based on a representation of the cavity rendered from preoperative MRI or CT images. Recent research suggests merging the endoscope image seen in minimally invasive surgery with the corresponding computer-generated surface from preoperative images. For a complete fusion, the virtual endoscopic view, which is a surface representation of the cavity, must be constructed from the CT/MRI data and the video image mapped onto this surface. Figure 10 shows an example of a merged display where the preoperative data, 3D reconstructed and segmented, is overlaid the video image from the laparoscope camera. The position sensor attached to the video laparoscope ensures a correctly oriented 3D view for the preoperative images corresponding to the camera live video view. This view may help the surgeons to quickly take a look beyond the surface of the retroperitoneum during laparoscopy with a view corresponding to the conventional video laparoscope. Future solutions may be to update and combine this view using navigated 3D ultrasound, so that IGS on moving organs will be feasible.

Conclusion

In this paper we have described a prototype research and development platform for navigation in laparoscopic surgery. We have also demonstrated clinical

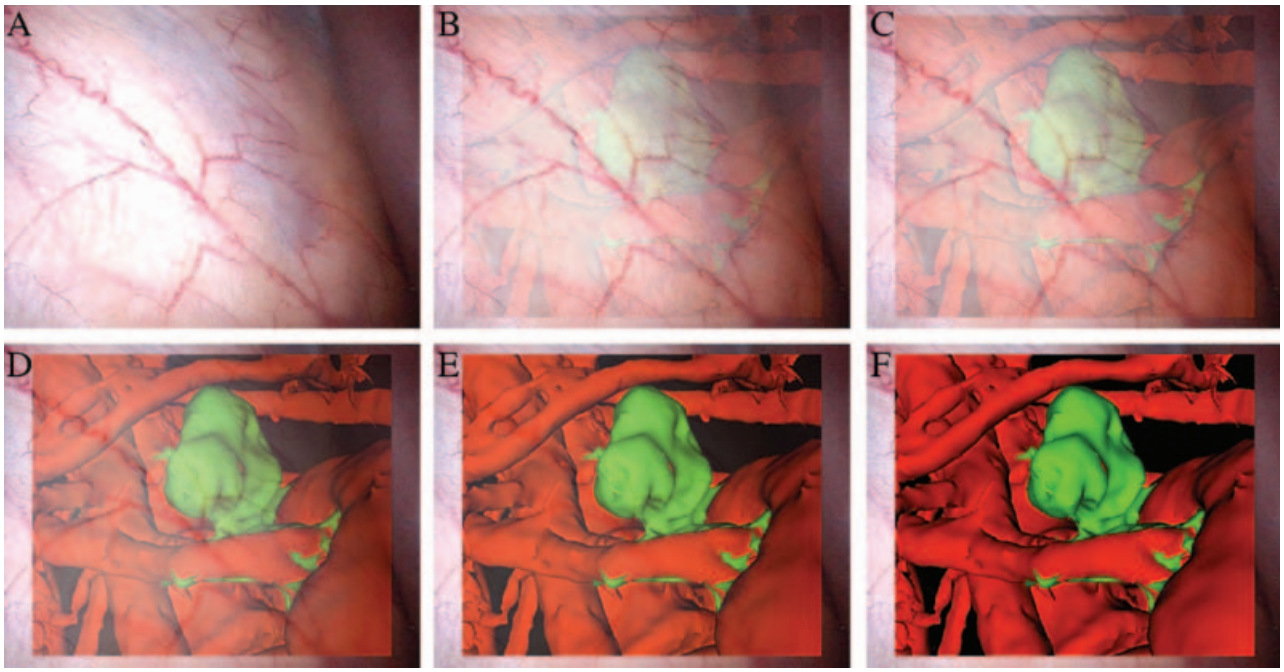

Figure 10. The images illustrate how image fusion techniques can be used to merge a video stream (A) from the video laparoscope with a preoperative radiological planning scene (F) to an augmented reality display (B–E). The two surface-rendered structures that can be observed in the 3D scene are a tumor in green and blood vessels in red, both extracted from CT data with contrast. Volume rendering could also be used. This view makes it possible to ''see'' beyond the surface of the organs providing the surgeon with an intuitive ''super vision''.

use of the system and pointed out some future directions. Our initial results are promising. However, we believe that the navigation system can be improved even further by introduction of intraoperative 3D imaging, more advanced multimedia display, and solutions that improve logistics and user friendliness in the OR. We are working on several solutions, some of which are mentioned and discussed in this paper. In order to evaluate the use of navigation systems in laparoscopy, we will conduct larger studies involving more patients with various types of lesions.

Acknowledgement

This work was supported by the Norwegian University of Science and Technology through the Strategic University Programme for Medical Technology, SINTEF through the Strategic Institute Programme, the Research Council of Norway through the FIFOS Programme Project 152831/530, and the Ministry of Health and Social Affairs of Norway through the National Centre of 3D Ultrasound in Surgery (Trondheim, Norway). We also want to thank Erik Harg, Arild Wollf, Øystein Skotheim, scientists at SINTEF, and radiologist Reidun Fougner, St Olav's University Hospital, for valuable discussions and collaboration during the technological developments and clinical pilots. In addition, we would like to thank the surgeons at Mesos Medical Center in Utrecht, The Netherlands, for valuable discussions and collaboration in the ongoing multicenter study.

References

1. Gronningsaeter A, Kleven A, Ommedal S, Aarseth TE, et al. SonoWand, An ultrasound-based neuronavigation system. Neurosurgery. 2000;47:1373–80.
2. Gumprecht HK, Widenka DC, Lumenta CB. BrainLab Vector Vision neuronavigation system: Technology and clinical experiences in 131 cases. Neurosurgery. 1999;44: 97–105.
3. Hata N, Dohi T, Iseki H, Takakura K. Development of a frameless and armless stereotactic neuronavigation system with ultrasonographic registration. Neurosurgery. 1997;41: 608–13.
4. Cartellieri M, Vorbeck F, Kremser J. Comparison of six three-dimensional navigation systems during sinus surgery. Acta Otolaryngol. 2001;121:500–4.
5. Labadie RF, Fenlon M, Cevikalp H, Harris S, et al. Image-guided otologic surgery. Int Congress Series. 2003;1256: 627–32.
6. Verstreken K, van C, Martens K, Marchal G, et al. An image-guided planning system for endosseous oral omplants. IEEE Trans Med Imaging. 1998;17:842–52.
7. Burns RP. Image-guided breast biopsy. Am J Surg. 1997;173: 9–11.
8. Gould SW, Lamb G, Lomax D, Gedroyc W, et al. Interventional MR-guided excisional biopsy of breast lesions. J Magn Reson Imaging. 1998;8:26–30.
9. Sato Y, Nakamoto M, Tamaki Y, Sasama T, et al. Image guidance of breast cancer surgery using 3-D ultrasound

images and augmented reality visualizations. IEEE Trans Med Imaging. 1998;17:681–93.
10. Chin JL, Downey DB, Mulligan M, Fenster A. Three-dimensional transrectal ultrasound guided cryoablation for localized prostate cancer in nonsurgical candidates: a feasibility study and report of early results. J Urol. 1998;159: 910–14.
11. Pathak SD, Grimm PD, Chalana V, Yongmin K. Pubic arch detection in transrectal ultrasound guided prostate cancer therapy. IEEE Trans Med Imaging. 1998;17: 5 762–71.
12. Tong S, Downey DB, Cardinal HN, Fenster A. A three-dimensional ultrasound prostate imaging system. Ultrasound Med Biol. 1996;22:735–46.
13. Brown GA, Willis MC, Firoozbakhsh K, Barmada A, et al. Computed tomography image-guided surgery in complex acetabular fractures. Clin Orthop. 2000;370:219–26.
14. Ellis RE, Tso CY, Rudan JF, Harrison MM. A surgical planning and guidance system for high tibial osteotomy. Comput Aided Surg. 1999;4:264–74.
15. Gueziec A, Kazanzides P, Williamson B, Taylor RH. Anatomy-based registration of CT-scan and intraoperative X-ray images for guiding a surgical robot. IEEE Trans Med Imaging. 1998;17:715–28.
16. Schwarz Y, Greif J, Becker HD, Ernst A, et al. Real-Time Electromagnetic Navigation Bronchoscopy to Peripheral Lung Lesions Using Overlaid CT Images, The First Human Study. Chest. 2006;129:988–94.
17. Herline AJ, Stefansic JD, Debelak J, Galloway RL, et al. Technical advances toward interactive image-guided laparoscopic surgery. Surg Endosc. 2000;14:675–9.
18. Herline AJ, Stefansic JD, Debelak JP, Hartmann SL, et al. Image-guided surgery: preliminary feasibility studies of frameless stereotactic liver surgery. Arch Surg. 1999;134: 644–50.
19. Lamade W, Vetter M, Hassenpflug P, Thorn M, et al. Navigation and image-guided HBP surgery: a review and preview. J Hepatobiliary Pancreat Surg. 2002;9:592–9.
20. Kaspersen JH, Sjølie E, Wesche J, Åsland J, et al. 3D ultrasound based navigation combined with preoperative CT during abdominal interventions, A feasibility study. CardioVasc Intervent Radiol. 2003;26:347–56.
21. Lamade W, Glombitza G, Demiris AM, Cardenas C, et al. Virtual operation planning in liver surgery. Chirurg. 1999;70: 239–45.
22. Soler L, Delingette H, Malandain G, Ayache N, et al. An automatic virtual patient reconstruction from CT-scans for hepatic surgical planning. Stud Health Technol Inform. 2000;70:316–22.
23. Soler L, Delingette H, Malandain G, Montagnat J, et al. Fully automatic anatomical, pathological and functional segmentation from CT scans for hepatic surgery. Comp Aided Surg. 2001;6:131–42.
24. Rousseau F, Barillot C. Quality Assessment of Electromagnetic Localizers in the Context of 3D Ultrasound. 2002, Research report, Institut National de Recherche en Informatique et en Automatique (INRIA): Rennes, France.
25. Birkfellner W, Watzinger F, Wanschitz F, Enislidis G, et al. Systematic distortions in magnetic position digitizers. Med Phys. 1998;25:2242–8.
26. West JBaMCR, Jr. Designing optically tracked instruments for image-guided surgery. IEEE Trans Med Imaging. 2004;23:533–45.
27. Lindseth F, Tangen GA, Langø T, Bang J. Probe calibration for freehand 3-D ultrasound. Ultrasound Med Biol. 2003;29:1607–23.
28. Treece GM, Gee AH, Prager RW, Cash CJC, et al. High-definition freehand 3-D ultrasound. Ultrasound Med Biol. 2003;29:4 529–46.
29. Meyer KaBFA. A Survey of Position Trackers. Presence: Teleoperators and Virtual Environments. 1992;1:173–200.
30. Cinquin P, Bainville E, Barbe C, Bittar E, et al. Computer assisted medical interventions. IEEE Eng Med Biol Magazine. 1995;14:254–63.
31. Maintz JBA, Viergever MA. A survey of medical image registration. Med Image Analysis. 1998;2:1–36.
32. Herline AJ, Herring JL, Stefansic JD, Chapman WC, et al. Surface registration for use in interactive, image-guided liver surgery. Comp Aided Surg. 2000;5:11–7.
33. Maurer CR, Jr, Fitzpatrick JM, Wang MY, et al. Registration of head volume images using implantable fiducial markers. IEEE Trans Med Imaging. 1997;16:447–62.
34. Maes F, Collignon A, Vandermeulen D, Marchal G, et al. Multimodality image registration by maximization of mutual information. IEEE Trans Med Imaging. 1997;16: 187–98.
35. Mårvik R, Langø T, Tangen GA, Andersen JON, et al. Laparoscopic navigation pointer for 3-D image guided surgery. Surg Endosc. 2004;18:1242–8.
36. Cervone A, Sardi A, Conaway GL. Intraoperative ultrasound (IOUS) is essential in the management of metastatic colorectal liver lesions. Am Surg. 2000;66:611–5.
37. Ellsmere J, Stoll J, Wells W, Kikinis R, et al. A new visualization technique for laparoscopic ultrasonography. Surgery. 2004;136:84–92.
38. Harms J, Feussner H, Baumgartner M, Schneider A, et al. Three-dimensional navigated laparoscopic ultrasonography. Surg Endosc. 2001;15:1459–62.
39. Ozsunar Y, Skjoldbye B, Court-Payen M, Kastrup S, et al. Impact of intraoperative ultrasonography on surgical treatment of liver tumours. Acta Surg Endosc. 2000;14:675–9.
40. Sjølie E, Langø T, Ystgaard B, Tangen G, et al. 3-D ultrasound-based navigation for radio frequency thermal ablation in treatment of liver malignancies. Surg Endosc. 2002;17:933–8.
41. Berber E, Herceg NL, Casto KJ, Siperstein AE. Laparoscopic radiofrequency ablation of hepatic tumors: Prospective clinical evaluation of ablation size comparing two treatment algorithms. Surg Endosc. 2004;18:390–6.
42. Curley SA. Radiofrequency ablation of malignant liver tumors. Oncologist. 2003;6:14–23.
43. Lezoche E, Paganini AM, Feliciotti F, Guerrieri M, et al. Ultrasound-guided laparoscopic cryoablation of hepatic tumours: Preliminary report. World J Surg. 1998;22:829–36.
44. Liu LX, Jiang HC, Piao DX. Radiofrequence ablation of liver cancers. World J Gastroenterol. 2002;8:393–9.
45. Bao P, Warmath J, Galloway R, Jr., Herline A. Ultrasound-to-computer-tomography registration for image-guided laparoscopic liver surgery. Surg Endosc. 2005;19:424–9.
46. Mercier L, Langø T, Lindseth F, Collins LD. A review of calibration techniques for freehand 3D ultrasound systems. J Ultrasound Med Biol. 2005;31:143–65.
47. Schroeder W, Martin K, Lorensen B. The Visualization Toolkit An Object Oriented Approach To 3D Graphics, VTK version 4.2. 3 ed. Vol. 4. 2003, New York: Kitware Inc. 520.
48. Ibanez L, Schroeder W, Ng L, Cates J. The ITK Software Guide: The Insight Segmentation and Registration Toolkit, version 2.4. 2005, New York: Kitware Inc.
49. Rosset A, Spadola L, Ratib O. OsiriX: An Open-Source Software for Navigating in Multidimensional DICOM Images. J Digital Imaging. 2004;17:205–16.

50. Yushkevich PA, Piven J, Hazlett HC, Smith RG, et al. User-guided 3D active contour segmentation of anatomical structures: Significantly improved efficiency and reliability. NeuroImage. 2006;31:1116–28.
51. Lindseth F, Langø T, Bang J, Hernes TAN. Accuracy evaluation of a 3D ultrasound-based neuronavigation system. Comp Aid Surg. 2002;7:197–222.
52. Unsgaard G, Gronningsaeter A, Ommedal S, Hernes TAN. Brain operations guided by real time 2D ultrasound New possibilities due to improved image quality. Neurosurgery. 2002;51:402–12.
53. Unsgaard G, Rygh OM, Selbekk T, Müller TB, et al. Intra-operative 3D ultrasound in neurosurgery. Acta Neurochirurgica. 2006;148:235–53.
54. Bucholz RD, Yeh DD, Trobaugh J, McDurmott LL, et al. The correction of stereotactic inaccuracy caused by brain shift using an intraoperative ultrasound device. in Lecture Notes in Computer Science Proceedings of the 1st Joint Conference on Computer Vision, Virtual Reality, and Robotics in Medicine and Medical Robotics and Computer Assisted Surgery (CVRMed MRCAS'97). 1997. Grenoble.
55. Hernes TAN, Lindseth F, Selbekk T, Rygh OM, et al. Technical developments for improved 3D ultrasound guided neurosurgery - Computer-assisted 3D ultrasound-guided neurosurgery: technological contributions, including multi-modal registration and advanced display, demonstrating future perspectives. International Journal of Medical Robotics and Computer Assisted Surgery. 2006;2:45–59.
56. Sethian JA. Level Set Methods and Fast Marching Methods: Evolving Interfaces in Computational Geometry, Fluid Mechanics, Computer Vision, and Materials Science. 1999, Cambridge: Cambridge University Press.
57. Ellsmere J, Stoll J, Rattner D, Brooks D, et al. A navigation system for augmenting laparoscopic ultrasound. Lecture Notes in Computer Science. 2003;2879:184–91.
58. Shahidi R, Bax MR, Maurer CR, Johnson JA, et al. Implementation, Calibration and Accuracy Testing of an Image Enhanced Endoscopy System. IEEE Trans Med Imaging. 2002;21:1524–35.

Paper IV

Minimally Invasive Therapy. 2009; 18:1; 36–53

informa
healthcare

ORIGINAL ARTICLE

Navigated ultrasound in laparoscopic surgery

O. V. SOLBERG[1,2,5], T. LANGØ[1,2], G. A. TANGEN[1,2], R. MÅRVIK[2,3,4,5], B. YSTGAARD[2,6], A. RETHY[3,5] & T. A. N. HERNES[1,2,3,5]

[1]*SINTEF Health Research, Dept. Medical Technology, Trondheim, Norway,* [2]*National Centre for 3D Ultrasound in Surgery, Trondheim, Norway,* [3]*The Future Operating Room, St. Olavs Hospital, Trondheim University Hospital, Norway,* [4]*National Center for Advanced Laparoscopic Surgery, St. Olavs Hospital, Trondheim, Norway,* [5]*Medical Faculty, Norwegian University of Science and Technology (NTNU), Trondheim, Norway, and* [6]*Department of Surgery, St. Olavs Hospital, Trondheim, Norway*

Abstract

Laparoscopic surgery is performed through small incisions that limit free sight and possibility to palpate organs. Although endoscopes provide an overview of organs inside the body, information beyond the surface of the organs is missing. Ultrasound can provide real-time essential information of inside organs, which is valuable for increased safety and accuracy in guidance of procedures. We have tested the use of 2D and 3D ultrasound combined with 3D CT data in a prototype navigation system. In our laboratory, micro-positioning sensors were integrated into a flexible intraoperative ultrasound probe, making it possible to measure the position and orientation of the real-time 2D ultrasound image as well as to perform freehand 3D ultrasound acquisitions. Furthermore, we also present a setup with the probe optically tracked from the shaft with the flexible part locked in one position. We evaluated the accuracy of the 3D laparoscopic ultrasound solution and obtained average values ranging from 1.6% to 3.6% volume deviation from the phantom specifications. Furthermore, we investigated the use of an electromagnetic tracking in the operating room. The results showed that the operating room setup disturbs the electromagnetic tracking signal by increasing the root mean square (RMS) distance error from 0.3 mm to 2.3 mm in the center of the measurement volume, but the surgical instruments and the ultrasound probe added no further inaccuracies. Tracked surgical tools, such as endoscopes, pointers, and probes, allowed surgeons to interactively control the display of both registered preoperative medical images, as well as intraoperatively acquired 3D ultrasound data, and have potential to increase the safety of guidance of surgical procedures.

Key words: *Intraoperative ultrasound, 3D ultrasound, surgical navigation, image-guided surgery, minimally invasive surgery, electromagnetic tracking*

Introduction

Compared to open surgery, laparoscopic surgery presents the surgeon with a set of challenges. One of these is the restricted view inside the body cavity through the video laparoscope. Another limitation is the inability to palpate tissue. In addition, little tactile feedback is possible through the rigid laparoscopic instruments. Ultrasound can compensate for some of these limitations intraoperatively by allowing the surgeon to see into tissues, i.e. beyond the surface of the organs. Furthermore, ultrasound can visualize blood vessels, important for avoiding bleeding, and its real-time capabilities provide the surgeons with immediate feedback of changes that occur. The image quality of ultrasound systems has also increased in recent years and the equipment is cheaper and more portable than alternative intraoperative imaging modalities such as CT and MRI.

Laparoscopic ultrasound

Laparoscopic ultrasound (LUS) was first introduced by Fukuda and coworkers in 1982 (1) with a system for screening of the liver during diagnostic laparoscopy and for staging of gastrointestinal malignancy. Following this, advances in CT and MRI technology have decreased the attention of diagnostic LUS.

Correspondence: O.V. Solberg, Dept. of Medical Technology, SINTEF Health Research, N-7465 Trondheim, Norway. Fax: +47 93070800. E-mail: ole.v.solberg@sintef.no

ISSN 1364-5706 print/ISSN 1365-2931 online © 2008 Informa UK Ltd
DOI: 10.1080/13645700802383975

However, a renewed enthusiasm for LUS came in the 1990s with the introduction of laparoscopic cholecystectomy as a standard procedure for cholecystolithiasis and more advanced ultrasound technology (2). Particularly, transducer development applicable to LUS resulted in achievements previously only reported in open surgery. Since this introduction, 2D LUS has expanded to being used for visualization of the anatomy during dissection, staging of gastrointestinal malignancies, detection of primary and secondary liver tumors, adrenalectomy, and delineation of the anatomy and examination of the common bile duct in laparoscopic cholecystectomy (2–8).

Nevertheless, to a clinician inexperienced with ultrasound, and in particular LUS, interpretation of the image in relation to the patient anatomy can be a challenge. The most important contributing factor to this is the orientation and position of the imaging transducer in relation to the displayed image on the screen, as the clinician only sees the probe indirectly through the video laparoscope. Also, the transducer's limited depth and width perception may give orientation and interpretation difficulties, especially for inexperienced users. The size of LUS images is small due to small transducer array size (foot print of the probe) as compared to CT and MR images. This is particularly true for laparoscopy, since the probe must pass through a trocar for introduction into the body cavity. Furthermore, ultrasound may have other disadvantages compared to CT and MRI. The signal-to-noise ratio may be low in some cases and although there is a continuous increase in image quality, the specular nature of the modality causes shadowing, multiple reflection artefacts, and variable contrast. The quality of the images may also be somewhat operator-dependent. However, the introduction of navigation technology in combination with 2D and 3D ultrasound imaging can solve the orientation problem and provide a helpful addition for interpretation of LUS.

Tracking technology for laparoscopic ultrasound

To achieve navigation with 2D and 3D ultrasound images and freehand 3D ultrasound acquisition based on 2D imaging probes, tracking technology is necessary. There are four common technologies for tracking medical instruments: Electromagnetic (EM), optical, mechanical arm and acoustic, which are described in detail by Cinquin et al. (9). A tracking system determines the position and orientation of a sensor attached to the instrument. A calibration procedure determines the position and orientation of the tip of the instrument in relation to the attached sensor. The different tracking methods have different advantages and drawbacks. Optical and EM systems are the most commonly used systems for tracking instruments in medicine, and both systems have their strengths and limitations (Table I). Optical systems may have satisfactory accuracy, but require a clear line of sight between the sensors/markers and the cameras. This is challenging to achieve as the operating rooms are generally cluttered and the freedom of movement is limited. Magnetic systems are unaffected by sensor occlusion, but distortions may occur due to metallic objects in the working space that induce perturbations of the magnetic field. In minimally invasive surgery, independence from line of sight is important in order to facilitate the tracking of instruments such as flexible video laparoscopes and endovascular catheters. Table I gives an overview of the accuracy of tracking systems reported by the manufacturers, but EM trackers have a non-uniform error distribution over the measurement volume and such simple statistics may not be enough to determine the best tracking system for a given application (10). Several groups have performed static and dynamic accuracy evaluations of different EM and optical trackers (10–15), which provide useful data for accuracy comparisons. In addition, using EM trackers in the OR introduces several distortion sources, and the impact may vary between the different trackers. A number of papers deal with distortions to the EM tracking systems from metals (14,16–18), surgical instruments (18–20), ultrasound probes (18–22), OR tables (13,16,21) and OR environments (23). In summary these papers also show that the EM trackers' robustness regarding distortion sources has improved over the last years.

Navigated LUS

There are basically four ways to achieve 2D and 3D navigated LUS using conventional 2D ultrasound probes and tracking systems:

- Optical tracking on the shaft of rigid ultrasound probes, either with front view or side view (Figure 1A–C).
- EM tracking at the tip of flexible LUS probes (Figure 1D).
- Optical tracking on the shaft of a flexible LUS probe that is fixed in one defined flex position.
- Optical tracking of a rigid 3D LUS probe.

It is theoretically possible to track a flexible probe using optical tracking on the shaft, but the probe must then be calibrated in each specific flexed position. Calibration in this case is the transformation determining the image position and orientation in relation to the sensor on the shaft.

Table I. Position accuracy of electromagnetic and optical tracking systems for medical applications as reported by the manufacturers. Caution must be taken when comparing the accuracy of the different models because the given statistics are often not equivalent

Manufacturer	Model	Accuracy
Northern Digital Inc. http://www.ndigital.com	Polaris Spectra (passive, active wireless, optical)	Position: 0.25 mm RMS* within 95-240 cm range, 0.30 mm RMS for extended volume (95–300 cm) Update rate: max 60 Hz
	Polaris Vicra (passive, active wireless, optical)	Position: 0.25 mm RMS, 56–134 cm range Update rate: max 20 Hz
	Optotrak Certus (optical)	Position: 0.1 mm RMS at 2.25 m, 3D resolution at 2.25 m distance: 0.15 mm Update rate: max 4600 Hz
	Aurora 5 DoF** sensors (EM) Sensor: small as 0.55 × 8 mm	Position: 0.7–1.3 mm RMS within 50 cm distance from field generator Update rate: max 40 Hz
	Aurora 6 DoF sensors (EM) Sensor: 1.8 mm × 9 mm	Position: 0.9–1.6 mm RMS, within 50 cm distance from field generator Update rate: max 40 Hz
atracsys http://atracsys.com/	accuTrack (passive, active wired/wireless, optical)	Position:<0.1 mm RMS up to 1 m, <0.2 mm RMS up to 2.5 m, <0.25 mm RMS up to 3 m Update rate: max 4000 Hz
	easyTrack500 (active, wired, optical)	Position:<0.2 mm RMS within 1 m, <0.3 mm RMS within 1.5 m Acquisition speed: 300 LED/s
	infiniTrack (passive, active, optical)	Working volume and calibration accuracy can be defined by user Update rate: max 30 Hz
Claron Technology http:// www.clarontech.com	MicronTracker 2 (passive, wireless, optical)	S60 model: 0.25 mm RMS within 115 × 70 × 55 cm, 30 Hz update rate H40 model: 0.20 mm RMS within 120 × 120 × 90 cm, 15 Hz update rate H60 model: 0.35 mm RMS within 200 × 130 × 100 cm, 15 Hz update rate
Polhemus http:// www.polhemus.com	Fastrack (EM) 6DoF	Position: 0.762 mm RMS (static x, y, z positions accuracy) within 1.5 m range Update rate: max 120 Hz
Ascension Technology http://www.ascension-tech.com	Flock of Birds / Class B Flock 6 DoF (EM)	Position: 1.8 mm RMS (static) within 1.2 m Update rate: max 144 Hz
	miniBIRD, 6 DoF (EM)	Position: 1.8 mm RMS (static) within 46 cm (model 500), within 76 cm (model 800) Update rate: max 120 Hz
	pciBIRD, 6 DoF (EM)	25 mm Sensor: 1.0 mm RMS within 76 cm range 8 mm Sensor: 1.4 mm RMS Update rate: max 105 Hz
	microBIRD 6 DoF (EM) 3D Guidance system (EM)	Position: 1.4 mm RMS (static) within 58 cm range for both 1.8 mm sensors and 1.3 mm sensors Update rate: max 375 Hz

* *RMS signifies Root Mean Square value.* ** *DoF: Degrees of Freedom.*

With a 3D probe, tracking allows us to know the position of an entire real-time ultrasound volume in relation to tracked instruments and also to registered preoperative images from CT or MRI. Such 3D probes for LUS are not readily available, but are currently being developed (24).

A few groups have already tested integration of tracking technology and LUS probes. Wilhelm and coworkers (25) integrated Flock of Birds (Acension Technology, USA) with a linear array LUS probe (Siemens, Germany). They found that navigated LUS was superior to both transcutaneous 3D ultrasound and 2D LUS. Harms and coworkers (26) used similar technology and found that 3D LUS with a navigated probe is technically feasible, particularly for the perception of complex liver pathologies. Ellsmere and his group (27) also used the miniBIRD (Acension Technology, USA) but with another laparoscopic ultrasound probe (BK Medical, USA). They focused on providing visual

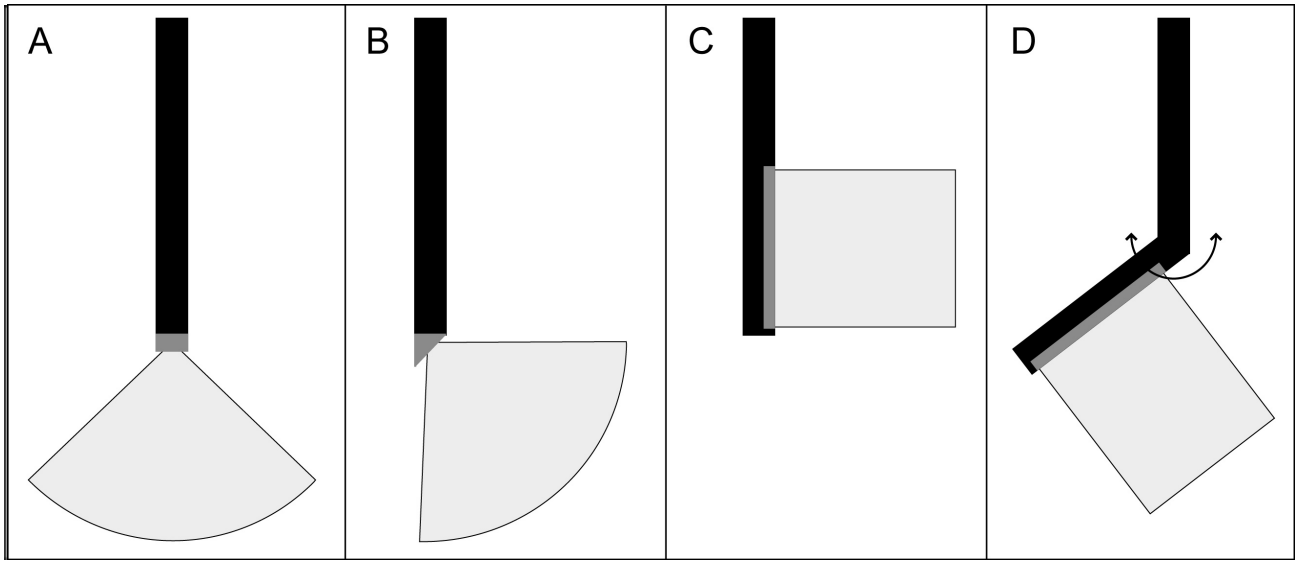

Figure 1. Configurations of LUS probes. (A) End viewing mechanical sector. (B) Side viewing mechanical sector. (C) Rigid side viewing linear array. (D) Flexible linear array.

orientation information to the operator and found that this significantly improved the surgeon's ability to interpret LUS images. Another group (28,29) used the US-Guide 2000® (Ultra-Guide, Tirat Hacarmel, Israel), an independent navigation system compatible with all ultrasound machines, and a similar setup as Ellsmere and his group to transfer navigated parenchyma dissection from open surgery to the laparoscopic technique. They found that this solution might be feasible for achieving increased precision in laparoscopic liver dissection. However, they used an $8 \times 8 \times 6$ mm sensor and, therefore, could not adapt this properly to the laparoscopic technique.

We present a navigation system capable of using both electro-magnetic (EM) and optical tracking with any kind of ultrasound system. The system is designed for navigation in laparoscopic surgery and other minimally invasive therapy applications. We demonstrate, using a phantom model and a liver model setup, how new visualization methods applied to 2D and 3D preoperative images and intraoperative ultrasound technology can be used to improve laparoscopic surgery. We also evaluated the accuracy of EM tracking in a realistic laparoscopic environment and compared it to an ideal laboratory setup. The 3D reconstruction accuracy for freehand 3D ultrasound scanning using the LUS probe was investigated using a 3D ultrasound phantom.

Material and methods

Navigation system

In the present study, we used our developed prototype navigation platform for research and development in navigated laparoscopic surgery (Figure 2A, SINTEF, Norway) (30). It consists of an optical position tracker (Polaris Spectra, Northern Digital Inc. (NDI), Canada), a desktop computer (Macintosh, Apple, USA), navigation pointers (Figure 2B), snap-on tracking devices for various laparoscopic instruments such as graspers (Figure 2C–D), a patient reference tracking frame, and our own developed software for processing of medical data, visualization, and navigation. The optical position tracking devices attached to the surgical instruments consist of three to four reflecting spheres. For the devices with four spheres, one can be elevated from the plane of the other three for optimal tracking conditions at oblique angles between the tracking cameras and the tracking frame.

EM tracking of the LUS probe

EM tracking was integrated with our navigation system. The EM tracker (Aurora, NDI, Canada) used in this project is shown in Figure 3. EM sensors were integrated into the tip of a flexible laparoscopic ultrasound probe (6 MHz prototype Tetrad, USA) used on a System FiVe ultrasound scanner (GE Vingmed Ultrasound, Norway) for one of the experiments. An ultrasound probe calibration procedure was performed using an in-house developed 2D alignment method and a phantom (31). This method establishes the transformation between the sensor attached to the ultrasound probe and the coordinate system of the 2D ultrasound image. The calibration enables us to track the real-time 2D image in space, and to perform 3D freehand ultrasound acquisitions. To obtain tracking of all six degrees of freedom (DoF),

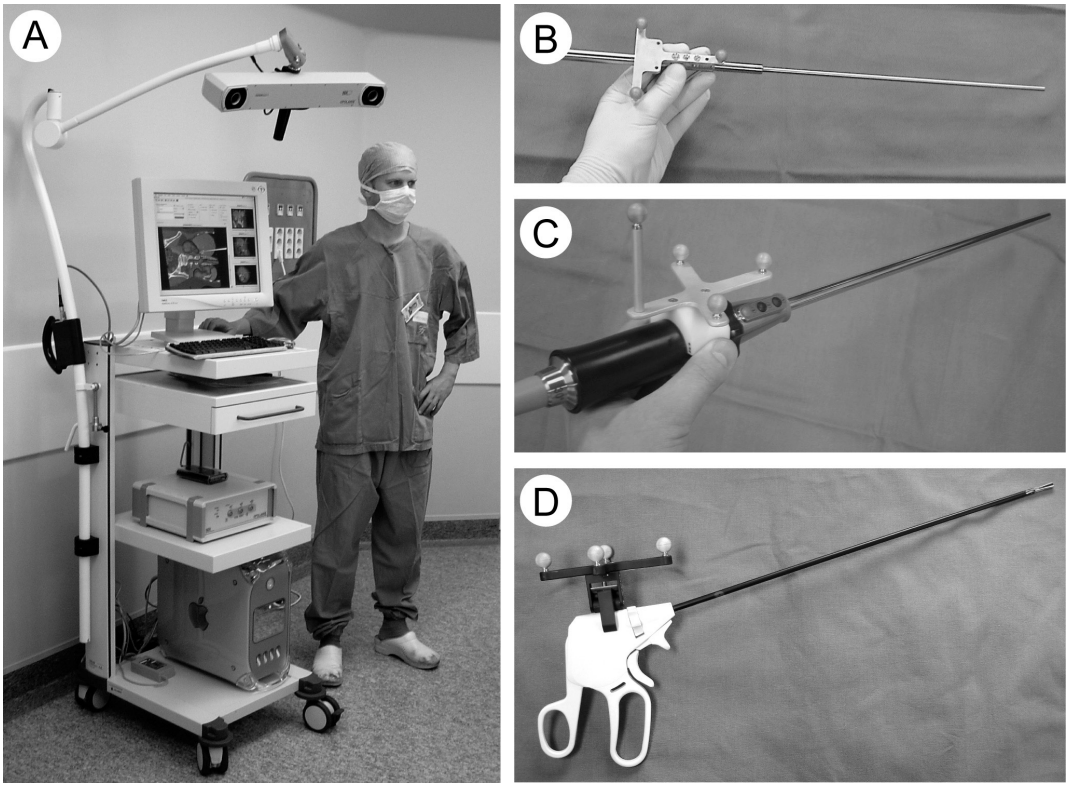

Figure 2. (A) The prototype surgical navigation system developed by our group is shown in the OR. The optical tracking cameras (Polaris Spectra, NDI, Canada) can be seen attached to the arm. (B) Laparoscopic navigation pointer. (C) Tracking on the video laparoscope. (D) Tracking on the laparoscopic grasper.

we used two 5 DoF sensors at approximately 90° angle to each other at each side of the tip of the probe (Figure 3). Having the EM sensors attached to the tip of the ultrasound probe makes it possible to obtain image positions when the probe was flexed at the tip. The LUS probe can be flexed stepwise as much as 90° in two directions.

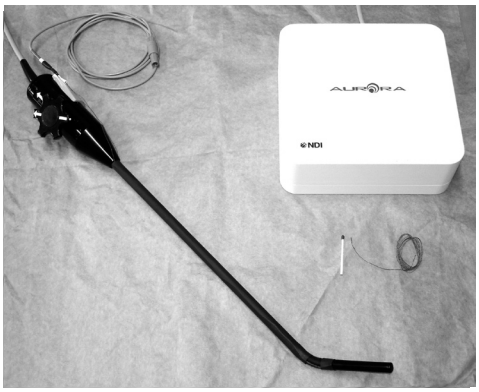

Figure 3. The LUS probe and EM tracking transmitter (Aurora, NDI Inc., Canada). One 5 DoF sensor (1.8 by 9 mm) is also shown. Two such sensors are integrated at the tip of the LUS probe, positioned at approximately 90° relative to each other to achieve proper 6 DOF tracking.

Ultrasound video image acquisition and 3D reconstruction

Ultrasound was imported in our navigation system (30) as 2D ultrasound video images (32) and the corresponding position and orientation of each image were stored. Using the ultrasound probe calibration information 2D images were reconstructed to a 3D volume. The 2D images may be reconstructed into 3D in several different ways (33). For rapid visualization, a reconstruction algorithm that adds each pixel in the input 2D images directly into the resulting 3D volume was used. This method is called Pixel Nearest Neighbor (33–36). In our system, visualization of preoperative data and intraoperative ultrasound data was performed in various ways (30).

Experiment 1 – EM tracking accuracy

Certain metallic objects inside the EM tracker field may influence the accuracy of EM tracking systems. To determine how much impact this will have in the practical operation situation, we performed both lab tests and tests in the operating room (OR). The OR setup study was performed both with and without instruments in the EM field (Figure 4). The instruments

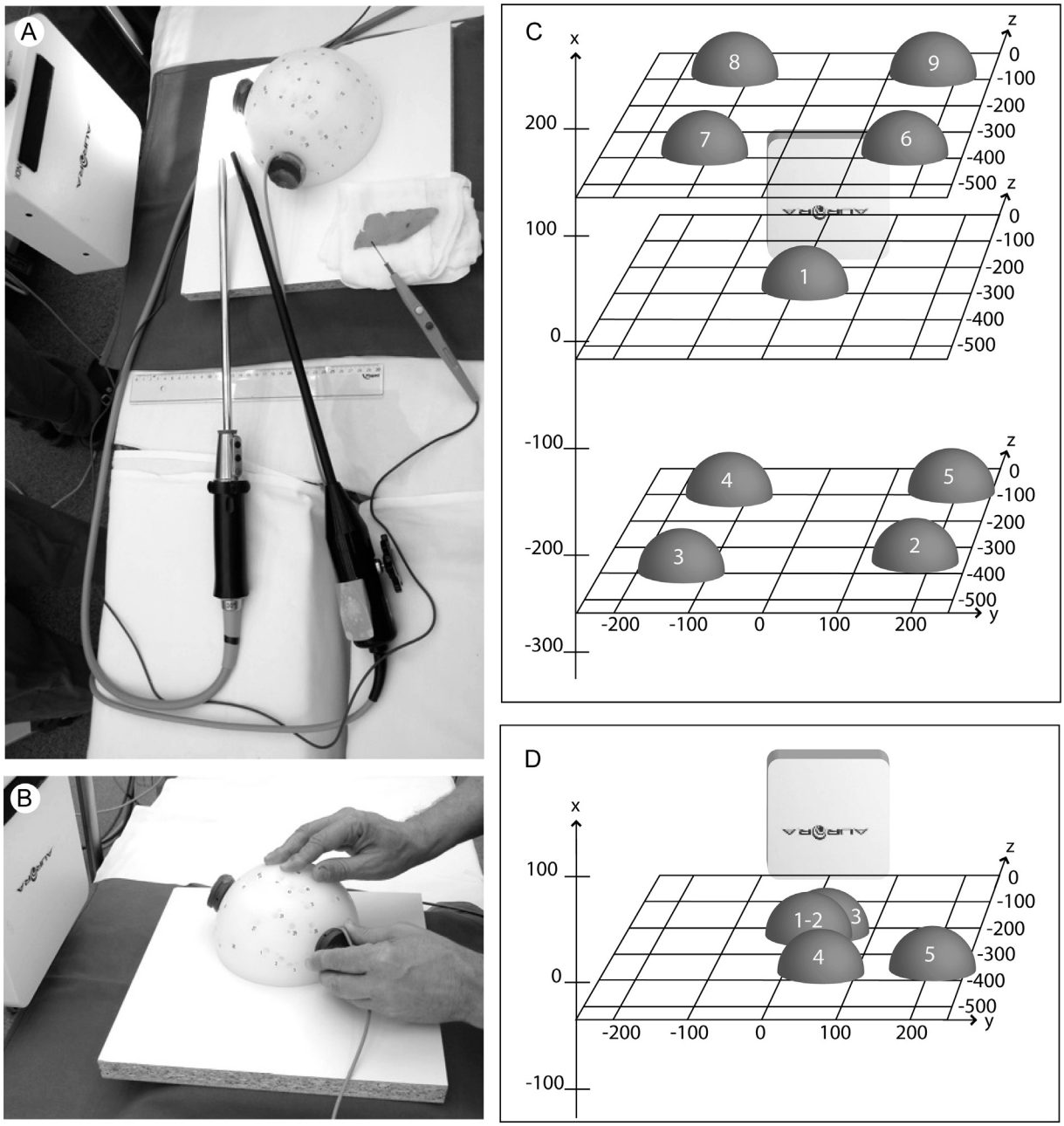

Figure 4. (A) The photo shows the setup during accuracy testing of the Aurora tracking in the operation room on a surgical table. The instruments were activated inside the tracking field during sampling of position data. The hemispheric sampling phantom and the Aurora transmitter (both NDI, Canada) can be seen. (B) The movement of the sensor from one position to the next was performed. (C)–(D) Approximate positions of the Aurora hemispheric sampling phantom used in the accuracy tests. The axes are in mm. (C) Laboratory positions. (D) Operating room positions.

used inside the tracking field in this experiment were: The laparoscopic ultrasound probe (scanning activated), a video laparoscope (switched on), and a monopolar cutter and coagulator (SurgMaster, Olympus Inc.) (Figure 4A). Cutting was performed during sampling of positions. The tests were performed with the Aurora tracking system (Figure 3, version FPG 1.1 08-16-2005, Firmware Rev 005.100, NDI, Canada). We used a hemispherical phantom containing 50 radially directed holes situated randomly about the surface (Figure 4A–B) (10). This allowed us to collect position and orientation data from the holes using a 6 DoF sensor plug (Figure 4B) that was moved from one position to the next. This procedure gave data with a uniform distribution in both rotational and translational space in relation to a reference sensor that was permanently attached to the hemisphere. The randomization of the holes prevented to some

extent the artificial systematic corrections that may occur with regular grids. The accuracy was determined from the Root Mean Square (RMS) value of the difference between the physical reference hole positions and the measured hole positions for each of the 50 holes. The angular accuracy was found by calculating the screw angle between the reference and the measured orientations. The phantom positions in the laboratory and the OR can be seen in Figure 4C–D. In the OR, the positions of the accuracy phantom were measured on the OR table (Maquet Alphastar, Getinge, Sweden), as this were the most important working positions.

Experiment 2: Accuracy of EM tracked LUS

To assess the accuracy of the reconstructed 3D ultrasound data using the EM tracked LUS probe we used an ultrasound phantom. The phantom contains two egg-shaped volumes of specified sizes with hyper-echoic surroundings and hypo-echoic interiors (Figure 5a–b, model 055, CIRS, USA). 3D freehand translation- and tilt acquisitions were performed on this phantom. Each translation data acquisition was performed by moving the probe parallel to the surface for five seconds, covering an approximate distance of 8 cm. During the tilt data acquisitions, the probe was moved approximately six seconds, covering a total angle of approximately 70°. The egg-shaped structures were segmented from the 3D volume using a 3D region growing method available in OsiriX (37), an open source radiological DICOM image processing software for Mac OSX (The software and source code is available from http://www.osirix-viewer.com). To give the segmentation algorithm smoother volumes to process, the 3D ultrasound was reconstructed by adding each input pixel to a result volume with a 3D ellipsoid truncated Gaussian weighted kernel (33,38). The

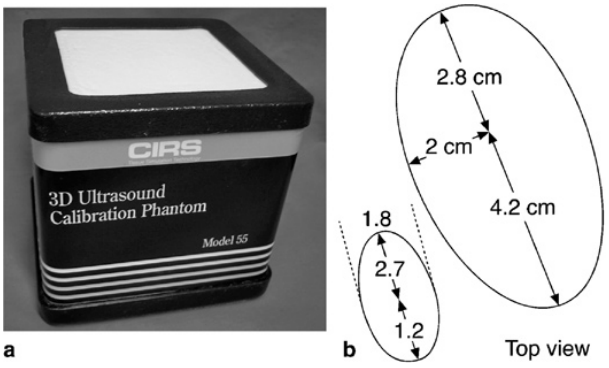

Figure 5. Ultrasound calibration evaluation phantom. (a) Phantom with ultrasound scanning window on top. (b) Specification of the phantom structures in one plane.

Figure 6. The multimodal abdominal phantom (CIRS Inc., USA), with fiducial markers, used in this experiment.

volume of the egg-shaped structure was then calculated and compared with the phantom specifications.

Experiment 3 – Multivolume visualization

The phantom used in this experiment was a multimodality (ultrasound, MR, CT compatible) interventional 3D abdominal phantom (Figure 6, CIRS Inc., USA). The laparoscopic ultrasound probe, with integrated EM tracking, was moved in a translational or tilt movement across the surface of the phantom to acquire a 3D ultrasound volume. We also scanned the abdominal multimodal phantom with CT. Both ultrasound and CT data were reconstructed into 3D volumes. Skin fiducials, donut-shaped markers (15 mm diameter, 3 mm thick, 4 mm hole) filled with CT contrast fluid, were glued to the phantom prior to scanning. These markers were used to register the 3D CT data to the physical phantom. No registration was needed for the 3D ultrasound data because the data was acquired in the same coordinate system as it was displayed. 3D ultrasound was displayed together with the 3D CT data. Various display modalities such as slicing, orthogonal slicing and volume rendering were tested in order to achieve experience on how intraoperative 2D and 3D ultrasound could be used in navigated laparoscopic surgery. In addition we have developed a novel multivolume display module with opacity and color transfer functions. Real-time multivolume 3D rendering was performed using the Graphical Processing Unit (GPU), and was implemented as 2D texture rendering of the volumes. For correct multivolume display, sorting of all 2D textures was performed. Both the texture sorting and the utilization of the opacity and color transfer function were performed on the GPU.

Experiment 4: Liver model with optically tracked LUS

A model to illustrate the use of ultrasound-based navigation for targeting a tumor-mimicking structure was created. The model was designed using a pulsating organ perfusion trainer (POP trainer, OPTIMIST, Austria) and a calf liver with a foam sphere (Oasis®) inserted between two of the liver lobes. The sphere Oasis® was soaked in CT contrast fluid before it was placed inside the liver. The entire model was then scanned with DynaCT (Siemens, Germany). Since CT imaging did not include the entire POP trainer, fiducial markers were placed directly on the liver for registration purposes. For visualization purposes, an additional CT scan without fiducial markers was also acquired without any movement of the liver between the two scans. The model was moved from the angiography lab with the C-arm into the laparoscopic OR to perform the navigation experiment. On the OR table, a pointer was used to mark the fiducials on the liver in physical space (Figure 7A). These positions were matched to the corresponding image positions to obtain an image-to-model registration of the CT data (Figure 7B–C). After the registration we changed to the CT image without the fiducial markers for a better visualization.

The optical positioning sensor was attached on the shaft of the laparoscopic ultrasound probe. The probe was fixed in one side looker position (Figure 1C) using heat-shrinkable tubing. The probe was calibrated so that the position of the ultrasound image could be measured using the positions of the optical position sensor on the shaft. This was done to allow optical tracking of all instruments; laparoscopic pointer, grasper, ultrasound probe, radio frequency ablation (RFA) probe, and video laparoscope. The liver was then scanned with the laparoscopic ultrasound probe and the 3D ultrasound volume was reconstructed. The 3D CT data was visualized together with real-time 2D ultrasound and reconstructed 3D ultrasound volumes in a 3D scene. A laparoscopic grasper and the radio frequency ablation probe were tracked and used to steer the display of data during the model experiment. The tracking of the ultrasound probe also allowed the use of the ultrasound probe to steer the display. Figure 8A–B shows the experimental setup during CT scanning of the phantom and during demonstration of navigated LUS. The flow of data is illustrated in Figure 8C.

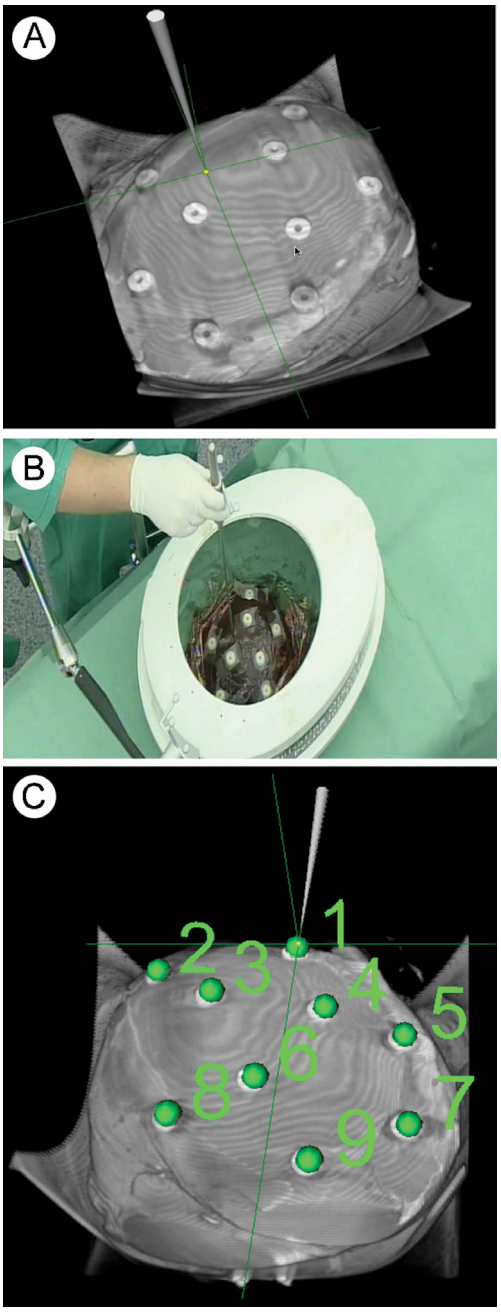

Figure 7. The registration of CT images (volume) to the model in the laparoscopic OR. (A) Navigation display with pointer visible. (B) Picture of the registration process. (C) Registration with a tracked pointer and image fiducials marked with green to aid physical space pinpointing of fiducials. The accuracy is calculated as a mean error difference based on the image points and the corresponding physical points.

Results

Experiment 1: EM tracking accuracy

The results of the measurements from the laboratory and from the OR are presented in Tables II and III. The numbers presented in the Tables are RMS and max error values calculated after registration as described in the *Material and methods* section.

It can be seen that the error is larger overall on the OR table than in the laboratory setup. The measurements also indicate that the surgical

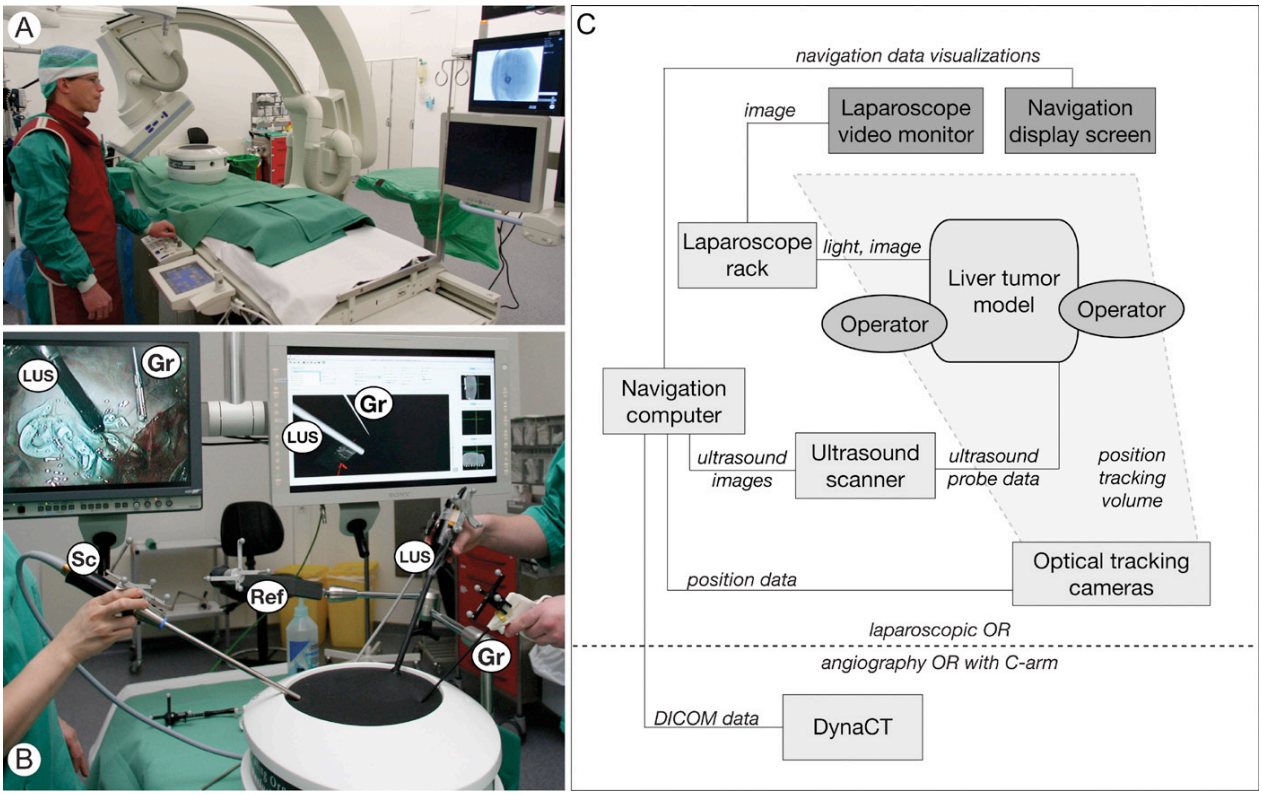

Figure 8. (A) Image shows the DynaCT scan of the phantom prior to the navigation setup. (B) Navigation setup with tracked tools and visualization screens in front of the operators. The tracked tools are: Laparoscopic ultrasound probe (LUS), grasper (Gr), phantom reference frame (Ref), and video laparoscope (Sc). The LUS and grasper tool can be seen in both the laparoscope video view and the navigation display. (C) The diagram shows an overview of the model setup and the flow of the most important data.

instruments do not influence the error significantly in the OR, when the signals are already distorted by the OR setup. Sources of disturbance are most likely the OR table, monitors, and power sources near the EM field.

The RMS distance error in the center of the measurement volume of the tracking system increased from 0.3 mm in the laboratory setup to 2.3 mm in the OR setup, and the accuracy near the edges of the measurement volume decreased much faster in the OR setup.

Experiment 2: Accuracy of EM tracked LUS

The flexible probe tracked with EM sensors seems to be accurate for this setup with respect to freehand

Table II. Laboratory setup with no distortion sources: RMS error values and maximum error values for both distance and angle. The positions of the different trials are indicated in Figure 4C.

Figure 4C position	**RMS distance error (mm)**	**Max distance error (mm)**	**RMS angular error (deg)**	**Max angular error (deg)**	**Comment on position (as seen towards the transmitter)**
1	0.28	0.72	0.72	1.33	Middle of measurement volume
2	0.83	2.51	0.77	1.40	Lower quadrant, far right
3	1.35	4.63	0.74	1.41	Lower quadrant, far left
4	0.36	0.92	0.65	1.56	Lower quadrant, close to transmitter, left side
5	0.38	0.91	0.73	1.81	Lower quadrant, close to transmitter, right side
6	0.65	1.60	0.69	1.28	Upper quadrant, far right
7	0.73	1.94	0.72	1.24	Upper quadrant, far left
8	0.33	0.59	0.70	1.49	Upper quadrant, close to transmitter, left side
9	0.40	1.00	0.64	1.21	Upper quadrant, close to transmitter, right side
Mean value ± STD	**0.56 ±0.35**	**1.65 ±1.28**	**0.71 ±0.04**	**1.41 ±0.19**	

Table III. Laparoscopic operating room setup: RMS error values and maximum error values for both distance and angle. The positions of the different trials are indicated in Figure 4D.

Figure 4 Dposition	RMS distance error (mm)	Max distance error (mm)	RMS angular error (deg)	Max angular error (deg)	Comment on position (as seen towards the transmitter) and surgical instruments
1	2.30	5.14	1.60	3.48	Middle of measurement volume with no surgical tools
2	2.29	5.04	1.60	3.17	Middle of measurement volume, with surgical tools inside measurement volume
3	1.78	4.14	1.18	2.36	Between center of measurement volume and limit of volume, with surgical tools
4	9.65	26.86	26.09	177.57	Edge of volume, with no surgical tools
5	7.09	14.53	3.79	6.44	Edge of volume, with no surgical tools
Mean value ± STD	**4.62 ±3.55**	**11.14 ±9.76**	**6.85 ±10.80**	**38.61 ±77.70**	

3D ultrasound acquisition. The 3D accuracy phantom calculations are summarized in Table IV.

It can be seen from the table that two of the tilt acquisitions resulted in a lower volume than the true volume, while all the translation scans yielded slightly higher values for the volume compared to the phantom vendor values. The average value for the tilt scans differs by only 1.6% from the specification of the phantom; while the average value from the translation scans differs by 3.6%.

Experiment 3: Multivolume visualization

Ultrasound was visualized on the navigation monitor in combination with CT data as shown in Figure 9. We experienced that displaying ultrasound together with CT data made it easier to obtain an overview, understand orientation, and interpret the 3D ultrasound data. We displayed a real-time 2D ultrasound image that was correctly oriented inside the volume rendering of the CT image (Figure 9A). Such a view made it easier to interpret the real-time 2D ultrasound image and could provide the surgeon with an indication of any anatomical shift that possibly occurred since the preoperative data acquisition and registration. A possible shift is also easy to detect in the view shown in Figure 9B. This is an anyplane view, i.e. the planes are the real-time 2D ultrasound image and the corresponding 2D slice from the 3D CT volume, picked by the position and orientation of the LUS probe. The multivolume display is a novel approach to visualize several volumes from different modalities in one display window. It is necessary to consider the color tables and transfer function settings (threshold) carefully to obtain a proper visualization where the volumes overlap, as shown in Figure 9C. Further demonstrations of multivolume visualization are shown in Experiment 4 for the liver model setup.

Anyplane view from a 3D ultrasound volume allows the user to view planes not obtainable (reachable) by scanning, i.e. it is not possible to physically position the probe to obtain certain 2D image planes. An example of three orthogonal planes from the 3D LUS scan of the phantom is shown in Figure 9D–F.

Table IV. 3D ultrasound volume calculations compared to the phantom specifications.

Acquisition	***Volume v (cm^3)***
Translation 1	6.91
Translation 2	6.96
Translation 3	6.97
Tilt 1	6.80
Tilt 2	6.42
Tilt 3	6.57
Mean translation value ± STD	6.94±0.03
Mean tilt value ± STD	6.60±0.19
Total mean value ± STD	6.77±0.23
Phantom egg volume specification	**6.70**

Experiment 4: Liver model with optically tracked LUS

The registration error from the model setup was 0.7 mm. This is much less than movements caused by scanning with the LUS probe and movements from active use of the grasper and RFA probe during the experiment. These movements could be directly observed in the real-time ultrasound image during use of the instruments. Nevertheless, we assume that similar registration accuracy could have been achieved with the fiducials on the outside of the POP trainer.

The LUS probe and grasper tool can be seen in both the laparoscope video view and the navigation display in the experimental setup (Figure 10). Both

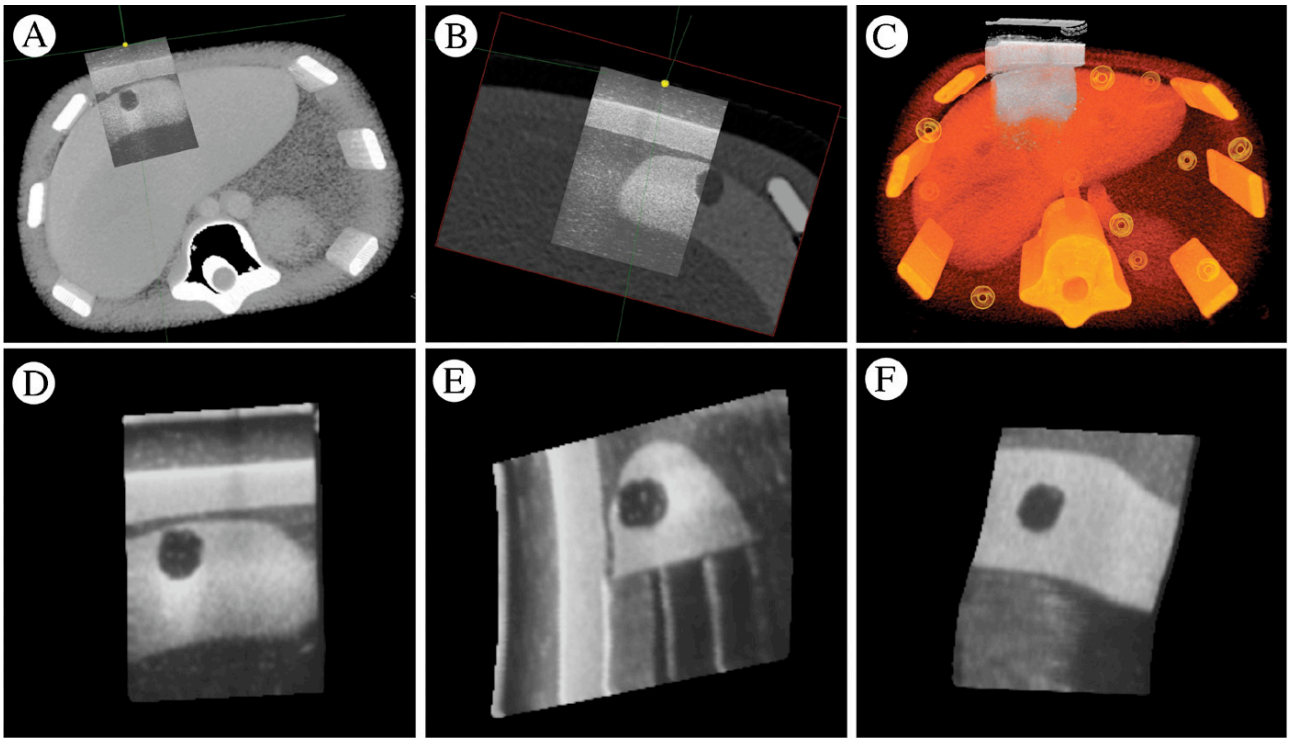

Figure 9. (A) 2D real-time ultrasound image, acquired from the tracked LUS probe, inside a 3D volume rendering of a CT volume of an abdominal phantom. (B) 2D real-time ultrasound image superimposed on a corresponding anyplane, i.e. reformatted, from the CT volume. (C) Multivolume display with 3D ultrasound in grey scale and 3D CT in color. A low level threshold has been applied to the volumes. The solid bars holding the phantom together and the fiducials attached to the phantom can be seen. (D)–(F) Orthogonal slices from the 3D LUS scan, reconstructed with a 3D ellipsoid truncated Gaussian weighted kernel. The image in (F) is not possible to obtain by scanning only with a real-time 2D LUS probe.

were shown in the same view direction as in physical space seen from the operator of the video laparoscope. This was obtained by setting the view direction with the direction-of-view of the tracked video laparoscope, including the 30° angle at the tip. To the operator holding the camera, this view is natural and corresponds well with physical space. The scene view setting could also be changed successfully by manual rotation and zooming of the navigation display. Figure 10 shows various visualizations from the model tumor setup; combining navigated 2D ultrasound with registered preoperative CT images and tool tracking with navigation.

We found that the navigation display allowed easier targeting of surgical tools to specific positions, such as the positioning of the RFA probe into the center of the Oasis® foam tumor model. The ultrasound provided a real-time image allowing detection of shifts in the CT data such that the RFA probe could be correctly positioned. The CT data and the segmented tumor (red in Figure 11) were used as spatial cues and overview during guiding. The experiment also showed that it was possible to navigate the RFA probe into the tumor model in the liver by using only the 2D/3D ultrasound without the preoperative data available. In addition, the combination of 2D/3D ultrasound and an endoscope allowed us to display updated intra-operative imaging of structures hidden by organs in the endoscopic view. Further, the ability to change view direction makes it more efficient to target the tumor and set the direction for a surgical tool prior to insertion. This is shown in Figure 11A–B, where the scene is set approximately from the shaft of the active tool (RFA probe).

After the RFA probe was inserted into the tumor, real-time 2D ultrasound images were successfully used to verify the position. CT slices provided an overview of the situation, while the combination of a semi-transparent segmented tumor together with real-time navigated ultrasound images presented the user with sufficient information to ensure proper placement of the RFA needle. Together with the verification of this procedure, this allowed the user to document the actual location of the RFA probe just prior to ablation.

Using multivolume visualization, i.e. rendering both the 3D ultrasound and 3D CT volumes simultaneously (Figure 12A–B), we were able to show the offset or anatomic shift in two directions directly in the navigation display (Figure 12B). In addition, Figure 12B demonstrates cut-plane functionality,

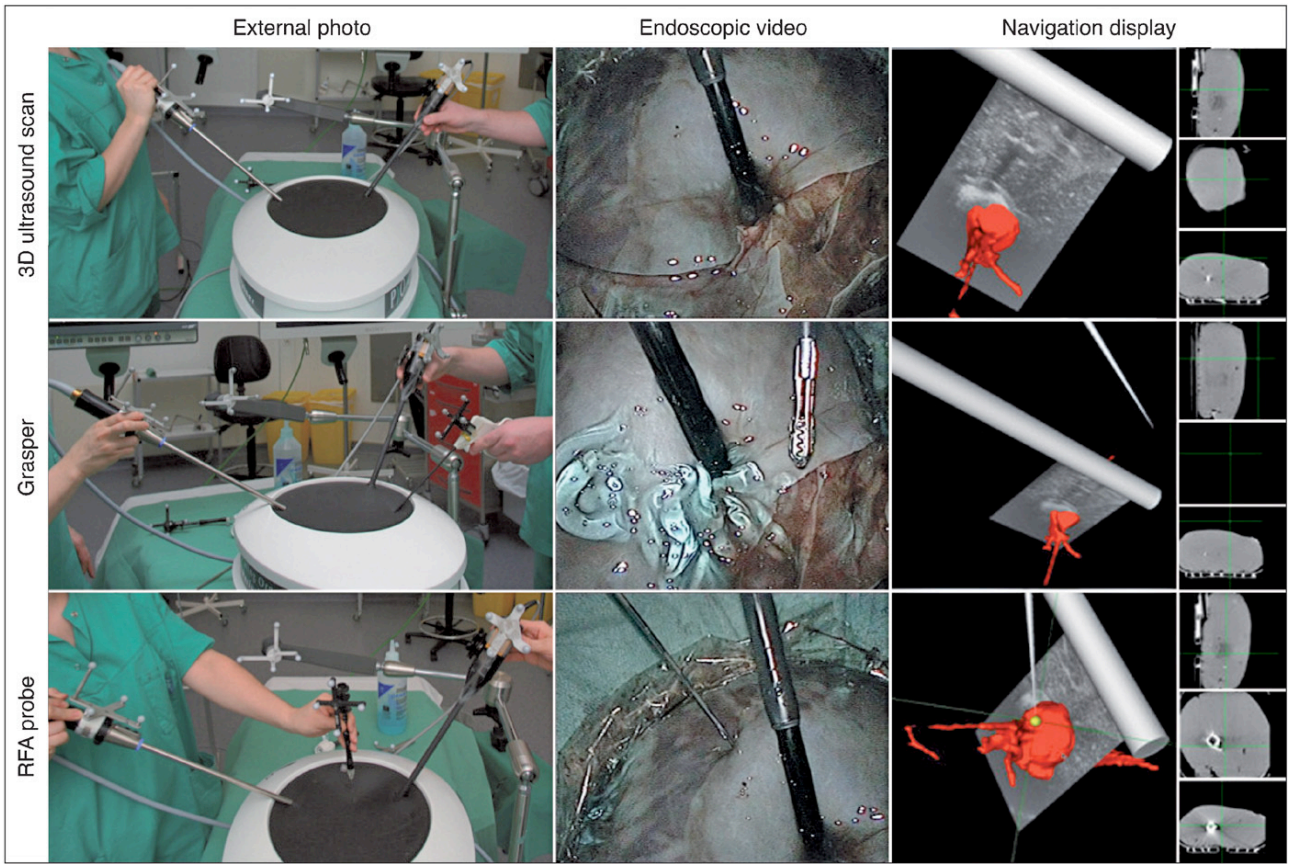

Figure 10. Corresponding images of the surgeon's view, laparoscopic video image, and navigation scene display. The segmented tumor from CT can be seen in red color. The navigation display may be oriented as needed for optimal visualization and is not restricted by the orientation of the endoscopy camera.

which proved to be useful in visualization of multi-volume data. With this functionality, a part of the volume was cut away, determined by the view direction and an offset value or by the real-time ultrasound image plane (LUS probe cut-plane). By adjusting the offset, it was possible to interactively cut away portions of the volumes between the observer and the cut-plane to allow for easy inspection and comparison of preoperative and intraoperative data during the procedure. The LUS probe pressure on the liver (Figure 12C) shifted the liver lobe and caused an anatomical shift in the tumor model position seen in Figure 12B. This may also be the case in a true clinical situation.

Discussion and further developments

In the present study we have demonstrated solutions for how 2D and 3D ultrasound can be integrated with navigation technologies to improve laparoscopic surgery. Combined LUS imaging and navigation enhanced the interpretation of ultrasound by improving orientation and image display user friendliness. Ultrasound without navigation is becoming standard in laparoscopic surgery for the liver (39–41). The reasons are numerous. The probes are small and can be manipulated with great flexibility, allowing real-time images at user-controlled orientations and positions, depending only on the specific probe configuration (see Figure 1). The ultrasound systems are inexpensive, compact, mobile, and have no requirements for special facilities for use in the OR. Ultrasound image quality has also improved in recent years and has in some applications shown to be comparable even to MR (42). In addition, introduction of ultrasound contrast agents and new processing techniques will add new possibilities due to improved image quality and structure detection. The real-time imaging capabilities of ultrasound to a large extent outweigh the deficiencies and ultrasound has therefore been used for years to guide interventions in breast (43,44), prostate (45,46), liver (47,48), and brain (49–51).

Navigated laparoscopic ultrasound

Integration of ultrasound with navigation technology has been shown to solve the orientation problems and

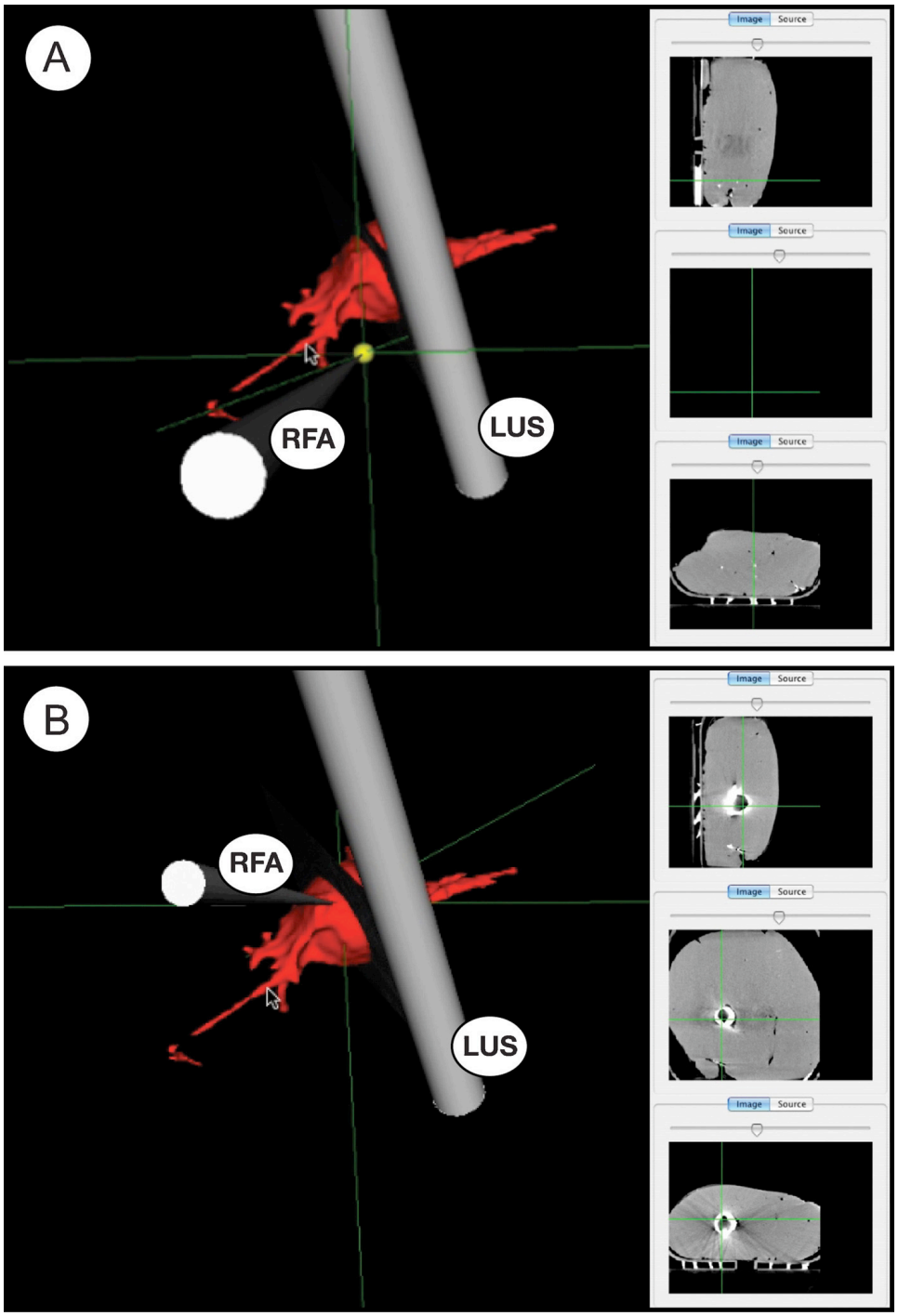

Figure 11. Navigation view set from the shaft of the RFA probe (RFA) for easier targeting of the tumor (red). The RFA probe (RFA) and the laparoscopic ultrasound probe (LUS) are indicated in the figure. The axial, sagittal, and coronal views also help to show more details on the direction of insertion, while the 3D visualization give a total overview. (A) Situation prior to insertion into the tumor. The RFA probe tip (yellow ball) can be seen outside the tumor, and the RFA probe is pointing in approximately the correct direction. (B) The RFA probe tip is now inside the tumor.

makes it possible to show real-time 2D ultrasound images in their correct orientation relative to the patient and to the MR/CT data and the surgeon's view (42,52–54). The orientation problem is even more challenging in laparoscopic surgery if the video laparoscope provides an image from a different angle than the ultrasound probe, neither of them necessarily viewing the patient at the same angle as the operator. Using navigation technology as demonstrated in the present study makes it possible to display the

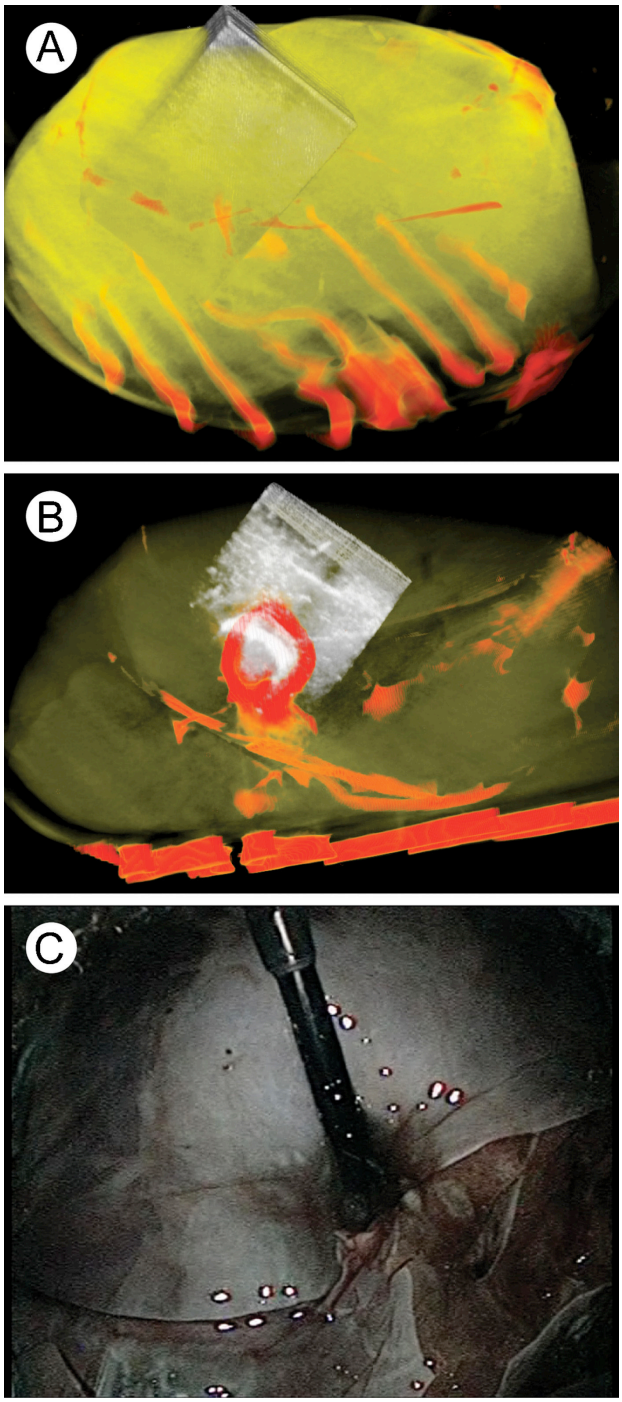

Figure 12. Multivolume visualizations of the 3D LUS and 3D DynaCT acquisition for the liver model setup. These images were created after the registration procedure was performed (Figure 7). (A) Visualization with semi-transparency of the CT data allows seeing the ultrasound volume orientation inside the CT volume. The dark red parts are parts of the POP Trainer box in the CT data. (B) A threshold (dynamic transfer function) has been applied in this cut-plane visualization through the middle of the model tumor in the liver. (C) The endoscopic view of the 3D LUS scan of the tumor model. The LUS probe pressure results in an anatomic shift as seen in (B).

ultrasound data from various directions independently of the ultrasound acquisition direction, which may be important for interpretation of essential structures and lesions. In addition, 3D ultrasound integrated with preoperative CT improved the orientation problem and understanding of the LUS images in correspondence with surrounding anatomy. We also experienced that image fusion techniques further made it easier to perceive the integration of two or more volumes in the same display (monitor) than mentally fusing the same volumes presented in their own separate displays. Both a non-linear opacity and a non-linear color transfer function were applied to the CT volume to enhance the visualization of the liver in a phantom and to better display the ultrasound volume. Ideally, relevant information should not only include anatomical structures for reference and pathological structures to be targeted (CT/MRI and US tissue), but also important structures to be avoided, like blood vessels (CT/MR contrast, ultrasound Doppler). We believe that this feature will be important when visualizing intraoperative ultrasound data together with preoperative CT data from a patient during surgery. The ultrasound data will show updated information that the surgeon relies on during surgery, while the advantages from CT, such as better overview and understanding of the anatomy and pathology, are displayed. Nevertheless, this type of multivolume visualization demands fast rendering algorithms, e.g. using graphics processing unit (GPU) hardware as demonstrated here. Such methods are becoming more available as GPU application interfaces are being developed and tested on various brands of GPU and platforms.

A laparoscopic surgeon performs the operation based on the endoscope view. This camera image must be related to all other radiological images during surgery. A technique that might become popular is "virtual endoscopy" 55 or image-enhanced endoscopy. This approach uses computer graphics to simulate the view seen by a navigated endoscope inside a body cavity, based on a representation of the cavity rendered from navigated preoperative MRI, CT or intraoperative ultrasound images. We believe that merging the endoscope image seen in minimally invasive surgery with the corresponding computer-generated surface from preoperative and intraoperative images might be a useful feature during minimally invasive therapy (30). Such a view may help the surgeons to quickly interpret important information beyond the surface of the organs seen in the conventional video laparoscope, without having to look at different displays.

Another challenge using navigation based on images in laparoscopic surgery is shifting anatomy.

The most important approach to solve the problem of shifting anatomy due to surgical manipulations is direct navigated surgery based on intraoperative ultrasound imaging, which is becoming routine in some neurosurgical departments (42,49,56). Another approach is also to correct preoperative data by using intraoperative ultrasound by shifting (57) or morphing (58) of preoperative images. In laparoscopy, we have experienced that as long as the lesion is located in the retroperitoneum, most changes in anatomy in this area probably are small and may be compensated for by using 3D ultrasound to acquire updated images.

Accuracy of navigated laparoscopic ultrasound

In the present study we have demonstrated the use of 3D ultrasound integrated with navigation technology. However, the accuracy of navigation based on 3D ultrasound is important if the technology should represent an improvement of instruments used in existing laparoscopic procedures. Many parameters may affect the accuracy of navigated laparoscopic ultrasound. Except for movement of organs, the most important factors influencing the accuracy may be the nature of the tracking system (electromagnetic or optical are the most common) and ultrasound probe calibration (31). As expected, our results showed that the error in position measurements with EM tracking in the operating room (OR) is generally higher than in the laboratory setup. This is probably due to the increased EM noise in the OR environment, particularly the OR table itself. However, introducing laparoscopic instruments close to the position sensor did not seem to affect the accuracy significantly. As expected, when the position sensors were moved toward the edges of the tracker volume, the accuracy seemed to drop faster in the OR setup compared to the laboratory setup. The reason for this is probably that an EM noisy environment will effectively reduce the optimal tracking volume. Hastenteufel et al. (22) have shown that 2D ultrasound probes do not affect EM tracking system accuracy significantly compared to the more complex 3D ultrasound probes when using the Flock of Birds tracking system. However, they found that the 2D probes significantly affected the Aurora tracking system accuracy. This is most likely due to the fact that Aurora is based on alternating current (AC) technology and Flock of Birds uses pulsed direct current (DC) technology, so they will have different advantages and drawbacks when used in various environments. Schicho et al. (20) also showed that a 2D ultrasound probe affects EM tracking accuracy in an ideal setup where the ultrasound probe is the only distortion factor. However, error values reported by the other groups are approximately what we found in the OR setup. Most probably, the error introduced by the 2D LUS probe did not add further distortion to the measurement than the contribution from the OR table and surrounding error sources in our setup. The largest distortion factor in our OR setup was probably the OR table, being quite close to the Aurora transmitter and sensor. Our OR setup error values are of the same magnitude as that published by other groups (13,17,23). We sampled position data with the LUS probe active and close to the accuracy phantom, but not completely comparable to the setup by Hastenteufel et al. (22). Although other equipment in the operating room may affect EM positioning systems, the accuracy of navigated 3D ultrasound using EM tracking seems sufficient to be exploited further in laparoscopy. The necessary accuracy may vary for different tasks, but the achieved accuracy seems to be within an acceptable range to be used for guidance of most laparoscopic procedures, given that the surgeon is made aware of the possible inaccuracy. However, in high precision tasks, a higher accuracy will be needed and only endoscopy and real-time 2D ultrasound may be accurate enough. Flexible instruments in general should be tracked by EM miniature sensors at the tip of the instruments and not on the shaft to fully take advantage of the flexibility of the instrument. Another important factor affecting the accuracy in navigated LUS is probe calibration. Incorrect probe calibration implies that an image point will be displaced from its "true" position in the navigation system. If the probe is shifted/rotated, the same shift/rotation occurs to the displacement. Probe calibration may be related to various error sources (59) and is perhaps the largest source of error in 3D freehand ultrasound acquisitions as shown previously (60). Additional sources of error that may explain the results found in Table IV are (60): Sensor attachment repeatability (only for optical system), position sensor tracking, synchronization between position data and ultrasound images, sound speed and thickness of the ultrasound plane. In addition, the segmentation method used in the OsiriX software is based on a semi-automatic algorithm where user-specified values will affect the result. Contrast differences in the ultrasound scans make it hard to achieve equal segmentation results for all the acquisitions.

The delicacy, precision, and extent of the work the surgeon can perform based on image information rely on his/her confidence in the overall clinical accuracy and the anatomical or pathological representation. The overall clinical accuracy in image-guided surgery is the difference between where a surgical tool is

located relative to some structure as indicated in the image information presented to the surgeon, and where the tool is actually located relative to the same structure in the patient. This accuracy is difficult to assess in a clinical setting, due to the lack of fixed and well-defined landmarks inside the patient that can be reached accurately by a pointer. Common practice is therefore to estimate the system's overall accuracy in a controlled laboratory setting using precisely built phantoms. In order to conclude on the potential clinical accuracy, the differences between the clinical and the laboratory settings must be carefully examined. We have previously done this for ultrasound-based navigation in neurosurgery (60). It is crucial that the users of image-based navigation systems are aware of the potential error sources and limitations in accuracy, e.g. expected accuracy and maximum differences in real position of instrument tip versus navigation displayed position.

The safety of the navigation system is affected by several factors as mentioned. The user is presented by the registration accuracy prior to surgery, showing the match between preoperative images and the patient. This value will provide an indication of error when using the preoperative images for guidance. However, this error will most likely increase during surgery due to shifting anatomy. Using multimodal imaging to show possible anatomy shifts will help in this aspect. Also, the endoscopy camera together with real-time 2D ultrasound shows the true situation. At any time during surgery a real-time 2D ultrasound slice may be acquired and placed together with the existing data to verify the system accuracy. We believe that using intraoperative imaging thus increases the safety of minimal access procedures.

Conclusions

In this paper we have described a solution for integration of intraoperative laparoscopic ultrasound and navigation technology for guidance of laparoscopic procedures. Using phantoms and liver models, we found that electromagnetic tracking of the ultrasound probe made it possible to fully use the flex functionality of the probe as well as to perform navigational guidance of laparoscopic procedures by 2D and 3D ultrasound within an acceptable range of accuracy in the operating room. Exploration of multivolume display of CT and 2D and 3D ultrasound in the navigation system made it easier to interpret ultrasound images and solved the orientation problem that sometimes may be severe during conventional laparoscopic ultrasound imaging. Future solutions may be to integrate the endoscope view with intraoperative ultrasound so that image-guided surgery on moving organs might be easier and safer than using existing technologies.

Acknowledgement

This work was supported by SINTEF, the Research Council of Norway through the FIFOS Programme Project 152831/530, and the Ministry of Health and Social Affairs of Norway through the National Centre of 3D Ultrasound in Surgery (Trondheim, Norway). Furthermore, we wish to thank the following people for helpful discussions, collaboration, and help in the experiments: Scientists Arild Wollf, Steinar Ommedal, Frank Lindseth, Cecilie Våpenstad, Tormod Selbekk, and Lisa Nilsson.

References

1. Fukuda M, Mima F, Nakano Y. Studies in echolaparoscopy. Scan J Gastroenterol. 1982;17:186.
2. Jakimowicz JJ. Intraoperative ultrasonography in open and laparoscopic abdominal surgery: an overview. Surg Endosc. 2006;20:S425–35.
3. Berber E, Siperstein AE. Laparoscopic Ultrasound. Surg Clin North Am. 2004;84:1061–84.
4. Patel AC, Arregui ME. Current Status of Laparoscopic Ultrasound. Surg Technol Int. 2006;15:23–31.
5. Catheline JM, Turner R, Champault G. Laparoscopic ultrasound of the liver. Eur J Ultrasound 2000;12:169–77.
6. Ganguli S, Kruskal JB, Brennan DD, Kane RA. Intraoperative laparoscopic ultrasound. Radiol Clin North Am. 2006;44:925–35.
7. Brennan DD, Kruskal JB, Kane RA. Intraoperative ultrasound of the pancreas. Ultrasound Clinics 2006;1:533–45.
8. Machi J. Intraoperative and laparoscopic ultrasound. Surg Oncol Clin N Am. 1999;8:205–26.
9. Cinquin P, Bainville E, Barbe C, et al. Computer assisted medical interventions. IEEE Eng Med Biol Magazine 1995;142:54–63.
10. Frantz DD, Wiles AD, Leis SE, Kirsch SR. Accuracy assessment protocols for electromagnetic tracking systems. Phys Med Biol. 2003;48:2241–51.
11. Chassat F, Lavallée S. Experimental protocol for accuracy evaluation of 6-D localizers for computer-integrated surgery: Application to four optical localizers. MICCAI 1998, Cambridge, USA, Springer, Lecture Notes in Computer Science 1998;1496:277–84.
12. Schmerber S, Chassat F. Accuracy evaluation of a CAS system: laboratory protocol and results with 6D localizers, and clinical experiences in otorhinolaryngology. Comput Aided Surg. 2001;6:1–13.
13. Nafis C, Jensen V, von Jako R. Method for evaluating compatibility of commercial electromagnetic (EM) micro sensor tracking systems with surgical and imaging tables. in Medical Imaging 2008: Visualization, Image-guided Procedures, and Modeling. 2008. San Diego, CA, USA: SPIE.

14. Nafis C, Jensen V, Beauregard L, Anderson P. Method for estimating dynamic EM tracking accuracy of surgical navigation tools. in Medical Imaging 2006: Visualization, Image-Guided Procedures, and Display. 2006. San Diego, CA, USA: SPIE.
15. Schneider M, Stevens C. Development and testing of a new magnetic-tracking device for image guidance. in Medical Imaging 2007: Visualization and Image-Guided Procedures. 2007. San Diego, CA, USA: SPIE.
16. Hummel JB, Bax MR, Figl ML, et al. Design and application of an assessment protocol for electromagnetic tracking systems.Med Phys. 2005;32:2371–9.
17. Kirsch SR, Schilling C, Brunner G. Assesment of metallic distortions of an electromagnetic tracking system. in Medical Imaging 2006: Visualization, Image-Guided Procedures, and Display. 2006. San Diego, CA, USA: SPIE.
18. Birkfellner W, Watzinger F, Wanschitz F, et al. Systematic distortions in magnetic position digitizers. Med Phys. 1998;25:2242–8.
19. Hummel J, Figl M, Kollmann C, et al. Evaluation of a miniature electromagnetic position tracker. Med Phys. 2002;29:2205–12.
20. Schicho K, Figl M, Donat M, et al. Stability of miniature electromagnetic tracking systems. Phys Med Biol. 2005;50:2089–98.
21. King DL. Errors as a result of metal in the near environment when using an electromagnetic locator with freehand three-dimensional echocardiography. Journal of the American Society of Echocardiography 2002;15:731–5.
22. Hastenteufel M, Vetter M, Meinzer HP, Wolf I. Effect of 3d ultrasound probes on the accuracy of electromagnetic tracking systems. Ultrasound Med Biol. 2006;32:1359–68.
23. Wilson E, Yaniv Z, Zhang H, et al. A hardware and software protocol for the evaluation of electromagnetic tracker accuracy in the clinical environment: a multi-center study. in Medical Imaging 2007: Visualization and Image-Guided Procedures. 2007. San Diego, CA, USA: SPIE.
24. Light ED, Idriss SF, Sullivan KF, et al. Real-time 3D laparoscopic ultrasonography. Ultrason Imaging. 2005;27:129–44.
25. Wilhelm D, Feussner H, Schneider A, Harms J. Electromagnetically navigated laparoscopic ultrasound. Surg Technol Int. 2003;11:50–4.
26. Harms J, Feussner H, Baumgartner M, et al. Three-dimensional navigated laparoscopic ultrasonography. Surg Endosc. 2001;15:1459–62.
27. Ellsmere J, Stoll J, Wells W, et al. A new visualization technique for laparoscopic ultrasonography. Surgery 2004;136:84–92.
28. Kleemann M, Hildebrand P, Birth M, Bruch HP. Laparoscopic ultrasound navigation in liver surgery: technical aspects and accuracy. Surg Endosc. 2006;20:726–9.
29. Birth M, Kleemann M, Hildebrand P, Bruch HP. Intraoperative online navigation of dissection of the hepatical tissue—a new dimension in liver surgery? in CARS 2004 – Computer Assisted Radiology and Surgery 2004.
30. Langø T, Tangen G, Mårvik R, et al. Navigation in laparoscopy – Prototype research platform for improved image-guided surgery.Minim Invasive Ther Allied Technol (MITAT). 2008;17:17–33.
31. Lindseth F, Tangen GA, Langø T, Bang J. Probe calibration for freehand 3-D ultrasound. Ultrasound Med Biol. 2003;29:1607–23.
32. Solberg OV, Tangen G-A, Lindseth F, et al. Integration of a real-time video grabber component with the open source image-guided surgery toolkit IGSTK. in Medical Imaging 2008: PACS and Imaging Informatics. 2008. San Diego, CA, USA: SPIE.
33. Solberg OV, Lindseth F, Torp H, et al. Freehand 3D Ultrasound Reconstruction Algorithms–A Review. Ultrasound in Medicine & Biology. 2007;33:991–1009.
34. Hottier F, Billon AC, eds. 3D echography: status and perspective.3D Imaging in Medicine, ed. Hohne KH, Fuchs H, and Pizer SM. Vol. F 60. 1990, Springer-Verlag Berlin Heidelberg. 21–41.
35. Nelson TR, Pretorius DH. Interactive acquisition, analysis, and visualization of sonographic volume data.Int J Imag Systems Technol. 1997;8:26–37.
36. Rohling R, Gee A, Berman L. A comparison of freehand three-dimensional ultrasound reconstruction techniques. Med Image Anal. 1999;3:339–59.
37. Rosset A, Spadola L, Ratib O. OsiriX: An Open-Source Software for Navigating in Multidimensional DICOM Images. J Digital Imaging 2004;17:205–16.
38. Ohbuchi R, Chen D, Fuchs H. Incremental volume reconstruction and rendering for 3-D ultrasound imaging. in Visualization in Biomedical Computing '92. 1992. Chapel Hill, NC, USA: SPIE.
39. Ozsunar Y, Skjoldbye B, Court-Payen M, et al. Impact of intraoperative ultrasonography on surgical treatment of liver tumours. Acta Surg Endosc. 2000;14:675–9.
40. Sjølie E, Langø T, Ystgaard B, et al. 3-D ultrasound-based navigation for radio frequency thermal ablation in treatment of liver malignancies. Surg Endosc. 2002;17:933–8.
41. Cervone A, Sardi A, Conaway GL. Intraoperative ultrasound (IOUS) is essential in the management of metastatic colorectal liver lesions. Am Surg. 2000;66:611–5.
42. Unsgaard G, Gronningsaeter A, Ommedal S, Hernes TAN. Brain operations guided by real time 2D ultrasound New possibilities due to improved image quality. Neurosurgery. 2002;51:402–12.
43. Sato Y, Nakamoto M, Tamaki Y, et al. Image guidance of breast cancer surgery using 3-D ultrasound images and augmented reality visualizations. IEEE Trans Med Imaging. 1998;17:681–93.
44. Davis PL, Staiger MJ, Harris KB, et al. Breast cancer measurements with magnetic resonance imaging, ultrasonography, and mammography. Breast Cancer Res Treat. 1996;37:1–9.
45. Tong S, Downey DB, Cardinal HN, Fenster A. A three-dimensional ultrasound prostate imaging system.Ultrasound Med Biol. 1996;22:735–46.
46. Downey DB, Fenster A. Three-dimensional power Doppler detection of prostatic cancer letter.American Journal of Roentgenology 1995;165:741.
47. Bao P, Warmath J, Galloway R, Jr., Herline A. Ultrasound-to-computer-tomography registration for image-guided laparoscopic liver surgery. Surg Endosc. 2005;19:424–9.
48. Giorgio A, Tarantino L, Mariniello N, et al. Pyogenic liver abscesses: 13 years of experience in percutaneous needle aspiration with US guidance. Radiology 1995;195:122–4.
49. Gronningsaeter A, Kleven A, Ommedal S, et al. SonoWand, An ultrasound-based neuronavigation system.Neurosurgery 2000;47:1373–80.
50. Koivukangas J, Louhisalmi Y, Alakuijala J, Oikarinen J. Ultrasound-controlled neuronavigator-guided brain surgery. J Neurosurg. 1993;79:36–42.
51. Auer LM, Velthoven V. Intraoperative ultrasound imaging in neurosurgery: Comparison with CT and MRI. 1990, New York: Springer Verlag.
52. Ellsmere J, Stoll J, Rattner D, et al. A navigation system for augmenting laparoscopic ultrasound. Lecture Notes in Computer Science 2003;2879:184–91.

53. Konishi K, Makato H, Masahiko N, et al. Augumented reality navigation system for endoscopic surgery based on three-dimensional ultrasound and computed tomography: Application to 20 clinical cases. in CARS 2005 – Computer Assisted Radiology and Surgery. 2005.
54. Estépar RSJ, Stylopoulus N, Ellis R, et al. Towards scarless surgery: An endoscipic ultrasound navigation system for transgastric access procedures. Computer Aided Surgery 2007;123:11–24.
55. Shahidi R, Bax MR, Maurer CR, et al. Implementation, Calibration and Accuracy Testing of an Image Enhanced Endoscopy System. IEEE Trans Med Imaging 2002;21: 1524–35.
56. Unsgaard G, Rygh OM, Selbekk T, et al. Intra-operative 3D ultrasound in neurosurgery. Acta Neurochirurgica 2006;148:235–53.
57. Reinertsen I, Lindseth F, Unsgaard G, Collins DL. Clinical validation of vessel-based registration for correction of brain-shift. Med Image Analysis 2007;11:673–84.
58. Bucholz RD, Yeh DD, Trobaugh J, et al. The correction of stereotactic inaccuracy caused by brain shift using an intraoperative ultrasound device. in Lecture Notes in Computer Science Proceedings of the 1st Joint Conference on Computer Vision, Virtual Reality, and Robotics in Medicine and Medical Robotics and Computer Assisted Surgery (CVRMed MRCAS'97). 1997. Grenoble.
59. Mercier L, Langø T, Lindseth F, Collins LD. A review of calibration techniques for freehand 3D ultrasound systems. J Ultrasound Med Biol. 2005;31:449–71.
60. Lindseth F, Langø T, Bang J, Hernes TAN. Accuracy evaluation of a 3D ultrasound-based neuronavigation system. Comp Aid Surg. 2002;7:197–222.

Paper V

Integration of a real-time video grabber component with the open source image-guided surgery toolkit IGSTK

Ole Vegard Solberg*[a,b], Geir-Arne Tangen[a], Frank Lindseth[a], Torleif Sandnes[a], Andinet A. Enquobahrie[c], Luis Ibáñez[c], Patrick Cheng[d], David Gobbi[e,f], Kevin Cleary[d]

[a]SINTEF Health Research, Medical Technology and the National Center for 3D Ultrasound in Surgery, Trondheim, Norway;
[b]Norwegian University of Science and Technology (NTNU), Faculty of Medicine; Department of Circulation and Medical Imaging, Trondheim, Norway;
[c]Kitware Inc., New York, NY, USA;
[d]Imaging Science and Information Systems (ISIS) Center, Department of Radiology, Washington, DC, USA;
[e]Atamai Inc., London, Ontario, Canada;
[f]School of Computing, Queen's University, Kingston, Ontario, Canada

ABSTRACT

The image-guided surgery toolkit (IGSTK) is an open source C++ library that provides the basic components required for developing image-guided surgery applications. While the initial version of the toolkit has been released, some additional functionalities are required for certain applications. With increasing demand for real-time intraoperative image data in image-guided surgery systems, we are adding a video grabber component to IGSTK to access intraoperative imaging data such as video streams. Intraoperative data could be acquired from real-time imaging modalities such as ultrasound or endoscopic cameras. The acquired image could be displayed as a single slice in a 2D window or integrated in a 3D scene. For accurate display of the intraoperative image relative to the patient's preoperative image, proper interaction and synchronization with IGSTK's tracker and other components is necessary. Several issues must be considered during the design phase: 1) Functions of the video grabber component 2) Interaction of the video grabber component with existing and future IGSTK components; and 3) Layout of the state machine in the video grabber component. This paper describes the video grabber component design and presents example applications using the video grabber component.

Keywords: image-guided surgery, intraoperative imaging, open source software, ultrasound, video import

1. INTRODUCTION

For the benefit of the patient, systems for image-guided minimal invasive surgery and therapy are increasingly being used to safely navigate surgical instruments inside the human body. For visual feedback to the clinician, a graphical representation of the surgical tool is overlaid medical images (CT, MR, ultrasound, etc.) in much the same way as modern GPS systems overlaying a vehicle location onto a road map. It is therefore paramount that the medical images show an accurate picture of the current patient anatomy. Ideally, this would be based on an intraoperative real-time 3D image map considering influences such as respiration, pulsation, and surgical manipulation, which change the shape or location of anatomical structures during the procedure.

* Ole.V.Solberg (at) sintef.no; Telephone: +47 98245191; Fax: +47 93070800

Medical Imaging 2008: PACS and Imaging Informatics, edited by Katherine P. Andriole, Khan M. Siddiqui,
Proc. of SPIE Vol. 6919, 69190Z, (2008) · 1605-7422/08/$18 · doi: 10.1117/12.772491

The basic building blocks of a surgical navigation system are a computer, a tracking system, software, and optionally a medical imaging device that can generate real-time images. While tracking systems typically provide an application programming interface (API) for communication with the device, almost no real-time medical imaging devices offer something similar (i.e. an API for streaming the images from the device that generated them into the navigation computer). To provide the functionality needed for real-world clinical procedures the navigation software can become fairly complex. At the same time mission-critical applications like surgical navigation must be safe, robust, and accurate. Unfortunately, many resources within the IGS field are wasted in "reinventing the wheel" (e.g. code for interfacing with tracking hardware) instead of focusing on new research efforts. The open source image-guided surgery toolkit (IGSTK) attempts to address these issues by providing the basic functionalities needed for a navigation system. However, currently IGSTK does not have a component for streaming real-time image data into the system, and the paper presented describes an effort to add support for this feature.

1.1 IGSTK overview

IGSTK is an open source C++ library for building image-guided surgery applications [1][2][3][4]. The toolkit is developed with support from the National Institute of Biomedical Imaging and Bioengineering (NIBIB) at the National Institute of Health (NIH). Both industrial and academic partners have contributed to the development of the toolkit. The toolkit aims at providing basic components required to develop image-guided surgery applications. The initial version of the toolkit was released in February 2006 at the SPIE Medical Imaging conference at San Diego. Since then applications built using the toolkit have been demonstrated at various scientific conferences (SPIE 2006, 2007 and SMIT 2007). Furthermore, an FDA approved single center clinical trial for electromagnetically tracked lung biopsy application developed using IGSTK has begun at Georgetown University Medical Center.

IGSTK follows a component-based architecture [1]. Each component has a well-defined set of behaviors governed by a state machine. Given that the implementation methods are correctly followed, the state machine will ensure that each component is always in a deterministic state and all state transitions are valid and meaningful. State machines were included as an integral part of the toolkit design with the purpose of producing a safe and reliable software library suitable for safety critical applications.

Key components in IGSTK are *views*, *spatial object representations*, *spatial objects*, and *a tracker component* [1]. View objects render virtual representations of physical objects on the computer display. Spatial Object Representations are visual representations of Spatial Objects, which in turn are geometrical representations of physical objects in the surgical field. A pulse generator drives the update of the view, which sends requests to the tracker tool to get its latest spatial position (through the representation and spatial object). This ensures the accurate rendering of the surgical scene. Events are used for communications between different components. Response to a service request is usually in some form of event with or without data payload.

1.2 Real-time image acquisition overview

Previous versions of IGSTK only supported preoperative data. The new video grabber component will allow importing intraoperative video stream into IGSTK. To develop a video component, we chose to include support for analog video first, since there is no digital video standard that is supported across a broad range of medical devices. This video stream may consist of 2D ultrasound data or other video sources such as endoscopy video. Imported 2D ultrasound may be presented relative to other imaging modalities, such as preoperative CT or MR, or be processed further into 3D ultrasound [5]. The processing and presentation of the imported video is naturally dependent on the other IGSTK components. The video grabber component is one of several important steps towards making IGSTK a complete toolkit for image-guided surgery.

The focus of the IGSTK video grabber component is the capture of an analog 2D real-time video stream, which is only one of many possible real-time imaging modalities. Figure 1 gives an overview of the IGSTK video grabber in relation to the other modalities. The digital branch will mostly consist of Software Development Kits (SDK) made for specific ultrasound scanners. These SDKs may provide either scan converted images or raw ultrasound data (radio frequency data).

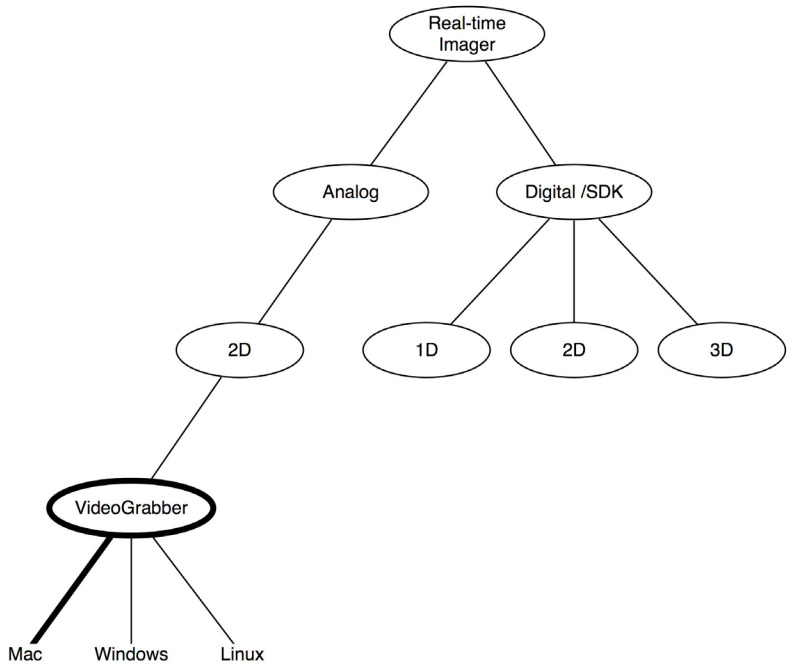

Fig. 1. Real-time imaging overview

2. VIDEO GRABBER COMPONENT

Currently the video grabber component is being developed by SINTEF, a Norwegian research foundation, in cooperation with the IGSTK development team. The IGSTK development process is based on an agile methodology [1]. For this component, we first brainstormed a list of requirements and made an initial design document. These were posted on a Wiki page and discussed both on the Wiki page and at bi-weekly teleconferences.

2.1 Requirements

The new video grabber component is based on the following list of requirements:

- Import real-time video without noticeable delay.
- Synchronization with other IGSTK components.
- Support cross platform development for portability
- Ensure operability with hardware used by IGSTK partners.
- Grab video stream and single image.
- Handle multiple input streams.
- Support different video input standards and output formats.
- Support buffering of video streams for subsequent processing (ultrasound 3D reconstruction etc.)

2.2 Design

During the design phase, the interaction of the video grabber component with existing and future IGSTK components was streamlined (Figure 2). The next step was designing a framework for the component based on the IGSTK state machine [1]. Figure 3 shows an illustration of the video grabber the state machine.

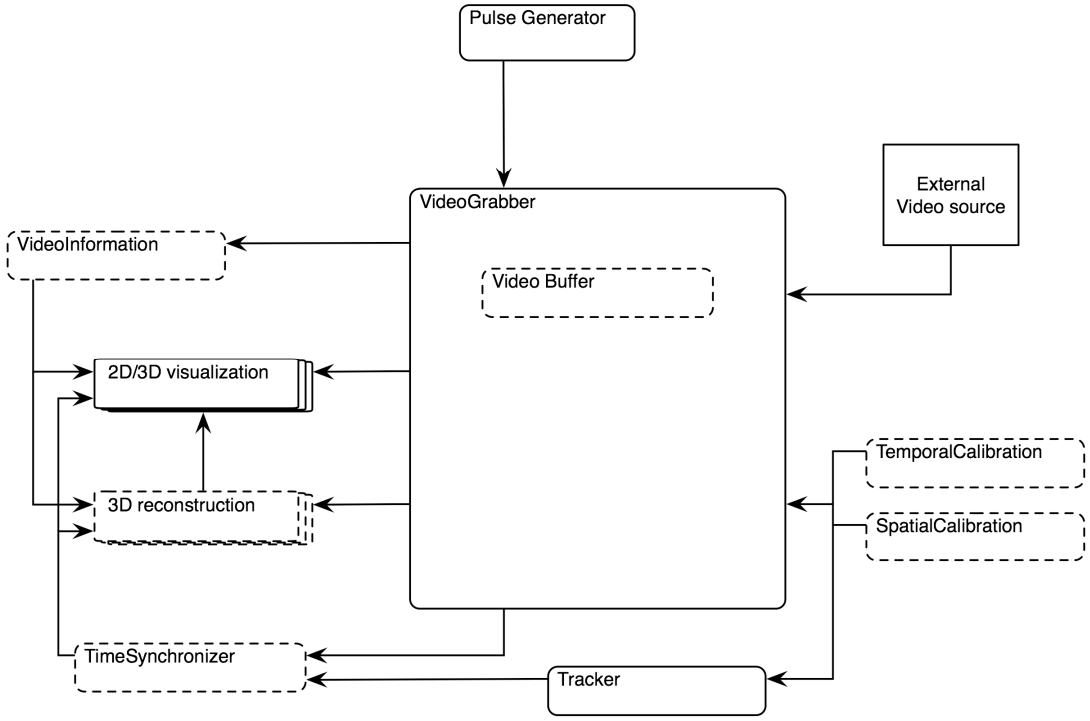

Fig. 2. Interaction between the video grabber component and existing and future IGSTK components. Future components are shown with dashed lines. The 2D/3D visualization consists of several components, where some are implemented and some are pending.

2.3 Implementation

As illustrated in Figure 1, platform specific classes of the video grabber components have to be implemented. Implementation starts with laying out the state machine that governs the functions of the video grabber component. State machines can help ensure that components are always in a known configuration. State machines contain a set of states, state inputs, and state transitions. IGSTK provides an *igstk::StateMachine* class that offers a set of public methods for programming, executing, and querying state machine logic. Figures 3 show the state machine diagrams for the *VideoGrabber* class. The class contains the following major states:

- *Idle* : Initial state.
- *GrabberReady* : Grabber ready to use.
- *GrabberActive* : Grabber activated. Allows *RequestGrabOneFrame()* calls.
- *Grabbing* : Grabbing video either to buffer, texture or both. A separate thread handles the updates.

In addition to these major states, transitional states exist that the grabber waits in until the requests are accomplished successfully. For example, the grabber makes a transition to *AttemptingToInitializeState* when a *RequestOpen()* method is invoked. Instead of *Set…()* methods that set parameters directly, the video grabber has *RequestSet…()* methods with a corresponding *AttemptingToSet…State* that can verify that the input value of the parameter is valid.

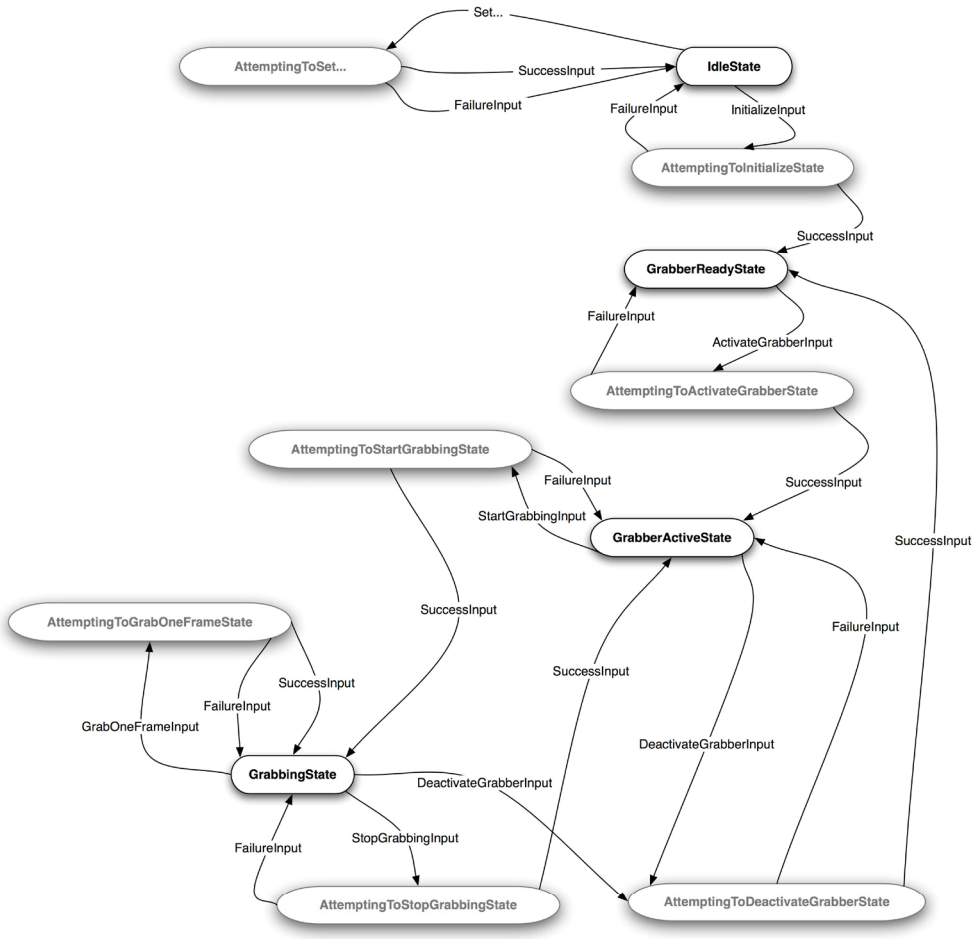

Fig. 3. VideoGrabber state machine.

2.4 Results

A first version of the video grabber component was implemented using the QuickTime framework. This code is available as open source (a Berkley Software Distribution-like license) in the IGSTK sandbox along with an example application. The QuickTime code is based on a video grabber implementation from CustusX [6], a research and development platform for image-guided surgery. The first version of the IGSTK video grabber was only implemented for Macintosh OS X.

2.5 Future work

The current implementation of the video grabber uses a deprecated branch of the QuickTime framework in an attempt to provide functionality on both Windows and OS X. However this approach seems to produce some problems, as some of the deprecated code no longer functions correctly on the new Intel Macintosh computers, so a future version might have to use the newer OS X specific functions in Core Video and Core Image. A Windows implementation will probably have to rely on DirectX, while a Linux implementation may need to use Video4Linux.

In order to be integrated into the main IGSTK branch the video grabber component should have various tests to ensure that the code performs as expected. The grabbed video may have a small delay, and this delay is not the same as the delay of the tracking system. In order to get the correct image at the correct position a temporal calibration [7] is needed

between the tracking and the grabbed video (as illustrated in figure 2). This is especially important for 3D ultrasound volume reconstructions [5].

3. EXAMPLE USE

The video grabber component will allow access to real-time data in the operating room. This data could be combined with preoperative data such as CT and MR images. The first use of the video grabber component will be to import 2D ultrasound data into IGSTK. The ultrasound probe has to be calibrated first [7] to find the transfer function between the tracked frame attached to the probe and the ultrasound scan plane. During surgery, the preoperative data is first registered to the patient reference frame, and then the ultrasound is imported into the same coordinate system. The ultrasound data may then be presented in different ways:

- A 2D presentation in a 2D view.
- A 2D presentation in a 3D view as shown in Figures 5 and 6.
- As a 3D reconstructed ultrasound volume.

All presentations could be combined with preoperative data in several possible ways. An example is a 2D slice through a reconstructed 3D ultrasound volume following a surgical tool, combined with a 3D preoperative volume. This allows the use of the most recent data during surgery while still showing the preoperative data. To allow for optimal use of the imported data, both a 3D ultrasound reconstruction and several visualization modes probably should be implemented. Both volume rendering and multiple volume visualization are modes that may enhance the user interface in addition to the 2D visualization modes that exist in IGSTK today.

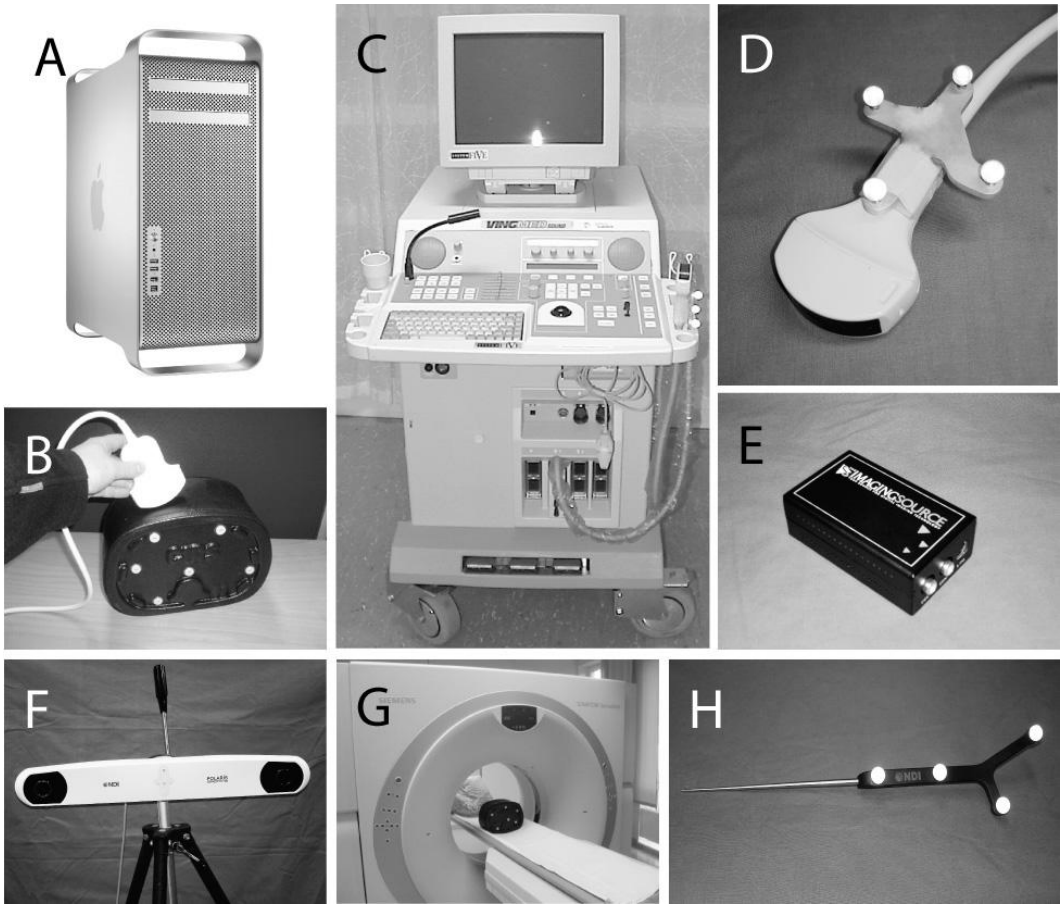

Fig. 4. Hardware used: a) Macintosh, b) abdominal phantom with skin fiducials, c) System FiVe ultrasound machine, d) ultrasound Curved Linear Array probe with optical tracking frame, e) Video-to-FireWire converter, f) Polaris Spectra optical tracking camera, g) CT scanner with abdominal phantom, h) pointer with optical tracking spheres

3.1 Simple example

A simple example application was completed and submitted to the IGSTK sandbox. The IGSTK sandbox is a testing environment for newly implemented code that is not stable enough to be integrated into the main IGSTK branch [2]. The example code contains simple implementations of a spatial object and a representation object, both needed for visualization with IGSTK. This software is currently only running on the OS X operating system on a Macintosh computer (Macintosh, Apple, USA) (Figure 4a). The testing was performed on an abdominal phantom (Model 57, CIRS Inc., USA) (Figure 4b). Ultrasound video was obtained from a System FiVe ultrasound machine (GE Vingmed Ultrasound, Norway) (Figure 4c) with a Curved Linear Array probe with center frequency 3.5 MHz (Figure 4d). The video from the ultrasound scanner was converted by a Video-to-FireWire converter (DFG/1394-1e, The Imaging Source, Germany) (Figure 4e). Positions were acquired with an optical position tracker (Polaris Spectra, Northern Digital Inc., Canada) (Figure 4f). The optical position tracking device attached to the ultrasound probe comprises of 4 reflecting spheres (Figure 4d).

The example application is able to track the movement of an ultrasound probe and import and visualize the ultrasound image and position in real-time in a 3D scene (Figure 5).

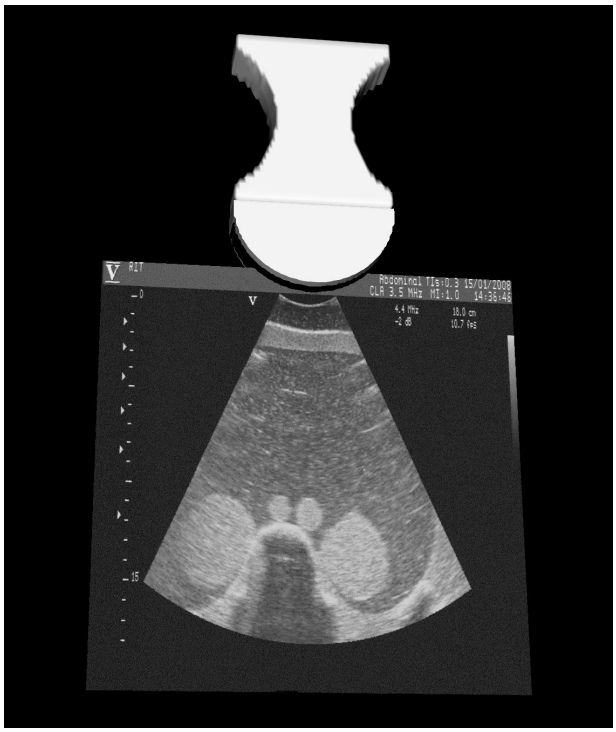

Fig. 5. Image from the example application showing a tracked ultrasound probe with the grabbed image in an otherwise empty 3D scene.

3.2 Real world application.

An extended application simulating real-life use was also completed. This extended application uses the same setup as the previous example, but with a few additions. The IGSTK Video grabber is integrated into a new version of CustusX [6] (SINTEF, Norway), a research and development platform for image-guided Surgery. This new CustusX version is based partly on IGSTK. All the software ran on a desktop computer (Macintosh, Apple, USA). Preoperative data was acquired by scanning the phantom with a CT scanner (Sensation 64, Siemens, Germany) (Figure 4g). Skin fiducials, donut-shaped markers (15 mm diameter, 3mm thick, 4 mm hole), were glued to the phantom prior to the CT scanning

(Figure 4b). These markers were used to register the 3D CT data to the physical phantom. The registration process was performed with a tracked pointer (Figure 4h). In addition to the CT volume, segmented objects from the CT volume were also imported into the visualization software (CustusX). The objects were segmented from the CT data with ITK Snap [8].

The real-life simulation is able to use both preoperative and intraoperative data. For this test, a CT image is used as preoperative data. This CT image is registered to the physical phantom, allowing the imported real-time ultrasound images to be positioned correctly with regard to the CT images of the phantom. This allows the use of real-time data together with preoperative data (Figure 6).

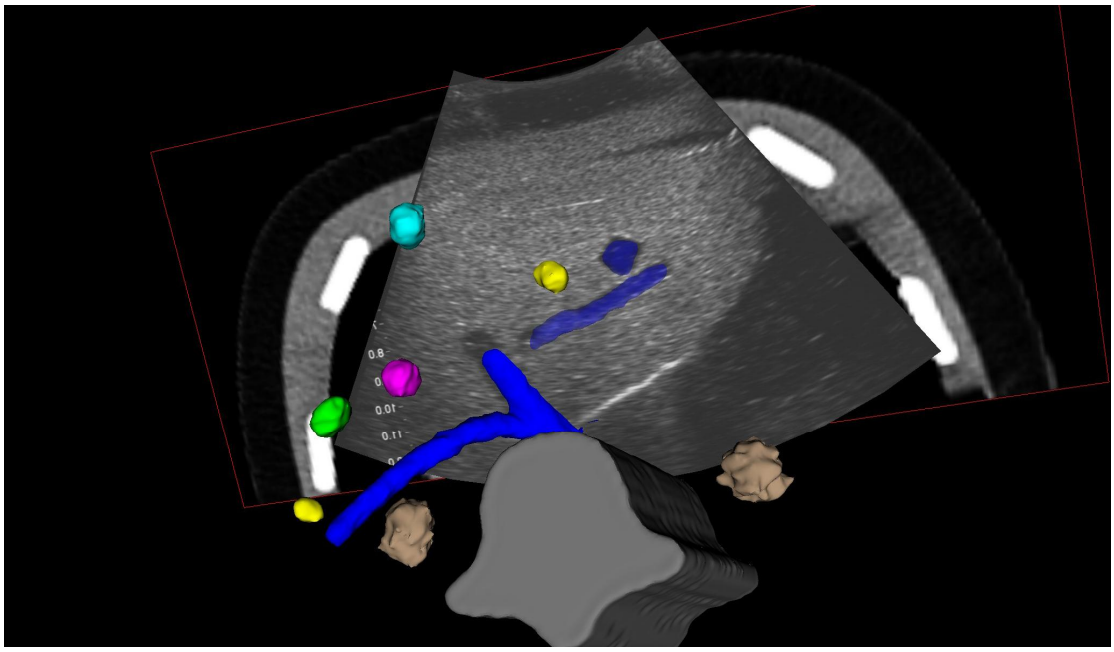

Fig. 6. Image from the real-world simulation application showing a 3D scene with 2D ultrasound, 2D CT, and 3D segmented objects from CT

4. CONCLUSIONS

It is feasible to integrate real-time data into IGSTK with the purpose of providing more relevant and updated data during surgery. IGSTK, as an open source project allows researchers to extend it as needed for additional functionality, while supplying a structure to allow for development of robust code. With continued enhancements such as the video component described here, IGSTK may be a suitable toolkit for fast prototyping and development of safe and reliable image-guided surgery applications, including applications incorporating intraoperative imaging.

ACKNOWLEDGMENTS

Integrating support for real-time 2D medical image acquisition in the Image-Guided Surgery Toolkit (IGSTK) is a collaboration between SINTEF Health Research, Georgetown University, Kitware Inc., Arizona State University, and Atamai Inc. The toolkit as well as the VideoGrabber component and the simple example illustrating its use is freely available for download and can be used in research or commercial applications. More information can be found on the website at http://www.igstk.org.

The development of the VideoGrabber component is supported by the Research Council of Norway, through the FIFOS Programme Project 152831/530; the Ministry of Health and Social Affairs of Norway, through the National Centre of 3D Ultrasound in Surgery; and by SINTEF Health Research.

The Image-Guided Surgery Toolkit (IGSTK) is funded by NIBIB/NIH grant R01 EB007195 under project officer John Haller. Additional support was provided by U.S. Army grant W81XWH-04-1-007, administered by the Telemedicine and Advanced Technology Research Center (TATRC), Fort Detrick, Maryland.

We thank our other collaborators throughout the project, including Janne Beate Lervik Bakeng, and Arild Wollf from SINTEF Health Research, Medical Technology (and the National Centre for 3D Ultrasound in Surgery), Norway; Ziv Yaniv from Georgetown University, USA; Matt Turek from Kitware Inc., USA; Kevin Gary from Arizona State University, USA; and Nobuhiko Hata of Brigham and Women's Hospital, USA.

REFERENCES

[1] Cleary K. and IGSTK Team, [IGSTK: The Book, An Open Source C++ Software Library], Gaithersburg, Maryland, Signature Book Printing, (2007).

[2] Enquobahrie A., Cheng P., Gary K., Ibanez L., Gobbi D., Lindseth F., Yaniv Z., Aylward S., Jomier J., and Cleary K., "The Image-Guided Surgery Toolkit IGSTK: An Open Source C++ Software Toolkit," Journal of Digital Imaging 20(1), 21-33 (2007).

[3] Gary K., Blake M. B., Ibanez L., Gobbi D., Aylward S., and Cleary K., "IGSTK: An open source software platform for image-guided surgery," IEEE Computer 39(4), 46-53 (2006).

[4] Cheng P., Zhang H., Kim H., Gary K., Blake M. B., Gobbi D., Aylward S., Jomier J., Enquobahrie A., Avila R., Ibanez L., and Cleary K., "IGSTK: Framework and example application using an open source toolkit for image-guided surgery applications," Proc. SPIE 6141, 61411Y-61419 (2006)

[5] Solberg O. V., Lindseth F., Torp H., Blake R. E., and Hernes T. A. N., "Freehand 3D Ultrasound Reconstruction Algorithms--A Review," Ultrasound in Medicine & Biology 33(7), 991-1009 (2007).

[6] Langø T., Tangen G. A., Mårvik R., Ystgaard B., Yavuz Y., Kaspersen J. H., Solberg O. V., Hernes T. A. N., "Navigation in laparoscopy – Prototype research platform for improved image-guided surgery," In Press in Minim Invasive Ther Allied Technol (MITAT), DOI: 10.1080/13645700701797879 (2008).

[7] Mercier L., Langø T., Lindseth F., and Collins L. D., "A review of calibration techniques for freehand 3-D ultrasound systems," Ultrasound in Medicine & Biology 31(2), 143-165 (2005).

[8] Yushkevich P. A., Piven J., Hazlett H. C., Smith R. G., Ho S., Gee J. C., and Gerig G., "User-guided 3D active contour segmentation of anatomical structures: Significantly improved efficiency and reliability," NeuroImage 31(3), 1116-1128 (2006).

Dissertations at the Faculty of Medicine, NTNU

1977

1. Knut Joachim Berg: EFFECT OF ACETYLSALICYLIC ACID ON RENAL FUNCTION
2. Karl Erik Viken and Arne Ødegaard: STUDIES ON HUMAN MONOCYTES CULTURED *IN VITRO*

1978

3. Karel Bjørn Cyvin: CONGENITAL DISLOCATION OF THE HIP JOINT.
4. Alf O. Brubakk: METHODS FOR STUDYING FLOW DYNAMICS IN THE LEFT VENTRICLE AND THE AORTA IN MAN.

1979

5. Geirmund Unsgaard: CYTOSTATIC AND IMMUNOREGULATORY ABILITIES OF HUMAN BLOOD MONOCYTES CULTURED IN VITRO

1980

6. Størker Jørstad: URAEMIC TOXINS
7. Arne Olav Jenssen: SOME RHEOLOGICAL, CHEMICAL AND STRUCTURAL PROPERTIES OF MUCOID SPUTUM FROM PATIENTS WITH CHRONIC OBSTRUCTIVE BRONCHITIS

1981

8. Jens Hammerstrøm: CYTOSTATIC AND CYTOLYTIC ACTIVITY OF HUMAN MONOCYTES AND EFFUSION MACROPHAGES AGAINST TUMOR CELLS *IN VITRO*

1983

9. Tore Syversen: EFFECTS OF METHYLMERCURY ON RAT BRAIN PROTEIN.
10. Torbjørn Iversen: SQUAMOUS CELL CARCINOMA OF THE VULVA.

1984

11. Tor-Erik Widerøe: ASPECTS OF CONTINUOUS AMBULATORY PERITONEAL DIALYSIS.
12. Anton Hole: ALTERATIONS OF MONOCYTE AND LYMPHOCYTE FUNCTIONS IN REALTION TO SURGERY UNDER EPIDURAL OR GENERAL ANAESTHESIA.
13. Terje Terjesen: FRACTURE HEALING AND STRESS-PROTECTION AFTER METAL PLATE FIXATION AND EXTERNAL FIXATION.
14. Carsten Saunte: CLUSTER HEADACHE SYNDROME.
15. Inggard Lereim: TRAFFIC ACCIDENTS AND THEIR CONSEQUENCES.
16. Bjørn Magne Eggen: STUDIES IN CYTOTOXICITY IN HUMAN ADHERENT MONONUCLEAR BLOOD CELLS.
17. Trond Haug: FACTORS REGULATING BEHAVIORAL EFFECTS OG DRUGS.

1985

18. Sven Erik Gisvold: RESUSCITATION AFTER COMPLETE GLOBAL BRAIN ISCHEMIA.
19. Terje Espevik: THE CYTOSKELETON OF HUMAN MONOCYTES.
20. Lars Bevanger: STUDIES OF THE Ibc (c) PROTEIN ANTIGENS OF GROUP B STREPTOCOCCI.
21. Ole-Jan Iversen: RETROVIRUS-LIKE PARTICLES IN THE PATHOGENESIS OF PSORIASIS.
22. Lasse Eriksen: EVALUATION AND TREATMENT OF ALCOHOL DEPENDENT BEHAVIOUR.
23. Per I. Lundmo: ANDROGEN METABOLISM IN THE PROSTATE.

1986

24. Dagfinn Berntzen: ANALYSIS AND MANAGEMENT OF EXPERIMENTAL AND CLINICAL PAIN.
25. Odd Arnold Kildahl-Andersen: PRODUCTION AND CHARACTERIZATION OF MONOCYTE-DERIVED CYTOTOXIN AND ITS ROLE IN MONOCYTE-MEDIATED CYTOTOXICITY.
26. Ola Dale: VOLATILE ANAESTHETICS.

1987

27. Per Martin Kleveland: STUDIES ON GASTRIN.
28. Audun N. Øksendal: THE CALCIUM PARADOX AND THE HEART.
29. Vilhjalmur R. Finsen: HIP FRACTURES

1988

30. Rigmor Austgulen: TUMOR NECROSIS FACTOR: A MONOCYTE-DERIVED REGULATOR OF CELLULAR GROWTH.
31. Tom-Harald Edna: HEAD INJURIES ADMITTED TO HOSPITAL.
32. Joseph D. Borsi: NEW ASPECTS OF THE CLINICAL PHARMACOKINETICS OF METHOTREXATE.
33. Olav F. M. Sellevold: GLUCOCORTICOIDS IN MYOCARDIAL PROTECTION.
34. Terje Skjærpe: NONINVASIVE QUANTITATION OF GLOBAL PARAMETERS ON LEFT VENTRICULAR FUNCTION: THE SYSTOLIC PULMONARY ARTERY PRESSURE AND CARDIAC OUTPUT.
35. Eyvind Rødahl: STUDIES OF IMMUNE COMPLEXES AND RETROVIRUS-LIKE ANTIGENS IN PATIENTS WITH ANKYLOSING SPONDYLITIS.
36. Ketil Thorstensen: STUDIES ON THE MECHANISMS OF CELLULAR UPTAKE OF IRON FROM TRANSFERRIN.
37. Anna Midelfart: STUDIES OF THE MECHANISMS OF ION AND FLUID TRANSPORT IN THE BOVINE CORNEA.
38. Eirik Helseth: GROWTH AND PLASMINOGEN ACTIVATOR ACTIVITY OF HUMAN GLIOMAS AND BRAIN METASTASES - WITH SPECIAL REFERENCE TO TRANSFORMING GROWTH FACTOR BETA AND THE EPIDERMAL GROWTH FACTOR RECEPTOR.
39. Petter C. Borchgrevink: MAGNESIUM AND THE ISCHEMIC HEART.
40. Kjell-Arne Rein: THE EFFECT OF EXTRACORPOREAL CIRCULATION ON SUBCUTANEOUS TRANSCAPILLARY FLUID BALANCE.
41. Arne Kristian Sandvik: RAT GASTRIC HISTAMINE.
42. Carl Bredo Dahl: ANIMAL MODELS IN PSYCHIATRY.

1989

43. Torbjørn A. Fredriksen: CERVICOGENIC HEADACHE.
44. Rolf A. Walstad: CEFTAZIDIME.
45. Rolf Salvesen: THE PUPIL IN CLUSTER HEADACHE.
46. Nils Petter Jørgensen: DRUG EXPOSURE IN EARLY PREGNANCY.
47. Johan C. Ræder: PREMEDICATION AND GENERAL ANAESTHESIA IN OUTPATIENT GYNECOLOGICAL SURGERY.
48. M. R. Shalaby: IMMUNOREGULATORY PROPERTIES OF TNF-α AND THE RELATED CYTOKINES.
49. Anders Waage: THE COMPLEX PATTERN OF CYTOKINES IN SEPTIC SHOCK.
50. Bjarne Christian Eriksen: ELECTROSTIMULATION OF THE PELVIC FLOOR IN FEMALE URINARY INCONTINENCE.
51. Tore B. Halvorsen: PROGNOSTIC FACTORS IN COLORECTAL CANCER.

1990

52. Asbjørn Nordby: CELLULAR TOXICITY OF ROENTGEN CONTRAST MEDIA.
53. Kåre E. Tvedt: X-RAY MICROANALYSIS OF BIOLOGICAL MATERIAL.
54. Tore C. Stiles: COGNITIVE VULNERABILITY FACTORS IN THE DEVELOPMENT AND MAINTENANCE OF DEPRESSION.
55. Eva Hofsli: TUMOR NECROSIS FACTOR AND MULTIDRUG RESISTANCE.
56. Helge S. Haarstad: TROPHIC EFFECTS OF CHOLECYSTOKININ AND SECRETIN ON THE RAT PANCREAS.
57. Lars Engebretsen: TREATMENT OF ACUTE ANTERIOR CRUCIATE LIGAMENT INJURIES.
58. Tarjei Rygnestad: DELIBERATE SELF-POISONING IN TRONDHEIM.
59. Arne Z. Henriksen: STUDIES ON CONSERVED ANTIGENIC DOMAINS ON MAJOR OUTER MEMBRANE PROTEINS FROM ENTEROBACTERIA.
60. Steinar Westin: UNEMPLOYMENT AND HEALTH: Medical and social consequences of a factory closure in a ten-year controlled follow-up study.
61. Ylva Sahlin: INJURY REGISTRATION, a tool for accident preventive work.
62. Helge Bjørnstad Pettersen: BIOSYNTHESIS OF COMPLEMENT BY HUMAN ALVEOLAR MACROPHAGES WITH SPECIAL REFERENCE TO SARCOIDOSIS.
63. Berit Schei: TRAPPED IN PAINFUL LOVE.
64. Lars J. Vatten: PROSPECTIVE STUDIES OF THE RISK OF BREAST CANCER IN A COHORT OF NORWEGIAN WOMAN.

1991

65. Kåre Bergh: APPLICATIONS OF ANTI-C5a SPECIFIC MONOCLONAL ANTIBODIES FOR THE ASSESSMENT OF COMPLEMENT ACTIVATION.
66. Svein Svenningsen: THE CLINICAL SIGNIFICANCE OF INCREASED FEMORAL ANTEVERSION.
67. Olbjørn Klepp: NONSEMINOMATOUS GERM CELL TESTIS CANCER: THERAPEUTIC OUTCOME AND PROGNOSTIC FACTORS.
68. Trond Sand: THE EFFECTS OF CLICK POLARITY ON BRAINSTEM AUDITORY EVOKED POTENTIALS AMPLITUDE, DISPERSION, AND LATENCY VARIABLES.
69. Kjetil B. Åsbakk: STUDIES OF A PROTEIN FROM PSORIATIC SCALE, PSO P27, WITH RESPECT TO ITS POTENTIAL ROLE IN IMMUNE REACTIONS IN PSORIASIS.
70. Arnulf Hestnes: STUDIES ON DOWN´S SYNDROME.
71. Randi Nygaard: LONG-TERM SURVIVAL IN CHILDHOOD LEUKEMIA.
72. Bjørn Hagen: THIO-TEPA.
73. Svein Anda: EVALUATION OF THE HIP JOINT BY COMPUTED TOMOGRAMPHY AND ULTRASONOGRAPHY.

1992

74. Martin Svartberg: AN INVESTIGATION OF PROCESS AND OUTCOME OF SHORT-TERM PSYCHODYNAMIC PSYCHOTHERAPY.
75. Stig Arild Slørdahl: AORTIC REGURGITATION.
76. Harold C Sexton: STUDIES RELATING TO THE TREATMENT OF SYMPTOMATIC NON-PSYCHOTIC PATIENTS.
77. Maurice B. Vincent: VASOACTIVE PEPTIDES IN THE OCULAR/FOREHEAD AREA.
78. Terje Johannessen: CONTROLLED TRIALS IN SINGLE SUBJECTS.
79. Turid Nilsen: PYROPHOSPHATE IN HEPATOCYTE IRON METABOLISM.
80. Olav Haraldseth: NMR SPECTROSCOPY OF CEREBRAL ISCHEMIA AND REPERFUSION IN RAT.
81. Eiliv Brenna: REGULATION OF FUNCTION AND GROWTH OF THE OXYNTIC MUCOSA.

1993

82. Gunnar Bovim: CERVICOGENIC HEADACHE.
83. Jarl Arne Kahn: ASSISTED PROCREATION.
84. Bjørn Naume: IMMUNOREGULATORY EFFECTS OF CYTOKINES ON NK CELLS.
85. Rune Wiseth: AORTIC VALVE REPLACEMENT.
86. Jie Ming Shen: BLOOD FLOW VELOCITY AND RESPIRATORY STUDIES.
87. Piotr Kruszewski: SUNCT SYNDROME WITH SPECIAL REFERENCE TO THE AUTONOMIC NERVOUS SYSTEM.
88. Mette Haase Moen: ENDOMETRIOSIS.
89. Anne Vik: VASCULAR GAS EMBOLISM DURING AIR INFUSION AND AFTER DECOMPRESSION IN PIGS.
90. Lars Jacob Stovner: THE CHIARI TYPE I MALFORMATION.
91. Kjell Å. Salvesen: ROUTINE ULTRASONOGRAPHY IN UTERO AND DEVELOPMENT IN CHILDHOOD.

1994

92. Nina-Beate Liabakk: DEVELOPMENT OF IMMUNOASSAYS FOR TNF AND ITS SOLUBLE RECEPTORS.
93. Sverre Helge Torp: *erb*B ONCOGENES IN HUMAN GLIOMAS AND MENINGIOMAS.
94. Olav M. Linaker: MENTAL RETARDATION AND PSYCHIATRY. Past and present.
95. Per Oscar Feet: INCREASED ANTIDEPRESSANT AND ANTIPANIC EFFECT IN COMBINED TREATMENT WITH DIXYRAZINE AND TRICYCLIC ANTIDEPRESSANTS.
96. Stein Olav Samstad: CROSS SECTIONAL FLOW VELOCITY PROFILES FROM TWO-DIMENSIONAL DOPPLER ULTRASOUND: Studies on early mitral blood flow.
97. Bjørn Backe: STUDIES IN ANTENATAL CARE.
98. Gerd Inger Ringdal: QUALITY OF LIFE IN CANCER PATIENTS.
99. Torvid Kiserud: THE DUCTUS VENOSUS IN THE HUMAN FETUS.
100. Hans E. Fjøsne: HORMONAL REGULATION OF PROSTATIC METABOLISM.
101. Eylert Brodtkorb: CLINICAL ASPECTS OF EPILEPSY IN THE MENTALLY RETARDED.
102. Roar Juul: PEPTIDERGIC MECHANISMS IN HUMAN SUBARACHNOID HEMORRHAGE.
103. Unni Syversen: CHROMOGRANIN A. Phsysiological and Clinical Role.

1995

104. Odd Gunnar Brakstad: THERMOSTABLE NUCLEASE AND THE *nuc* GENE IN THE DIAGNOSIS OF *Staphylococcus aureus* INFECTIONS.
105. Terje Engan: NUCLEAR MAGNETIC RESONANCE (NMR) SPECTROSCOPY OF PLASMA IN MALIGNANT DISEASE.
106. Kirsten Rasmussen: VIOLENCE IN THE MENTALLY DISORDERED.
107. Finn Egil Skjeldestad: INDUCED ABORTION: Timetrends and Determinants.
108. Roar Stenseth: THORACIC EPIDURAL ANALGESIA IN AORTOCORONARY BYPASS SURGERY.
109. Arild Faxvaag: STUDIES OF IMMUNE CELL FUNCTION *in mice infected with* MURINE RETROVIRUS.

1996

110. Svend Aakhus: NONINVASIVE COMPUTERIZED ASSESSMENT OF LEFT VENTRICULAR FUNCTION AND SYSTEMIC ARTERIAL PROPERTIES. Methodology and some clinical applications.
111. Klaus-Dieter Bolz: INTRAVASCULAR ULTRASONOGRAPHY.
112. Petter Aadahl: CARDIOVASCULAR EFFECTS OF THORACIC AORTIC CROSS-CLAMPING.
113. Sigurd Steinshamn: CYTOKINE MEDIATORS DURING GRANULOCYTOPENIC INFECTIONS.
114. Hans Stifoss-Hanssen: SEEKING MEANING OR HAPPINESS?
115. Anne Kvikstad: LIFE CHANGE EVENTS AND MARITAL STATUS IN RELATION TO RISK AND PROGNOSIS OF CANCER.
116. Torbjørn Grøntvedt: TREATMENT OF ACUTE AND CHRONIC ANTERIOR CRUCIATE LIGAMENT INJURIES. A clinical and biomechanical study.
117. Sigrid Hørven Wigers: CLINICAL STUDIES OF FIBROMYALGIA WITH FOCUS ON ETIOLOGY, TREATMENT AND OUTCOME.
118. Jan Schjøtt: MYOCARDIAL PROTECTION: Functional and Metabolic Characteristics of Two Endogenous Protective Principles.
119. Marit Martinussen: STUDIES OF INTESTINAL BLOOD FLOW AND ITS RELATION TO TRANSITIONAL CIRCULATORY ADAPATION IN NEWBORN INFANTS.
120. Tomm B. Müller: MAGNETIC RESONANCE IMAGING IN FOCAL CEREBRAL ISCHEMIA.
121. Rune Haaverstad: OEDEMA FORMATION OF THE LOWER EXTREMITIES.
122. Magne Børset: THE ROLE OF CYTOKINES IN MULTIPLE MYELOMA, WITH SPECIAL REFERENCE TO HEPATOCYTE GROWTH FACTOR.
123. Geir Smedslund: A THEORETICAL AND EMPIRICAL INVESTIGATION OF SMOKING, STRESS AND DISEASE: RESULTS FROM A POPULATION SURVEY.

1997

124. Torstein Vik: GROWTH, MORBIDITY, AND PSYCHOMOTOR DEVELOPMENT IN INFANTS WHO WERE GROWTH RETARDED *IN UTERO*.
125. Siri Forsmo: ASPECTS AND CONSEQUENCES OF OPPORTUNISTIC SCREENING FOR CERVICAL CANCER. Results based on data from three Norwegian counties.
126. Jon S. Skranes: CEREBRAL MRI AND NEURODEVELOPMENTAL OUTCOME IN VERY LOW BIRTH WEIGHT (VLBW) CHILDREN. A follow-up study of a geographically based year cohort of VLBW children at ages one and six years.
127. Knut Bjørnstad: COMPUTERIZED ECHOCARDIOGRAPHY FOR EVALUTION OF CORONARY ARTERY DISEASE.
128. Grethe Elisabeth Borchgrevink: DIAGNOSIS AND TREATMENT OF WHIPLASH/NECK SPRAIN INJURIES CAUSED BY CAR ACCIDENTS.
129. Tor Elsås: NEUROPEPTIDES AND NITRIC OXIDE SYNTHASE IN OCULAR AUTONOMIC AND SENSORY NERVES.
130. Rolf W. Gråwe: EPIDEMIOLOGICAL AND NEUROPSYCHOLOGICAL PERSPECTIVES ON SCHIZOPHRENIA.
131. Tonje Strømholm: CEREBRAL HAEMODYNAMICS DURING THORACIC AORTIC CROSSCLAMPING. An experimental study in pigs.

1998

132. Martinus Bråten: STUDIES ON SOME PROBLEMS REALTED TO INTRAMEDULLARY NAILING OF FEMORAL FRACTURES.

133. Ståle Nordgård: PROLIFERATIVE ACTIVITY AND DNA CONTENT AS PROGNOSTIC INDICATORS IN ADENOID CYSTIC CARCINOMA OF THE HEAD AND NECK.
134. Egil Lien: SOLUBLE RECEPTORS FOR **TNF** AND **LPS**: RELEASE PATTERN AND POSSIBLE SIGNIFICANCE IN DISEASE.
135. Marit Bjørgaas: HYPOGLYCAEMIA IN CHILDREN WITH DIABETES MELLITUS
136. Frank Skorpen: GENETIC AND FUNCTIONAL ANALYSES OF DNA REPAIR IN HUMAN CELLS.
137. Juan A. Pareja: SUNCT SYNDROME. ON THE CLINICAL PICTURE. ITS DISTINCTION FROM OTHER, SIMILAR HEADACHES.
138. Anders Angelsen: NEUROENDOCRINE CELLS IN HUMAN PROSTATIC CARCINOMAS AND THE PROSTATIC COMPLEX OF RAT, GUINEA PIG, CAT AND DOG.
139. Fabio Antonaci: CHRONIC PAROXYSMAL HEMICRANIA AND HEMICRANIA CONTINUA: TWO DIFFERENT ENTITIES?
140. Sven M. Carlsen: ENDOCRINE AND METABOLIC EFFECTS OF METFORMIN WITH SPECIAL EMPHASIS ON CARDIOVASCULAR RISK FACTORES.

1999

141. Terje A. Murberg: DEPRESSIVE SYMPTOMS AND COPING AMONG PATIENTS WITH CONGESTIVE HEART FAILURE.
142. Harm-Gerd Karl Blaas: THE EMBRYONIC EXAMINATION. Ultrasound studies on the development of the human embryo.
143. Noèmi Becser Andersen:THE CEPHALIC SENSORY NERVES IN UNILATERAL HEADACHES. Anatomical background and neurophysiological evaluation.
144. Eli-Janne Fiskerstrand: LASER TREATMENT OF PORT WINE STAINS. A study of the efficacy and limitations of the pulsed dye laser. Clinical and morfological analyses aimed at improving the therapeutic outcome.
145. Bård Kulseng: A STUDY OF ALGINATE CAPSULE PROPERTIES AND CYTOKINES IN RELATION TO INSULIN DEPENDENT DIABETES MELLITUS.
146. Terje Haug: STRUCTURE AND REGULATION OF THE HUMAN UNG GENE ENCODING URACIL-DNA GLYCOSYLASE.
147. Heidi Brurok: MANGANESE AND THE HEART. A Magic Metal with Diagnostic and Therapeutic Possibilites.
148. Agnes Kathrine Lie: DIAGNOSIS AND PREVALENCE OF HUMAN PAPILLOMAVIRUS INFECTION IN CERVICAL INTRAEPITELIAL NEOPLASIA. Relationship to Cell Cycle Regulatory Proteins and HLA DQBI Genes.
149. Ronald Mårvik: PHARMACOLOGICAL, PHYSIOLOGICAL AND PATHOPHYSIOLOGICAL STUDIES ON ISOLATED STOMACS.
150. Ketil Jarl Holen: THE ROLE OF ULTRASONOGRAPHY IN THE DIAGNOSIS AND TREATMENT OF HIP DYSPLASIA IN NEWBORNS.
151. Irene Hetlevik: THE ROLE OF CLINICAL GUIDELINES IN CARDIOVASCULAR RISK INTERVENTION IN GENERAL PRACTICE.
152. Katarina Tunòn: ULTRASOUND AND PREDICTION OF GESTATIONAL AGE.
153. Johannes Soma: INTERACTION BETWEEN THE LEFT VENTRICLE AND THE SYSTEMIC ARTERIES.
154. Arild Aamodt: DEVELOPMENT AND PRE-CLINICAL EVALUATION OF A CUSTOM-MADE FEMORAL STEM.
155. Agnar Tegnander: DIAGNOSIS AND FOLLOW-UP OF CHILDREN WITH SUSPECTED OR KNOWN HIP DYSPLASIA.
156. Bent Indredavik: STROKE UNIT TREATMENT: SHORT AND LONG-TERM EFFECTS
157. Jolanta Vanagaite Vingen: PHOTOPHOBIA AND PHONOPHOBIA IN PRIMARY HEADACHES

2000

158. Ola Dalsegg Sæther: PATHOPHYSIOLOGY DURING PROXIMAL AORTIC CROSS-CLAMPING CLINICAL AND EXPERIMENTAL STUDIES
159. xxxxxxxxx (blind number)
160. Christina Vogt Isaksen: PRENATAL ULTRASOUND AND POSTMORTEM FINDINGS – A TEN YEAR CORRELATIVE STUDY OF FETUSES AND INFANTS WITH DEVELOPMENTAL ANOMALIES.
161. Holger Seidel: HIGH-DOSE METHOTREXATE THERAPY IN CHILDREN WITH ACUTE LYMPHOCYTIC LEUKEMIA: DOSE, CONCENTRATION, AND EFFECT CONSIDERATIONS.

162. Stein Hallan: IMPLEMENTATION OF MODERN MEDICAL DECISION ANALYSIS INTO CLINICAL DIAGNOSIS AND TREATMENT.
163. Malcolm Sue-Chu: INVASIVE AND NON-INVASIVE STUDIES IN CROSS-COUNTRY SKIERS WITH ASTHMA-LIKE SYMPTOMS.
164. Ole-Lars Brekke: EFFECTS OF ANTIOXIDANTS AND FATTY ACIDS ON TUMOR NECROSIS FACTOR-INDUCED CYTOTOXICITY.
165. Jan Lundbom: AORTOCORONARY BYPASS SURGERY: CLINICAL ASPECTS, COST CONSIDERATIONS AND WORKING ABILITY.
166. John-Anker Zwart: LUMBAR NERVE ROOT COMPRESSION, BIOCHEMICAL AND NEUROPHYSIOLOGICAL ASPECTS.
167. Geir Falck: HYPEROSMOLALITY AND THE HEART.
168. Eirik Skogvoll: CARDIAC ARREST Incidence, Intervention and Outcome.
169. Dalius Bansevicius: SHOULDER-NECK REGION IN CERTAIN HEADACHES AND CHRONIC PAIN SYNDROMES.
170. Bettina Kinge: REFRACTIVE ERRORS AND BIOMETRIC CHANGES AMONG UNIVERSITY STUDENTS IN NORWAY.
171. Gunnar Qvigstad: CONSEQUENCES OF HYPERGASTRINEMIA IN MAN
172. Hanne Ellekjær: EPIDEMIOLOGICAL STUDIES OF STROKE IN A NORWEGIAN POPULATION. INCIDENCE, RISK FACTORS AND PROGNOSIS
173. Hilde Grimstad: VIOLENCE AGAINST WOMEN AND PREGNANCY OUTCOME.
174. Astrid Hjelde: SURFACE TENSION AND COMPLEMENT ACTIVATION: Factors influencing bubble formation and bubble effects after decompression.
175. Kjell A. Kvistad: MR IN BREAST CANCER – A CLINICAL STUDY.
176. Ivar Rossvoll: ELECTIVE ORTHOPAEDIC SURGERY IN A DEFINED POPULATION. Studies on demand, waiting time for treatment and incapacity for work.
177. Carina Seidel: PROGNOSTIC VALUE AND BIOLOGICAL EFFECTS OF HEPATOCYTE GROWTH FACTOR AND SYNDECAN-1 IN MULTIPLE MYELOMA.

2001

178. Alexander Wahba: THE INFLUENCE OF CARDIOPULMONARY BYPASS ON PLATELET FUNCTION AND BLOOD COAGULATION – DETERMINANTS AND CLINICAL CONSEQUENSES
179. Marcus Schmitt-Egenolf: THE RELEVANCE OF THE MAJOR hISTOCOMPATIBILITY COMPLEX FOR THE GENETICS OF PSORIASIS
180. Odrun Arna Gederaas: BIOLOGICAL MECHANISMS INVOLVED IN 5-AMINOLEVULINIC ACID BASED PHOTODYNAMIC THERAPY
181. Pål Richard Romundstad: CANCER INCIDENCE AMONG NORWEGIAN ALUMINIUM WORKERS
182. Henrik Hjorth-Hansen: NOVEL CYTOKINES IN GROWTH CONTROL AND BONE DISEASE OF MULTIPLE MYELOMA
183. Gunnar Morken: SEASONAL VARIATION OF HUMAN MOOD AND BEHAVIOUR
184. Bjørn Olav Haugen: MEASUREMENT OF CARDIAC OUTPUT AND STUDIES OF VELOCITY PROFILES IN AORTIC AND MITRAL FLOW USING TWO- AND THREE-DIMENSIONAL COLOUR FLOW IMAGING
185. Geir Bråthen: THE CLASSIFICATION AND CLINICAL DIAGNOSIS OF ALCOHOL-RELATED SEIZURES
186. Knut Ivar Aasarød: RENAL INVOLVEMENT IN INFLAMMATORY RHEUMATIC DISEASE. A Study of Renal Disease in Wegener's Granulomatosis and in Primary Sjögren's Syndrome
187. Trude Helen Flo: RESEPTORS INVOLVED IN CELL ACTIVATION BY DEFINED URONIC ACID POLYMERS AND BACTERIAL COMPONENTS
188. Bodil Kavli: HUMAN URACIL-DNA GLYCOSYLASES FROM THE UNG GENE: STRUCTRUAL BASIS FOR SUBSTRATE SPECIFICITY AND REPAIR
189. Liv Thommesen: MOLECULAR MECHANISMS INVOLVED IN TNF- AND GASTRIN-MEDIATED GENE REGULATION
190. Turid Lingaas Holmen: SMOKING AND HEALTH IN ADOLESCENCE; THE NORD-TRØNDELAG HEALTH STUDY, 1995-97
191. Øyvind Hjertner: MULTIPLE MYELOMA: INTERACTIONS BETWEEN MALIGNANT PLASMA CELLS AND THE BONE MICROENVIRONMENT

192. Asbjørn Støylen: STRAIN RATE IMAGING OF THE LEFT VENTRICLE BY ULTRASOUND. FEASIBILITY, CLINICAL VALIDATION AND PHYSIOLOGICAL ASPECTS
193. Kristian Midthjell: DIABETES IN ADULTS IN NORD-TRØNDELAG. PUBLIC HEALTH ASPECTS OF DIABETES MELLITUS IN A LARGE, NON-SELECTED NORWEGIAN POPULATION.
194. Guanglin Cui: FUNCTIONAL ASPECTS OF THE ECL CELL IN RODENTS
195. Ulrik Wisløff: CARDIAC EFFECTS OF AEROBIC ENDURANCE TRAINING: HYPERTROPHY, CONTRACTILITY AND CALCUIM HANDLING IN NORMAL AND FAILING HEART
196. Øyvind Halaas: MECHANISMS OF IMMUNOMODULATION AND CELL-MEDIATED CYTOTOXICITY INDUCED BY BACTERIAL PRODUCTS
197. Tore Amundsen: PERFUSION MR IMAGING IN THE DIAGNOSIS OF PULMONARY EMBOLISM
198. Nanna Kurtze: THE SIGNIFICANCE OF ANXIETY AND DEPRESSION IN FATIQUE AND PATTERNS OF PAIN AMONG INDIVIDUALS DIAGNOSED WITH FIBROMYALGIA: RELATIONS WITH QUALITY OF LIFE, FUNCTIONAL DISABILITY, LIFESTYLE, EMPLOYMENT STATUS, CO-MORBIDITY AND GENDER
199. Tom Ivar Lund Nilsen: PROSPECTIVE STUDIES OF CANCER RISK IN NORD-TRØNDELAG: THE HUNT STUDY. Associations with anthropometric, socioeconomic, and lifestyle risk factors
200. Asta Kristine Håberg: A NEW APPROACH TO THE STUDY OF MIDDLE CEREBRAL ARTERY OCCLUSION IN THE RAT USING MAGNETIC RESONANCE TECHNIQUES

2002

201. Knut Jørgen Arntzen: PREGNANCY AND CYTOKINES
202. Henrik Døllner: INFLAMMATORY MEDIATORS IN PERINATAL INFECTIONS
203. Asta Bye: LOW FAT, LOW LACTOSE DIET USED AS PROPHYLACTIC TREATMENT OF ACUTE INTESTINAL REACTIONS DURING PELVIC RADIOTHERAPY. A PROSPECTIVE RANDOMISED STUDY.
204. Sylvester Moyo: STUDIES ON STREPTOCOCCUS AGALACTIAE (GROUP B STREPTOCOCCUS) SURFACE-ANCHORED MARKERS WITH EMPHASIS ON STRAINS AND HUMAN SERA FROM ZIMBABWE.
205. Knut Hagen: HEAD-HUNT: THE EPIDEMIOLOGY OF HEADACHE IN NORD-TRØNDELAG
206. Li Lixin: ON THE REGULATION AND ROLE OF UNCOUPLING PROTEIN-2 IN INSULIN PRODUCING ß-CELLS
207. Anne Hildur Henriksen: SYMPTOMS OF ALLERGY AND ASTHMA VERSUS MARKERS OF LOWER AIRWAY INFLAMMATION AMONG ADOLESCENTS
208. Egil Andreas Fors: NON-MALIGNANT PAIN IN RELATION TO PSYCHOLOGICAL AND ENVIRONTENTAL FACTORS. EXPERIENTAL AND CLINICAL STUDES OF PAIN WITH FOCUS ON FIBROMYALGIA
209. Pål Klepstad: MORPHINE FOR CANCER PAIN
210. Ingunn Bakke: MECHANISMS AND CONSEQUENCES OF PEROXISOME PROLIFERATOR-INDUCED HYPERFUNCTION OF THE RAT GASTRIN PRODUCING CELL
211. Ingrid Susann Gribbestad: MAGNETIC RESONANCE IMAGING AND SPECTROSCOPY OF BREAST CANCER
212. Rønnaug Astri Ødegård: PREECLAMPSIA – MATERNAL RISK FACTORS AND FETAL GROWTH
213. Johan Haux: STUDIES ON CYTOTOXICITY INDUCED BY HUMAN NATURAL KILLER CELLS AND DIGITOXIN
214. Turid Suzanne Berg-Nielsen: PARENTING PRACTICES AND MENTALLY DISORDERED ADOLESCENTS
215. Astrid Rydning: BLOOD FLOW AS A PROTECTIVE FACTOR FOR THE STOMACH MUCOSA. AN EXPERIMENTAL STUDY ON THE ROLE OF MAST CELLS AND SENSORY AFFERENT NEURONS

2003

216. Jan Pål Loennechen: HEART FAILURE AFTER MYOCARDIAL INFARCTION. Regional Differences, Myocyte Function, Gene Expression, and Response to Cariporide, Losartan, and Exercise Training.
217. Elisabeth Qvigstad: EFFECTS OF FATTY ACIDS AND OVER-STIMULATION ON INSULIN SECRETION IN MAN
218. Arne Åsberg: EPIDEMIOLOGICAL STUDIES IN HEREDITARY HEMOCHROMATOSIS: PREVALENCE, MORBIDITY AND BENEFIT OF SCREENING.
219. Johan Fredrik Skomsvoll: REPRODUCTIVE OUTCOME IN WOMEN WITH RHEUMATIC DISEASE. A population registry based study of the effects of inflammatory rheumatic disease and connective tissue disease on reproductive outcome in Norwegian women in 1967-1995.
220. Siv Mørkved: URINARY INCONTINENCE DURING PREGNANCY AND AFTER DELIVERY: EFFECT OF PELVIC FLOOR MUSCLE TRAINING IN PREVENTION AND TREATMENT
221. Marit S. Jordhøy: THE IMPACT OF COMPREHENSIVE PALLIATIVE CARE
222. Tom Christian Martinsen: HYPERGASTRINEMIA AND HYPOACIDITY IN RODENTS – CAUSES AND CONSEQUENCES
223. Solveig Tingulstad: CENTRALIZATION OF PRIMARY SURGERY FOR OVARAIN CANCER. FEASIBILITY AND IMPACT ON SURVIVAL
224. Haytham Eloqayli: METABOLIC CHANGES IN THE BRAIN CAUSED BY EPILEPTIC SEIZURES
225. Torunn Bruland: STUDIES OF EARLY RETROVIRUS-HOST INTERACTIONS – VIRAL DETERMINANTS FOR PATHOGENESIS AND THE INFLUENCE OF SEX ON THE SUSCEPTIBILITY TO FRIEND MURINE LEUKAEMIA VIRUS INFECTION
226. Torstein Hole: DOPPLER ECHOCARDIOGRAPHIC EVALUATION OF LEFT VENTRICULAR FUNCTION IN PATIENTS WITH ACUTE MYOCARDIAL INFARCTION
227. Vibeke Nossum: THE EFFECT OF VASCULAR BUBBLES ON ENDOTHELIAL FUNCTION
228. Sigurd Fasting: ROUTINE BASED RECORDING OF ADVERSE EVENTS DURING ANAESTHESIA – APPLICATION IN QUALITY IMPROVEMENT AND SAFETY
229. Solfrid Romundstad: EPIDEMIOLOGICAL STUDIES OF MICROALBUMINURIA. THE NORD-TRØNDELAG HEALTH STUDY 1995-97 (HUNT 2)
230. Geir Torheim: PROCESSING OF DYNAMIC DATA SETS IN MAGNETIC RESONANCE IMAGING
231. Catrine Ahlén: SKIN INFECTIONS IN OCCUPATIONAL SATURATION DIVERS IN THE NORTH SEA AND THE IMPACT OF THE ENVIRONMENT
232. Arnulf Langhammer: RESPIRATORY SYMPTOMS, LUNG FUNCTION AND BONE MINERAL DENSITY IN A COMPREHENSIVE POPULATION SURVEY. THE NORD-TRØNDELAG HEALTH STUDY 1995-97. THE BRONCHIAL OBSTRUCTION IN NORD-TRØNDELAG STUDY
233. Einar Kjelsås: EATING DISORDERS AND PHYSICAL ACTIVITY IN NON-CLINICAL SAMPLES
234. Arne Wibe: RECTAL CANCER TREATMENT IN NORWAY – STANDARDISATION OF SURGERY AND QUALITY ASSURANCE

2004

235. Eivind Witsø: BONE GRAFT AS AN ANTIBIOTIC CARRIER
236. Anne Mari Sund: DEVELOPMENT OF DEPRESSIVE SYMPTOMS IN EARLY ADOLESCENCE
237. Hallvard Lærum: EVALUATION OF ELECTRONIC MEDICAL RECORDS – A CLINICAL TASK PERSPECTIVE
238. Gustav Mikkelsen: ACCESSIBILITY OF INFORMATION IN ELECTRONIC PATIENT RECORDS; AN EVALUATION OF THE ROLE OF DATA QUALITY
239. Steinar Krokstad: SOCIOECONOMIC INEQUALITIES IN HEALTH AND DISABILITY. SOCIAL EPIDEMIOLOGY IN THE NORD-TRØNDELAG HEALTH STUDY (HUNT), NORWAY
240. Arne Kristian Myhre: NORMAL VARIATION IN ANOGENITAL ANATOMY AND MICROBIOLOGY IN NON-ABUSED PRESCHOOL CHILDREN
241. Ingunn Dybedal: NEGATIVE REGULATORS OF HEMATOPOIETEC STEM AND PROGENITOR CELLS
242. Beate Sitter: TISSUE CHARACTERIZATION BY HIGH RESOLUTION MAGIC ANGLE SPINNING MR SPECTROSCOPY

243. Per Arne Aas: MACROMOLECULAR MAINTENANCE IN HUMAN CELLS – REPAIR OF URACIL IN DNA AND METHYLATIONS IN DNA AND RNA
244. Anna Bofin: FINE NEEDLE ASPIRATION CYTOLOGY IN THE PRIMARY INVESTIGATION OF BREAST TUMOURS AND IN THE DETERMINATION OF TREATMENT STRATEGIES
245. Jim Aage Nøttestad: DEINSTITUTIONALIZATION AND MENTAL HEALTH CHANGES AMONG PEOPLE WITH MENTAL RETARDATION
246. Reidar Fossmark: GASTRIC CANCER IN JAPANESE COTTON RATS
247. Wibeke Nordhøy: MANGANESE AND THE HEART, INTRACELLULAR MR RELAXATION AND WATER EXCHANGE ACROSS THE CARDIAC CELL MEMBRANE

2005

248. Sturla Molden: QUANTITATIVE ANALYSES OF SINGLE UNITS RECORDED FROM THE HIPPOCAMPUS AND ENTORHINAL CORTEX OF BEHAVING RATS
249. Wenche Brenne Drøyvold: EPIDEMIOLOGICAL STUDIES ON WEIGHT CHANGE AND HEALTH IN A LARGE POPULATION. THE NORD-TRØNDELAG HEALTH STUDY (HUNT)
250. Ragnhild Støen: ENDOTHELIUM-DEPENDENT VASODILATION IN THE FEMORAL ARTERY OF DEVELOPING PIGLETS
251. Aslak Steinsbekk: HOMEOPATHY IN THE PREVENTION OF UPPER RESPIRATORY TRACT INFECTIONS IN CHILDREN
252. Hill-Aina Steffenach: MEMORY IN HIPPOCAMPAL AND CORTICO-HIPPOCAMPAL CIRCUITS
253. Eystein Stordal: ASPECTS OF THE EPIDEMIOLOGY OF DEPRESSIONS BASED ON SELF-RATING IN A LARGE GENERAL HEALTH STUDY (THE HUNT-2 STUDY)
254. Viggo Pettersen: FROM MUSCLES TO SINGING: THE ACTIVITY OF ACCESSORY BREATHING MUSCLES AND THORAX MOVEMENT IN CLASSICAL SINGING
255. Marianne Fyhn: SPATIAL MAPS IN THE HIPPOCAMPUS AND ENTORHINAL CORTEX
256. Robert Valderhaug: OBSESSIVE-COMPULSIVE DISORDER AMONG CHILDREN AND ADOLESCENTS: CHARACTERISTICS AND PSYCHOLOGICAL MANAGEMENT OF PATIENTS IN OUTPATIENT PSYCHIATRIC CLINICS
257. Erik Skaaheim Haug: INFRARENAL ABDOMINAL AORTIC ANEURYSMS – COMORBIDITY AND RESULTS FOLLOWING OPEN SURGERY
258. Daniel Kondziella: GLIAL-NEURONAL INTERACTIONS IN EXPERIMENTAL BRAIN DISORDERS
259. Vegard Heimly Brun: ROUTES TO SPATIAL MEMORY IN HIPPOCAMPAL PLACE CELLS
260. Kenneth McMillan: PHYSIOLOGICAL ASSESSMENT AND TRAINING OF ENDURANCE AND STRENGTH IN PROFESSIONAL YOUTH SOCCER PLAYERS
261. Marit Sæbø Indredavik: MENTAL HEALTH AND CEREBRAL MAGNETIC RESONANCE IMAGING IN ADOLESCENTS WITH LOW BIRTH WEIGHT
262. Ole Johan Kemi: ON THE CELLULAR BASIS OF AEROBIC FITNESS, INTENSITY-DEPENDENCE AND TIME-COURSE OF CARDIOMYOCYTE AND ENDOTHELIAL ADAPTATIONS TO EXERCISE TRAINING
263. Eszter Vanky: POLYCYSTIC OVARY SYNDROME – METFORMIN TREATMENT IN PREGNANCY
264. Hild Fjærtoft: EXTENDED STROKE UNIT SERVICE AND EARLY SUPPORTED DISCHARGE. SHORT AND LONG-TERM EFFECTS
265. Grete Dyb: POSTTRAUMATIC STRESS REACTIONS IN CHILDREN AND ADOLESCENTS
266. Vidar Fykse: SOMATOSTATIN AND THE STOMACH
267. Kirsti Berg: OXIDATIVE STRESS AND THE ISCHEMIC HEART: A STUDY IN PATIENTS UNDERGOING CORONARY REVASCULARIZATION
268. Björn Inge Gustafsson: THE SEROTONIN PRODUCING ENTEROCHROMAFFIN CELL, AND EFFECTS OF HYPERSEROTONINEMIA ON HEART AND BONE

2006

269. Torstein Baade Rø: EFFECTS OF BONE MORPHOGENETIC PROTEINS, HEPATOCYTE GROWTH FACTOR AND INTERLEUKIN-21 IN MULTIPLE MYELOMA
270. May-Britt Tessem: METABOLIC EFFECTS OF ULTRAVIOLET RADIATION ON THE ANTERIOR PART OF THE EYE

271. Anne-Sofie Helvik: COPING AND EVERYDAY LIFE IN A POPULATION OF ADULTS WITH HEARING IMPAIRMENT
272. Therese Standal: MULTIPLE MYELOMA: THE INTERPLAY BETWEEN MALIGNANT PLASMA CELLS AND THE BONE MARROW MICROENVIRONMENT
273. Ingvild Saltvedt: TREATMENT OF ACUTELY SICK, FRAIL ELDERLY PATIENTS IN A GERIATRIC EVALUATION AND MANAGEMENT UNIT – RESULTS FROM A PROSPECTIVE RANDOMISED TRIAL
274. Birger Henning Endreseth: STRATEGIES IN RECTAL CANCER TREATMENT – FOCUS ON EARLY RECTAL CANCER AND THE INFLUENCE OF AGE ON PROGNOSIS
275. Anne Mari Aukan Rokstad: ALGINATE CAPSULES AS BIOREACTORS FOR CELL THERAPY
276. Mansour Akbari: HUMAN BASE EXCISION REPAIR FOR PRESERVATION OF GENOMIC STABILITY
277. Stein Sundstrøm: IMPROVING TREATMENT IN PATIENTS WITH LUNG CANCER – RESULTS FROM TWO MULITCENTRE RANDOMISED STUDIES
278. Hilde Pleym: BLEEDING AFTER CORONARY ARTERY BYPASS SURGERY - STUDIES ON HEMOSTATIC MECHANISMS, PROPHYLACTIC DRUG TREATMENT AND EFFECTS OF AUTOTRANSFUSION
279. Line Merethe Oldervoll: PHYSICAL ACTIVITY AND EXERCISE INTERVENTIONS IN CANCER PATIENTS
280. Boye Welde: THE SIGNIFICANCE OF ENDURANCE TRAINING, RESISTANCE TRAINING AND MOTIVATIONAL STYLES IN ATHLETIC PERFORMANCE AMONG ELITE JUNIOR CROSS-COUNTRY SKIERS
281. Per Olav Vandvik: IRRITABLE BOWEL SYNDROME IN NORWAY, STUDIES OF PREVALENCE, DIAGNOSIS AND CHARACTERISTICS IN GENERAL PRACTICE AND IN THE POPULATION
282. Idar Kirkeby-Garstad: CLINICAL PHYSIOLOGY OF EARLY MOBILIZATION AFTER CARDIAC SURGERY
283. Linn Getz: SUSTAINABLE AND RESPONSIBLE PREVENTIVE MEDICINE. CONCEPTUALISING ETHICAL DILEMMAS ARISING FROM CLINICAL IMPLEMENTATION OF ADVANCING MEDICAL TECHNOLOGY
284. Eva Tegnander: DETECTION OF CONGENITAL HEART DEFECTS IN A NON-SELECTED POPULATION OF 42,381 FETUSES
285. Kristin Gabestad Nørsett: GENE EXPRESSION STUDIES IN GASTROINTESTINAL PATHOPHYSIOLOGY AND NEOPLASIA
286. Per Magnus Haram: GENETIC VS. AQUIRED FITNESS: METABOLIC, VASCULAR AND CARDIOMYOCYTE ADAPTATIONS
287. Agneta Johansson: GENERAL RISK FACTORS FOR GAMBLING PROBLEMS AND THE PREVALENCE OF PATHOLOGICAL GAMBLING IN NORWAY
288. Svein Artur Jensen: THE PREVALENCE OF SYMPTOMATIC ARTERIAL DISEASE OF THE LOWER LIMB
289. Charlotte Björk Ingul: QUANITIFICATION OF REGIONAL MYOCARDIAL FUNCTION BY STRAIN RATE AND STRAIN FOR EVALUATION OF CORONARY ARTERY DISEASE. AUTOMATED VERSUS MANUAL ANALYSIS DURING ACUTE MYOCARDIAL INFARCTION AND DOBUTAMINE STRESS ECHOCARDIOGRAPHY
290. Jakob Nakling: RESULTS AND CONSEQUENCES OF ROUTINE ULTRASOUND SCREENING IN PREGNANCY – A GEOGRAPHIC BASED POPULATION STUDY
291. Anne Engum: DEPRESSION AND ANXIETY – THEIR RELATIONS TO THYROID DYSFUNCTION AND DIABETES IN A LARGE EPIDEMIOLOGICAL STUDY
292. Ottar Bjerkeset: ANXIETY AND DEPRESSION IN THE GENERAL POPULATION: RISK FACTORS, INTERVENTION AND OUTCOME – THE NORD-TRØNDELAG HEALTH STUDY (HUNT)
293. Jon Olav Drogset: RESULTS AFTER SURGICAL TREATMENT OF ANTERIOR CRUCIATE LIGAMENT INJURIES – A CLINICAL STUDY
294. Lars Fosse: MECHANICAL BEHAVIOUR OF COMPACTED MORSELLISED BONE – AN EXPERIMENTAL IN VITRO STUDY
295. Gunilla Klensmeden Fosse: MENTAL HEALTH OF PSYCHIATRIC OUTPATIENTS BULLIED IN CHILDHOOD
296. Paul Jarle Mork: MUSCLE ACTIVITY IN WORK AND LEISURE AND ITS ASSOCIATION TO MUSCULOSKELETAL PAIN

297. Björn Stenström: LESSONS FROM RODENTS: I: MECHANISMS OF OBESITY SURGERY – ROLE OF STOMACH. II: CARCINOGENIC EFFECTS OF *HELICOBACTER PYLORI* AND SNUS IN THE STOMACH

2007

298. Haakon R. Skogseth: INVASIVE PROPERTIES OF CANCER – A TREATMENT TARGET ? IN VITRO STUDIES IN HUMAN PROSTATE CANCER CELL LINES
299. Janniche Hammer: GLUTAMATE METABOLISM AND CYCLING IN MESIAL TEMPORAL LOBE EPILEPSY
300. May Britt Drugli: YOUNG CHILDREN TREATED BECAUSE OF ODD/CD: CONDUCT PROBLEMS AND SOCIAL COMPETENCIES IN DAY-CARE AND SCHOOL SETTINGS
301. Arne Skjold: MAGNETIC RESONANCE KINETICS OF MANGANESE DIPYRIDOXYL DIPHOSPHATE (MnDPDP) IN HUMAN MYOCARDIUM. STUDIES IN HEALTHY VOLUNTEERS AND IN PATIENTS WITH RECENT MYOCARDIAL INFARCTION
302. Siri Malm: LEFT VENTRICULAR SYSTOLIC FUNCTION AND MYOCARDIAL PERFUSION ASSESSED BY CONTRAST ECHOCARDIOGRAPHY
303. Valentina Maria do Rosario Cabral Iversen: MENTAL HEALTH AND PSYCHOLOGICAL ADAPTATION OF CLINICAL AND NON-CLINICAL MIGRANT GROUPS
304. Lasse Løvstakken: SIGNAL PROCESSING IN DIAGNOSTIC ULTRASOUND: ALGORITHMS FOR REAL-TIME ESTIMATION AND VISUALIZATION OF BLOOD FLOW VELOCITY
305. Elisabeth Olstad: GLUTAMATE AND GABA: MAJOR PLAYERS IN NEURONAL METABOLISM
306. Lilian Leistad: THE ROLE OF CYTOKINES AND PHOSPHOLIPASE A_2s IN ARTICULAR CARTILAGE CHONDROCYTES IN RHEUMATOID ARTHRITIS AND OSTEOARTHRITIS
307. Arne Vaaler: EFFECTS OF PSYCHIATRIC INTENSIVE CARE UNIT IN AN ACUTE PSYCIATHRIC WARD
308. Mathias Toft: GENETIC STUDIES OF LRRK2 AND PINK1 IN PARKINSON'S DISEASE
309. Ingrid Løvold Mostad: IMPACT OF DIETARY FAT QUANTITY AND QUALITY IN TYPE 2 DIABETES WITH EMPHASIS ON MARINE N-3 FATTY ACIDS
310. Torill Eidhammer Sjøbakk: MR DETERMINED BRAIN METABOLIC PATTERN IN PATIENTS WITH BRAIN METASTASES AND ADOLESCENTS WITH LOW BIRTH WEIGHT
311. Vidar Beisvåg: PHYSIOLOGICAL GENOMICS OF HEART FAILURE: FROM TECHNOLOGY TO PHYSIOLOGY
312. Olav Magnus Søndenå Fredheim: HEALTH RELATED QUALITY OF LIFE ASSESSMENT AND ASPECTS OF THE CLINICAL PHARMACOLOGY OF METHADONE IN PATIENTS WITH CHRONIC NON-MALIGNANT PAIN
313. Anne Brantberg: FETAL AND PERINATAL IMPLICATIONS OF ANOMALIES IN THE GASTROINTESTINAL TRACT AND THE ABDOMINAL WALL
314. Erik Solligård: GUT LUMINAL MICRODIALYSIS
315. Elin Tollefsen: RESPIRATORY SYMPTOMS IN A COMPREHENSIVE POPULATION BASED STUDY AMONG ADOLESCENTS 13-19 YEARS. YOUNG-HUNT 1995-97 AND 2000-01; THE NORD-TRØNDELAG HEALTH STUDIES (HUNT)
316. Anne-Tove Brenne: GROWTH REGULATION OF MYELOMA CELLS
317. Heidi Knobel: FATIGUE IN CANCER TREATMENT – ASSESSMENT, COURSE AND ETIOLOGY
318. Torbjørn Dahl: CAROTID ARTERY STENOSIS. DIAGNOSTIC AND THERAPEUTIC ASPECTS
319. Inge-Andre Rasmussen jr.: FUNCTIONAL AND DIFFUSION TENSOR MAGNETIC RESONANCE IMAGING IN NEUROSURGICAL PATIENTS
320. Grete Helen Bratberg: PUBERTAL TIMING – ANTECEDENT TO RISK OR RESILIENCE ? EPIDEMIOLOGICAL STUDIES ON GROWTH, MATURATION AND HEALTH RISK BEHAVIOURS; THE YOUNG HUNT STUDY, NORD-TRØNDELAG, NORWAY
321. Sveinung Sørhaug: THE PULMONARY NEUROENDOCRINE SYSTEM. PHYSIOLOGICAL, PATHOLOGICAL AND TUMOURIGENIC ASPECTS
322. Olav Sande Eftedal: ULTRASONIC DETECTION OF DECOMPRESSION INDUCED VASCULAR MICROBUBBLES
323. Rune Bang Leistad: PAIN, AUTONOMIC ACTIVATION AND MUSCULAR ACTIVITY RELATED TO EXPERIMENTALLY-INDUCED COGNITIVE STRESS IN HEADACHE PATIENTS

324. Svein Brekke: TECHNIQUES FOR ENHANCEMENT OF TEMPORAL RESOLUTION IN THREE-DIMENSIONAL ECHOCARDIOGRAPHY
325. Kristian Bernhard Nilsen: AUTONOMIC ACTIVATION AND MUSCLE ACTIVITY IN RELATION TO MUSCULOSKELETAL PAIN
326. Anne Irene Hagen: HEREDITARY BREAST CANCER IN NORWAY. DETECTION AND PROGNOSIS OF BREAST CANCER IN FAMILIES WITH *BRCA1*GENE MUTATION
327. Ingebjørg S. Juel : INTESTINAL INJURY AND RECOVERY AFTER ISCHEMIA. AN EXPERIMENTAL STUDY ON RESTITUTION OF THE SURFACE EPITHELIUM, INTESTINAL PERMEABILITY, AND RELEASE OF BIOMARKERS FROM THE MUCOSA
328. Runa Heimstad: POST-TERM PREGNANCY
329. Jan Egil Afset: ROLE OF ENTEROPATHOGENIC *ESCHERICHIA COLI* IN CHILDHOOD DIARRHOEA IN NORWAY
330. Bent Håvard Hellum: *IN VITRO* INTERACTIONS BETWEEN MEDICINAL DRUGS AND HERBS ON CYTOCHROME P-450 METABOLISM AND P-GLYCOPROTEIN TRANSPORT
331. Morten André Høydal: CARDIAC DYSFUNCTION AND MAXIMAL OXYGEN UPTAKE MYOCARDIAL ADAPTATION TO ENDURANCE TRAINING

2008

332. Andreas Møllerløkken: REDUCTION OF VASCULAR BUBBLES: METHODS TO PREVENT THE ADVERSE EFFECTS OF DECOMPRESSION
333. Anne Hege Aamodt: COMORBIDITY OF HEADACHE AND MIGRAINE IN THE NORD-TRØNDELAG HEALTH STUDY 1995-97
334. Brage Høyem Amundsen: MYOCARDIAL FUNCTION QUANTIFIED BY SPECKLE TRACKING AND TISSUE DOPPLER ECHOCARDIOGRAPHY – VALIDATION AND APPLICATION IN EXERCISE TESTING AND TRAINING
335. Inger Anne Næss: INCIDENCE, MORTALITY AND RISK FACTORS OF FIRST VENOUS THROMBOSIS IN A GENERAL POPULATION. RESULTS FROM THE SECOND NORD-TRØNDELAG HEALTH STUDY (HUNT2)
336. Vegard Bugten: EFFECTS OF POSTOPERATIVE MEASURES AFTER FUNCTIONAL ENDOSCOPIC SINUS SURGERY
337. Morten Bruvold: MANGANESE AND WATER IN CARDIAC MAGNETIC RESONANCE IMAGING
338. Miroslav Fris: THE EFFECT OF SINGLE AND REPEATED ULTRAVIOLET RADIATION ON THE ANTERIOR SEGMENT OF THE RABBIT EYE
339. Svein Arne Aase: METHODS FOR IMPROVING QUALITY AND EFFICIENCY IN QUANTITATIVE ECHOCARDIOGRAPHY – ASPECTS OF USING HIGH FRAME RATE
340. Roger Almvik: ASSESSING THE RISK OF VIOLENCE: DEVELOPMENT AND VALIDATION OF THE BRØSET VIOLENCE CHECKLIST
341. Ottar Sundheim: STRUCTURE-FUNCTION ANALYSIS OF HUMAN ENZYMES INITIATING NUCLEOBASE REPAIR IN DNA AND RNA
342. Anne Mari Undheim: SHORT AND LONG-TERM OUTCOME OF EMOTIONAL AND BEHAVIOURAL PROBLEMS IN YOUNG ADOLESCENTS WITH AND WITHOUT READING DIFFICULTIES
343. Helge Garåsen: THE TRONDHEIM MODEL. IMPROVING THE PROFESSIONAL COMMUNICATION BETWEEN THE VARIOUS LEVELS OF HEALTH CARE SERVICES AND IMPLEMENTATION OF INTERMEDIATE CARE AT A COMMUNITY HOSPITAL COULD PROVIDE BETTER CARE FOR OLDER PATIENTS. SHORT AND LONG TERM EFFECTS
344. Olav A. Foss: "THE ROTATION RATIOS METHOD". A METHOD TO DESCRIBE ALTERED SPATIAL ORIENTATION IN SEQUENTIAL RADIOGRAPHS FROM ONE PELVIS
345. Bjørn Olav Åsvold: THYROID FUNCTION AND CARDIOVASCULAR HEALTH
346. Torun Margareta Melø: NEURONAL GLIAL INTERACTIONS IN EPILEPSY
347. Irina Poliakova Eide: FETAL GROWTH RESTRICTION AND PRE-ECLAMPSIA: SOME CHARACTERISTICS OF FETO-MATERNAL INTERACTIONS IN DECIDUA BASALIS
348. Torunn Askim: RECOVERY AFTER STROKE. ASSESSMENT AND TREATMENT; WITH FOCUS ON MOTOR FUNCTION
349. Ann Elisabeth Åsberg: NEUTROPHIL ACTIVATION IN A ROLLER PUMP MODEL OF CARDIOPULMONARY BYPASS. INFLUENCE ON BIOMATERIAL, PLATELETS AND COMPLEMENT

350. Lars Hagen: REGULATION OF DNA BASE EXCISION REPAIR BY PROTEIN INTERACTIONS AND POST TRANSLATIONAL MODIFICATIONS
351. Sigrun Beate Kjøtrød: POLYCYSTIC OVARY SYNDROME – METFORMIN TREATMENT IN ASSISTED REPRODUCTION
352. Steven Keita Nishiyama: PERSPECTIVES ON LIMB-VASCULAR HETEROGENEITY: IMPLICATIONS FOR HUMAN AGING, SEX, AND EXERCISE
353. Sven Peter Näsholm: ULTRASOUND BEAMS FOR ENHANCED IMAGE QUALITY
354. Jon Ståle Ritland: PRIMARY OPEN-ANGLE GLAUCOMA & EXFOLIATIVE GLAUCOMA. SURVIVAL, COMORBIDITY AND GENETICS
355. Sigrid Botne Sando: ALZHEIMER'S DISEASE IN CENTRAL NORWAY. GENETIC AND EDUCATIONAL ASPECTS
356. Parvinder Kaur: CELLULAR AND MOLECULAR MECHANISMS BEHIND METHYLMERCURY-INDUCED NEUROTOXICITY
357. Ismail Cüneyt Güzey: DOPAMINE AND SEROTONIN RECEPTOR AND TRANSPORTER GENE POLYMORPHISMS AND EXTRAPYRAMIDAL SYMPTOMS. STUDIES IN PARKINSON'S DISEASE AND IN PATIENTS TREATED WITH ANTIPSYCHOTIC OR ANTIDEPRESSANT DRUGS
358. Brit Dybdahl: EXTRA-CELLULAR INDUCIBLE HEAT-SHOCK PROTEIN 70 (Hsp70) – A ROLE IN THE INFLAMMATORY RESPONSE ?
359. Kristoffer Haugarvoll: IDENTIFYING GENETIC CAUSES OF PARKINSON'S DISEASE IN NORWAY
360. Nadra Nilsen: TOLL-LIKE RECEPTOR 2 –EXPRESSION, REGULATION AND SIGNALING
361. Johan Håkon Bjørngaard: PATIENT SATISFACTION WITH OUTPATIENT MENTAL HEALTH SERVICES – THE INFLUENCE OF ORGANIZATIONAL FACTORS.
362. Kjetil Høydal : EFFECTS OF HIGH INTENSITY AEROBIC TRAINING IN HEALTHY SUBJECTS AND CORONARY ARTERY DISEASE PATIENTS; THE IMPORTANCE OF INTENSITY,, DURATION AND FREQUENCY OF TRAINING.
363. Trine Karlsen: TRAINING IS MEDICINE: ENDURANCE AND STRENGTH TRAINING IN CORONARY ARTERY DISEASE AND HEALTH.
364. Marte Thuen: MANGANASE-ENHANCED AND DIFFUSION TENSOR MR IMAGING OF THE NORMAL, INJURED AND REGENERATING RAT VISUAL PATHWAY
365. Cathrine Broberg Vågbø: DIRECT REPAIR OF ALKYLATION DAMAGE IN DNA AND RNA BY 2-OXOGLUTARATE- AND IRON-DEPENDENT DIOXYGENASES
366. Arnt Erik Tjønna: AEROBIC EXERCISE AND CARDIOVASCULAR RISK FACTORS IN OVERWEIGHT AND OBESE ADOLESCENTS AND ADULTS
367. Marianne W. Furnes: FEEDING BEHAVIOR AND BODY WEIGHT DEVELOPMENT: LESSONS FROM RATS
368. Lene N. Johannessen: FUNGAL PRODUCTS AND INFLAMMATORY RESPONSES IN HUMAN MONOCYTES AND EPITHELIAL CELLS
369. Anja Bye: GENE EXPRESSION PROFILING OF *INHERITED* AND *ACQUIRED* MAXIMAL OXYGEN UPTAKE – RELATIONS TO THE METABOLIC SYNDROME.
370. Oluf Dimitri Røe: MALIGNANT MESOTHELIOMA: VIRUS, BIOMARKERS AND GENES. A TRANSLATIONAL APPROACH
371. Ane Cecilie Dale: DIABETES MELLITUS AND FATAL ISCHEMIC HEART DISEASE. ANALYSES FROM THE HUNT1 AND 2 STUDIES
372. Jacob Christian Hølen: PAIN ASSESSMENT IN PALLIATIVE CARE: VALIDATION OF METHODS FOR SELF-REPORT AND BEHAVIOURAL ASSESSMENT
373. Erming Tian: THE GENETIC IMPACTS IN THE ONCOGENESIS OF MULTIPLE MYELOMA
374. Ole Bosnes: KLINISK UTPRØVING AV NORSKE VERSJONER AV NOEN SENTRALE TESTER PÅ KOGNITIV FUNKSJON
375. Ola M. Rygh: 3D ULTRASOUND BASED NEURONAVIGATION IN NEUROSURGERY. A CLINICAL EVALUATION
376. Astrid Kamilla Stunes: ADIPOKINES, PEROXISOME PROFILERATOR ACTIVATED RECEPTOR (PPAR) AGONISTS AND SEROTONIN. COMMON REGULATORS OF BONE AND FAT METABOLISM
377. Silje Engdal: HERBAL REMEDIES USED BY NORWEGIAN CANCER PATIENTS AND THEIR ROLE IN HERB-DRUG INTERACTIONS
378. Kristin Offerdal: IMPROVED ULTRASOUND IMAGING OF THE FETUS AND ITS CONSEQUENCES FOR SEVERE AND LESS SEVERE ANOMALIES

379. Øivind Rognmo: HIGH-INTENSITY AEROBIC EXERCISE AND CARDIOVASCULAR HEALTH
380. Jo-Åsmund Lund: RADIOTHERAPY IN ANAL CARCINOMA AND PROSTATE CANCER

2009

381. Tore Grüner Bjåstad: HIGH FRAME RATE ULTRASOUND IMAGING USING PARALLEL BEAMFORMING
382. Erik Søndenaa: INTELLECTUAL DISABILITIES IN THE CRIMINAL JUSTICE SYSTEM
383. Berit Rostad: SOCIAL INEQUALITIES IN WOMEN'S HEALTH, HUNT 1984-86 AND 1995-97, THE NORD-TRØNDELAG HEALTH STUDY (HUNT)
384. Jonas Crosby: ULTRASOUND-BASED QUANTIFICATION OF MYOCARDIAL DEFORMATION AND ROTATION
385. Erling Tronvik: MIGRAINE, BLOOD PRESSURE AND THE RENIN-ANGIOTENSIN SYSTEM
386. Tom Christensen: BRINGING THE GP TO THE FOREFRONT OF EPR DEVELOPMENT
387. Håkon Bergseng: ASPECTS OF GROUP B STREPTOCOCCUS (GBS) DISEASE IN THE NEWBORN. EPIDEMIOLOGY, CHARACTERISATION OF INVASIVE STRAINS AND EVALUATION OF INTRAPARTUM SCREENING
388. Ronny Myhre: GENETIC STUDIES OF CANDIDATE TENE3S IN PARKINSON'S DISEASE
389. Torbjørn Moe Eggebø: ULTRASOUND AND LABOUR
390. Eivind Wang: TRAINING IS MEDICINE FOR PATIENTS WITH PERIPHERAL ARTERIAL DISEASE
391. Thea Kristin Våtsveen: GENETIC ABERRATIONS IN MYELOMA CELLS
392. Thomas Jozefiak: QUALITY OF LIFE AND MENTAL HEALTH IN CHILDREN AND ADOLESCENTS: CHILD AND PARENT PERSPECTIVES
393. Jens Erik Slagsvold: N-3 POLYUNSATURATED FATTY ACIDS IN HEALTH AND DISEASE – CLINICAL AND MOLECULAR ASPECTS
394. Kristine Misund: A STUDY OF THE TRANSCRIPTIONAL REPRESSOR ICER. REGULATORY NETWORKS IN GASTRIN-INDUCED GENE EXPRESSION
395. Franco M. Impellizzeri: HIGH-INTENSITY TRAINING IN FOOTBALL PLAYERS. EFFECTS ON PHYSICAL AND TECHNICAL PERFORMANCE
396. Kari Hanne Gjeilo: HEALTH-RELATED QUALITY OF LIFE AND CHRONIC PAIN IN PATIENTS UNDERGOING CARDIAC SURGERY
397. Øyvind Hauso: NEUROENDOCRINE ASPECTS OF PHYSIOLOGY AND DISEASE
398. Ingvild Bjellmo Johnsen: INTRACELLULAR SIGNALING MECHANISMS IN THE INNATE IMMUNE RESPONSE TO VIRAL INFECTIONS
399. Linda Tømmerdal Roten: GENETIC PREDISPOSITION FOR DEVELOPMENT OF PREEMCLAMPSIA – CANDIDATE GENE STUDIES IN THE HUNT (NORD-TRØNDELAG HEALTH STUDY) POPULATION
400. Trude Teoline Nausthaug Rakvåg: PHARMACOGENETICS OF MORPHINE IN CANCER PAIN
401. Hanne Lehn: MEMORY FUNCTIONS OF THE HUMAN MEDIAL TEMPORAL LOBE STUDIED WITH fMRI
402. Randi Utne Holt: ADHESION AND MIGRATION OF MYELOMA CELLS – IN VITRO STUDIES –
403. Trygve Solstad: NEURAL REPRESENTATIONS OF EUCLIDEAN SPACE
404. Unn-Merete Fagerli: MULTIPLE MYELOMA CELLS AND CYTOKINES FROM THE BONE MARROW ENVIRONMENT; ASPECTS OF GROWTH REGULATION AND MIGRATION
405. Sigrid Bjørnelv: EATING– AND WEIGHT PROBLEMS IN ADOLESCENTS, THE YOUNG HUNT-STUDY
406. Mari Hoff: CORTICAL HAND BONE LOSS IN RHEUMATOID ARTHRITIS. EVALUATING DIGITAL X-RAY RADIOGRAMMETRY AS OUTCOME MEASURE OF DISEASE ACTIVITY, RESPONSE VARIABLE TO TREATMENT AND PREDICTOR OF BONE DAMAGE
407. Siri Bjørgen: AEROBIC HIGH INTENSITY INTERVAL TRAINING IS AN EFFECTIVE TREATMENT FOR PATIENTS WITH CHRONIC OBSTRUCTIVE PULMONARY DISEASE
408. Susanne Lindqvist: VISION AND BRAIN IN ADOLESCENTS WITH LOW BIRTH WEIGHT
409. Torbjørn Hergum: 3D ULTRASOUND FOR QUANTITATIVE ECHOCARDIOGRAPHY

410. Jørgen Urnes: PATIENT EDUCATION IN GASTRO-OESOPHAGEAL REFLUX DISEASE. VALIDATION OF A DIGESTIVE SYMPTOMS AND IMPACT QUESTIONNAIRE AND A RANDOMISED CONTROLLED TRIAL OF PATIENT EDUCATION
411. Elvar Eyjolfsson: 13C NMRS OF ANIMAL MODELS OF SCHIZOPHRENIA
412. Marius Steiro Fimland: CHRONIC AND ACUTE NEURAL ADAPTATIONS TO STRENGTH TRAINING
413. Øyvind Støren: RUNNING AND CYCLING ECONOMY IN ATHLETES; DETERMINING FACTORS, TRAINING INTERVENTIONS AND TESTING
414. Håkon Hov: HEPATOCYTE GROWTH FACTOR AND ITS RECEPTOR C-MET. AUTOCRINE GROWTH AND SIGNALING IN MULTIPLE MYELOMA CELLS
415. Maria Radtke: ROLE OF AUTOIMMUNITY AND OVERSTIMULATION FOR BETA-CELL DEFICIENCY. EPIDEMIOLOGICAL AND THERAPEUTIC PERSPECTIVES
416. Liv Bente Romundstad: ASSISTED FERTILIZATION IN NORWAY: SAFETY OF THE REPRODUCTIVE TECHNOLOGY
417. Erik Magnus Berntsen: PREOPERATIV PLANNING AND FUNCTIONAL NEURONAVIGATION – WITH FUNCTIONAL MRI AND DIFFUSION TENSOR TRACTOGRAPHY IN PATIENTS WITH BRAIN LESIONS
418. Tonje Strømmen Steigedal: MOLECULAR MECHANISMS OF THE PROLIFERATIVE RESPONSE TO THE HORMONE GASTRIN
419. Vidar Rao: EXTRACORPOREAL PHOTOCHEMOTHERAPY IN PATIENTS WITH CUTANEOUS T CELL LYMPHOMA OR GRAFT-vs-HOST DISEASE
420. Torkild Visnes: DNA EXCISION REPAIR OF URACIL AND 5-FLUOROURACIL IN HUMAN CANCER CELL LINES

2010

421. John Munkhaugen: BLOOD PRESSURE, BODY WEIGHT, AND KIDNEY FUNCTION IN THE NEAR-NORMAL RANGE: NORMALITY, RISK FACTOR OR MORBIDITY ?
422. Ingrid Castberg: PHARMACOKINETICS, DRUG INTERACTIONS AND ADHERENCE TO TREATMENT WITH ANTIPSYCHOTICS: STUDIES IN A NATURALISTIC SETTING
423. Jian Xu: BLOOD-OXYGEN-LEVEL-DEPENDENT-FUNCTIONAL MAGNETIC RESONANCE IMAGING AND DIFFUSION TENSOR IMAGING IN TRAUMATIC BRAIN INJURY RESEARCH
424. Sigmund Simonsen: ACCEPTABLE RISK AND THE REQUIREMENT OF PROPORTIONALITY IN EUROPEAN BIOMEDICAL RESEARCH LAW. WHAT DOES THE REQUIREMENT THAT BIOMEDICAL RESEARCH SHALL NOT INVOLVE RISKS AND BURDENS DISPROPORTIONATE TO ITS POTENTIAL BENEFITS MEAN?
425. Astrid Woodhouse: MOTOR CONTROL IN WHIPLASH AND CHRONIC NON-TRAUMATIC NECK PAIN
426. Line Rørstad Jensen: EVALUATION OF TREATMENT EFFECTS IN CANCER BY MR IMAGING AND SPECTROSCOPY
427. Trine Moholdt: AEROBIC EXERCISE IN CORONARY HEART DISEASE
428. Øystein Olsen: ANALYSIS OF MANGANESE ENHANCED MRI OF THE NORMAL AND INJURED RAT CENTRAL NERVOUS SYSTEM
429. Bjørn H. Grønberg: PEMETREXED IN THE TREATMENT OF ADVANCED LUNG CANCER
430. Vigdis Schnell Husby: REHABILITATION OF PATIENTS UNDERGOING TOTAL HIP ARTHROPLASTY WITH FOCUS ON MUSCLE STRENGTH, WALKING AND AEROBIC ENDURANCE PERFORMANCE
431. Torbjørn Øien: CHALLENGES IN PRIMARY PREVENTION OF ALLERGY. THE PREVENTION OF ALLERGY AMONG CHILDREN IN TRONDHEIM (PACT) STUDY.
432. Kari Anne Indredavik Evensen: BORN TOO SOON OR TOO SMALL: MOTOR PROBLEMS IN ADOLESCENCE
433. Lars Adde: PREDICTION OF CEREBRAL PALSY IN YOUNG INFANTS. COMPUTER BASED ASSESSMENT OF GENERAL MOVEMENTS
434. Magnus Fasting: PRE- AND POSTNATAL RISK FACTORS FOR CHILDHOOD ADIPOSITY
435. Vivi Talstad Monsen: MECHANISMS OF ALKYLATION DAMAGE REPAIR BY HUMAN AlkB HOMOLOGUES

436. Toril Skandsen: MODERATE AND SEVERE TRAUMATIC BRAIN INJURY. MAGNETIC RESONANCE IMAGING FINDINGS, COGNITION AND RISK FACTORS FOR DISABILITY
437. Ingeborg Smidesang: ALLERGY RELATED DISORDERS AMONG 2-YEAR OLDS AND ADOLESCENTS IN MID-NORWAY – PREVALENCE, SEVERITY AND IMPACT. THE PACT STUDY 2005, THE YOUNG HUNT STUDY 1995-97
438. Vidar Halsteinli: MEASURING EFFICIENCY IN MENTAL HEALTH SERVICE DELIVERY: A STUDY OF OUTPATIENT UNITS IN NORWAY
439. Karen Lehrmann Ægidius: THE PREVALENCE OF HEADACHE AND MIGRAINE IN RELATION TO SEX HORMONE STATUS IN WOMEN. THE HUNT 2 STUDY
440. Madelene Ericsson: EXERCISE TRAINING IN GENETIC MODELS OF HEART FAILURE
441. Marianne Klokk: THE ASSOCIATION BETWEEN SELF-REPORTED ECZEMA AND COMMON MENTAL DISORDERS IN THE GENERAL POPULATION. THE HORDALAND HEALTH STUDY (HUSK)
442. Tomas Ottemo Stølen: IMPAIRED CALCIUM HANDLING IN ANIMAL AND HUMAN CARDIOMYOCYTES REDUCE CONTRACTILITY AND INCREASE ARRHYTHMIA POTENTIAL – EFFECTS OF AEROBIC EXERCISE TRAINING
443. Bjarne Hansen: ENHANCING TREATMENT OUTCOME IN COGNITIVE BEHAVIOURAL THERAPY FOR OBSESSIVE COMPULSIVE DISORDER: THE IMPORTANCE OF COGNITIVE FACTORS
444. Mona Løvlien: WHEN EVERY MINUTE COUNTS. FROM SYMPTOMS TO ADMISSION FOR ACUTE MYOCARDIAL INFARCTION WITH SPECIAL EMPHASIS ON GENDER DIFFERECES
445. Karin Margaretha Gilljam: DNA REPAIR PROTEIN COMPLEXES, FUNCTIONALITY AND SIGNIFICANCE FOR REPAIR EFFICIENCY AND CELL SURVIVAL
446. Anne Byriel Walls: NEURONAL GLIAL INTERACTIONS IN CEREBRAL ENERGY – AND AMINO ACID HOMEOSTASIS – IMPLICATIONS OF GLUTAMATE AND GABA
447. Cathrine Fallang Knetter: MECHANISMS OF TOLL-LIKE RECEPTOR 9 ACTIVATION
448. Marit Følsvik Svindseth: A STUDY OF HUMILIATION, NARCISSISM AND TREATMENT OUTCOME IN PATIENTS ADMITTED TO PSYCHIATRIC EMERGENCY UNITS
449. Karin Elvenes Bakkelund: GASTRIC NEUROENDOCRINE CELLS – ROLE IN GASTRIC NEOPLASIA IN MAN AND RODENTS
450. Kirsten Brun Kjelstrup: DORSOVENTRAL DIFFERENCES IN THE SPATIAL REPRESENTATION AREAS OF THE RAT BRAIN
451. Roar Johansen: MR EVALUATION OF BREAST CANCER PATIENTS WITH POOR PROGNOSIS
452. Rigmor Myran: POST TRAUMATIC NECK PAIN. EPIDEMIOLOGICAL, NEURORADIOLOGICAL AND CLINICAL ASPECTS
453. Krisztina Kunszt Johansen: GENEALOGICAL, CLINICAL AND BIOCHEMICAL STUDIES IN *LRRK2* – ASSOCIATED PARKINSON'S DISEASE
454. Pål Gjerden: THE USE OF ANTICHOLINERGIC ANTIPARKINSON AGENTS IN NORWAY. EPIDEMIOLOGY, TOXICOLOGY AND CLINICAL IMPLICATIONS
455. Else Marie Huuse: ASSESSMENT OF TUMOR MICROENVIRONMENT AND TREATMENT EFFECTS IN HUMAN BREAST CANCER XENOGRAFTS USING MR IMAGING AND SPECTROSCOPY
456. Khalid S. Ibrahim: INTRAOPERATIVE ULTRASOUND ASSESSMENT IN CORONARY ARTERY BYPASS SURGERY – WITH SPECIAL REFERENCE TO CORONARY ANASTOMOSES AND THE ASCENDING AORTA
457. Bjørn Øglænd: ANTHROPOMETRY, BLOOD PRESSURE AND REPRODUCTIVE DEVELOPMENT IN ADOLESCENCE OF OFFSPRING OF MOTHERS WHO HAD PREECLAMPSIA IN PREGNANCY
458. John Olav Roaldset: RISK ASSESSMENT OF VIOLENT, SUICIDAL AND SELF-INJURIOUS BEHAVIOUR IN ACUTE PSYCHIATRY – A BIO-PSYCHO-SOCIAL APPROACH
459. Håvard Dalen: ECHOCARDIOGRAPHIC INDICES OF CARDIAC FUNCTION – NORMAL VALUES AND ASSOCIATIONS WITH CARDIAC RISK FACTORS IN A POPULATION FREE FROM CARDIOVASCULAR DISEASE, HYPERTENSION AND DIABETES: THE HUNT 3 STUDY
460. Beate André: CHANGE CAN BE CHALLENGING. INTRODUCTION TO CHANGES AND IMPLEMENTATION OF COMPUTERIZED TECHNOLOGY IN HEALTH CARE

461. Latha Nrugham: ASSOCIATES AND PREDICTORS OF ATTEMPTED SUICIDE AMONG DEPRESSED ADOLESCENTS – A 6-YEAR PROSPECTIVE STUDY
462. Håvard Bersås Nordgaard: TRANSIT-TIME FLOWMETRY AND WALL SHEAR STRESS ANALYSIS OF CORONARY ARTERY BYPASS GRAFTS – A CLINICAL AND EXPERIMENTAL STUDY

2011

463. Marte Helene Bjørk: DO BRAIN RHYTHMS CHANGE BEFORE THE MIGRAINE ATTACK? A LONGITUDINAL CONTROLLED EEG STUDY
464. Carl-Jørgen Arum: A STUDY OF UROTHELIAL CARCINOMA: GENE EXPRESSION PROFILING, TUMORIGENESIS AND THERAPIES IN ORTHOTOPIC ANIMAL MODELS
465. Ingunn Harstad: TUBERCULOSIS INFECTION AND DISEASE AMONG ASYLUM SEEKERS IN NORWAY. SCREENING AND FOLLOW-UP IN PUBLIC HEALTH CARE
466. Leif Åge Strand: EPIDEMIOLOGICAL STUDIES AMONG ROYAL NORWEGIAN NAVY SERVICEMEN. COHORT ESTABLISHMENT, CANCER INCIDENCE AND CAUSE-SPECIFIC MORTALITY
467. Katrine Høyer Holgersen: SURVIVORS IN THEIR THIRD DECADE AFTER THE NORTH SEA OIL RIG DISASTER OF 1980. LONG-TERM PERSPECTIVES ON MENTAL HEALTH
468. MarianneWallenius: PREGNANCY RELATED ASPECTS OF CHRONIC INFLAMMATORY ARTHRITIDES: DISEASE ONSET POSTPARTUM, PREGNANCY OUTCOMES AND FERTILITY. DATA FROM A NORWEGIAN PATIENT REGISTRY LINKED TO THE MEDICAL BIRTH REGISTRY OF NORWAY
469. Ole Vegard Solberg: 3D ULTRASOUND AND NAVIGATION – APPLICATIONS IN LAPAROSCOPIC SURGERY